Cyclo- and Polyphosphazenes Grafted with Tridentate Ligands Coordinated to Iron(II) and Ruthenium(II)

A thesis presented in partial fulfilment of the requirements for the degree of Doctor of Philosophy in Chemistry at Massey University, Palmerston North

Ross James Davidson

2011

Acknowledgements

First, I would like to thank my supervisors, Prof. Andrew Brodie, Assoc. Prof. Eric Ainscough and Dr Mark Waterland for their continued support during the course of this project and for allowing me the freedom to pursue a project of my own design.

I would also like to thank Prof. Geoff Jameson for his extensive help with both teaching me crystallography and helping me with all the difficult structures; Prof. Keith Murray, Dr Boujemaa Moubaraki and Prof. Jean-François Létard for the magnetic moment measurements; Prof. Keith Gordon and Raphael Horvath for collecting the variable temperature solid-state resonance Raman data; Prof. Guy Jameson for collecting the Mössbauer data; Prof. Harry Allcock and Dr Mark Hindenlang for the GPC and DSC measurements; Dr Matthias Lein for the use of his supercomputer; and the MacDiarmid Institute for access to their range of instruments. Without these people, much of this project would not have been possible.

The Massey University PhD scholarship must also be acknowledged for the financial support during the course of the project.

Finally, I would like to thank my girlfriend Helen Hsu for her support through the best and worst this project had to offer.

Abstract

This thesis sought to explore the chemical and physical properties of a series of cyclotri- and polyphosphazenes with substituted tridentate ligands coordinated to iron(II) and ruthenium(II). There were two main objective of this research i) to graft spin crossover (SCO) groups to a polymer backbone, potentially making a new malleable material, ii) to demonstrate that ruthenium(II) complexes can be used to link groups to a polyphosphazene backbone.

Seven cyclotriphosphazene (L^1–L^7) and four polyphosphazene (L^{1P}–L^{4P}) ligands[1] were synthesised with 2,6-di(pyridine-2-yl)pyridine-4(1*H*)-onate (OTerpy); 4-(2,6-di{pyridin-2-yl}-pyridine-4-yl)phenolate (OPhTerpy); 2,6-di(1*H*-benzimidazol-2-yl)pyridine-4(1*H*)-onate (Obbp); and 4-(2,6-di{1*H*-pyrazol-1-yl}pyridine-4-yl)phenolate (OPhbpp) moieties. These ligands were subsequently coordinated to either iron(II) or ruthenium(II) and the optical, vibrational, electrochemical and magnetic properties of the subsequent small molecule complexes and polymers were measured.

Sixteen iron(II) complexes were synthesised by reacting iron(II) salts with the respective ligand (L^1–L^7). Where X-ray crystal structures have been obtained, each of the small molecule iron complexes were homoleptic. Using electronic absorbance, resonance Raman (rR), magnetic and Mössbauer spectroscopy, it was shown that the polymer complex cores in the resulting cross-linked polymers were the same as those of the small molecule analogues (SMA). In addition, these techniques confirmed that the iron complexes formed with the ligands L^1, L^2, L^{1P} and L^{2P} were each determined to be low spin (LS), while those formed with L^3 displayed SCO, and the iron complex formed with L^4 remained high spin (HS) for all temperatures while its polymeric analogue remained LS for all measurable temperatures.

Fourteen ruthenium(II) small molecule complexes were synthesised by reacting ruthenium complexes of the appropriate co-ligands (2,2':6',2''-terpyridine (Terpy); 2,6-di(pyridin-2-yl)-4-phenylpyridine (PhTerpy); 2,6-di(1*H*-benzimidzol-2-yl)pyridine (bbp); and 2,6-di(1*H*-pyrazol-1-yl)pyridine) with the respective ligand (L^1–L^4). Using electronic absorption and rR spectroscopy it was determined that only the polymers L^{1P} and L^{2P} formed complexes ([Ru(L^{1P})(Terpy)]Cl_2, [Ru(L^{1P})(PhTerpy)]Cl_2,

[1] See pull out sheet for ligand structures.

[Ru(L^{2P})(Terpy)]Cl_2 and [Ru(L^{2P})(PhTerpy)]Cl_2) analogous to that of their SMA ([Ru(L^1)(Terpy)]$(PF_6)_2$, [Ru(L^1)(PhTerpy)]$(PF_6)_2$, [Ru(L^2)(Terpy)]$(PF_6)_2$ and [Ru(L^2)(PhTerpy)]$(PF_6)_2$), and are therefore the most suitable for linking groups to polyphosphazenes.

Although the ruthenium-bbp-terpy based complexes proved to be unsuitable for attaching groups to a phosphazene due to the low loading of metal complex on the polymer (L^{3P}), the SMA ([Ru(L^1)(bbp)]$(PF_6)_2$, [Ru(L^2)(bbp)]$(PF_6)_2$, [Ru(L^3)(Terpy)]$(PF_6)_2$ and [Ru(L^3)(PhTerpy)]$(PF_6)_2$) displayed a dependence on the basicity of the solution. As it was increased, the imidazole groups were deprotonated causing a bathochromic shifting of the metal-to-ligand charge transfer, oxidation potential and selected vibrational modes.

Table of Contents

List of Figures

List of Tables

Chapter 1

An introduction to phosphazenes

1.0 Abbreviations used in Chapter 1

Biphen	2,2′-Biphenol
NLO	Non-linear optics
PEO	Polyethylene oxide
OLED	Organic light emitting diode
ROP	Ring opening polymerization
TFE	Trifluoroethanol

1.1 Introduction and applications

The name phosphazene refers to a large class of inorganic molecules that have an unsaturated phosphorus-nitrogen backbone,[1] as shown in Figure 1.1.1.

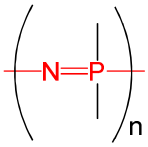

Figure 1.1.1 The PN backbone of a phosphazene.

Parent phosphazenes, which have the formula $[NPCl_2]_n$, are readily functionalized by nucleophilic attack. By removing a proton from an alcohol, amine or thiol, the chlorine is readily replaced by the nucleophile, making it a simple process to attach different substituents to the phosphazene backbone (see Figure 1.1.2 for an example[2]) and making phosphazenes useful for a variety of different applications.

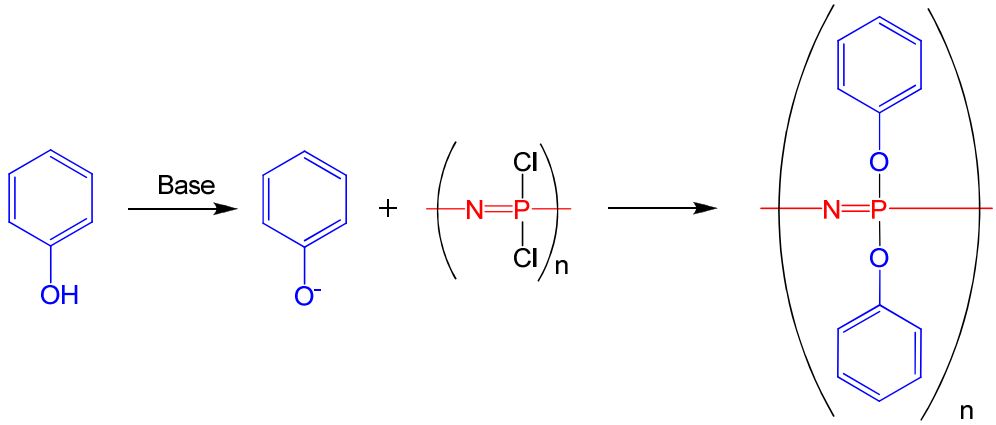

Figure 1.1.2 Example of a phosphazene substitution reaction with phenol.[2]

As well as the polymer chains, phosphazenes also form cyclic molecules with varied ring sizes.[3-5] Also, other heteroatoms may be included in the ring (see Figure 1.1.3).[6-8]

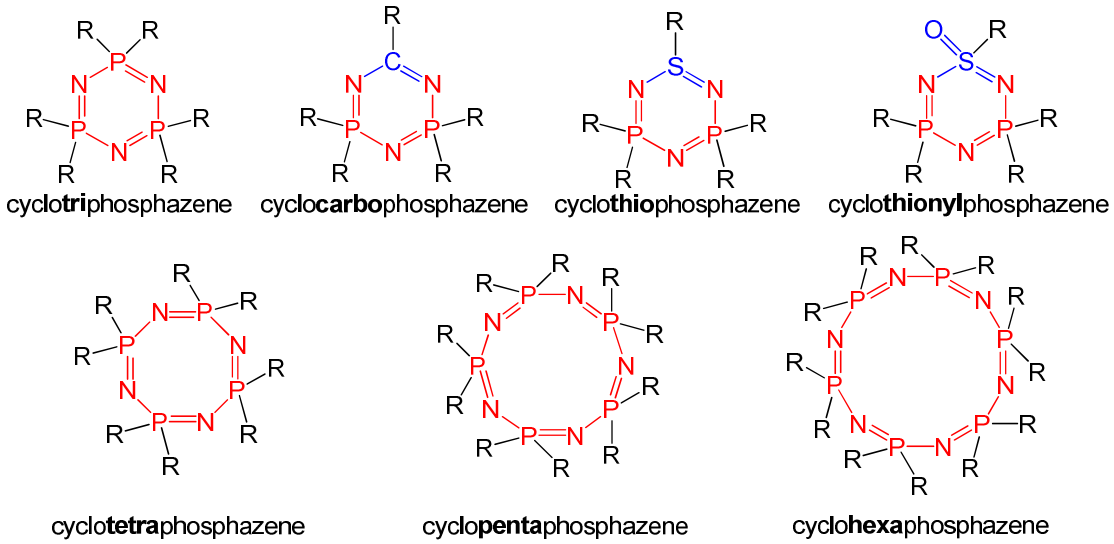

Figure 1.1.3 Examples of cyclic phosphazenes (R can be any substituent).[3-8]

Cyclotriphosphazene (trimer) and cyclotetraphosphazene (tetramer) are the most studied of the cyclic phosphazenes,[9] as they are more easily and cheaply synthesized.[10] Unlike the polymer, it is possible to get well-resolved X-ray structures of trimeric[11-13] and tetrameric[14-16] species, allowing their molecular structures to be studied more accurately than the polymer and making them ideal models for the polymer systems.

Both cyclomers and polymers have found applications ranging from flame retardant materials[17] to drug delivery systems[18]. One of the most thoroughly studied applications is the production of solid state polymer membranes for the purpose of lithium ion batteries.[19,20] In these systems, an assortment of ether groups was attached to the phosphazene backbone, and the polymer was then soaked in a solution containing a LiX (X = anion) salt. When a potential is applied to the polymer, this causes the lithium ions to migrate (see Figure 1.1.4).

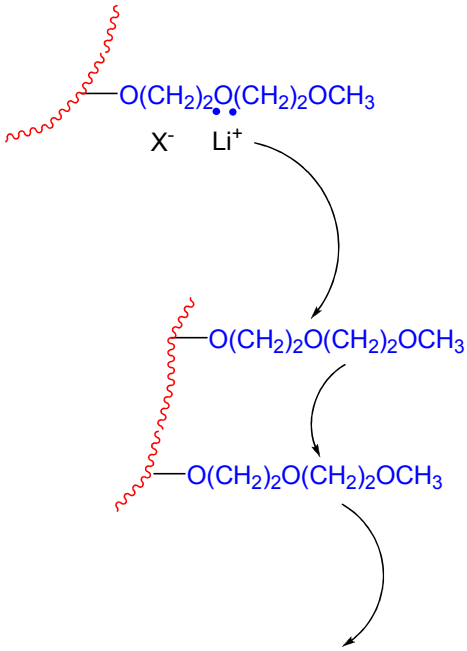

Figure 1.1.4 A schematic view of how a phosphazene-lithium ion membrane works.[19,20]

Using a material with a polyphosphazene backbone has three advantages over polyethylene oxide (PEO), currently used for lithium ion membranes:[21,22]

i) the phosphazene polymers are more flexible than PEO;
ii) they are completely amorphous; and
iii) they have a higher concentration of etheric oxygen atoms per repeating unit in which increases the number of cation coordination sites.[9]

Phosphazene trimers have also been used for an assortment of optical applications. Recently, one was used to produce an organic light-emitting diode (OLED).[23] In this case, the trimer unit was substituted with amino-pyrene groups, forming the dendrimer unit (shown in Figure 1.1.5). This system is ideal because it is able to be produced in high purity via chromatography and it also has the advantage of being soluble, allowing it to be dip-coated onto a surface containing a conducting polymer, thus providing a convenient method for electro-luminescent device production.

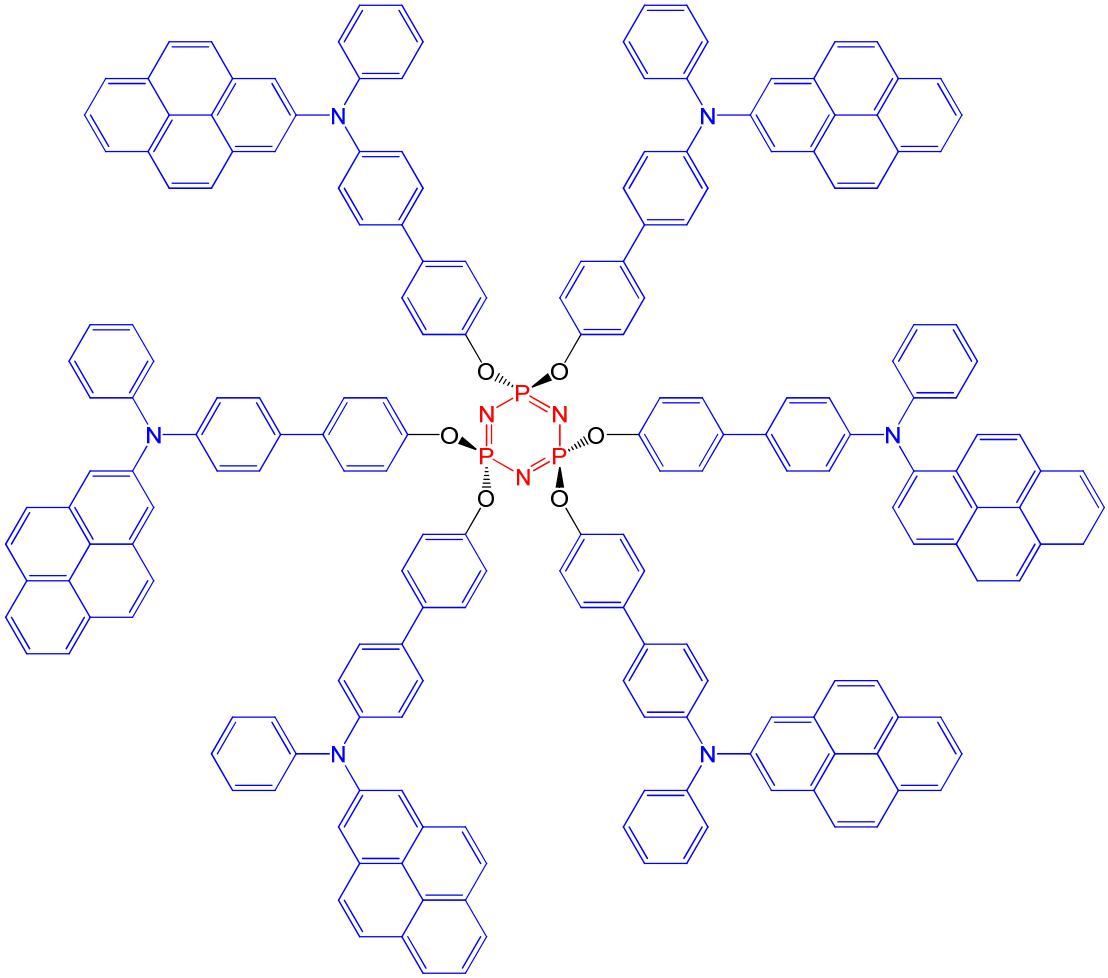

Figure 1.1.5 An example of an OLED dendrimer unit based on a phosphazene trimer.[23]

Polyphosphazenes also have interesting optical properties. While the phosphazene backbone is optically invisible until the infrared region, the addition of aromatic groups can form a polymer with refractive indices to the order of 1.75[24] (fused silica has a refractive index of 1.459[25]). Unlike the carbon-based analogues, the polymer remains stable after continued exposure to laser light.[9] The polyphosphazene also shows non-linear optical (NLO) properties, displaying second order (χ^2) and third order (χ^3) behaviour. For a material to display χ^2 behaviour requires the presence of a non-centrosymmetric solid state structure.[26] This was achieved by Dembak and Allcock by attaching groups similar to those found in liquid crystalline species to the phosphazene backbone (Figure 1.1.6).[27-30] To maximize the χ^2 behaviour, the polymer should ideally be fully substituted, as each unit has a strong dipole, resulting in delocalization. However, in practice, this causes the polymer to be very insoluble and, to account for

this, trifluoroethanol is used as a co-substituent in varying ratios.[28, 29] This resulted in a decrease in χ^2 but it increased the solubility and the T_g temperature.

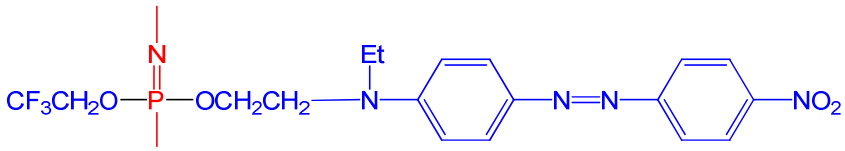

Figure 1.1.6 A phosphazene polymer substituted with a liquid crystalline-type substituent for NLO properties.[28]

Due to the zwitterionic nature of the PN bond, research was performed to obtain χ^3 optical materials based on phosphazenes. It was found that by adding electron-donating groups to the phosphazene (such as SMe) to perturb the backbone bonding, resulted in a χ^3 value almost as large as CS_2.[9] However, to date, this has only been tentatively explored.

These are only a few examples of applications relating to the physical properties of the phosphazene. However, they have found applications in most areas of society, such as elastomers[31], protective coatings[32], semiconductors[33], magnetic recording media[34], adhesives[35], bone replacement[36] and even lubricants[37].

1.2 Benefits and effects of heterosubstituted phosphazenes

A benefit of the phosphazene system is that it is able to be hetero-substituted (i.e. two or more different substituents can be attached) relatively easily. There can be many reasons for doing this, such as altering solubility[12], crystal engineering[38], additional functionalities[39], and simplifying chemistry[40].

2,2´-biphenol (biphen) is one of the most common substituents that can be added to a phosphazene because this makes it possible to control the number of biphens that are attached (see Figure 1.2.1).[41] Mono and bis-biphen substituted phosphazenes can be more soluble in organic solvents than the fully substituted phosphazene. Their introduction also reduces the number of reactive sites and thereby provides greater control over substitution reactions, and also it can add additional sites for π-π interactions.[42] Phenols are used for similar purposes. However, it is more difficult to control the number being attached.[43] They are typically more soluble than the biphen groups, due to the additional degrees of freedom. Phenols can be used to replace unreacted chlorines to make the molecule more stable.[39]

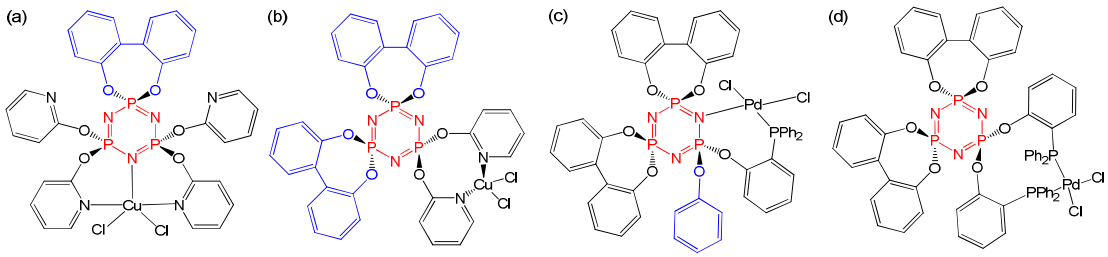

Figure 1.2.1 (a) One biphenol used to control coordination. (b) Two biphenols used to control coordination. (c) a phenol controlling coordinating behaviour. (d) the absence of a phenol controlling the coordination behaviour.[11,39,40,44]

As seen in Figure 1.2.1 (left), adding an additional biphen group to the phosphazene has reduced the number of pyridoxy groups capable of coordinating, resulting in the copper no longer bonding to the phosphazene ring nitrogen.[40] However, when a phosphine group[11] is replaced with a phenol (Figure 1.2.1 (right)), it causes the palladium to coordinate to the phosphazene ring nitrogen, as there are no other coordination sites available.[39]

Different substituents can also be added to provide additional functions or tune an existing system, such as adding a hard donor group to a soft donor group[39] (see Figure 1.2.2) for catalysis. This feature makes phosphazenes unique, as no other synthetic macromolecule provides this ease of modification.

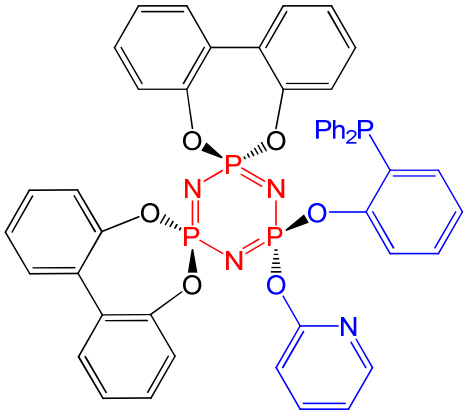

Figure 1.2.2 Semi-hard donor (pyridine) and soft donor (phosphine) groups attached to a phosphazene.[39]

Not only can the substituents be varied but also the linkers can be changed. The linkers are the atoms, or groups, that join the substituent to the phosphorus atom. The two most common ones are oxygen and nitrogen. However, sulfur and other substituents can also be directly attached to the phosphorus atoms. Changing these linkers can have an effect on the reactivity of the phosphazene.[45] Nitrogen atoms are more electron-donating than oxygens.[46] Therefore, using a nitrogen linker causes the ring nitrogen to be more basic, resulting in the ring nitrogen being more likely to coordinate to metal ions. The length of the linker can also be varied, resulting in strained, or very relaxed bonding angles, depending on the lengths (see Figure 1.2.3).[47-52]

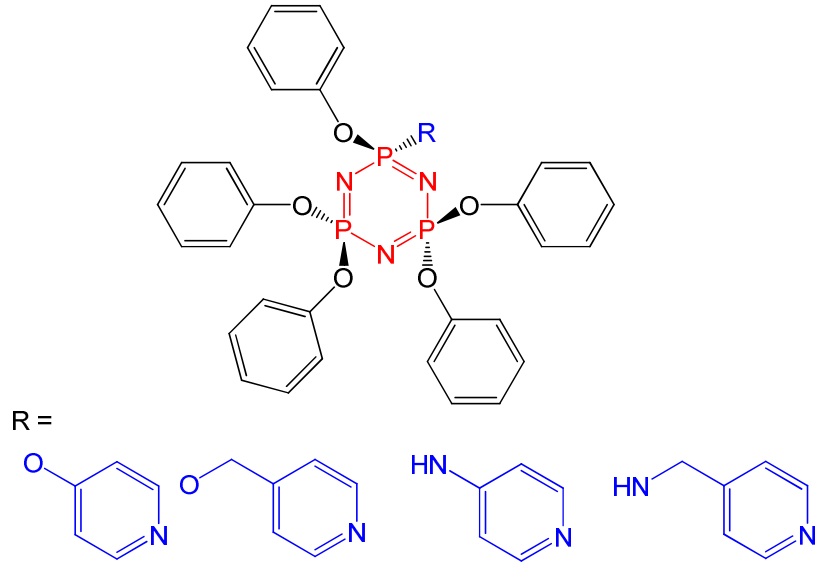

Figure 1.2.3 Examples of the variation of substituent linkers.[47-52]

1.3 Phosphazenes and metals

A phosphazene can interact with a metal in five different ways:[45]

i) form a cationic salt with the metal ion;
ii) coordinate to the ring nitrogen;
iii) coordinate via exocyclic groups substituted to the phosphazene ring;
iv) coordinate to the phosphorus atom via a covalent bond; and
v) form an anionic bond with the phosphazene ring.

Examples of each of these types are now given.

Cationic salts normally occur when the substituents attached to the phosphazene are strong electron donors. For these phosphazenes, the ring nitrogen is readily protonated, forming a cation - this cation then forms a salt with a metal complex, such as $PtCl_4^{2-}$ (see Figure 1.3.1).[53]

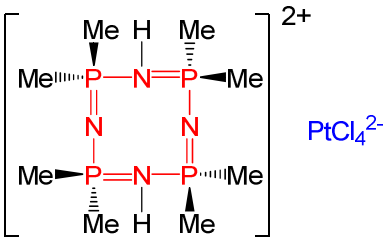

Figure 1.3.1 Example of an ionic phosphazene salt.[53]

If the phosphazene is not protonated, it is possible to coordinate the metal ion directly to the ring phosphazene (see Figure 1.3.2). It is noted that, when this coordination occurs, the flanking PN bonds lengthen due to electron density being removed from the PN bonding orbital and going into the 4s or 5s orbital of the metal ion.[54]

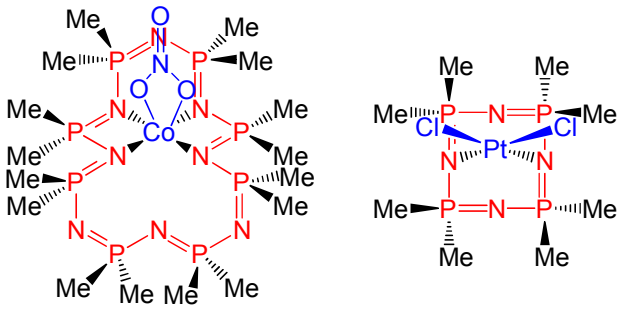

Figure 1.3.2 Examples of metal ions coordinating to ring nitrogens.[55,56]

Substituents attached to the phosphazene can act as ligands themselves. This is a rich area of research due to the numerous potential ligands that could be attached. Shown in Figure 1.3.3 are just four examples.[11,57,58]

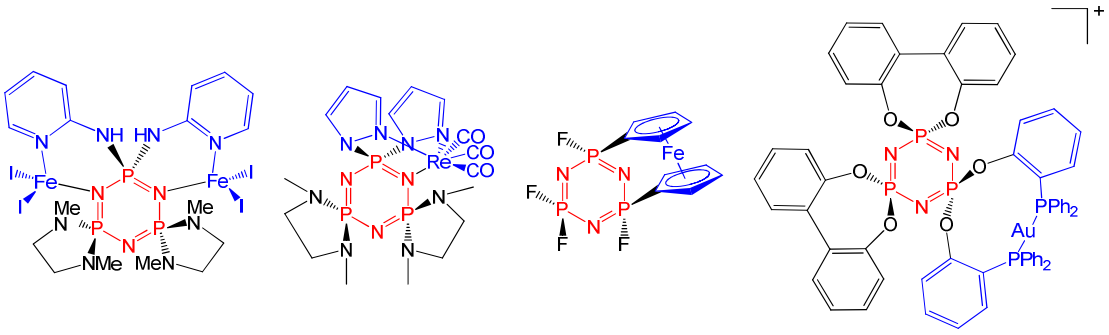

Figure 1.3.3 Examples of exocyclic substituents coordinating to metal ions.[11,57,58]

In some cases, the metal itself can act as the substituent, forming a covalent bond with the phosphorus atom. This is a somewhat specialized case and occurs when the phosphorus has a vacant site. This can occur via a tautomer of the hydridocyclophosphazene (see Figure 1.3.4).[59] Covalent bonds can also be formed via a nucleophilic substitution, using an organometallic anion similar to other nucleophilic substitutions with other substituents (see Figure 1.3.4).[60]

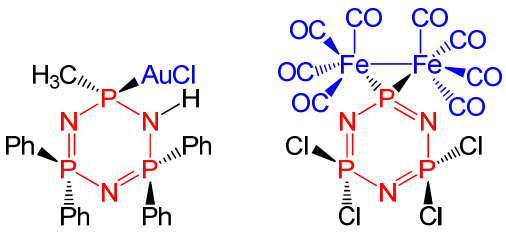

Figure 1.3.4 Example of a metal coordinating to the phosphazene phosphorus.[59,60]

The final form of interaction with a metal is when the phosphazene is anionic, and this typically occurs when a strong base, such as n-butyllithium, is reacted with an amine-substituted phosphazene, removing the proton from the amine and leaving the phosphazene with an overall negative charge (see Figure 1.3.5).[61]

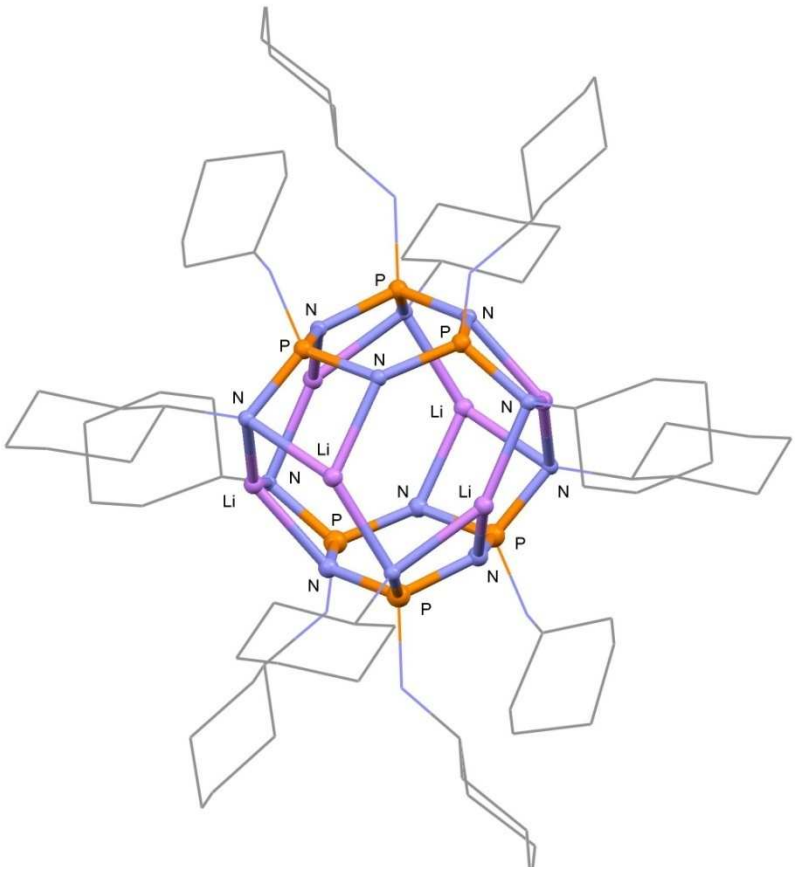

Figure 1.3.5 An example of an anionic phosphazene interacting with a metal, $Li_6[P_3N_3\{N(C_6H_{10})_6\}]_2$.[61]

1.4 Phosphazene polymers

1.4.1 Phosphazene polymer history

The phosphazene trimer was obtained and purified over 160 years ago by Lieberg, Wohler[62] and Rose[63] from reactions with PCl_5 and NH_3. However, it was not until the 1890s that the first polymer was produced by Stokes[64-68]. This was achieved by heating the trimer to form an 'inorganic rubber'. This polymer was cross-linked and, therefore, not soluble in any solvents. It did swell, however, showing that solvent was being absorbed into the polymer matrix. In the 1960s, three key papers were published by Allcock, Kugel and Valan. The first[69] stated that the polymer had a tendency to hydrolyze and suggested that it was very reactive so that other groups could be added. The second[70] suggested that Stokes' polymer may have been cross-linked, due to its swelling when in a solvent. It also said that, if the polymer had been linear, it may be soluble and substitutions may go to completion. In this paper, Allcock and Best described that, by careful control of reaction times and conditions, a linear polymer could be formed.

The third paper by Allcock and Kugel[71] showed that it was possible to replace chlorine groups with organic nucleophiles. These key papers effectively started the phosphazene polymer age which has given rise to an assortment of polymers with different substituents and a variety of ways for forming the polymer.

1.4.2 Polymerization methods

1.4.2.1 The ring opening polymerization

The phosphazene polymer can be made using a variety of methods - the simplest and most commonly used in research laboratories is the ring opening polymerization (ROP) of the trimer unit.[9] This can be performed with a substituted or halogenated trimer unit. The general procedure is as follows:

i) The trimer is sublimed to remove any impurities that may inhibit the polymerization (see Figure 1.4.2.1.1).

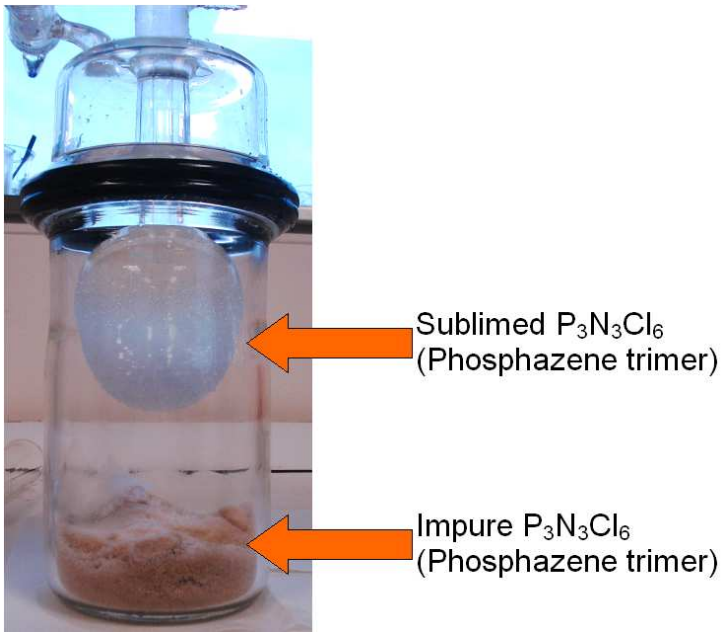

Figure 1.4.2.1.1 Trimer initially being sublimed.

ii) The freshly sublimed trimer is ground down into a fine powder and placed into a glass tube. It is necessary to use a freshly annealed tube because it has been suggested that the polymerization is initiated through the interaction between the silica and the trimer. It is also necessary to thoroughly dry the trimer using a high vacuum (see Figure 1.4.2.1.2) - as the trimer absorbs water from the atmosphere, and this inhibits the formation of the polymer in high concentrations.[72]

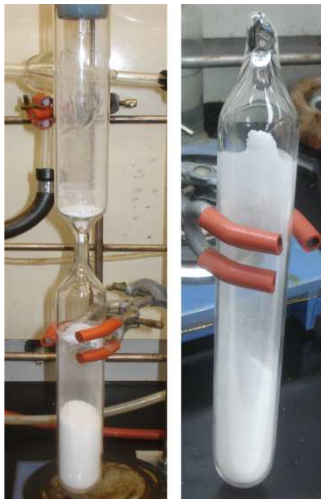

Figure 1.4.2.1.2 Left: Trimer under vacuum in tube. Right: Trimer in sealed tube.

iii) The trimer is then rocked gently in an oven at 250°C - this is the polymerization step. The rocking is continued until the free-flowing liquid becomes very viscous (see Figure 1.4.2.1.3), showing almost no movement while rocking. This can take anywhere from 6-11 hours.[9]

Figure 1.4.2.1.3 Left: Trimer rocked in oven. Right: Molten polymer.

iv) The final step is to sublime the unreacted trimer out of the polymer (see Figure 1.4.2.1.4), leaving a white elastic solid - the polymer. The chlorinated polymer must be stored in an inert environment to prevent it from hydrolyzing.

Figure 1.4.2.1.4 Polymer remaining at the bottom of the sublimator.

The accepted mechanism for the ring opening polymerization is shown in Figure 1.4.2.1.5.[73] However, there is still much speculation over the initiation of the polymerization: it is known that the silica surface has significant involvement and that, for polymerization to occur, it is necessary to have traces of water present. Early studies were performed prior to the distinction between cross-linked and linear polymers having been made,[74-76] making the measurements less meaningful.

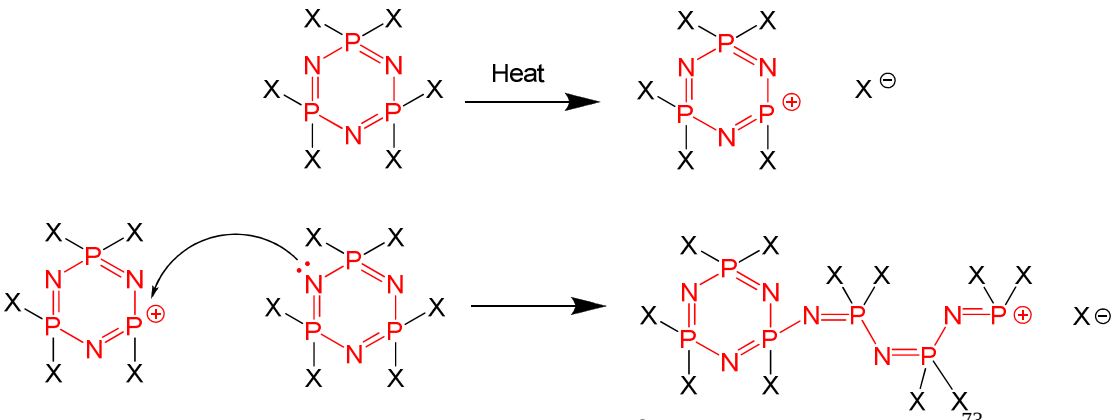

Figure 1.4.2.1.5 Accepted mechanism for ROP, X = Cl, Br or F.[73]

Due to the negative hyper-conjugation component of the bonding,[46] the halogen is able to be removed as Cl^-, allowing another ring nitrogen to attack the positive phosphorus atom. If the polymerization was performed with hexakischlorocyclotriphosphazene, further reactions can then performed to add the substituents, as is the case for the trimer species.[9]

1.4.2.2 Living Cationic Polymerization

The next most common method is the Living Cationic Polymerization of $Me_3SiN{=}PCl_3$. In this method, a condensation between $Cl_3P{=}NSiMe_3$ and PCl_5 occurs. The polymerization is normally initiated by the addition of a Lewis acid and propagates as follows:[77]

Initiation

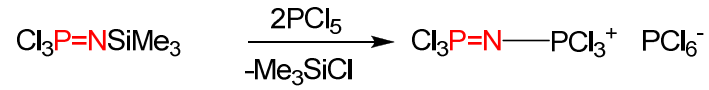

Chain Growth

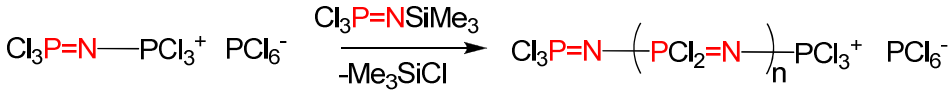

Halogen Replacement

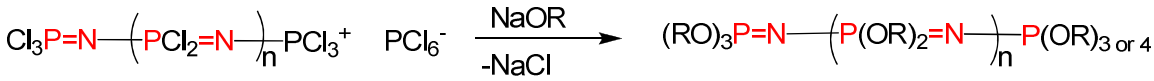

The Living Cationic Polymerization has several advantages over the ROP: it gives far greater control over the molecular weight, a much lower polydispersive index (PDI), and the ability to form block polymers.[78] However, this method can be difficult to use due to the high reactivity of the intermediate species. There are several other methods used, such as condensations of PCl_5 and NH_4Cl[9] or $Cl_3P{=}NP(O)Cl_2$[79], or anionic condensation.[80] However, these are either less reliable or more complex to perform than the ROP or Living Cationic methods.

1.4.3 Polyphosphazenes and their Common Substituents

Like the cyclic phosphazenes, the polymer can also have hetero-substituents used to alter its physical and chemical properties. A common one used is 2,2,2-trifluoroethanol (TFE) (see Figure 1.4.3.1).[81] This has the effect of making the polymer insoluble in water or chloroform, allowing the reactants to be separated from the polymer.

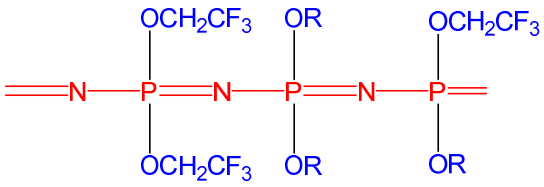

Figure 1.4.3.1 A TFE-substituted polymer (R can be any substituent).[81]

Once again, biphen is a commonly used substituent,[41] and this, unlike TFE, occupies two available sites on each phosphorus atom, leaving two sites available on the unsubstituted phosphorus atoms (see Figure 1.4.3.2).

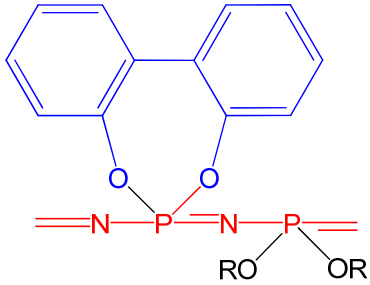

Figure 1.4.3.2 Biphen-substituted polymer (R can be substituent).[41]

The substituents also play a significant role in the stability of the polymer. In some cases, the substituents will attack the polymer backbone which is a major problem with substituents that have nitrogens held close to the backbone,[82] such as pyridine-substituted polymers. For these systems, the pyridine causes the polymer to break down and, to compensate for this, the ratio of pyridine to the other substituent is decreased (see Figure 1.4.3.3).[83]

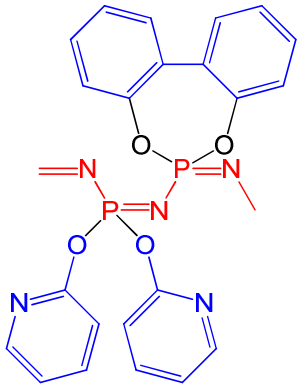

Figure 1.4.3.3 A pyridine-substituted polymer stabilized with biphen.[83]

1.4.4 Polyphosphazene Structure

The structure of the polymer has been a topic of debate but it has now been accepted that the polymer backbone occurs in a cis-trans conformation to reduce steric hindrance.[9]

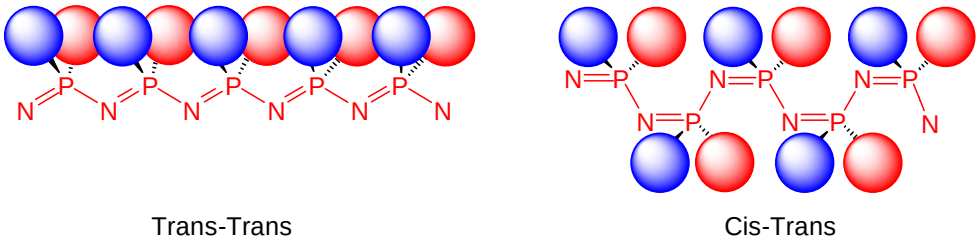

Figure 1.4.4.1 A schematic diagram showing the difference in steric hindrance between a trans-trans and cis-trans polymer.[9]

Further information using powder diffraction suggested that a stretched polymer has a helical structure to the PN backbone (see Figure 1.4.4.2).[9] These measurements are of particular importance for the design of systems as the aromatic groups can be held over each other slightly displaced through rotation. While no evidence has shown that substituents interact with each other along the chain (as opposed to intermolecular interactions), interactions could be possible with bulky groups attached. It has been found that attaching large aromatic groups increases the crystalline regions found in the polymer.

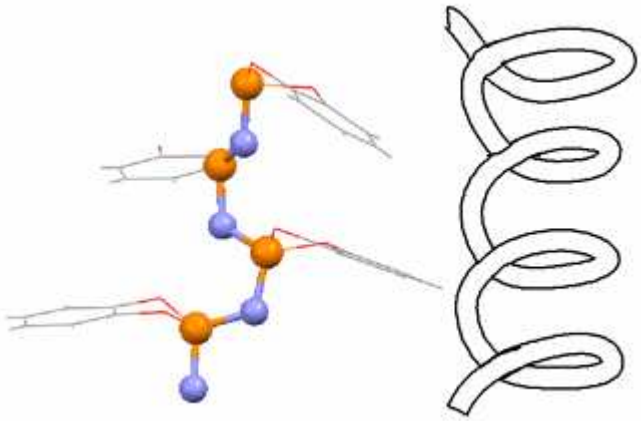

Figure 1.4.4.2 Proposed structure of the phosphazene backbone.[9]

1.5 References

1. Shriver, D. F.; Atkins, P. W. *Inorganic Chemistry*; 3rd ed.; Springer: New York, **2002**.

2. Ye, C. F.; Zhang, Z. F.; Liu, W. M. P. *Synthetic Communications* **2002**, *32*, 203-209.

3. Gallicano, K. D.; Oakley, R. T.; Paddock, N. L.; Rettig, S. J.; Trotter, J. *Canadian Journal of Chemistry-Revue Canadienne De Chimie* **1977**, *55*, 304-309.

4. Gallicano, K. D.; Paddock, N. L.; Rettig, S. J.; Trotter, J. *Canadian Journal of Chemistry-Revue Canadienne De Chimie* **1981**, *59*, 2435-2440.

5. Oakley, R. T.; Paddock, N. L.; Rettig, S. J.; Trotter, J. *Canadian Journal of Chemistry-Revue Canadienne De Chimie* **1977**, *55*, 2530-2533.

6. Bolhuis, F.; Grampel, J. C. *Acta Crystallographica* **1976**, *B32*, 1192.

7. Allcock, H. R.; Coley, S. M.; Manners, I.; Visscher, K. B.; Parvez, M.; Nuyken, O.; Renner, G. *Inorganic Chemistry* **1993**, *32*, 5088-5094.

8. Dodge, J. A.; Manners, I.; Allcock, H. R.; Renner, G.; Nuyken, O. *Journal of the American Chemical Society* **1990**, *112*, 1268-1269.

9. Allcock, H. R. *Chemistry and Applications of Polyphosphazenes*; John Wiley & Sons Inc: Hoboken, **2003**.

10. Lund, L. G.; Paddock, N. L.; Proctor, J. E.; Searle, H. T. *Journal of the Chemical Society* **1960**, 2542-2547.

11. Ainscough, E. W.; Brodie, A. M.; Chaplin, A. B.; O'Connor, J. M.; Otter, C. A. *Dalton Transactions* **2006**, 1264-1266.

12. Ainscough, E. W.; Brodie, A. M.; Jameson, G. B.; Otter, C. A. *Polyhedron* **2007**, *26*, 460-471.

13. Allcock, H. R.; Cho, S. Y.; Steely, L. B. *Macromolecules* **2006**, *39*, 8334-8338.

14. Muralidharan, K.; Omotowa, B. A.; Twamley, B.; Piekarski, C.; Shreeve, J. M. *Chemical Communications* **2005**, 5193-5195.

15. Jung, J. H.; Pomeroy, J. C.; Zhang, H. M.; Wisian-Neilson, P. *Journal of the American Chemical Society* **2003**, *125*, 15537-15542.

16. Ainscough, E. W.; Brodie, A. M.; Derwahl, A. *Polyhedron* **2003**, *22*, 189-197.

17. Sasakura, T.; Yamazoe, O. In *Japanese Patent*; Ltd, N. B. C. L. a. N. I. K., Ed. Japan, **1998**; Vol. 77/139, p 156.

18. Vandorpe, J.; Schacht, E.; Dunn, S.; Hawley, A.; Stolnik, S.; Davis, S. S.; Garnett, M. C.; Davies, M. C.; Ilium, L. *Biomaterials* **1997**, *16*, 1147-1152.

19. Blonsky, P. M.; Shriver, D. F.; Austin, P.; Allcock, H. R. *Journal of the American Chemical Society* **1984**, *106*, 6854-6855.

20. Allcock, H. R.; Austin, P. E.; Neenan, T. X.; Sisko, J. T.; Blonsky, P. M.; Shriver, D. F. *Macromolecules* **1986**, *19*, 1508-1512.

21. Ratner, M. A.; Shriver, D. F. *Chemical Reviews* **1988**, *88*, 109-124.

22. Fenton, D. E.; Parker, J. M.; Wright, P. V. *Polymer* **1973**, *14*, 589-589.

23. Bolink, H. J.; Barea, E.; Costa, R. D.; Coronado, E.; Sudhakar, S.; Zhen, C.; Sellinger, A. *Organic Electronics* **2008**, *9*, 155-163.

24. Allcock, H. R.; Bender, J. D.; Chang, Y. K.; McKenzie, M.; Fone, M. M. *Chemistry of Materials* **2003**, *15*, 473-477.

25. Lide, D. R. *Hand Book of Chemistry and Physics*; 71st ed.; CRC Press: USA, **1991**.

26. Pedrotti, F. L. *Introduction to Optics*; 2nd ed.; Prince Hall International: London, **1993**.

27. Dembek, A. A.; Kim, C.; Allcock, H. R.; Devine, R. L. S.; Steier, W. H.; Spangler, C. W. *Chemistry of Materials* **1990**, *2*, 97-99.

28. Allcock, H. R.; Dembek, A. A.; Kim, C.; Devine, R. L. S.; Shi, Y. Q.; Steier, W. H.; Spangler, C. W. *Macromolecules* **1991**, *24*, 1000-1010.

29. Allcock, H. R.; Ravikiran, R.; Olshavsky, M. A. *Macromolecules* **1998**, *31*, 5206-5214.

30. Rojo, G.; Agullo-Lopez, F.; Carriedo, G. A.; Alonso, F. J. G.; Martinez, J. I. F. *Synthetic Metals* **2000**, *115*, 241-244.

31. Rose, S.; Reynard, K. P., Elastomer In *U.S. Patent*; Inc., H., Ed. U.S., **1974**; Vol. Patent 3, p 713.

32. Chattopadhyay, A. K.; Hinrichs, R. L.; Rose, S. H. *Journal of Coatings Technology* **1979**, *51*, 87-98.

33. Allcock, H. R.; Levin, M. L.; Austin, P. E. *Inorganic Chemistry* **1986**, *25*, 2281-2288.

34. Co., I. P. In *Japanese Patent* Japan, **1987**; Vol. 87/299, p 676.

35. Yaguchi, A. In *Japanese Patent*; Ltd, I. P. C., Ed. Japan, **1990**; Vol. 90/2, p 187.

36. Nukavarapu, S. P.; Kumbar, S. G.; Brown, J. L.; Krogman, N. R.; Weikel, A. L.; Hindenlan, M. D.; Nair, L. S.; Allcock, H. R.; Laurencin, C. T. *Biomacromolecules* **2008**, *9*, 1818-1825.

37. Singler, R.; Bieberich, M. *Sythetic Lubricants and High Performance Functional Fluids*; Shubkin, R., Dekker: New York, **1992**.

38. Itaya, T.; Sasaki, Y.; Tanigaki, T.; Matsumoto, A.; Inoue, K. *Chemistry Letters* **1996**, 305-306.

39. Ainscough, E. W.; Brodie, A. M.; Otter, C. A. *Unpublished results*.

40. Ainscough, E. W.; Brodie, A. M.; Derwahl, A.; Kirk, S.; Otter, C. A. *Inorganic Chemistry* **2007**, *46*, 9841-9852.

41. Carriedo, G. A.; FernandezCatuxo, L.; Azonso, F. J. G.; GomezElipe, P.; Gonzalez, P. A. *Macromolecules* **1996**, *29*, 5320-5325.

42. Ainscough, E. W.; Brodie, A. M.; Chaplin, A. B.; Derwahl, A.; Harrison, J. A.; Otter, C. A. *Inorganic Chemistry* **2007**, *46*, 2575-2583.

43. McBee, E. T.; Okuhara, K.; Morton, C. J. *Inorganic Chemistry* **1966**, *5*, 450-457.

44. Ainscough, E. W.; Brodie, A. M.; Depree, C. V.; Moubaraki, B.; Murray, K. S.; Otter, C. A. *Dalton Transactions* **2005**, 3337-3343.

45. Gleria, M.; De Jaeger, R. *Phosphazenes: a worldwide insight*; Nova Science Publishers: New York, **2004**.

46. Chaplin, A. B.; Harrison, J. A.; Dyson, P. J. *Inorganic Chemistry* **2005**, *44*, 8407-8417.

47. Carriedo, G. A.; Elipe, P. G.; Alonso, F. J. G.; Fernandezcatuxo, L.; Diaz, M. R.; Granda, S. G. *Journal of Organometallic Chemistry* **1995**, *498*, 207-212.

48. Cho, Y. H.; Baek, H.; Sohn, Y. S. *Macromolecules* **1982**, *15*, 689.

49. Cho, Y. H.; Baek, H.; Sohn, Y. S. *Macromolecules* **1999**, *32*, 2167-2172.

50. Diefenbach, U.; Kretschmann, M.; Cavdarci, O. *Phosphorus Sulfur and Silicon and the Related Elements* **1994**, *93*, 415-416.

51. Inoue, K.; Itaya, T. *Supramolecular Science* **1998**, *5*, 163-166.

52. Bloy, M.; Kretschmann, M.; Scholz, S.; Teichert, M.; Diefenbach, U. *Zeitschrift Fur Anorganische Und Allgemeine Chemie* **2000**, *626*, 1946-1957.

53. Obrien, J. P.; Allen, R. W.; Allcock, H. R. *Inorganic Chemistry* **1979**, *18*, 2230-2235.

54. Ainscough, E. W.; Brodie, A. M.; Davidson, R. J.; Moubaraki, B.; Murray, K. S.; Otter, C. A.; Waterland, M. R. *Inorganic Chemistry* **2008**, *47*, 9182-9192.

55. Calhoun, H. P.; Paddock, N. L.; Wingfield, J. N. *Canadian Journal of Chemistry-Revue Canadienne De Chimie* **1975**, *53*, 1765-1774.

56. Allcock, H. R.; Allen, R. W.; Obrien, J. P. *Journal of the American Chemical Society* **1977**, *99*, 3984-3987.

57. Harmjanz, M.; Piglosiewicz, I. M.; Scott, B. L.; Burns, C. J. *Inorganic Chemistry* **2004**, *43*, 642-650.

58. Saraceno, R. A.; Riding, G. H.; Allcock, H. R.; Ewing, A. G. *Journal of the American Chemical Society* **1988**, *110*, 7254-7255.

59. Schmidpeter, A.; Blanck, K.; Hess, H.; Riffel, H. *Angewandte Chemie-International Edition in English* **1980**, *19*, 650-651.

60. Allcock, H. R.; Suszko, P. R.; Wagner, L. J.; Whittle, R. R.; Boso, B. *Journal of the American Chemical Society* **1984**, *106*, 4966-4977.

61. Steiner, A.; Wright, D. S. *Chemical Communications* **1997**, 283-284.

62. Liebig, J. *Journal of Annular Chemistry* **1834**, *11*, 139-145.

63. Rose, H. *Journal of Annular Chemistry* **1834**, *11*, 131-139.

64. Stokes, H. N. *American Chemical Journal* **1896**, *18*, 629-663.

65. Stokes, H. N. *American Chemical Journal* **1896**, *18*, 780-789.

66. Stokes, H. N. *American Chemical Journal* **1897**, *19*, 782-796.

67. Stokes, H. N. *American Chemical Journal* **1898**, *20*, 740-760.

68. Stokes, H. N. *Chemische Berichte* **1895**, *28*, 437-439.

69. Allcock, H. R.; Kugel, R. L. *Journal of the American Chemical Society* **1965**, *87*, 4216-4217.

70. Allcock, H. R.; Kugel, R. L.; Valan, K. J. *Inorganic Chemistry* **1966**, *5*, 1709-1715.

71. Allcock, H. R.; Kugel, R. L. *Inorganic Chemistry* **1966**, *5*, 1716-1718.

72. Allcock, H. R.; Gardner, J. E.; Smeltz, K. M. *Macromolecules* **1975**, *8*, 36-42.

73. Mark, J. E.; Allcock, H. R.; West, R. *Inorganic Polymers*; 2nd ed.; Oxford Press: Oxford, **2005**.

74. Schmitz-DuMont, O. *Angewandte Chemie International Ed* **1939**, *52*, 498.

75. Chakrabartty, D.; Ghosh, B. N. *Journal of Polymer Science* **1962**, *62*, S130-132.

76. Konecny, J. O.; Douglas, C. M. *Journal of Polymer Science* **1959**, *36*, 195-203.

77. Allcock, H. R.; Reeves, S. D.; Nelson, J. M.; Crane, C. A.; Manners, I. *Macromolecules* **1997**, *30*, 2213-2215.

78. Matyjaszewski, K.; Moore, M. K.; White, M. L. *Macromolecules* **1993**, *26*, 6741-6748.

79. Potin, P.; Dejaeger, R. *Phosphorus Sulfur and Silicon and the Related Elements* **1993**, *76*, 487-490.

80. Montague, R. A.; Matyjaszewski, K. *Journal of the American Chemical Society* **1990**, *112*, 6721-6723.

81. Singh, A.; Steely, L.; Allcock, H. R. *Langmuir* **2005**, *21*, 11604-11607.

82. Diefenbach, U.; Allcock, H. R. *Inorganic Chemistry* **1994**, *33*, 4562-4565.

83. Kirk, S. *Cyclo- and Polyphosphazenes Containing 2-oxypyridine Moieties Coordinated to Selected Transition Metals*, Massey University, Palmerston North, **2008**.

Chapter 2

Synthesis and characterisation of cyclotriphosphazene based ligands.

2.0 Abbreviations used in Chapter 2

SCO	Spin crossover
NMR	Nuclear magnetic resonance
ESMS	Electrospray mass spectroscopy
HOPhTerpy	4-(2,6-di{pyridin-2-yl}-pyridine-4-yl)phenol
OPhTerpy	4-(2,6-di{pyridin-2-yl}-pyridine-4-yl)phenolate
HOTerpy	2,6-di(pyridine-2-yl)pyridine-4(1*H*)-one
OTerpy	2,6-di(pyridine-2-yl)pyridine-4(1*H*)-onate
HObbp	2,6-di(1*H*-benzimidazol-2-yl)pyridine-4(1*H*)-one
Obbp	2,6-di(1*H*-benzimidazol-2-yl)pyridine-4(1*H*)-onate
HOPhbpp	4-(2,6-di{1*H*-pyrazol-1-yl}pyridine-4-yl)phenol
OPhbpp	4-(2,6-di{1*H*-pyrazol-1-yl}pyridine-4-yl)phenolate
HObpp	2,6-di(1*H*-pyrazol-1-yl)pyridine-4(1*H*)-one
HOPhbbp	4-(2,6-di{1*H*-benzimidazol-2-yl}pyridine-4-yl)phenol
HOQsal	(*E*)-2-({quinolin-8-ylimino}methyl)benzene-1,4-diol
Biphen	2,2´-Biphenol
TBAB	Tetrabutyl ammonium bromide
NfF	1,1,2,2,3,3,4,4,4-nonafluorobutane-1-sulfonyl fluoride
$HOPh^{tBu}$	4-*tert*-butylphenol
THF	Tetrahydrofuran

2.1 Introduction

The body of this research has two overall aims:

(i) To undertake the synthesis of polyphosphazenes containing spin crossover (SCO) groups attached. Such a system would allow systems that have long been suggested to form circuits or devices that could take advantage of the switching ability of SCO materials.[1]

(ii) To undertake the synthesis of polyphosphazenes containing coordination linking groups for the purposes of attaching other functionalities to the polyphosphazene backbone without the need of alcohol, amines or basic conditions.

In order to elucidate possible pathways and develop new polyphosphazenes, the role of small cyclic model systems is crucial to establish that the substitution of these functionalities is possible and to identify the optimal conditions for these reactions to occur. The use of small molecules as templates allows for ease of synthesis and, since the chloropolymer $[NPCl_2]_n$ is exceedingly sensitive to hydrolysis,[2] permits the use of standard techniques for analysis, such as Electrospray Mass Spectra (ESMS) and X-ray crystallography which are not suitable for polymer materials. In addition the CHN micro-analytical figures for polymers invariably demonstrate greater variance than for small molecules.[3]

Accurate characterisation of polymeric materials is fraught with uncertainty, especially when more than one side group or co-substituent is attached to the polymer backbone. By their very nature polyphosphazenes are flexible, having a very low bond torsion[4] and random orientations which lead to localised, semi-ordered aggregations, hence the formation of lamellae and semi-crystalline regions with amorphous phases. These different phases are greatly affected by the size and chemical nature of the side groups as well as the distribution of these groups along the backbone. For a short chain length polymer, end group concentration may also become a factor in the micro- and macroscopic properties. In co-substituent polymers the distribution of the side groups and degree of tacticity can only be reasoned in terms of statistical probability, although for phosphazene polymers with organic side groups, $^{31}P\{^{1}H\}$ Nuclear Magnetic Resonance (NMR) spectra can give insight into the number distribution of the side

groups by integration of spectral peaks, though random nature of the polymers often leads to line broadening and thus a degree of uncertainty.[4] Also, unlike the cyclophosphazenes, the polymer may exist in various conformations due to the random orientation of the backbone. The inherent flexibility may also reduce the ability to coordinate to transition metals by favouring π-π stacking, for example, aryloxy pendant moieties.

2.1.1 Synthetic approach

The synthetic approach to forming substituted phosphazenes typically relies on the substitution of the chlorine atoms of the hexachlorocyclotriphosphazene with a suitable nucleophile (Nuc^-) (see Figure 2.1.1.1).

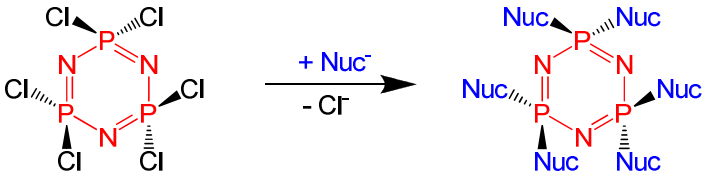

Figure 2.1.1.1 Nucleophilic substitution of hexachlorocyclotriphosphazene.

The mechanism for this substitution is still a field of scholarly debate. For amines and many other nucleophiles the substitution patterns (and therefore the mechanism) are dependent on the amine (or nucleophile); however, there is strong evidence to show that the base and the solvent used can play a role.

The substitution of phenols has a much simpler mechanism than other nucleophiles. From previous studies it has been suggested that they substitute via an S_N2 type mechanism (see Figure 2.1.1.2).[4]

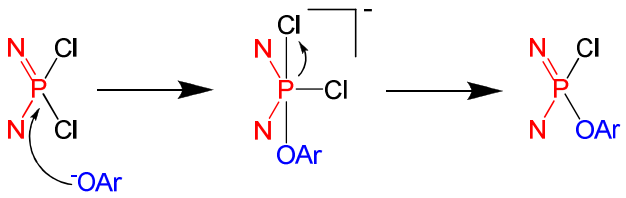

Figure 2.1.1.2 Mechanism for the aryloxy substitution of a chlorine for a phosphazene.[4]

This systematic substitution typically results in non-geminal substitution; depending on the size of the substituent either the *cis* or *trans* species can be formed. If the substituent is large then the *trans* form is favoured to reduce steric hindrance. For smaller substituents a mixture of *cis* and *trans* tends to be formed (see Figure 2.1.1.3).[5-7]

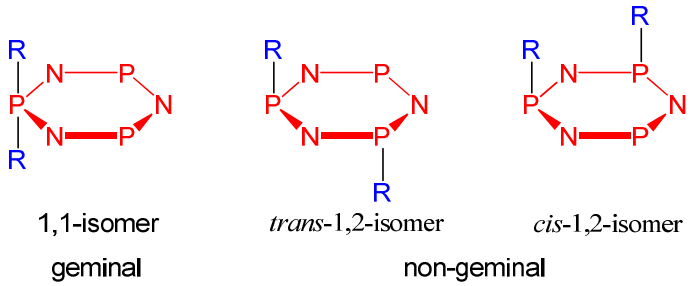

Figure 2.1.1.3 Potential substitution patterns for a cyclotriphosphazene.

2.1.2 Phosphazene Decay

The stability of phosphazenes has often been their downfall. They can break down by two different mechanisms i) by hydrolytic decay or ii) by substituent interactions. Hydrolytic decay occurs as a result of water or hydroxide substituting the groups attached to the phosphazene, most commonly chlorine. This substitution gradually leads to the formation of a phosphate and ammonia (see Figure 2.1.2.1).[2] This can be reduced by preventing water reacting with the phosphazene, either by keeping it dry or using highly hydrophobic substituents. Alternatively, strongly attached substituents could be used to prevent substitution with water or hydroxide ions.

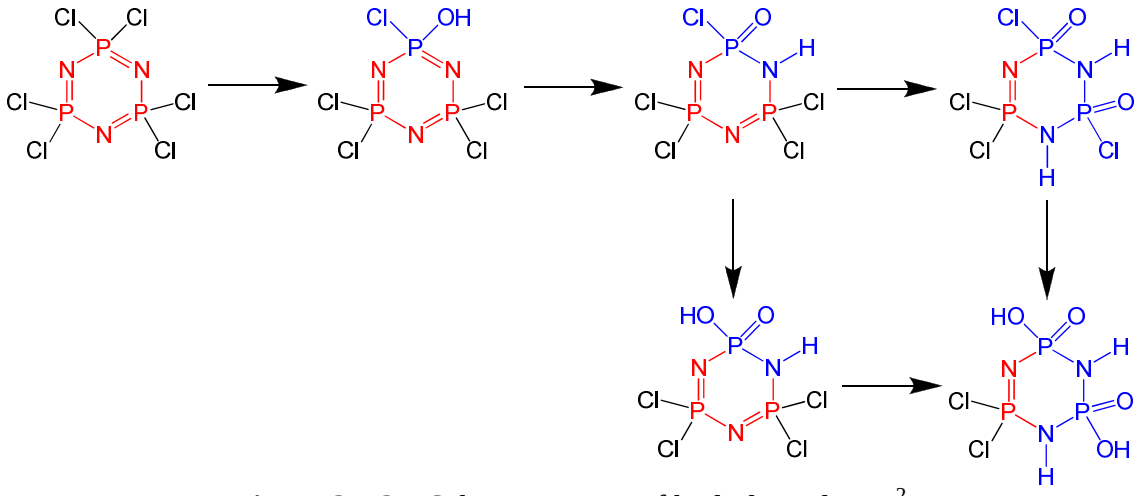

Figure 2.1.2.1 Schematic view of hydrolytic decay.[2]

The second and less understood decay mechanism occurs via substituent interaction. This often occurs when pyridine nitrogens are held ortho to the phosphazene linker. In each example the lone pair of the nitrogen is interacting with a π orbital of the phosphazene ring, resulting in the pyridine being held over the phosphazene ring.[8] It was suggested by Davidson *et al.*[9] that this interaction facilitates the breaking of the P=N bond promoting decay (see Figure 2.1.2.2).

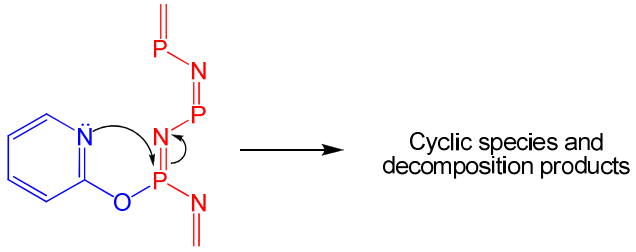

Figure 2.1.2.2 Schematic view of decay via a substituent interaction.[9]

2.2 Synthesis of ligands

A brief overview of the literature[10-25] was performed to find SCO ligands that contained a phenol and when coordinated to iron forms SCO complexes or can be systematically coordinated to ruthenium to build larger complexes. The candidates chosen for investigation are shown in Figure 2.2.1.

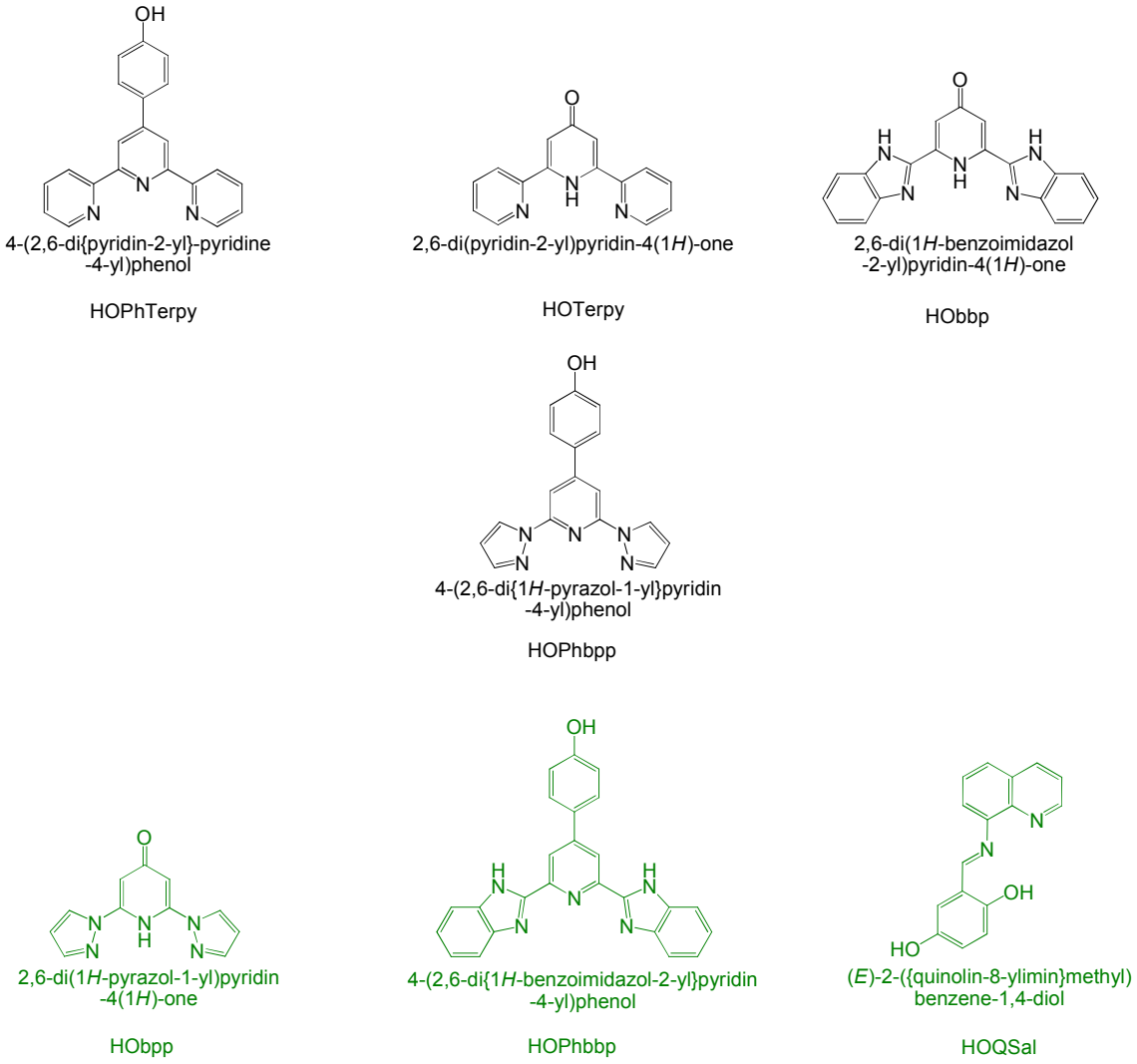

Figure 2.2.1 Ligands investigated using the trimeric phosphazene. Black: compounds that have already been reported. Green: proposed compounds.

Depending on the substituents, three possible phosphazene combinations were used as part of the investigation shown in Figure 2.2.2.

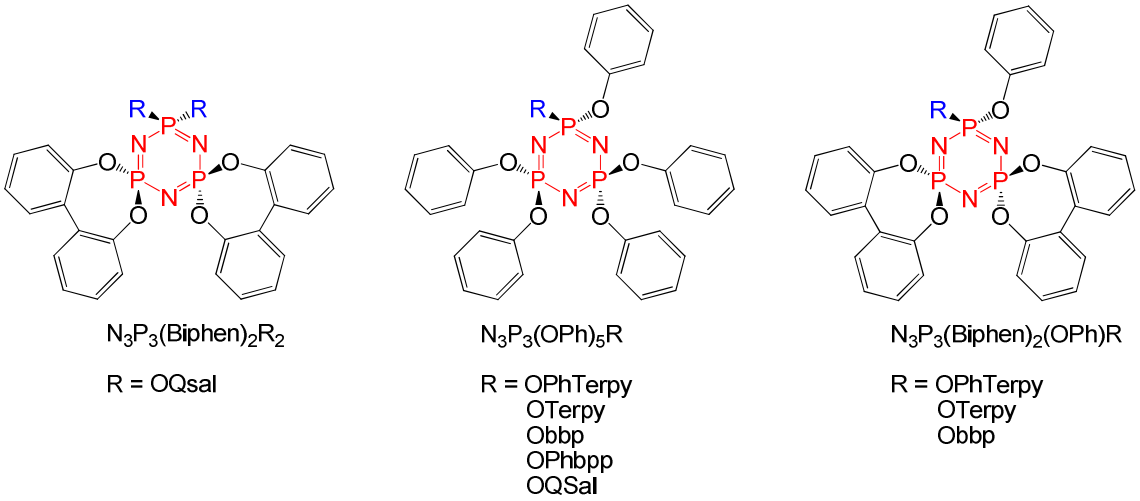

Figure 2.2.2 Substitution patterns of the proposed compounds.

The 2,2′-biphenol (biphen) substituents were used because their substitution can be controlled to substitute one or two phosphorus atoms in a *geminal* fashion.[26] The phenols were used because it is possible to control the substitution,[27] and the complexes formed with this type of phosphazene tend to form crystals more often than other substituents.[28] In addition, it is intended to use 4-*tert*-butylphenol (OPh^{tBu}) as the co-substituent for the polyphosphazene to maintain high solubility. However, phosphazene trimer complexes formed with OPh^{tBu} as a co-substituent tend to form oils, therefore this was not used for the small molecule model. The experimental data for the synthesis of each ligand is described in Appendix A.

2.3 Comments and observations about the ligand synthesis

By the addition of the appropriate nucleophiles (refer to Figure 2.2.1) to the phosphazene units (refer to Figure 2.2.2) eight phosphazene ligands were successfully synthesised and characterised (see Figure 2.3.1). These will serve as models for their polyphosphazene analogues.

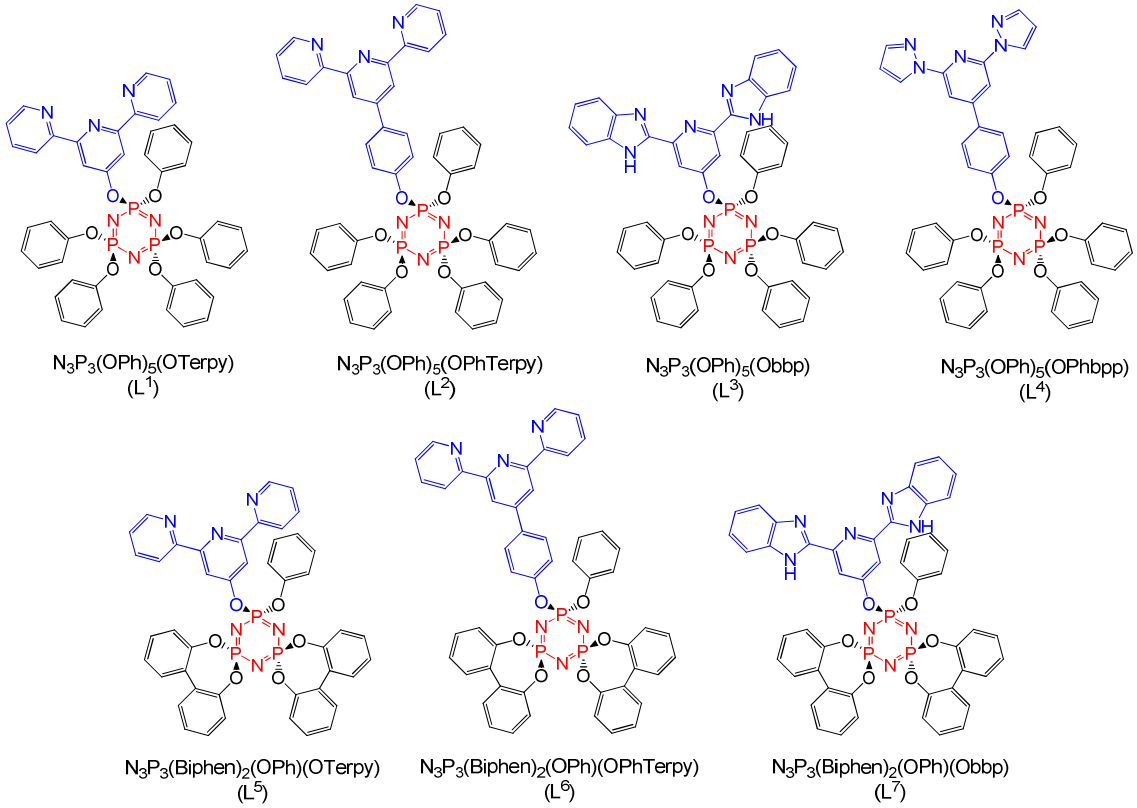

Figure 2.3.1 Synthesised ligands.

2.3.1 2,6-bis(2-pyridyl)-4(1*H*)-pyridonate and 2,6-di(1*H*-benzimidazol-2-yl)pyridine-4(1*H*)-onate based ligands

The ligands L^1, L^3, L^5 and L^7 were synthesised by reacting the respective enone with either $N_3P_3(OPh)_5Cl$ (L^1 and L^3) and $N_3P_3(Biphen)_2Cl_2$ (L^5 and L^7). In comparison to analogous reactions with phenol the reactions with 2,6-bis(2-pyridyl)-4(1*H*)-pyridonate (OTerpy) and 2,6-di(1*H*-benzimidazol-2-yl)pyridine-4(1*H*)-onate (Obbp) are slow taking three days and five days respectively. The reactions were slow because HOTerpy and HObbp exist as the enone tautomers (see Figure 2.3.1.1).

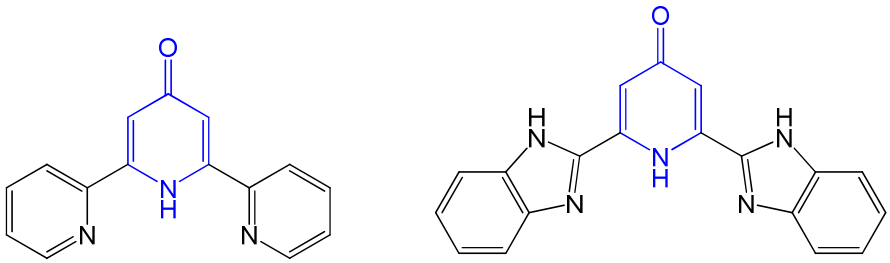

Figure 2.3.1.1 The enone structures of HOTerpy (left) and HObbp (right).

The enone tautomer causes the proton to be much less acidic than it would be for an analogous phenol, therefore lowering the reactivity of the nucleophile. Further evidence is provided during the synthesis of L^5 or L^7, where either HOTerpy or HObbp is reacted with $N_3P_3(Biphen)_2Cl_2$. Despite the ratios of the substituent or the addition of a promoter (such as a TBAB) the reaction will only proceed to the monosubstituted species.

As proof that it is the poor acidity of the substituent rather than the deactivation of the phosphorus atom, the unreacted chlorine is able to be replaced with a phenol (see Figure 2.3.1.2).

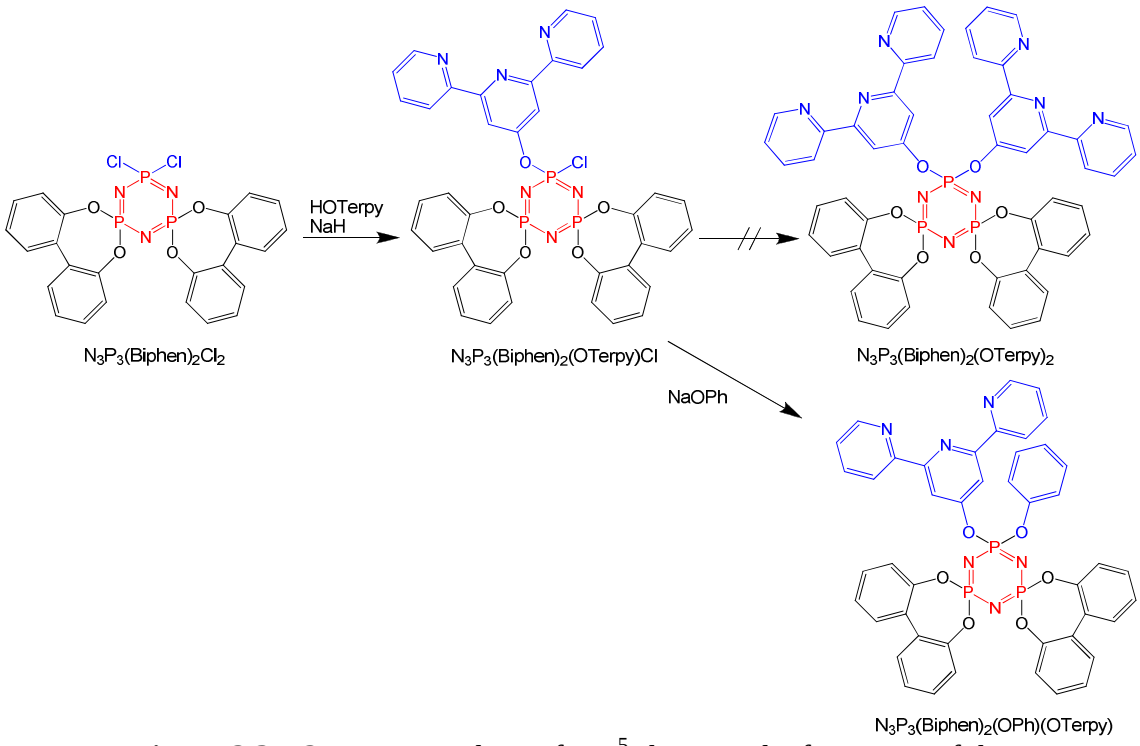

Figure 2.3.1.2 Reaction scheme for L^5 showing the formation of the $N_3P_3(Biphen)_2(OTerpy)Cl$ intermediate species.

The reaction of HObbp was notably slower than that of HOTerpy for two reasons: i) a carbonate base was used to prevent the imidazole ring from being deprotonated and potentially reacting with the phosphazene, ii) HObbp was insoluble in most solvents except acetone, this decreased solubility and being a solvent with a low boiling point adds to the slow reaction.

2.3.2 4-(2,6-di{pyridin-2-yl}-pyridine-4-yl)phenolate and 4-(2,6-di{1*H*-pyrazol-1-yl}pyridine-4-yl)phenolate based ligands

L^2, L^4 and L^6 were synthesised by reacting the respective nucleophile with either $N_3P_3(OPh)_5Cl$ (L^2 and L^4) or $N_3P_3(Biphen)_2Cl_2$ (L^6) in THF. Unlike OTerpy and Obbp, 4-(2,6-di{pyridin-2-yl}-pyridine-4-yl)phenolate (OPhTerpy) and 4-(2,6-di{1*H*-pyrazol-1-yl}pyridine-4-yl)phenolate (OPhbpp) do not favour the enone tautomers, therefore the nucleophiles behave as phenols. This results in the reaction occurring overnight rather than 3-5 days. The enone isn't favoured for these complexes because the phenyl rings

are almost perpendicular to each other resulting in low charge delocalisation (see Figure 2.3.2.1).

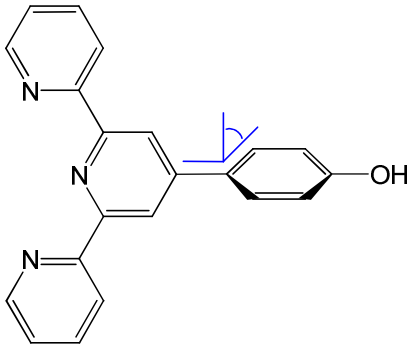

Figure 2.3.2.1 Phenyl ring twisting.

The reactivity of the nucleophiles is further displayed when reacting with $N_3P_3(Biphen)_2Cl_2$, if care is not taken in the ratios of the reactants the geminal disubstituted species is formed instead of monosubstituted species.

The reaction of the $N_3P_3(Biphen)_2Cl_2$ and HOPhbpp was not explored due to difficulty of producing HOPhbpp.

2.3.4 HOQSal

Attempts were made to react (*E*)-2-({quinolin-8-ylimino}methylbenzene-1,4-diol) (HOQSal) (see Appendix A) with both $N_3P_3(Biphen)_2Cl_2$ and $N_3P_3(OPh)_5Cl$, using both potassium carbonate and triethylamine as bases. However, no signs of reaction were observed. This may be due to the delocalisation of charge around the 2,5-dihydroxybenzene group, reducing its acidity (see Figure 2.3.4.1).

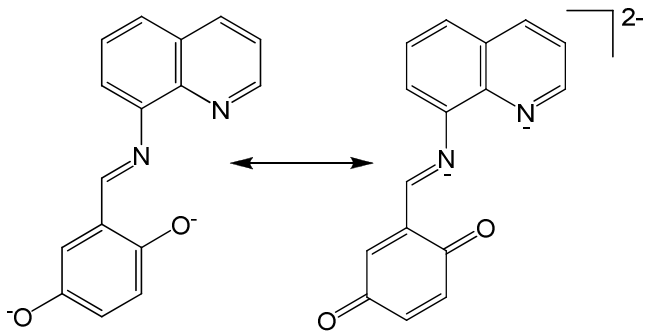

Figure 2.3.4.1 [OQSal]$^{2-}$ resonance structure.

Several different approaches could be employed to increase the chances of a successful reaction: i) NaH could be used, being a stronger base it may drive the reaction further; however, it is likely that this base would damage the imine bond; ii) coordinating the ligand to iron before reacting it with a phosphazene would make the phenol group more acidic; however, this would result in a diphenol system which would result in cross linking – not an ideal candidate for forming a polymer.

2.3.5 2,6-di(1*H*-pyrazol-1-yl)pyridine-4(1*H*)-one and 4-(2,6-di{1*H*-benzimidazol-2-yl}pyridine-4-yl)phenol

Neither 2,6-di(1*H*-pyrazol-1-yl)pyridine-4(1*H*)-one (HObpp) nor 4-(2,6-di{1*H*-benzimidazol-2-yl}pyridine-4-yl)phenol (HOPhbbp) were successfully synthesised. While 4-methoxy-2,6-di(1*H*-pyrazol-1-yl)pyridine (MeObpp) was synthesised according to the literature, the yields for this were poor, most likely due to the methoxy groups deactivating the pyridine ring towards nucleophilic reactions. In addition a successful deprotection step was not found for the removal of the methyl group. PyHCl and BBr_3 were both tried; however, these typically resulted in reactions with the pyrazol groups in addition to the methyl group. While further approaches could have been investigated it was outside the scope of this project (see Figure 2.3.5.1).

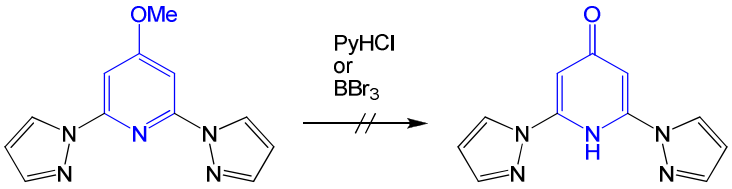

Figure 2.3.5.1 Proposed deprotection of MeObpp.

HOPhbbp may have been synthesised (see Figure 2.3.5.2) as indicated by the ESMS mass spectroscopy data collected (see Appendix A); however, the product was so insoluble that it would be impossible to dissolve it in a solvent suitable for a phosphazene substitution.

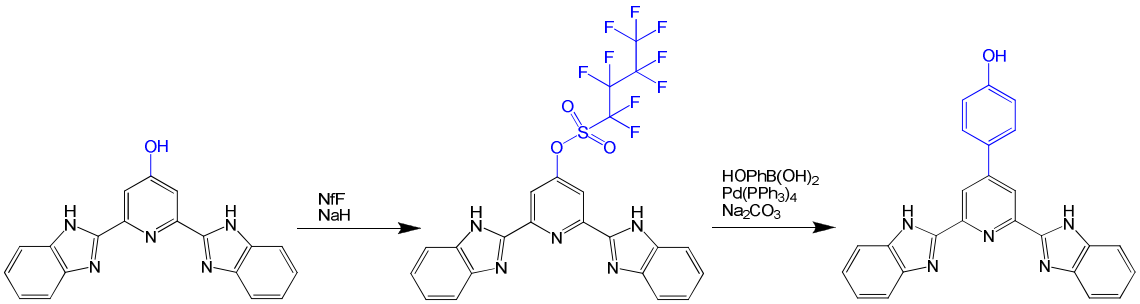

Figure 2.3.5.2 Reaction scheme for the formation of HOPhbbp.

2.4 Crystallography

The X-ray data for $L^5 \cdot 2CH_2Cl_2$ was collected on a Siemens P4 four-circle diffractometer, using a Siemens SMART 1K CCD area detector. The crystal was mounted in an inert oil, transferred into the cold gas stream of the detector and irradiated with graphite monochromated Mo Kα (λ = 0.71073 Å) X-rays. The data was collected by the SMART program and processed with SAINT to apply Lorentz and polarisation corrections to diffract spots (integrated 3-dimensionally).

$L^3 \cdot 3H_2O \cdot C_3H_6O$ and $L^7 \cdot C_3H_6O \cdot H_2O$ data were collected at low temperature with a Rigaku-Spider X-ray diffractometer, comprising a Rigaku MM007 microfocus copper rotating-anode generator, high-flux Osmic monochromating and focusing multilayer mirror optics (Cu K radiation, λ = 1.5418 Å), and a curved image-plate detector. CrystalClear[29] was utilised for data collection and *FSProcess*[30] in *PROCESS-AUTO* for cell refinement and data reduction.

The structures were solved by direct methods and refined using both the *SHELX*[31] and *OLEX*^{2} [32] programs. Hydrogen atoms were calculated at ideal positions. Refinement data for the X-ray crystal structures are given in Table 2.4.1.

Table 2.4.1 Crystal and refinement data for the ligands.

Compound	**L^3 ·3H_2O·C_3H_6O**	**L^5 ·2CH_2Cl_2**	**L^7 ·C_3H_6O·H_2O**
Molecular formula	$C_{52}H_{49}N_8O_{10}P_3$	$C_{47}H_{35}Cl_4N_6O_6P_3$	$C_{52}H_{41}N_8P_3O_8$
M (g mol^{-1})	1038.91	1014.52	998.84
Temperature (K)	163 (2)	170 (2)	138 (2)
Crystal system	Triclinic	Monoclinic	Triclinic
Space group	$P\bar{1}$	$P2_1/a$	$P\bar{1}$
a(Å)	11.8419 (4)	10.740 (2)	10.782 (2)
b(Å)	14.0379 (4)	39.690 (8)	14.678 (3)
c(Å)	15.3918 (11)	11.160 (2)	14.910 (3)
α(°)	91.665 (7)	90	97.30 (3)
β(°)	90.322 (6)	104.14 (3)	92.03 (3)
γ(°)	96.231 (2)	90	96.59 (3)
V(Å^3)	2542.4 (2)	4163.0 (16)	2322.38 (8)
Z	2	4	2
μ(Mo Kα) mm^{-1}	-	0.418	-
μ(Cu Kα) mm^{-1}	1.634	-	1.736
ρ_{calc} (g cm^{-3})	1.357	1.461	1.429
$2\theta_{max}$(°)	117.88	50.70	130.16
Number of unique reflections	7193	7821	7656
Data/restrains/parameters	7193/60/685	7821/26/624	7656/113/651
Final R indices [I>2σ(I)]	$R1$ = 0.0756	$R1$ = 0.0555	$R1$ = 0.0689
	$wR2$ = 0.1775	$wR2$ = 0.1052	$wR2$ = 0.1663
R indices (all data)	$R1$ = 0.1347	$R1$ = 0.0649	$R1$ = 0.1044
	$wR2$ = 0.2407	$wR2$ = 0.1089	$wR2$ = 0.1907
Goodness-of-fit on F^2	1.074	1.124	1.062

Table 2.4.1 indicates that the refinement data for each structure are acceptable for publication. CIF files are included on the accompanying compact disc for reference. On conducting an online CIF check, all significant alerts have been explained in the CIF file.

2.4.1 Crystal structure of $N_3P_3(OPh)_5(Obbp)$ (L^3)

Triclinic L^3 crystallises in space group $P\bar{1}$ with 3 molecules of water and one of acetone per unit cell. The cell refines with one ligand molecule per unit cell, having no centre of symmetry.

Neither the imidazole (N5, N6, N7 and N8) nor pyridine (N4) nitrogens show any interaction with the phosphazene ring (see Figure 2.4.1.1). This is of particular importance for the polymer synthesis, as this means that there is no route for polymer decay. The phenol groups also appear to have no interaction with the phosphazene ring or the Obbp moiety, therefore it is likely that a substitution to the phenyl groups will not affect the behaviour of the ligand. In addition, as there is no interaction between the phosphazene ring and Obbp it is likely that the polymer will not degrade. The bond lengths of the phosphazene ring are typical of a phenoxy substituted ring (see Appendix A).

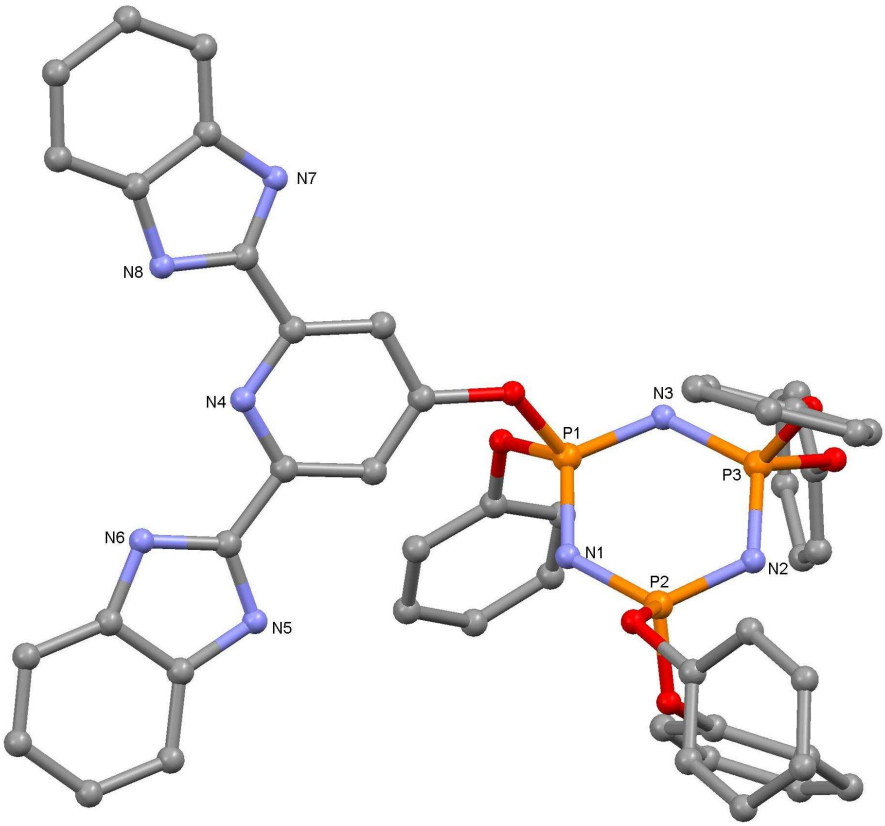

Figure 2.4.1.1 Unit cell for $L^3 \cdot 3H_2O \cdot C_3H_6O$ (hydrogen atoms removed for clarity).

L^3 packs as a result of water and acetone molecules hydrogen bonding with the imidazole groups of the Obbp moiety and the lone pair of the phosphazene ring nitrogen. Although the Obbp groups appear to be π-bonding (see Figure 2.4.2.2), this is simply the result of the hydrogen bonds holding the adjacent rings near each other, the distance between the Obbp groups is greater than 3.8 Å, too distant for a π-π interaction.

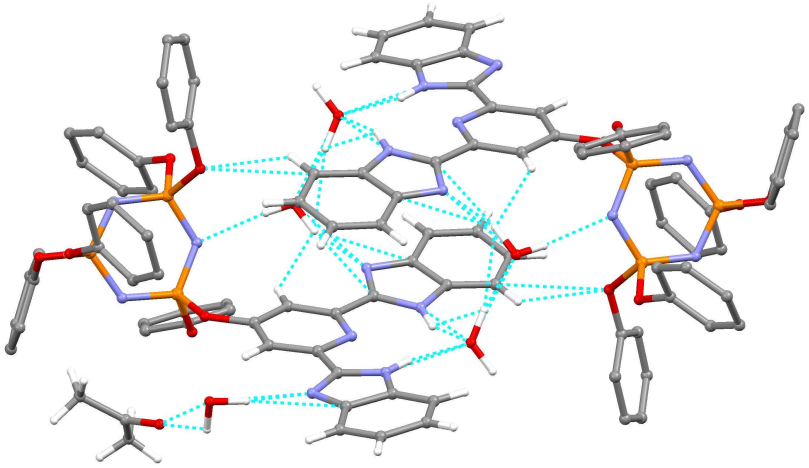

Figure 2.4.1.2 Packing behaviour of $L^3 \cdot 3H_2O \cdot C_3H_6O$ (phenoxy hydrogens were removed for clarity), lines indicating hydrogen bonding.

2.4.2 Crystal structure of $N_3P_3(Biphen)_2(OPh)(OTerpy)$ (L^5)

Monoclinic L^5 crystallises in space group $P2_1/a$ with two molecules of dichloromethane. The cell refines with one ligand molecule per unit cell, having no centre of symmetry.

The OTerpy moiety points directly away from the phosphazene ring showing no interaction between it and the phosphazene ring (see Figure 2.4.2.1). This is particularly important because many 2-hydroxy-pyridine substituted phosphazenes are unstable due to an interaction between the aromatic nitrogen and the phosphazene. This means that the analogous polymer is likely to be stable. The bond lengths of the phosphazene ring are typical of a biphen substituted ring (see Appendix A).

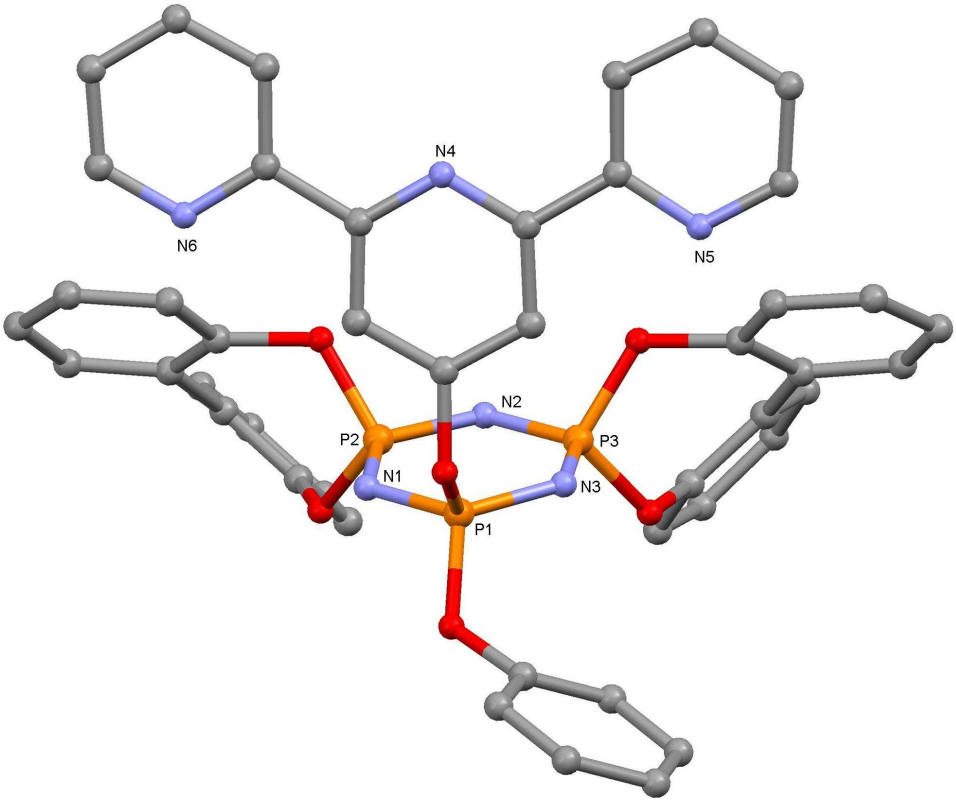

Figure 2.4.2.1 Unit cell of $L^5 \cdot 2CH_2Cl_2$ (hydrogen atoms and dichloromethane molecules removed for clarity).

One molecule of L^5 is bound to the other with π-π interactions via the OTerpy moieties. The pyridine rings of the OTerpy are facing in an opposite direction to the central pyridine nitrogen, due to the lowering on steric hindrance of the OTerpy protons and the

opportunity for hydrogen bonding between the OTerpy nitrogen and the OTerpy aromatic proton. The ligand packs via a combination of hydrogen bonding between the biphen protons, the phosphazene nitrogen and the dichloromethane chlorines (see Figure 2.4.2.2).

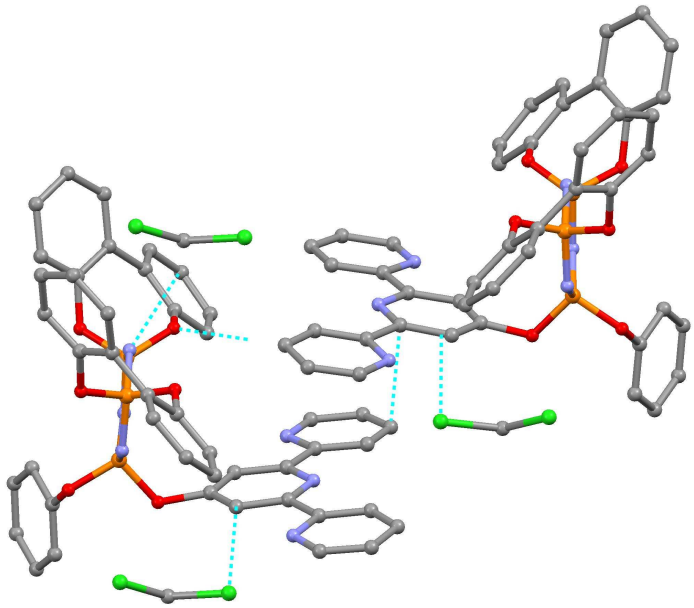

Figure 2.4.2.2 Packing of $L^5 \cdot 2CH_2Cl_2$, dotted lines indicate bonding interactions (hydrogen atoms removed for clarity).

2.4.3 Crystal structure of $N_3P_3(Biphen)_2(OPh)(Obbp)$ (L^7)

Triclinic L^7 crystallises in space group $P\bar{1}$ with two molecules of acetone and two molecules of water. Two ligand molecules exist in the unit cell which refines as two complete molecules, each having no centre of symmetry.

Unlike L^3, the Obbp group lies directly over the phosphazene ring; however, there is no indication of interaction. It is likely that it is simply the result of packing rather than any electronic effects. As previously mentioned, as there is no evidence of interaction between the Obbp moiety and the phosphazene it is likely that the polymer will remain stable. In addition the Obbp moiety shows similar hydrogen bonding with the pyridine and benzimidazole (N4, N6 and N8) groups to a water molecule as observed in L^3, however, the other two water molecules that are exclusively hydrogen bonded to the remaining imidazole nitrogens (N7 and N5) are not observed (see Figure 2.4.3.1). The bond lengths of the phosphazene ring are typical of a biphen substituted ring (see Appendix A).

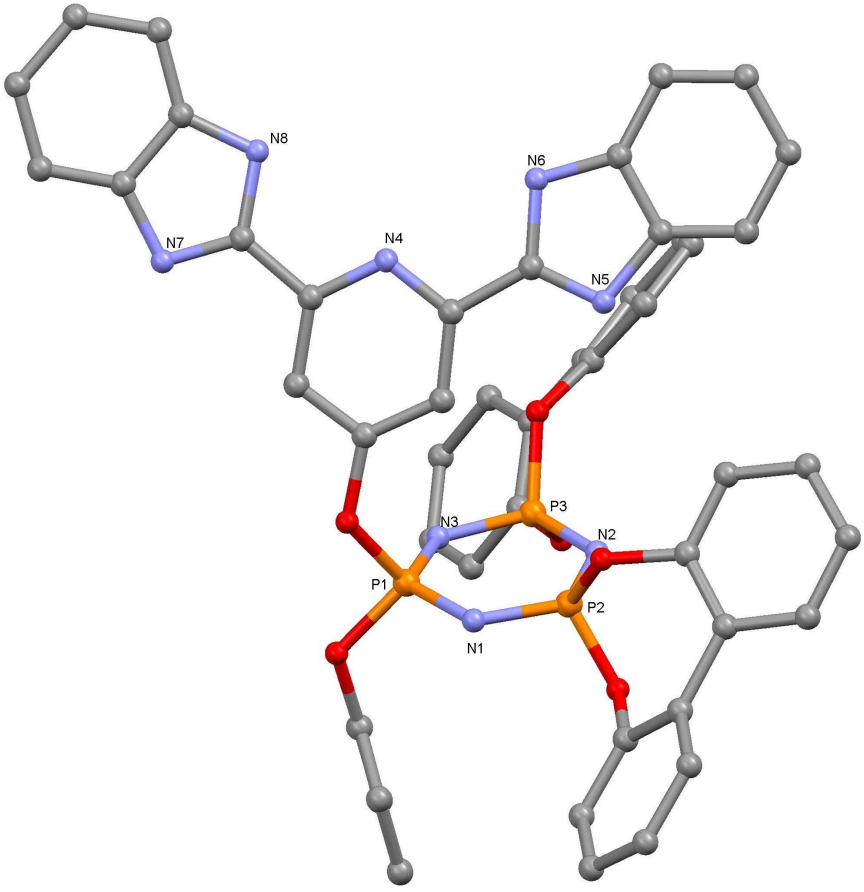

Figure 2.4.3.1 Unit cell for $L^7 \cdot C_3H_6O \cdot H_2O$ (hydrogen atoms removed for clarity).

The two ligand molecules are held together via hydrogen bonding between acetone, water and Obbp moiety (see Figure 2.4.3.2). Such interactions are similar to those observed for L^3. This shows that, while there is a small conformation change as a result of replacing the phenols with biphen, all of the key structural features of the molecule remains the same, suggesting variations in the co-substituents has no significant effects on the primary substituent of the molecule.

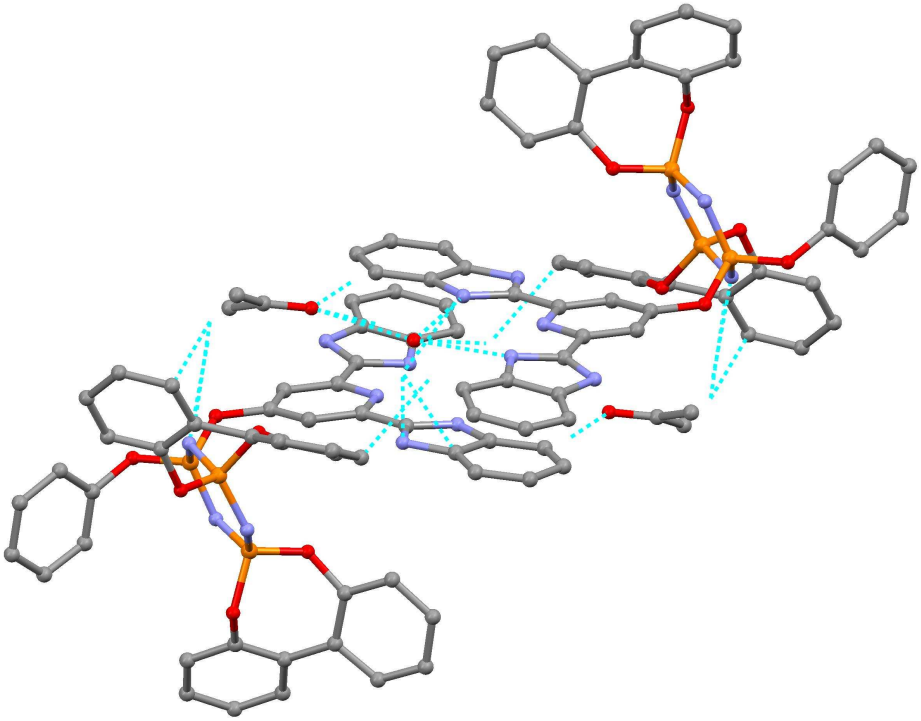

Figure 2.4.3.2 Crystal structure of a single molecule of $L^7 \cdot C_3H_6O \cdot H_2O$ (hydrogen atoms and solvents removed for clarity), dotted lines indicate bonding interactions.

2.5 Conclusion

Seven ligands were successfully synthesised and characterised containing OTerpy, OPhTerpy, Obbp and OPhbpp moieties as coordination centres, with phenol and biphen co-substituents to occupy the remaining reactive sites.

HOTerpy and HObbp were slow to react as the result of the formation of the enone tautomers. For HOTerpy and HObbp, this resulted in only the mono-substituted species being formed despite the reaction conditions used. With a large excess of the nucleophile and the addition of a promoter it was possible to drive the reaction to the disubstituted species. Both the HOPhTerpy and HOPhbpp species were far more reactive due to the phenyl spacer, reducing the stability of the enone. This information is crucial for the design and synthesis of the polymers.

Only three crystal structures were obtained: L^3, L^5 and L^7. However, they each provided information about all of the ligands. From L^3, L^5, L^7 it could be determined that there are no interactions between the coordinating substituents and the phosphazene ring, which means that the polymer is more likely to be stable. It can therefore be assumed that phenyl-spaced substituents will behave in the same fashion, except the chances of any interactions occurring will be lowered due to the increased distance between the coordinating centre and the phosphazene ring.

2.6 References

1. Kahn, O.; Martinez, C. J. *Science* **1998**, *279*, 44-48.

2. Gabler, D. G.; Haw, J. F. *Inorganic Chemistry* **1990**, *29*, 4018-4021.

3. Kirk, S. *Cyclo- and Polyphosphazenes Containing 2-oxypyridine Moieties Coordinated to Selected Transition Metals*, Massey University, Palmerston North, **2008**.

4. Allcock, H. R. *Chemistry and Applications of Polyphosphazenes*; John Wiley & Sons Inc: Hoboken, **2003**.

5. Krause, W. E.; Parvez, M.; Visscher, K. B.; Allcock, H. R. *Inorganic Chemistry* **1996**, *35*, 6337-6338.

6. Jung, O. S.; Park, S. H.; Lee, Y. A.; Cho, Y. H.; Kim, K. M.; Lee, S. G.; Chae, H. K.; Sohn, Y. S. *Inorganic Chemistry* **1996**, *35*, 6899-6901.

7. Chandrasekhar, V.; Vivekanandan, K.; Nagendran, S.; Andavan, G. T. S.; Weathers, N. R.; Yarbrough, J. C.; Cordes, A. W. *Inorganic Chemistry* **1998**, *37*, 6192-6198.

8. Ainscough, E. W.; Brodie, A. M.; Derwahl, A.; Kirk, S.; Otter, C. A. *Inorganic Chemistry* **2007**, *46*, 9841-9852.

9. Davidson, R. J. *DFT Calculations on the Interaction of Phosphazenes with Transition Metals* Massey University, Palmerston North, **2007**.

10. Spahni, W.; Calzaferri, G. *Helvetica Chimica Acta* **1984**, *67*, 450-454.

11. Constable, E. C.; Ward, M. D. *Journal of the Chemical Society-Dalton Transactions* **1990**, 1405-1409.

12. Drew, M. G. B.; Hill, C.; Hudson, M. J.; Iveson, P. B.; Madic, C.; Vaillant, L.; Youngs, T. G. A. *New Journal of Chemistry* **2004**, *28*, 462-470.

13. Chandrasekar, R.; Schramm, F.; Fuhr, O.; Ruben, M. *European Journal of Inorganic Chemistry* **2008**, 2649-2653.

14. Moran, D. B.; Morton, G. O.; Albright, J. D. *Journal of Heterocyclic Chemistry* **1986**, *23*, 1071-1077.

15. Demko, Z. P.; Sharpless, K. B. *Journal of Organic Chemistry* **2001**, *66*, 7945-7950.

16. Djukic, B.; Dube, P. A.; Razavi, F.; Seda, T.; Jenkins, H. A.; Britten, J. F.; Lemaire, M. T. *Inorganic Chemistry* **2009**, *48*, 699-707.

17. Haga, M.; Takasugi, T.; Tomie, A.; Ishizuya, M.; Yamada, T.; Hossain, M. D.; Inoue, M. *Dalton Transactions* **2003**, 2069-2079.

18. Terada, K.; Kobayashi, K.; Haga, M. *Dalton Transactions* **2008**, 4846-4854.

19. Hossain, M. D.; Ueno, R.; Haga, M. *Inorganic Chemistry Communications* **2000**, *3*, 35-38.

20. Bhaumik, C.; Das, S.; Saha, D.; Dutta, S.; Baitalik, S. *Inorganic Chemistry*, *49*, 5049-5062.

21. Wang, K.; Haga, M.; Hossain, M. D.; Shindo, H.; Hasebe, K.; Monjushiro, H. *Langmuir* **2002**, *18*, 3528-3536.

22. Yu, S. C.; Hou, S. J.; Chan, W. K. *Macromolecules* **1999**, *32*, 5251-5256.

23. Schramm, F.; Chandrasekar, R.; Zevaco, T. A.; Rudolph, M.; Gorls, H.; Poppitz, W.; Ruben, M. *European Journal of Inorganic Chemistry* **2009**, 53-61.

24. Constable, E. C. *Chemical Society Reviews* **2007**, *36*, 246-253.

25. Andres, P. R.; Schubert, U. S. *Advanced Materials* **2004**, *16*, 1043-1068.

26. Carriedo, G. A.; Alonso, F. J. G.; Soto, A. P. *Journal of Inorganic and Organometallic Polymers and Materials* **2007**, *17*, 399-406.

27. McBee, E. T.; Okuhara, K.; Morton, C. J. *Inorganic Chemistry* **1966**, *5*, 450-457.

28. Horvath, R.; Otter, C. A.; Gordon, K. C.; Brodie, A. M.; Ainscough, E. W. *Inorganic Chemistry* **2010**, *49*, 4073-4083.

29. Rigaku; Version 1.4.0 ed.; Rigaku Americas Corp: The Woodlands, **2007**, p program for area detector data collection.

30. Rigaku; Rigaku Corporation: Matsubara, **1998**, p Automatic Data Acquisition and Processing Package for Imaging Plate and CCD Diffractometers.

31. Sheldrick, G. M. *Acta Crystallographica Section A* **2008**, *64*, 112-122.

32. Dolomanov, O. V.; Bourhis, L. J.; Gildea, R. J.; Howard, J. A. K.; Puschmann, H. *Journal of Applied Crystallography* **2009**, *42*, 339-341.

Chapter 3

Reactions of cyclotriphosphazene ligands with selected iron(II) salts

3.0 Abbreviations used in Chapter 3

SCO	Spin crossover
LIESST	Light induced spin state trapping
Terpy	2,2′:6′,2″-terpyridine
PhTerpy	2,6-di(pyridin-2-yl)-4-phenylpyridine
Bbp	2,6-di(1*H*-benzimidzol-2-yl)pyridine
Bpp	2,6-di(1*H*-pyrazol-1-yl)pyridine
HOTerpy	2,6-bis(2-pyridyl)-4(1*H*)-pyridone
HOPhTerpy	4-(2,6-di{pyridin-2-yl}-pyridine-4-yl)phenol
HObbp	2,6-di(1*H*-benzimidazol-2-yl)pyridine-4(1*H*)-one
HOPhbpp	4-(2,6-di{1*H*-pyrazol-1-yl}pyridine-4-yl)phenol
NMR	Nuclear Magnetic Resonance

3.1 Introduction

For almost 40 years phosphazenes have been coordinated to metal ions. Due to their ease of modification a range complexes with assorted properties have been formed. As a result it has been proposed that they could be used for a range of applications[1] such as anti-cancer drugs[2], organic light emitting diodes (OLED)[3], selective metal extraction[4-6], and heterogeneous catalysts[7].

The cyclotrimer has been crucial in the development of these materials. This is because its reactions can be optimised, and potential side reactions determined. In addition the products can be characterised with techniques such as X-ray crystallography which is unavailable for polymers.[1]

As previously mentioned in Chapter 1, phosphazenes have long been associated with coordination of metal ions. They are able to do this in five typical ways:[8] i) form a cationic salt with the metal ion; ii) coordinate to the ring nitrogen; iii) coordinate via exocyclic groups substituted to the phosphazene ring; iv) coordinate to the phosphorus atom via a covalent bond; and finally v) form an anionic bond with the phosphazene ring.

It is the third form of coordination that is the most pertinent to this project. Here an assortment of ligands that typically form spin crossover complexes were chosen to attach to a cyclophosphazene. While choosing substituents that may promote the coordination of the phosphazene itself may give rise to unique properties, such behaviour is often unpredictable.[9-11]

Substituent selection was based on six main factors: i) when coordinated to iron(II) the complexes show SCO behaviour; ii) the SCO temperature for similar complexes occurs near room temperature, making it possible to investigate any changes with the available equipment; iii) the SCO behaviour is not dependent on inter-molecular interactions, rather it is based on the ligand strength and bond strain; iv) phenol bearing analogues of the substituents must be able to be made in sufficient scales to attach to the polymer; v) the substituents must be stable with strong bases to allow phosphazene substitution; vi) ideally similar complexes display Light Induced Excited Spin State Trapping (LIESST).

A selection of suitable substituents was initially investigated to assess their reactivity with cyclophosphazenes in Chapter 2. Eight new ligands were chosen from Chapter 2 to coordinate iron, each of them contained the following coordination sites: 2,2′:6′,2″-terpyridine (Terpy), 2,6-di(pyridin-2-yl)-4-phenylpyridine (PhTerpy), 2,6-di(1*H*-benzimidazol-2-yl)pyridine (bbp) and 2,6-di(1*H*-pyrazol-1-yl)pyridine (bpp). Each of these groups will be described in turn.

3.1.1 2,2′:6′,2″-terpyridines

2,2′:6′,2″-terpyridines are a class of classic multidentate ligands which have been extensively studied because of their high affinity for binding transition metal ions[12-14] and their interesting optical properties[15-18]. With the recent developments by Constable[19-25] and others[26-31], it has become simpler to functionalise them. As a result of the large variety of substituted terpys that are now available, they have found applications in areas from actinide metal extraction to solar cell dyes (an example of a terpy-based Grätzel dye for a solar cell shown in Figure 3.1.1.1)[32].

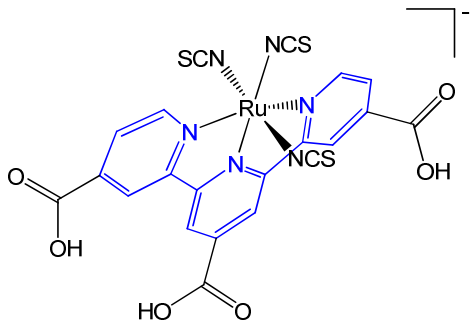

Figure 3.1.1.1 A Grätzel dye based on a terpy for use in a solar cell.[32]

When coordinated to iron(II), typically LS complexes are formed that cannot be excited to the HS state.[33] However, it is possible to induce SCO behaviour by adding sterically bulky groups near the coordinating site.[34] To reduce the steric strain the iron-nitrogen bond lengths are increased reducing the energy difference between the HS and LS states (ΔE_{HL}), making SCO thermally accessible. An example of this occurs when the ortho and para hydrogens of one of the terpy rings are substituted by phenyl groups,[34] this results in SCO occurring at room temperature (see Figure 3.1.1.2).

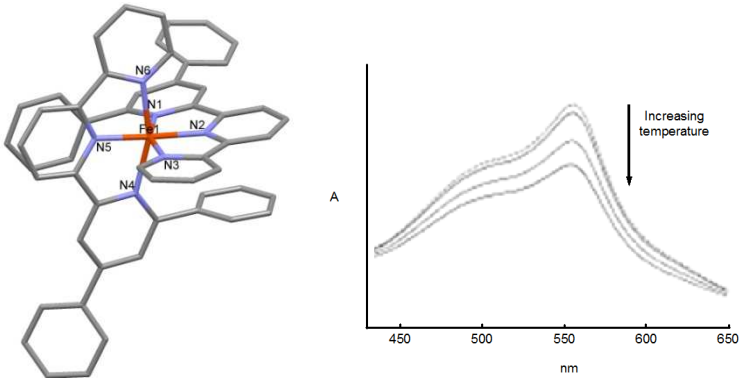

Figure 3.1.1.2 Left: A crystal structure of a terpy complex substituted at the ortho and para positions reducing the SCO temperature (hydrogens, anions and solvent removed for clarity). Right: The visible spectrum of this compound as a function of temperature (300 – 323 K).[34]

In addition to bulky groups near the coordination site causing changes in SCO behaviour, changes in the para position (see Figure 3.1.1.3) also have significant effects. Varying the electron withdrawing or donating ability of the substituent alters the spin state of the complex. However, the effects of the substitution cannot be predicted as they are both dependent on electronic effects and solid state interactions.[35-37]

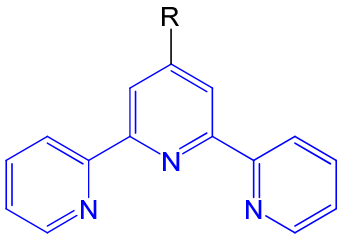

Figure 3.1.1.3 Substitution of terpy at the para position, where R can be any substituent.

Not only do terpy complexes provide a path for thermal SCO, they also show light-excited SCO behaviour.[38,39] They are able to do this via the charge transfer band observed when iron(II) is coordinated. The optical SCO behaviour could also be tuned via substitution, just as the thermal behaviour can be.

3.1.2 2,6-di(1*H*-benzimidazol-2-yl)pyridine

2,6-di(1*H*-benzimidazol-2-yl)pyridines has drawn a great deal of interest due to its imidazole rings. The rings are more electron poor than pyridine resulting in a stronger σ-donor coordination than pyridine. Such a difference greatly alters the metal complexes behaviour, e.g. lowering the energy difference between the ground and excited state. In addition to this feature the protons of the imidazole rings can be removed[40-43] or substituted[44] (see Figure 3.1.2.1), greatly altering the metal complexes behaviour.

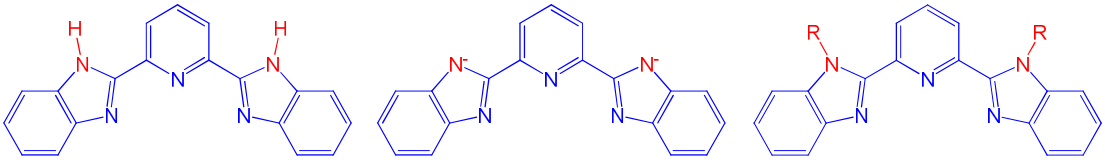

Figure 3.1.2.1 From left: Parent bbp, deprotonated bbp, N-substituted bbp (where R can be a range of substituents).

It is due to these ligands' tuneable properties that they have been used for a range of applications such as luminescence[45,46], actinide separation[47], hydrogen production[48,49] and high temperature SCO[40-43].

The σ-donor behaviour lowers the ΔE_{HS-LS} relative to terpy, resulting in SCO to occur near room temperature.[33] As the variation on the imidazole nitrogen changes its luminescence and metal affinity properties, the SCO behaviour is also greatly altered. The general behaviour observed when the imidazole is deprotonated is that the SCO temperature increases, this increase is due to an increase in electron-density strengthening the Fe-N bond. When the proton is substituted with an alkyl group the SCO temperature is generally increased due to the increase in electron density; however, this can be altered if the substituent causes the system additional strain (see Figure 3.1.2.2).[44]

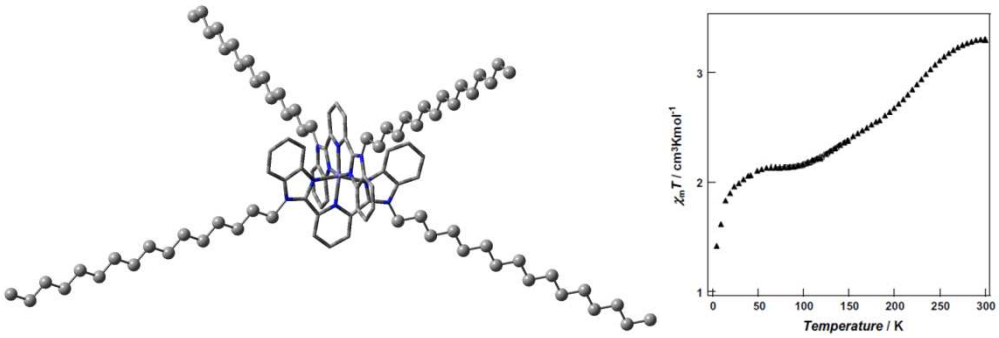

Figure 3.1.2.2 Left: A Monte-Carlo simulation of a substituted iron-bbp complex. Right: The magnetic behaviour of the complex.[44]

To date there have been few studies that have focused on the SCO behaviour of the para-substituted bbp ligands. The single paper that has been published observed that as the electron-withdrawing effect of the substituent is increased, ΔE_{HS-LS} decreased resulting in the HS state being favoured (see Figure 3.1.2.3). This is due to reduction in the electron density available for coordination to the metal ion, i.e. it produces a weaker field ligand.[50]

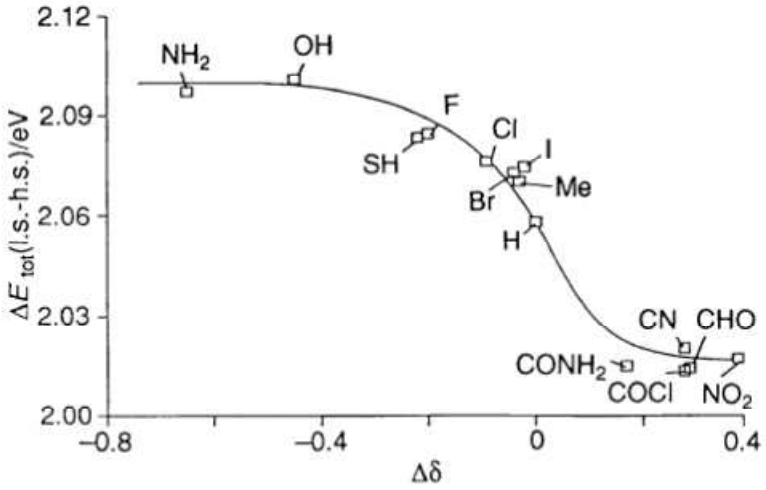

Figure 3.1.2.3 Differences in the calculated heats of formation between the HS and LS forms (ΔE_{tot} since calculations are for single molecules) in $[Fe(Xbbp)_2]^{2+}$ *vs.* Δδ (^{1}H NMR increment for para-substituents X in benzene).[50]

3.1.3 2,6-di(1*H*-pyrazol-yl)pyridine

2,6-di(1*H*-pyrazol-yl)pyridines was originally introduced as a terpy analogue for ruthenium complexes because it can be easily functionalised by varying the pyrazole attached; [50] however, it is now primarily used to form SCO complexes (Figure 3.1.3.1) with brief interludes into solar cell dyes[51,52] and lanthanide luminescence[53-55]. As with bbp the pyrazole ring is more electron poor than pyridine resulting in more σ-donor coordination behaviour, resulting in ΔE_{HS-LS} being smaller than that of terpy and bbp. This in turn results in the SCO temperatures being lower than that of terpy or bbp.[56]

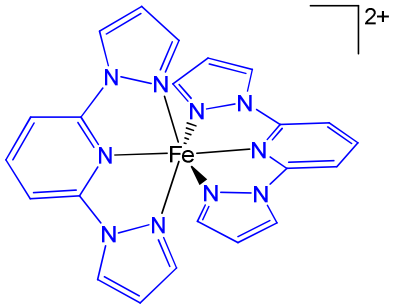

Figure 3.1.3.1 A schematic view of iron(II) coordinating to a bpp ligand, forming a SCO complex.

The variations in SCO behaviour have been extensively investigated in relation to the pyrazole substitution; however, it is only recently that the effects of substitution at the para position of the pyridine have been investigated.[57-63] It has been found that the addition of a phenyl group to the para position maintains its SCO behaviour and allows further substitution.[58] It is noted that variations in crystal lattice do alter the SCO behaviour but do not prevent it (see Figure 3.1.3.2),[61] this has also been found to be true for substitutions of the pyrazole ring[64-66] – the SCO behaviour will be altered; however, no examples of substitution have been shown to prevent it.

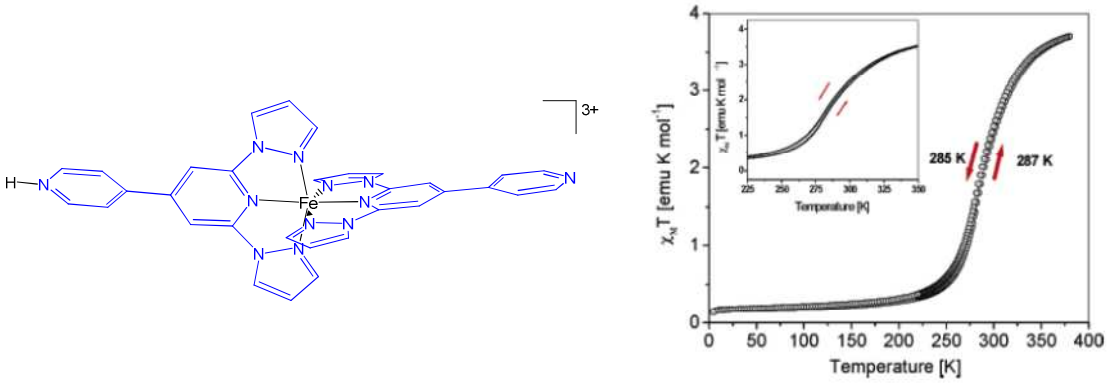

Figure 3.1.3.2 Left: $[Fe(Pybpp)_2]^{3+}$. Right: thermal magnetic behaviour of $[Fe(Pybpp)_2]^{3+}$.[61]

These complexes have also been studied for its photomagnetic behaviour. This, like many other SCO complexes, showed that the LS complex could be excited to the HS state through the use of laser excitation and held in the HS state for extended periods of time by keeping the complex at cryogenic temperatures. This effect is called light induced excited spin state trapping (LIESST)[64,65] (see an example in Figure 3.1.3.3).

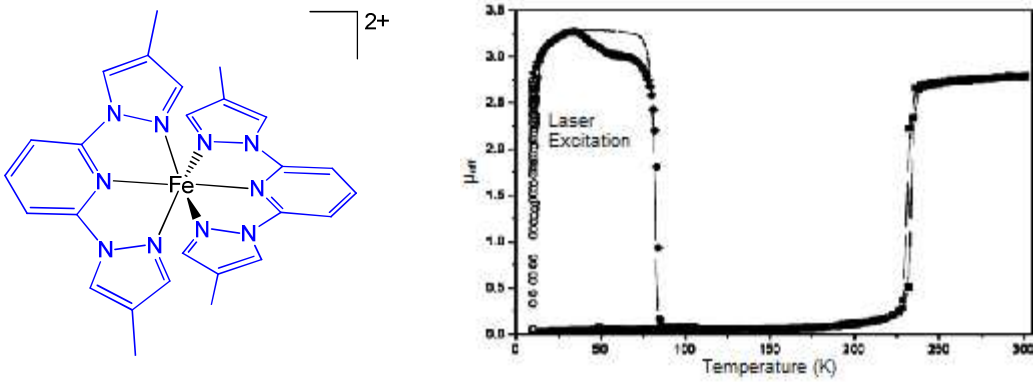

Figure 3.1.3.3 Left: $[Fe(bppMe)_2]^{2+}$. Right: thermal and LIESST magnetic behaviour of $[Fe(bppMe)_2]^{2+}$.[65]

3.2 Synthesis of the iron(II) complexes

In this chapter the ligands produced in Chapter 2 (see Figure 3.2.1) were reacted with an assortment of iron(II) salts to produce the respective complexes. This investigation was performed in order to eludicate the coordination behaviour of the complexes providing insight to the coordination behaviour of the polymer analogues. The experimental details are fully given in Appendix B.

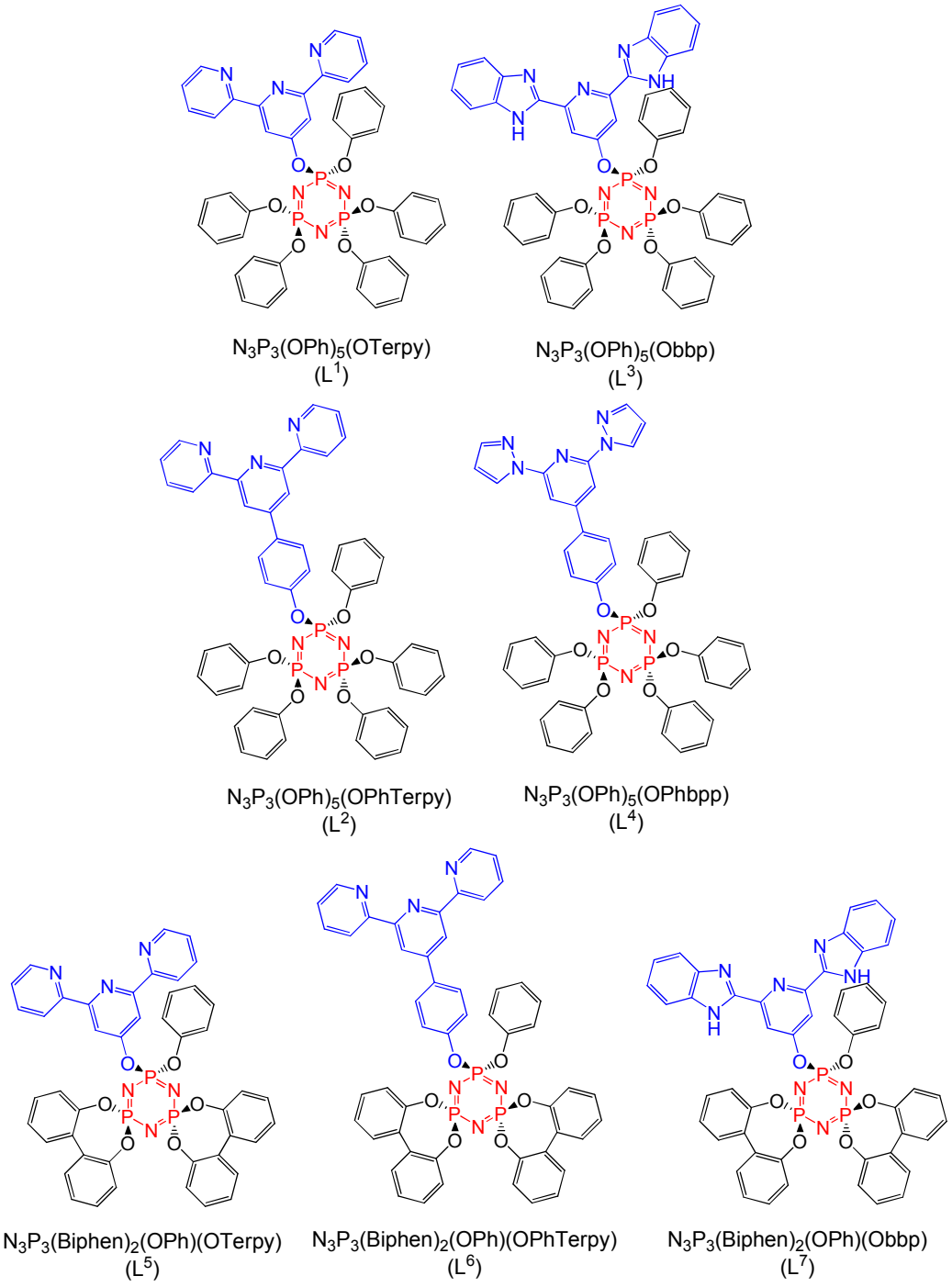

Figure 3.2.1 Ligands to be coordinated with iron(II).

3.3 Observations from synthesis

By the addition of the appropriate iron(II) salt with each of the ligands, 16 complexes were successfully synthesised and characterised (see Figure 3.3.1). These will serve as models for their polyphosphazene analogues.

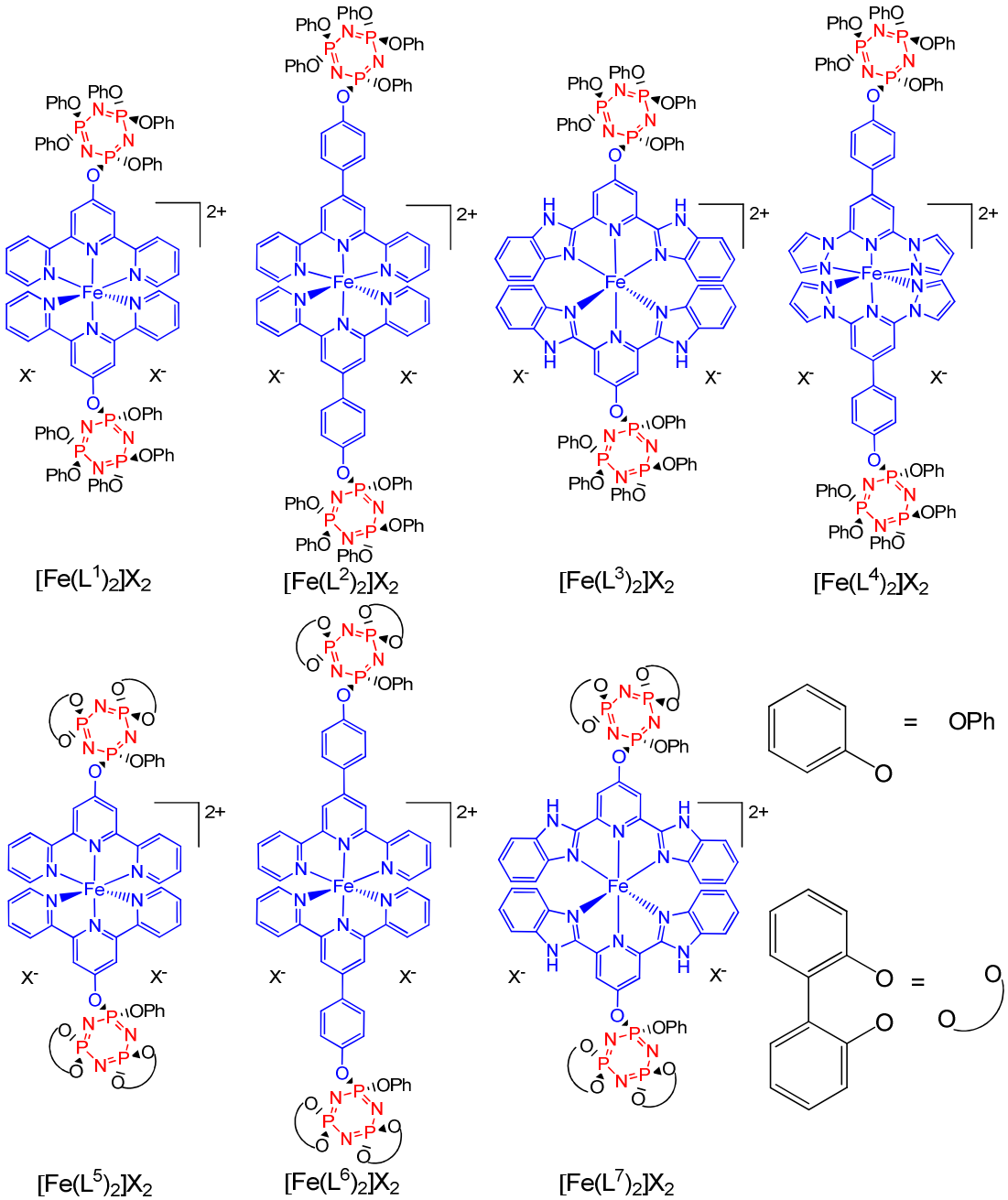

Figure 3.3.1 Iron(II) complexes synthesised in this chapter, X = ClO_4^-, PF_6^- or BF_4^-.

Each of the 2,6-bis(2-pyridyl)-4(1*H*)-pyridonate (OTerpy)-, 4-(2,6-di{pyridin-2-yl}-pyridine-4-yl)phenolate (OPhTerpy)-, 2,6-bis(benzimidazole)-4(1*H*)-pyridonate (Obbp)- and 4-(2,6-(pyraz-1-yl)-pyridine-4-yl)phenolate (OPhbpp)-based ligands formed bis-ligand iron(II) complexes, by the addition of the respective metal salt to two equivalents of each ligand (see Figure 3.3.1.1). The reactions were typically instantaneous, however, stirring was continued to assure complete reactions. The reaction with L^4 required heating for an extended period of time, which is typical of this class of ligand. In the case of the terpy-based complexes it was possible to metathesise the anions with silver salts; however, both the Obbp- and OPhbpp-based complexes became unstable in the presence of these salts, unpredictably breaking down into an assortment of products. This restricted the synthesis of these complexes to the anions of the available metal salts, however, it was noted that each complex grew crystals with the perchlorate counter ion, although only one perchlorate complex gave a diffractable crystal.

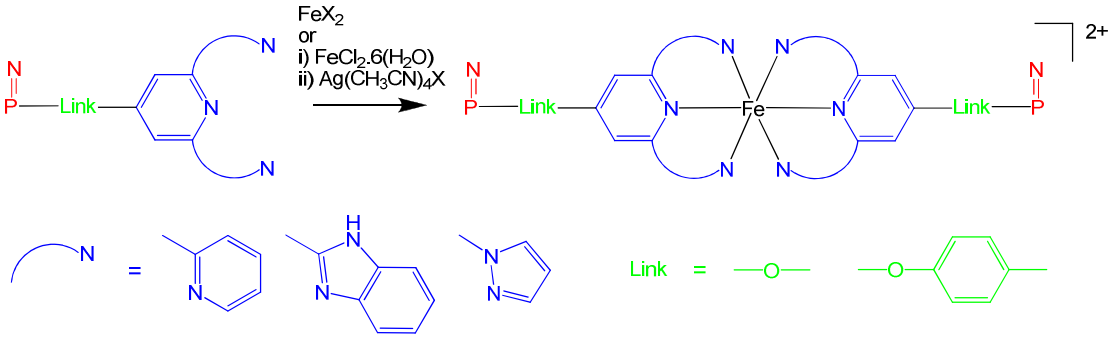

Figure 3.3.2 The schematic reaction for the tridentate ligands.

No differences were observed in the reactivity of ligands containing biphenol or phenol co-substituents. This is of particular importance for the synthesis of the polymers as this suggests that the coordinating group will behave the same way in spite of the co-substituents attached to the polymer backbone. Another feature observed is that the yields and solubilities remain similar in spite of the anions used. Therefore, it can be assumed that the synthesis of the polymer analogues will occur in the same way despite the anion used. In all the mass-spectra, no species containing anions or solvents were observed, showing that the anions or solvent molecules were not bound to the cationic complex. However, the elemental analysis for each of the complexes contained solvent molecules, typical behaviour of phosphazenes.[1]

All of the terpy-based complexes appeared to be in the LS state in both solid state and solution. This was assumed by the purple colour[67] and high resolution of the NMR spectra. The Obpp-based complexes appeared to be LS in the solid state; however, in solution they displayed a slight red colour and the NMR spectra were less resolved than expected for diamagnetic complexes,[41] suggesting the presence of a low ratio of HS species. The complex formed by the OPhbpp-based ligand formed a pale yellow solid and solution, and NMR data was unavailable due to the solutions being paramagnetic, pointing to the complex being HS.[66] The magnetic behaviour is thoroughly investigated in Chapter 7.

3.4 Crystallography

The X-ray data for $[Fe(L^1)_2](PF_6)_2 \cdot CH_3CN$ and $[Fe(L^2)_2](PF_6)_2 \cdot CH_3CN$ was collected on a Siemens P4 four-circle diffractometer, using a Siemens SMART 1K CCD area detector. The crystal was mounted in an inert oil, transferred into the cold gas stream of the detector and irradiated with graphite monochromated Mo Kα (λ = 0.71073 Å) X-rays. The data was collected by the SMART program and processed with SAINT to apply Lorentz and polarisation corrections to diffract spots (integrated 3-dimensionally).

$[Fe(L^1)_2](ClO_4)_2 \cdot CH_3CN$ and $[Fe(L^3)_2](BF_4)_2 \cdot C_3H_6O \cdot C_5H_{12}O$ data were collected at low temperature with a Rigaku-Spider X-ray diffractometer, comprising a Rigaku MM007 microfocus copper rotating-anode generator, high-flux Osmic monochromating and focusing multilayer mirror optics (Cu K radiation, λ = 1.5418 Å), and a curved image-plate detector. CrystalClear was utilised for data collection and *FSProcess* in *PROCESS-AUTO* for cell refinement and data reduction.

The structures were solved by direct methods and refined using both the *SHELX*[68] and *OLEX* [2 69] programs. Hydrogen atoms were calculated at ideal positions. Tables 3.4.1 and 3.4.2 indicate that the refinement data for each structure are acceptable for publication. CIF files are included on the accompanying compact disc for reference. On conducting an online CIF check, all significant alerts have been explained in the CIF file.

Refinement data for the X-ray crystal structures are given in Tables 3.4.1 and 3.4.2.

Table 3.4.1 Crystallographic and refinement data for complexes $[Fe(L^1)_2](PF_6)_2$ and $[Fe(L^1)_2](ClO_4)_2$

Compound	**$[Fe(L^1)_2](PF_6)_2 \cdot CH_3CN$**	**$[Fe(L^1)_2](ClO_4)_2 \cdot CH_3CN$**
Molecular formula	$C_{92}H_{73}F_{12}FeN_{13}O_{12}P_8$	$C_{92}H_{73}Cl_2FeN_{13}O_{20}P_6$
M (g mol^{-1})	2084.26	1993.23
Temperature (K)	90 (2)	123 (2)
Crystal system	Triclinic	Triclinic
Space group	$P\bar{1}$	$P\bar{1}$
a(Å)	15.042 (8)	14.767 (3)
b(Å)	16.340 (10)	16.334 (3)
c(Å)	20.999 (13)	21.024 (4)
α(°)	100.59 (5)	104.25 (3)
β(°)	91.53 (3)	100.82 (3)
γ(°)	91.53 (5)	91.04 (3)
V(Å^3)	4936 (5)	4816.7 (17)
Z	2	2
μ(Mo Kα) mm^{-1}	0.368	-
μ(Cu Kα) mm^{-1}	-	3.317
ρ_{calc} (g cm^{-3})	1.402	1.374
$2\theta_{max}$(°)	58.28	130.16
Number of unique reflections	26163	15495
Data/restrains/parameters	26163/130/1264	15495/96/1208
Final R indices [I>2σ(I)]	$R1$ = 0.0585	$R1$ = 0.0727
	$wR2$ = 0.1320	$wR2$ = 0.1879
R indices (all data)	$R1$ = 0.0748	$R1$ = 0.0955
	$wR2$ = 0.1385	$wR2$ = 0.2111
Goodness-of-fit on F^2	1.084	1.087

Table 3.4.2 Crystallographic and refinement data for complexes $[Fe(L^2)_2](PF_6)_2$, $[Fe(L^3)_2](BF_4)_2$.

Compound	**$[Fe(L^2)_2](PF_6)_2 \cdot CH_3CN$**	**$[Fe(L^3)_2](BF_4)_2 \cdot C_3H_6O \cdot C_5H_{12}O$**
Molecular formula	$C_{106}H_{84}F_{12}FeN_{14}O_{12}P_8$	$C_{106}H_{92}B_2F_8FeN_{16}O_{14}P_6$
M (g mol^{-1})	2277.50	2229.26
Temperature (K)	90 (2)	123 (2)
Crystal system	Triclinic	Triclinic
Space group	$P\bar{1}$	$P\bar{1}$
a(Å)	9.823 (3)	12.880 (3)
b(Å)	20.681 (9)	17.690 (4)
c(Å)	24.932 (10)	24.070 (5)
α(°)	86.15 (3)	85.16 (3)
β(°)	84.188 (14)	83.21 (3)
γ(°)	87.457 (13)	75.32 (3)
V(Å^3)	5024 (3)	5259.6 (21)
Z	2	2
μ(Mo Kα) mm^{-1}	0.368	-
μ(Cu Kα) mm^{-1}	-	2.736
ρ_{calc} (g cm^{-3})	1.451	1.407
$2\theta_{max}$(°)	56.56	102.26
Number of unique reflections	24825	11111
Data/restrains/parameters	24825/297/1359	11111/2766/1494
Final R indices [I>2σ(I)]	$R1$ = 0.0710	$R1$ = 0.0916
	$wR2$ = 0.1843	$wR2$ = 0.2155
R indices (all data)	$R1$ = 0.1120	$R1$ = 0.1137
	$wR2$ = 0.2069	$wR2$ = 0.2296
Goodness-of-fit on F^2	0.926	0.967

3.4.1 Crystal structure of $[Fe(L^1)_2](PF_6)_2 \cdot CH_3CN$

Triclinic $[Fe(L^1)_2](PF_6)_2 \cdot CH_3CN$ crystallises in space group $P\bar{1}$ with one molecule of acetonitrile. 63 electrons per cell were removed via *PLATON/SQUEEZE*[70] corresponding to 1.5 molecules of diethyl ether. The structure refines with one cationic complex and two hexafluorophosphate anions per unit cell.

The complex shows the typical iron(II) bis-terpy arrangement, with each of the pyridine nitrogens coordinating to the iron atom, confirming the spectroscopic data collected. The phosphazene rings sit in two different positions, one pointing away from the central terpy complex, while the other folds over forming a pocket, due to π-π interactions between the non-geminal phenol rings and the hydrogen atoms of the terpy (3.196(2) Å) (see Figure 3.4.1.1).

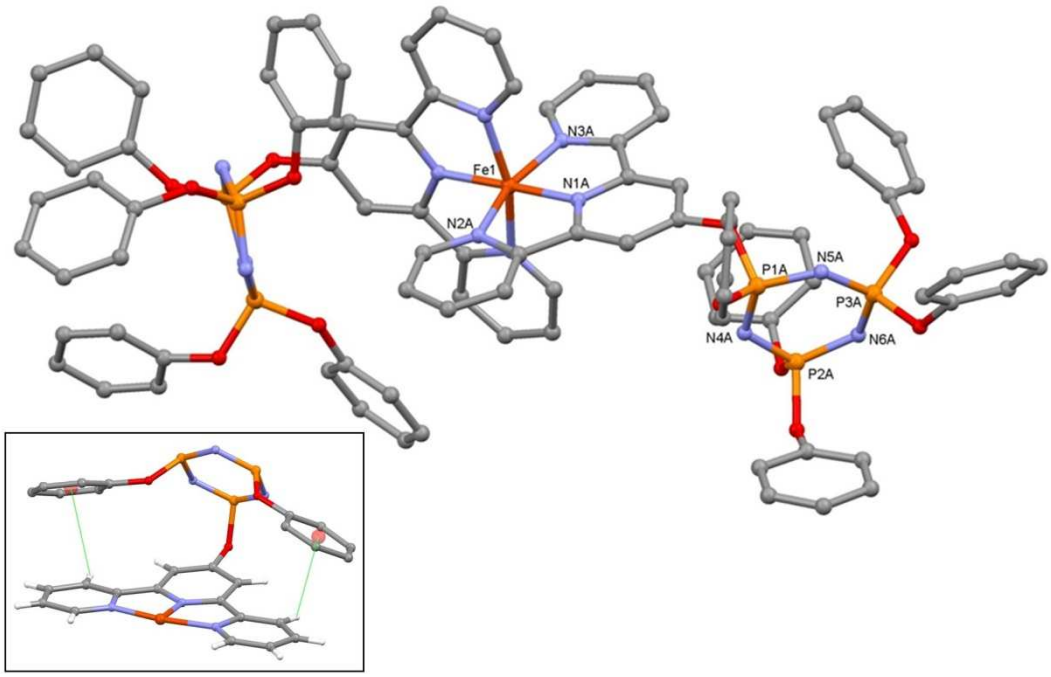

Figure 3.4.1.1 Unit cell of $[Fe(L^1)_2](PF_6)_2 \cdot CH_3CN$ (hydrogen atoms, solvents and anions were removed for clarity). Insert: Green lines indicate π-H interactions.

Both the hexafluorophosphate anions show hydrogen bonding with the protons of the terpy units of the cationic complex, forming a channel of anions between the cationic complexes. The localised acetonitrile fills in the voids formed between the phenol and terpy groups.

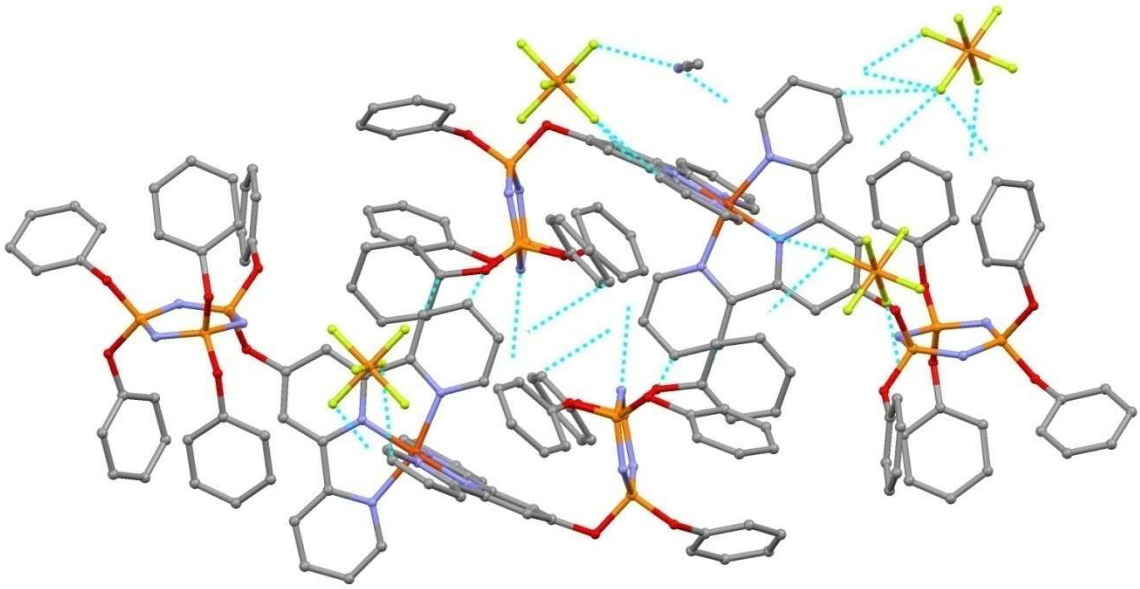

Figure 3.4.1.2 Packing of $[Fe(L^1)_2](PF_6)_2 \cdot CH_3CN$, dotted lines indicate bonding interactions.

The iron-nitrogen axial bond lengths (Fe1–N1A and –N1B) are 1.883(2) Å and the equatorial bond lengths (Fe1–N2A, –N3A, –N2B and –N3B) are 1.975(2) – 1.992(2) Å (see Appendix B). These are typical bond lengths for LS iron(II) terpy complexes[21,71-73] and this is consistent with the purple colour of the complex. The phosphazene bond lengths are also of typical size for phenoxy-substituted cyclotriphosphazene[74] (Appendix B).

3.4.2 Crystal structure of $[Fe(L^1)_2](ClO_4)_2 \cdot CH_3CN$

Triclinic $[Fe(L^1)_2](ClO_4)_2 \cdot CH_3CN$ crystallises in space group $P\bar{1}$ with one molecule of acetonitrile. 58 electrons per cell were removed via *PLATON/SQUEEZE*[70] corresponding to 1.38 molecules of diethyl ether. The structure refines with one cationic complex and two perchlorate anions per unit cell (see Figure 3.4.2.1).

The complex shows the typical iron(II) bis-terpy arrangement, with each of the pyridine nitrogens coordinating to the iron atom as seen with $[Fe(L^1)_2](PF_6)_2 \cdot CH_3CN$.

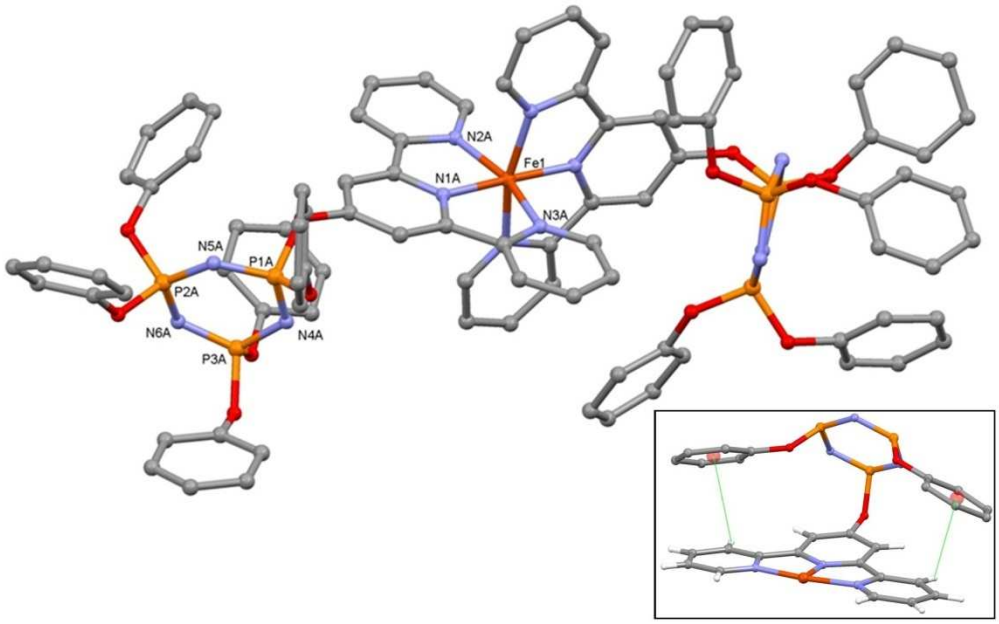

Figure 3.4.2.1 Unit cell for $[Fe(L^1)_2](ClO_4)_2 \cdot CH_3CN$ (hydrogen atoms, solvents and anions were removed for clarity). Insert: Green lines indicate π-H interactions.

As with $[Fe(L^1)_2](PF_6)_2 \cdot CH_3CN$, $[Fe(L^1)_2](ClO_4)_2 \cdot CH_3CN$ shows the typical iron-bis terpy coordination with the phosphazene units forming two pockets around the central complex. Also as with hexafluorophosphate, perchlorate anions show hydrogen bonding with the hydrogen atoms of the terpy moieties, forming a column of anions between the cationic complexes. The complex has iron-nitrogen axial (Fe1–N1A and –N1B) bond lengths of 1.887(3) – 1.890(3) Å and equatorial (Fe1–N2A, –N3A, –N2B and –N3B) bond lengths are 1.954(4) – 1.975(4) Å (see Appendix B). These are typical bond lengths for an LS iron(II) bis-terpy complex[21,71-73] and are consistent with the purple colour of the complex. With the exceptions of the anions, $[Fe(L^1)_2](PF_6)_2 \cdot CH_3CN$ and $[Fe(L^1)_2](ClO_4)_2 \cdot CH_3CN$ have isomorphous structures.

3.4.3 Crystal structure of $[Fe(L^2)_2](PF_6)_2 \cdot CH_3CN$

Triclinic $[Fe(L^2)_2](PF_6)_2 \cdot CH_3CN$ crystallises in space group $P\bar{1}$. 57 electrons per cell were removed via *PLATON/SQUEEZE*[70] corresponding to 2.59 molecules of acetonitrile. The structure refines with one cationic complex and two hexafluorophosphate anions per unit cell (see Figure 3.4.3.1).

The complex shows the typical iron(II) bis-terpy arrangement, with each of the terpy nitrogens coordinating to the iron atom. The phosphazene rings show the same orientations as with $[Fe(L^1)_2](PF_6)_2$ and $[Fe(L^1)_2](ClO_6)_2$. Both the phosphazene units are identical, pointing away from the iron(II) bis-terpy complex. No π-π interactions were observed as in the previous examples.

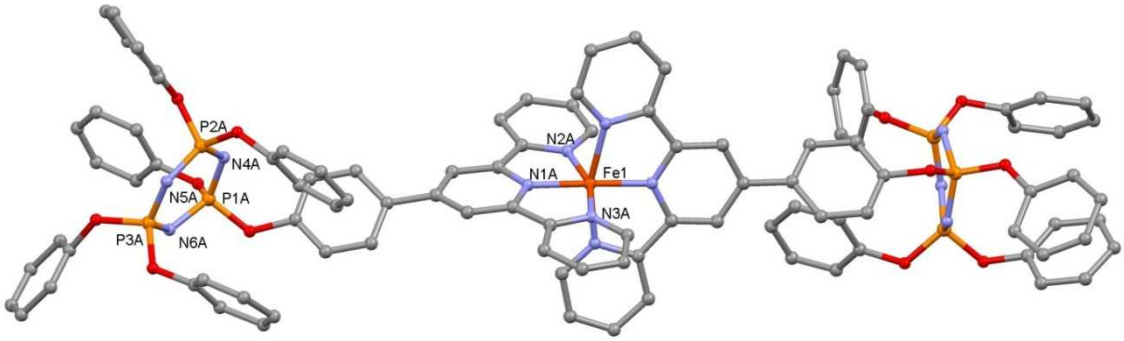

Figure 3.4.3.1 Unit cell for $[Fe(L^2)_2](PF_6)_2 \cdot CH_3CN$ (hydrogen atoms, solvents and anions were removed for clarity).

The hexafluorophosphate anions show hydrogen bonding with the hydrogen atoms of the terpy units and the phenyl spacer forming anionic columns between the cationic complexes. Hydrogen bonding is also observed between the hydrogen atoms of the phenol group and the oxygen atom of an adjacent phenol group (see Figure 3.4.3.2).

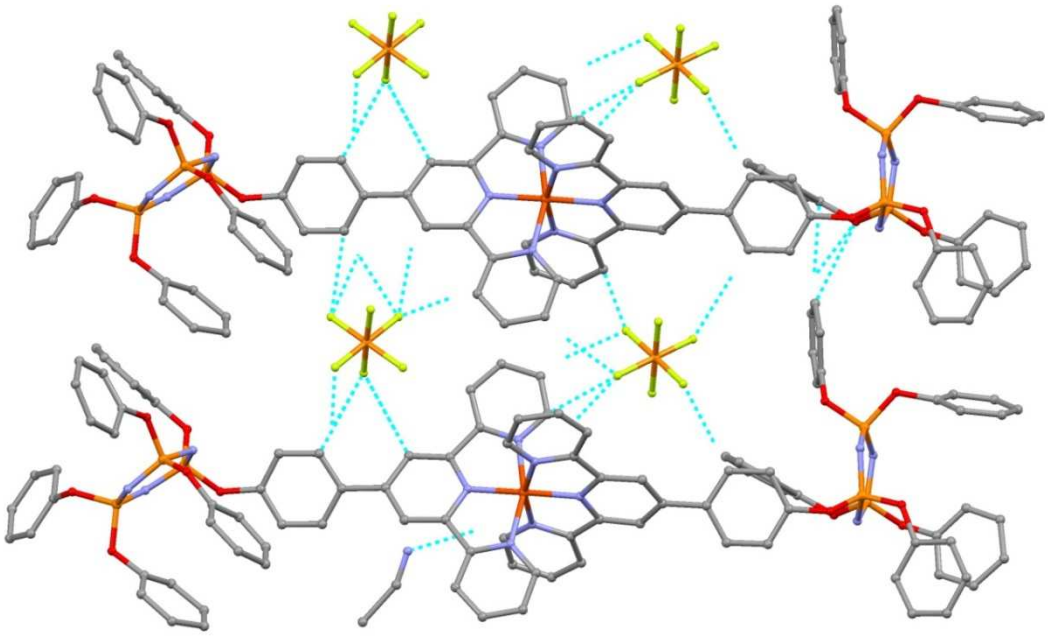

Figure 3.4.3.2 Packing of $[Fe(L^2)_2](PF_6)_2 \cdot CH_3CN$, dotted lines indicate hydrogen bonding (hydrogen atoms removed for clarity).

The iron nitrogen axial bond (Fe1–N1A and –N1B) lengths are 1.878(3) – 1.888(3) Å and the equatorial bond (Fe1–N2A, –N3A, –N2B and –N3B) lengths are 1.975(3) – 1.994(3) Å (see Appendix B). These are typical of an LS iron(II) bis-terpy complex,[21,71-73] which is consistent with the purple colour of the complex. The phenyl spacers have tetrahedral angle of 35.8(9)^o and 46.4(9)^o, which would reduce an electronic effects from the phosphazene. As with the previous complexes, the phosphazene bond lengths are typical of a phenoxy-substituted cyclotriphosphazene[74] (see Appendix B).

3.4.4 Crystal structure of $[Fe(L^3)_2](BF_4)_2 \cdot C_3H_6O \cdot C_5H_{12}O$

Triclinic $[Fe(L^3)_2](BF_4)_2 \cdot C_3H_6O \cdot C_5H_{12}O$ crystallises in space group $P\bar{1}$ with one molecule of acetone and one of tert-butyl methyl ether. The structure refines with one cationic complex and two tetrafluoroborate anions per unit cell (see Figure 3.4.4.1).

The complex shows the typical iron(II) bis-bbp arrangement, with each of the pyridine and four imidazole nitrogen's coordinating to the iron atom; as previously mentioned this is typical for iron(II) complexes. The phosphazene rings also show the same behaviour as in $[Fe(L^2)_2](PF_6)_2$, with both phosphazene rings facing away from the iron(II) bis-bbp complex.

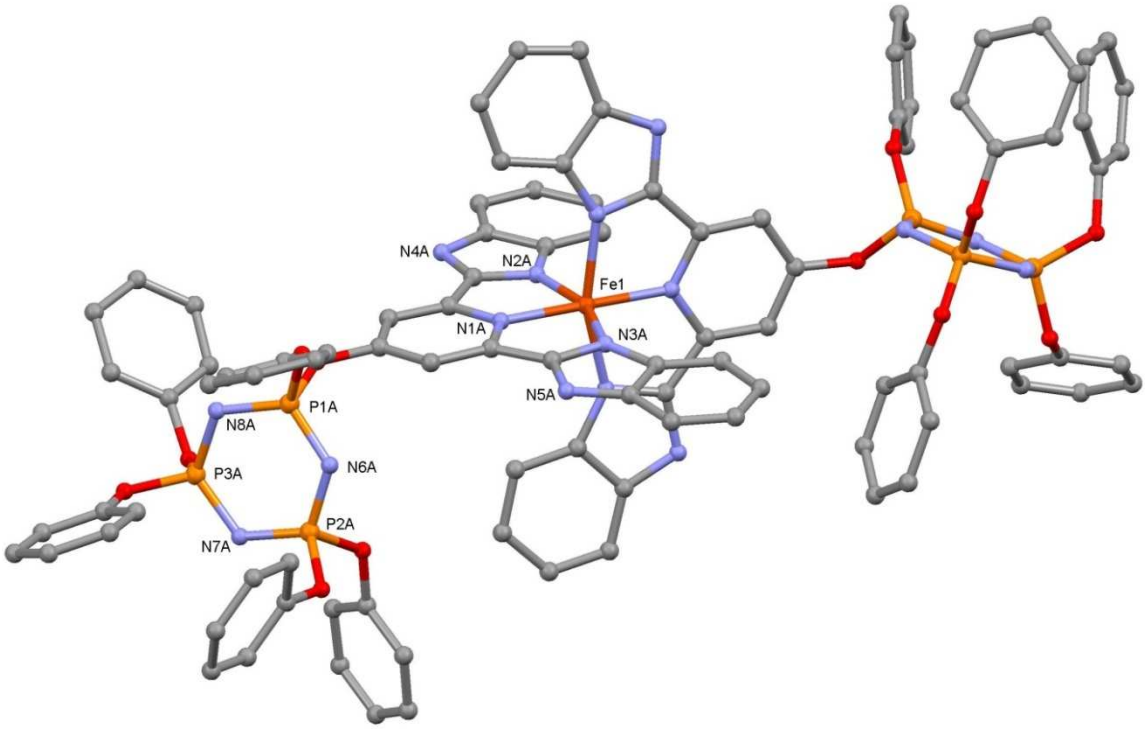

Figure 3.4.4.1 Unit cell contents for $[Fe(L^3)_2](BF_4)_2 \cdot C_3H_6O \cdot C_5H_{12}O$ (hydrogen atoms, solvents and anions were removed for clarity).

The fluorine atoms of the tetrafluoroborate anion forms hydrogen bonds with the hydrogen of the imidazole, the remaining imidazole protons forms a hydrogen bondn with the acetone and tert-butyl methyl ether (see Figure 3.4.4.2).

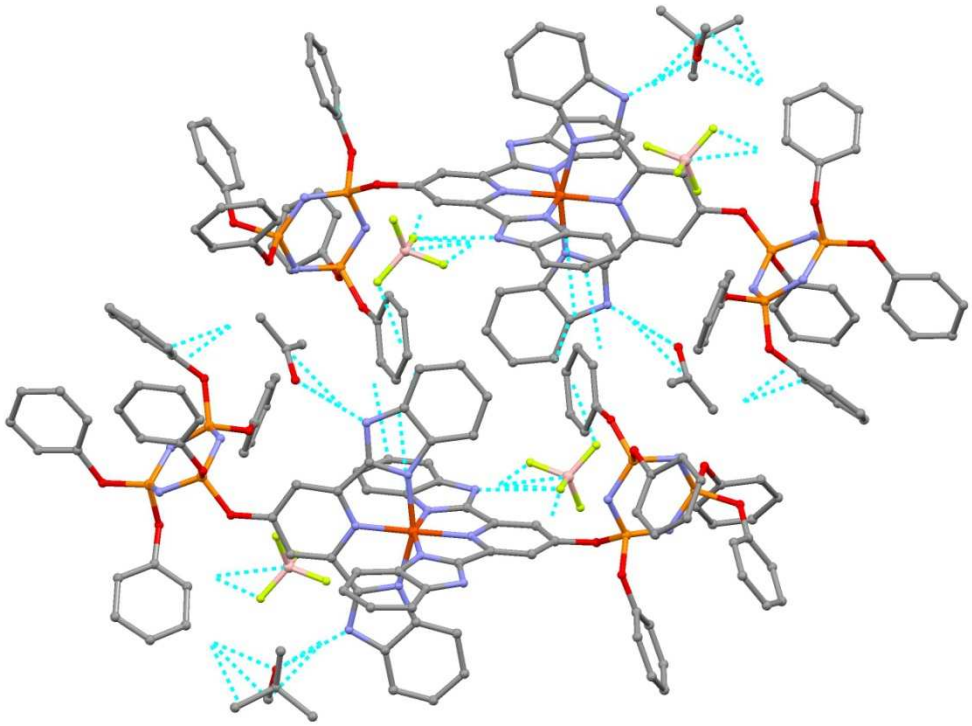

Figure 3.4.4.2 Packing structure of $[Fe(L^3)_2](BF_4)_2 \cdot C_3H_6O \cdot C_5H_{12}O$, dotted lines indicate hydrogen bonding (hydrogen atoms removed for clarity).

The iron nitrogen$_{pyridine}$ axial bond lengths (Fe1–N1A and –N1B) are 1.907(5) – 1.909(6) Å and the equatorial iron nitrogen$_{benzimidazole}$ bond lengths (Fe1–N2A, –N3A, –N2B and –N3B) are 1.987(5) – 1.996(5) Å (see Appendix B), typical bonds lengths of an LS iron(II) bis-bbp,[75] which corresponds to the purple colour of the complex. By the comparison to the bond lengths of L^3 (in Chapter 2), no significant differences in bond lengths are observed for the phosphazene ring therefore the metal complex has no interaction with the phosphazene ring (see Appendix B).

3.5 Conclusion

Sixteen iron(II) complexes were synthesised and characterised by reacting the ligands produced in Chapter 3 (L^1, L^2, L^3, L^4, L^5, L^6 and L^7) with the respective iron salt.

The crystal structures obtained for the $[Fe(L^1)_2](PF_6)_2$, $[Fe(L^1)_2](ClO_4)_2$, $[Fe(L^2)_2](PF_6)_2$ and $[Fe(L^3)_2](BF_4)_2$, show that the ligands coordinated to iron in a bis fashion which is consistent with the purple colour and other characterisation techniques used. As L^4 is also a tridentate ligand, it can be assumed that it will coordinate to iron in the same fashion as $[Fe(L^2)_2](PF_6)_2$. Another feature that is observed from the crystal structures is that the anions are located in approximately the same position for each of the complexes – both anions sit in a channel between the cationic complexes, hydrogen bonding to the iron-ligand centre. This is observed for hexfluorophosphate, perchlorate and tetrafluoroborate anions, therefore it can be assumed that all weakly coordinating anions will behave in the same way.

From these small molecule models it can be assumed that the same coordination behaviour will be observed in the polymer, as the phosphazene rings displayed no interaction with the coordination centre. As such, any metallo-polymer complexes that will be formed will be cross-linked via the metal-ligand centre.

3.6 References

1. Kirk, S. *Cyclo- and Polyphosphazenes Containing 2-oxypyridine Moieties Coordinated to Selected Transition Metals*, Massey University, Palmerston North, **2008**.

2. Allen, R. W.; Obrien, J. P.; Allcock, H. R. *Journal of the American Chemical Society* **1977**, *99*, 3987-3991.

3. Bolink, H. J.; Santamaria, S. G.; Sudhakar, S.; Zhen, C. G.; Sellinger, A. *Chemical Communications* **2008**, 618-620.

4. Diefenbach, U.; Stromburg, B. *Journal of Inorganic and Organometallic Polymers and Materials* **2006**, *16*, 295-306.

5. Diefenbach, U.; Bloy, M.; Stromburg, B. *Phosphorus Sulfur and Silicon and the Related Elements* **1999**, *146*, 65-68.

6. Diefenbach, U.; Kretschmann, M.; Stromburg, B. *Phosphorus Sulfur and Silicon and the Related Elements* **1997**, *125*, 143-152.

7. Allcock, H. R.; Manners, I.; Mang, M. N.; Parvez, M. *Inorganic Chemistry* **1990**, *29*, 522-529.

8. Gleria, M.; De Jaeger, R. *Phosphazenes: a worldwide insight*; Nova Science Publishers: New York, **2004**.

9. Ainscough, E. W.; Brodie, A. M.; Depree, C. V. *Journal of the Chemical Society-Dalton Transactions* **1999**, 4123-4124.

10. Ainscough, E. W.; Brodie, A. M.; Depree, C. V.; Jameson, G. B.; Otter, C. A. *Inorganic Chemistry* **2005**, *44*, 7325-7327.

11. Ainscough, E. W.; Brodie, A. M.; Depree, C. V.; Otter, C. A. *Polyhedron* **2006**, *25*, 2341-2352.

12. Constable, E. C. *Chemical Society Reviews* **2007**, *36*, 246-253.

13. Andres, P. R.; Schubert, U. S. *Advanced Materials* **2004**, *16*, 1043-1068.

14. Thompson, A. *Coordination Chemistry Reviews* **1997**, *160*, 1-52.

15. Puntoriero, F.; Campagna, S.; Stadler, A. M.; Lehn, J. M. *Coordination Chemistry Reviews* **2008**, *252*, 2480-2492.

16. Sauvage, J. P.; Collin, J. P.; Chambron, J. C.; Guillerez, S.; Coudret, C.; Balzani, V.; Barigelletti, F.; Decola, L.; Flamigni, L. *Chemical Reviews* **1994**, *94*, 993-1019.

17. Eryazici, I.; Moorefield, C. N.; Newkome, G. R. *Chemical Reviews* **2008**, *108*, 1834-1895.

18. Flamigni, L.; Collin, J. P.; Sauvage, J. P. *Accounts of Chemical Research* **2008**, *41*, 857-871.

19. Constable, E. C.; Hermann, B. A.; Housecroft, C. E.; Neuburger, M.; Schaffner, S.; Scherer, L. J. *New Journal of Chemistry* **2005**, *29*, 1475-1481.

20. Constable, E. C.; Zhang, G. Q.; Housecroft, C. E.; Neuburger, M. *Inorganic Chemistry Communications* **2010**, *13*, 878-881.

21. Constable, E. C.; Housecroft, C. E.; Price, J. R.; Schweighauser, L.; Zampese, J. A. *Inorganic Chemistry Communications* **2010**, *13*, 495-497.

22. Constable, E. C.; Housecroft, C. E.; Kokatam, S. L.; Medlycott, E. A.; Zampese, J. A. *Inorganic Chemistry Communications* **2010**, *13*, 457-460.

23. Constable, E. C.; Housecroft, C. E.; Neuburger, M.; Schneider, A. G. *Inorganic Chemistry Communications* **2003**, *6*, 912-915.

24. Beves, J. E.; Constable, E. C.; Housecroft, C. E.; Neuburger, M.; Schaffner, S.; Zampese, J. A. *Helvetica Chimica Acta* **2009**, *92*, 2214-2226.

25. Constable, E. C.; Housecroft, C. E.; Neuburger, M.; Price, J. R.; Schaffner, S. *Dalton Transactions* **2008**, 3795-3797.

26. Bhaumik, C.; Das, S.; Saha, D.; Dutta, S.; Baitalik, S. *Inorganic Chemistry* **2010**, *49*, 5049-5062.

27. Wadman, S. H.; Kroon, J. M.; Bakker, K.; Havenith, R. W. A.; van Klink, G. P. M.; van Koten, G. *Organometallics*, *29*, 1569-1579.

28. Whittle, B.; Horwood, E. L.; Rees, L. H.; Batten, S. R.; Jeffery, J. C.; Ward, M. D. *Polyhedron* **1998**, *17*, 373-379.

29. Louerat, F.; Gros, P. C. *Tetrahedron Letters*, *51*, 3558-3560.

30. Heller, M.; Schubert, U. S. *European Journal of Organic Chemistry* **2003**, 947-961.

31. Tu, S. J.; Jia, R.; Jiang, B.; Zhang, J. Y.; Zhang, Y.; Yao, C. S.; Ji, S. J. *Tetrahedron* **2007**, *63*, 381-388.

32. Bauer, C.; Boschloo, G.; Mukhtar, E.; Hagfeldt, A. *Journal of Physical Chemistry B* **2002**, *106*, 12693-12704.

33. Halcrow, M. A. *Polyhedron* **2007**, *26*, 3523-3576.

34. Constable, E. C.; Baum, G.; Bill, E.; Dyson, R.; van Eldik, R.; Fenske, D.; Kaderli, S.; Morris, D.; Neubrand, A.; Neuburger, M., *et al. Chemistry-a European Journal* **1999**, *5*, 498-508.

35. Hathcock, D. J.; Stone, K.; Madden, J.; Slattery, S. *Inorganica Chimica Acta* **1998**, *282*, 131-135.

36. Chambers, J.; Eaves, B.; Parker, D.; Claxton, R.; Ray, P. S.; Slattery, S. J. *Inorganica Chimica Acta* **2006**, *359*, 2400-2406.

37. Nielsen, P.; Toftlund, H.; Bond, A. D.; Boas, J. F.; Pilbrow, J. R.; Hanson, G. R.; Noble, C.; Riley, M. J.; Neville, S. M.; Moubaraki, B., *et al. Inorganic Chemistry* **2009**, *48*, 7033-7047.

38. Renz, F.; Oshio, H.; Ksenofontov, V.; Waldeck, M.; Spiering, H.; Gutlich, P. *Angewandte Chemie-International Edition* **2000**, *39*, 3699-3700.

39. Oshio, H.; Spiering, H.; Ksenofontov, V.; Renz, F.; Gutlich, P. *Inorganic Chemistry* **2001**, *40*, 1143-1150.

40. Boca, R.; Renz, F.; Boca, M.; Fuess, H.; Haase, W.; Kickelbick, G.; Linert, W.; Vrbova-Schikora, M. *Inorganic Chemistry Communications* **2005**, *8*, 227-230.

41. Enamullah, M.; Linert, W. *Thermochimica Acta* **2002**, *388*, 401-406.

42. Hasegawa, M.; Renz, F.; Hara, T.; Kikuchi, Y.; Fukada, Y.; Okubo, J.; Hoshi, T.; Linert, W. *Chemical Physics* **2002**, *277*, 21-30.

43. Boca, R.; Boca, M.; Dlhan, L.; Falk, K.; Fuess, H.; Haase, W.; Jarosciak, R.; Papankova, B.; Renz, F.; Vrbova, M., *et al. Inorganic Chemistry* **2001**, *40*, 3025-3033.

44. Hayami, S.; Motokawa, N.; Shuto, A.; Moriyama, R.; Masuhara, N.; Inoue, K.; Maeda, Y. *Polyhedron* **2007**, *26*, 2375-2380.

45. Riis-Johannessen, T.; Bernardinelli, G.; Filinchuk, Y.; Clifford, S.; Favera, N. D.; Piguet, C. *Inorganic Chemistry* **2009**, *48*, 5512-5525.

46. Grove, L. J.; Oliver, A. G.; Krause, J. A.; Connick, W. B. *Inorganic Chemistry* **2008**, *47*, 1408-1410.

47. Froidevaux, P.; Harrowfield, J. M.; Sobolev, A. N. *Inorganic Chemistry* **2000**, *39*, 4678-4687.

48. Concepcion, J. J.; Tsai, M. K.; Muckerman, J. T.; Meyer, T. J. *Journal of the American Chemical Society* **2010**, *132*, 1545-1557.

49. Concepcion, J. J.; Jurss, J. W.; Norris, M. R.; Chen, Z. F.; Templeton, J. L.; Meyer, T. J. *Inorganic Chemistry* **2010**, *49*, 1277-1279.

50. Linert, W.; Konecny, M.; Renz, F. *Journal of the Chemical Society-Dalton Transactions* **1994**, 1523-1531.

51. Philippopoulos, A. I.; Terzis, A.; Raptopoulou, C. P.; Catalano, V. J.; Falaras, P. *European Journal of Inorganic Chemistry* **2007**, 5633-5644.

52. Chryssou, K.; Catalano, V. J.; Kurtaran, R.; Falaras, P. *Inorganica Chimica Acta* **2002**, *328*, 204-209.

53. Stanley, J. M.; Zhu, X. J.; Yang, X. P.; Holliday, B. J. *Inorganic Chemistry*, *49*, 2035-2037.

54. Kadjane, P.; Starck, M.; Camerel, F.; Hill, D.; Hildebrandt, N.; Ziessel, R.; Charbonniere, L. J. *Inorganic Chemistry* **2009**, *48*, 4601-4603.

55. Mato-Iglesias, M.; Rodriguez-Blas, T.; Platas-Iglesias, C.; Starck, M.; Kadjane, P.; Ziessel, R.; Charbonniere, L. *Inorganic Chemistry* **2009**, *48*, 1507-1518.

56. Carbonera, C.; Kilner, C. A.; Letard, J. F.; Halcrow, M. A. *Dalton Transactions* **2007**, 1284-1292.

57. Alam, M. S.; Stocker, M.; Gieb, K.; Muller, P.; Haryono, M.; Student, K.; Grohmann, A. *Angewandte Chemie-International Edition* **2010**, *49*, 1159-1163.

58. Rajadurai, C.; Fuhr, O.; Kruk, R.; Ghafari, M.; Hahn, H.; Ruben, M. *Chemical Communications* **2007**, 2636-2638.

59. Money, V. A.; Elhaik, J.; Halcrow, M. A.; Howard, J. A. K. *Dalton Transactions* **2004**, 1516-1518.

60. Chandrasekar, R.; Schramm, F.; Fuhr, O.; Ruben, M. *European Journal of Inorganic Chemistry* **2008**, 2649-2653.

61. Rajadurai, C.; Schramm, F.; Brink, S.; Fuhr, O.; Ghafari, M.; Kruk, R.; Ruben, M. *Inorganic Chemistry* **2006**, *45*, 10019-10021.

62. Nihei, M.; Han, L. Q.; Oshio, H. *Journal of the American Chemical Society* **2007**, *129*, 5312-5313.

63. Nihei, M.; Maeshima, T.; Kose, Y.; Oshio, H. *Polyhedron* **2007**, *26*, 1993-1996.

64. Money, V. A.; Carbonera, C.; Elhaik, J.; Halcrow, M. A.; Howard, J. A. K.; Letard, J. F. *Chemistry-a European Journal* **2007**, *13*, 5503-5514.

65. Carbonera, C.; Costa, J. S.; Money, V. A.; Elhaik, J.; Howard, J. A. K.; Halcrow, M. A.; Letard, J. F. *Dalton Transactions* **2006**, 3058-3066.

66. Holland, J. M.; Barrett, S. A.; Kilner, C. A.; Halcrow, M. A. *Inorganic Chemistry Communications* **2002**, *5*, 328-332.

67. Braterman, P. S.; Song, J. I.; Peacock, R. D. *Inorganic Chemistry* **1992**, *31*, 555-559.

68. Sheldrick, G. M. *Acta Crystallographica Section A* **2008**, *64*, 112-122.

69. Dolomanov, O. V.; Bourhis, L. J.; Gildea, R. J.; Howard, J. A. K.; Puschmann, H. *Journal of Applied Crystallography* **2009**, *42*, 339-341.

70. Vandersluis, P.; Spek, A. L. *Acta Crystallographica Section A* **1990**, *46*, 194-201.

71. Beves, J. E.; Constable, E. C.; Housecroft, C. E.; Neuburger, M.; Schaffner, S.; Zampese, J. A. *Polyhedron* **2009**, *28*, 3828-3838.

72. Beves, J. E.; Chwalisz, P.; Constable, E. C.; Housecroft, C. E.; Neuburger, M.; Schaffner, S.; Zampese, J. A. *Inorganic Chemistry Communications* **2008**, *11*, 1009-1011.

73. Beves, J. E.; Constable, E. C.; Housecroft, C. E.; Neuburger, M.; Schaffner, S.; Zampese, J. A. *Inorganic Chemistry Communications* **2008**, *11*, 1006-1008.

74. Marsh, W. C.; Trotter, J. *Journal of the Chemical Society a -Inorganic Physical Theoretical* **1971**, 169-73.

75. Boca, R.; Baran, P.; Boca, M.; Dlhan, L.; Fuess, H.; Hasse, W.; Linert, W.; Papankova, B.; Werner, R. *Inorganica Chimica Acta* **1998**, *278*, 190-196.

Chapter 4

Reactions of cyclotriphosphazene ligands with selected ruthenium(II) complexes

4.0 Abbreviations used in Chapter 4

Terpy	2,2′:6′,2″-terpyridine
PhTerpy	2,6-di(pyridin-2-yl)-4-phenylpyridine
Bbp	2,6-di(1*H*-benzimidzol-2-yl)pyridine
Bpp	2,6-di(1*H*-pyrazol-1-yl)pyridine
NMR	Nuclear magnetic resonance
MLCT	Metal-to-ligand charge transfer
DSC	Differential scanning calorimetry

4.1 Introduction

This chapter focuses on the use of metal complexes as linkers to build supramolecular structures on a polymer backbone. As previously discussed in Chapter 3, the cyclotriphosphazene is often used as small molecule analogue of the polymer as it can be characterised more accurately than a polymer can be.

Ruthenium(II) was chosen as the metal to be used because it is less labile than iron(II) allowing the complexes to be built in a stepwise fashion,[1] which means other groups can be attached rather than forming a cross-linked polymer.

Tridentate ligands and co-ligands were chosen for four reasons: i) only two ligands can coordinate to one metal ion, providing a control for the ligand-metal ratio; ii) when substituted at the 4-position of the central unit the complexes formed are linear, giving control over the orientation; iii) the physical properties (e.g. electronic, vibrational, electrochemical) have been thoroughly investigated, therefore any changes in behaviour attributed to the attachment to the phosphazene can be compared and explained; iv) examples of the ligands being substituted with other groups via mild reactions such as Suzuki coupling.[2]

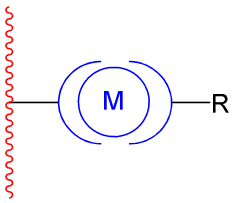

Figure 4.1.1 Schematic view of the metal complex used as a linker between a polymer and the R group.

A selection of suitable substituents was initially investigated to assess their reactivity with cyclophosphazenes in Chapter 2. Four ligands were chosen to coordinate to ruthenium, each of them contained the following ligand cores: 2,2':6',2''-terpyridine (terpy), 2,6-di(pyridin-2-yl)-4-phenylpyridine (PhTerpy), 2,6-di(1*H*-benzimidazol-2-yl)pyridine (bbp) and 2,6-di(1*H*-pyrazol-1-yl)pyridine (bpp). The properties of each group are described in turn.

4.1.1 2,2':6',2"-terpyridine

2,2':6',2"-terpyridines have been studied extensively due to their high affinity for metal ions and their interesting optical properties.[3-5] It is the latter that is the reason for their coordination to ruthenium. Ruthenium terpy complexes typically have high extinction coefficients making them suitable for applications such as dyes for solar cells,[6-8] photocatalysts and photo-activated drugs.

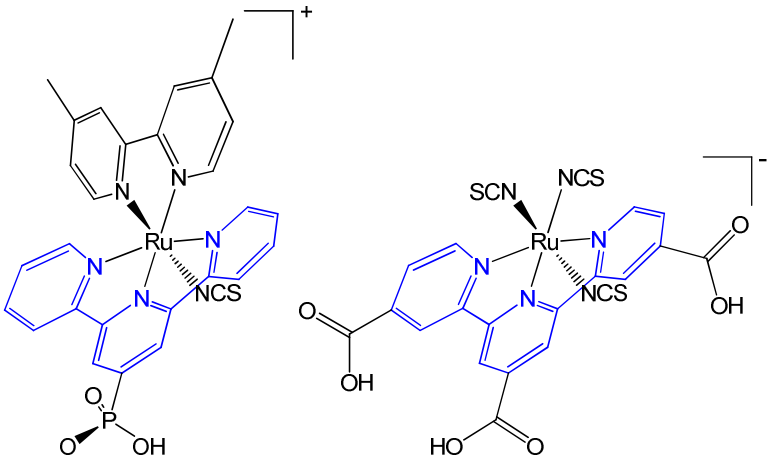

Figure 4.1.1.1 Examples of ruthenium(II)-terpy solar cell dyes.

Typically bis-terpy ruthenium(II) ($[Ru(Terpy)_2]^{2+}$) complexes have MLCT absorption bands near 450 nm with extinction coefficients of the order of 50,000 L mol^{-1} cm^{-1}. While this is large, the bands only cover a small section of the light spectrum, therefore a large portion of potential energy is lost. By making complexes with electron donor groups on one side and withdrawing ones on the other (dyads) it has been possible to direct the flow of electron density. It has also been possible through the formation of heteroleptic complexes to extend the peak absorbance range, allowing a larger portion of the visible spectrum to be converted to useable energy.[9]

4.1.2 2,6-di(1*H*-benzimidazol-2-yl)pyridine

The benzimidazolyl group is a stronger σ donor compared to 2-pyridyl or pyrazolyl, which results in different physical properties. 2,6-di(1*H*-benzimidazol-2-yl)pyridine (bbp) was first coordinated to ruthenium to form a complex analogous to terpy, capable of acting as a dye for the use in dye-sensitised solar cells (DSSC),[10,11] (see an example in Figure 4.1.2.1).

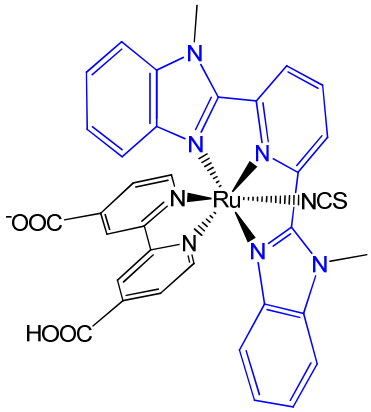

Figure 4.1.2.1 Solar cell dye based on bbp.[10]

However, despite its increased absorbance range it suffered from a decreased covering of TiO_2 and a decrease of electron injection efficiencies, resulting in a rapid decay of the dye, making it unsuitable for practical use.[10] Despite these limitations ruthenium-bbp complexes have found other applications that include anti-HIV drugs,[12] fluorescent conducting polymers,[13] and the catalytic of reduction reactions with acetonitrile[14] and water[15,16], they have it has been shown marked improvement over the terpy analogue.

Although all of these previously mentioned applications use the methyl-substituted bbp the proton-substituted ligands make many of the complex's properties pH dependent,[17-20] which can result in tuning of its behaviour (see Figure 4.1.2.2).

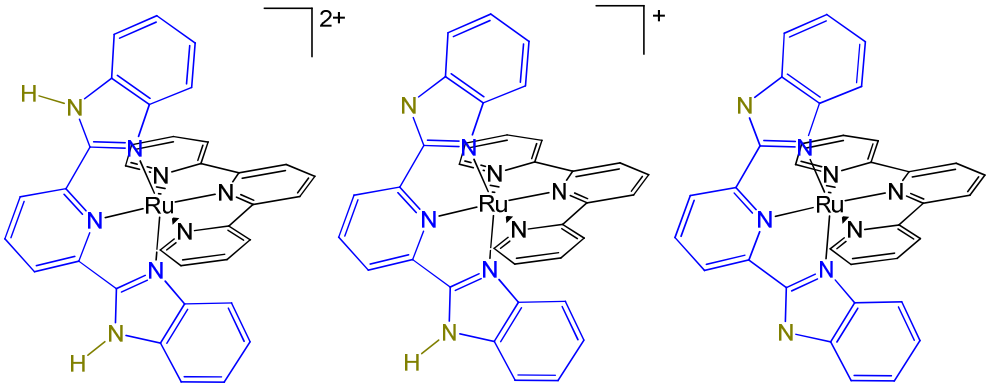

Figure 4.1.2.2 Various states of protonation for $[Ru(bbp)(Terpy)]^{2+}$. From left: $[Ru(bbp)(Terpy)]^{2+}$, $[Ru(bbp)(Terpy)]^{+}$ and $[Ru(bbp)(Terpy)]$.[20]

$[Ru(bbp)(Terpy)]^{2+}$ exhibits an MLCT at 475 nm and π-π^* transitions at 347 and 314 nm at pH 5. However, at pH 5–7 the MLCT is red-shifted to 498 nm and at pH > 7 it shifts to 509 nm. In addition to the red-shift of the MLCT additional transitions are observed > 650 nm as the pH is increased beyond 7 (see Figure 4.1.2.3). Other properties such as electrochemical and NMR behaviour are also altered by pH.[20]

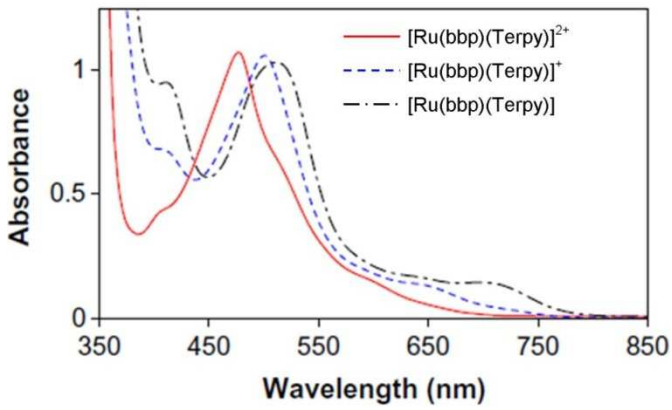

Figure 4.1.2.3 pH dependence of $[Ru(bbp)(Terpy)]^{n+}$ (n = 0–2) electronic spectra.[20]

4.1.3 2,6-di(1*H*-pyrazol-1-yl)pyridine

2,6-di(1*H*-pyrazol-1-yl)pyridine (bpp) was originally produced as an analogue to terpy.[21] Ruthenium complexes of bpp have been used for solar cell dyes[22] and catalysts[23-25].

The solar cell dyes formed with this ligand are analogues to the terpy and bbp, with one bpp ligand, a bipyridine and thiocyanide or cyanide (see Figure 4.1.3.1).[22]

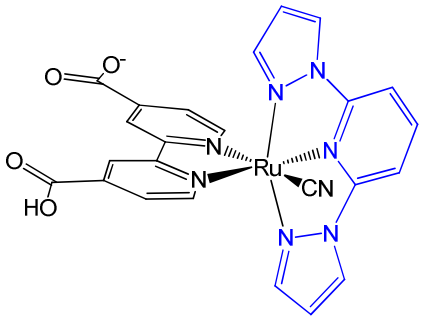

Figure 4.1.3.1 Solar cell dye based on bpp.[22]

The overall efficiencies were approximately 40% less than that of the terpy analogue, possibly due to the lower extinction coefficient. However, this is a higher efficiency than the bbp complex.

The catalysts are typically used for the conversion of alkenes to epoxides;[25] however, as with terpy and bbp, bpp has also been investigated for its reduction of water,[23] but there is no significant improvement over the terpy analogue. Few studies have been performed on the emission properties of ruthenium-bpp complexes. One study did show that measurable emissions could only be detected at low temperatures (see Figure 4.1.3.2),[26] which may account for the limited number of examples.

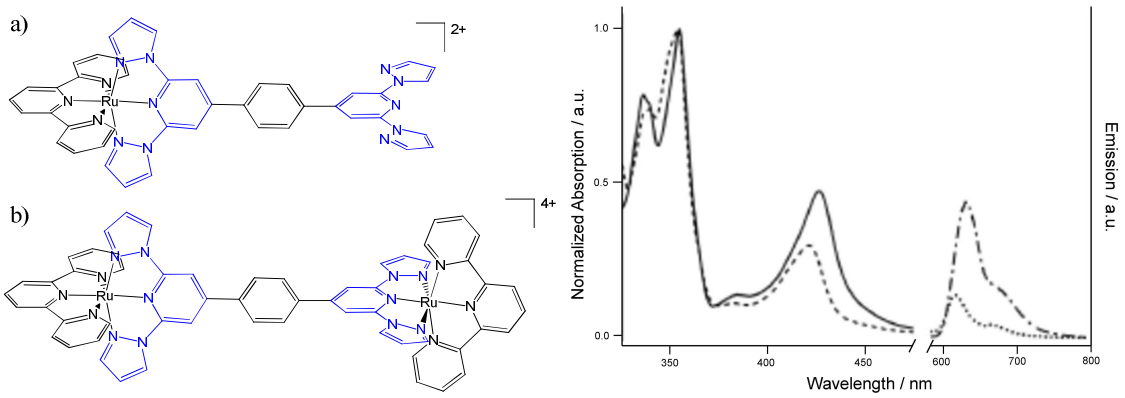

Figure 4.1.3.2 Left: a) monomer and b) dimer ruthenium complexes of bpp. Right: Absorbance (dashed line monomer, solid line dimer) and emission (dotted line monomer, dash-dotted line dimer) spectra of the monomer and dimer ruthenium complexes.[26]

It has been suggested that the weak fluorescence is attributed to the σ-donor behaviour of the ligand and the repulsion of the two ruthenium centres destabilising the ^{3}MLCT energy level; however, no lifetime or other measurements were made to further investigate this behaviour.[26]

4.2 Synthesis of the ruthenium(II) complexes

In this chapter the ligands produced in Chapter 2 and co-ligands (see Figure 4.2.1) were reacted with an assortment of ruthenium(II) complexes to produce the respective homo and heteroleptic complexes. This investigation was performed in order to elucidate the coordination behaviour of the complexes hence providing insight to the coordination behaviour of the polymer analogues. The experimental details are given in Appendix C. By comparison to the complexes formed in Chapter 3, only the phenoxy-substituted phosphazene ligands grew diffractable crystals, therefore these were the only ligands used in this investigation.

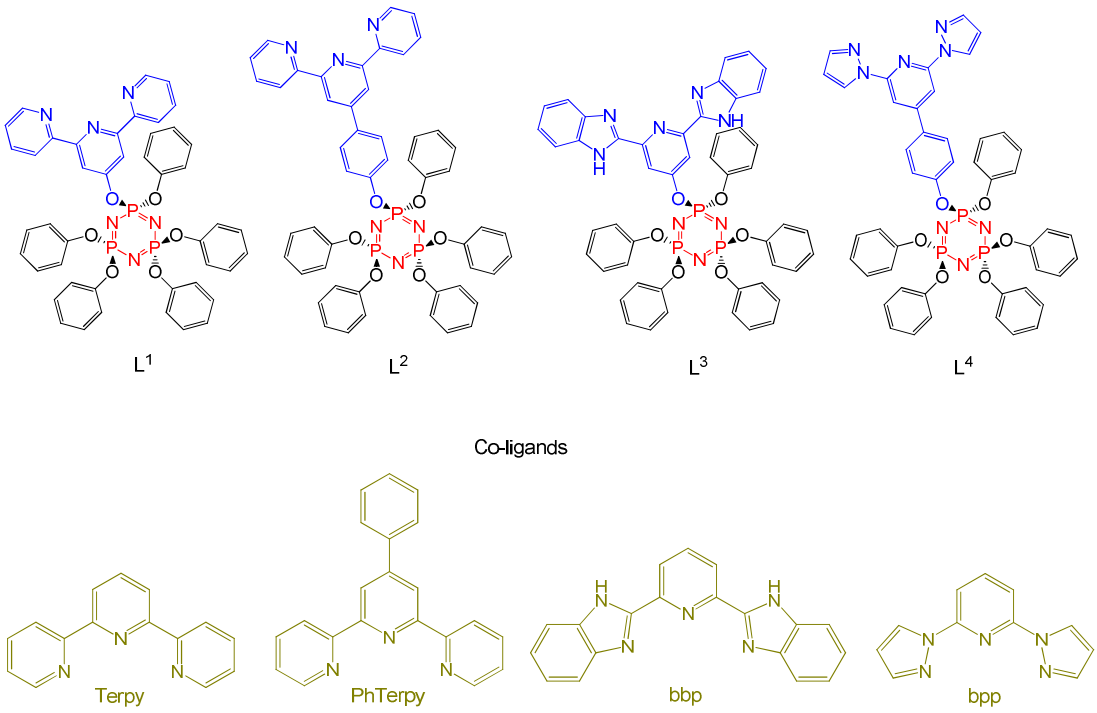

Figure 4.2.1 Ligands to be coordinated with ruthenium(II), green indicates co-ligands.

4.3 Observations from synthesis

By the addition of the appropriate ruthenium complex to each of the ligands, 15 complexes were successfully synthesised and characterised (see Figure 4.3.1). These will serve as models for their polyphosphazene analogues.

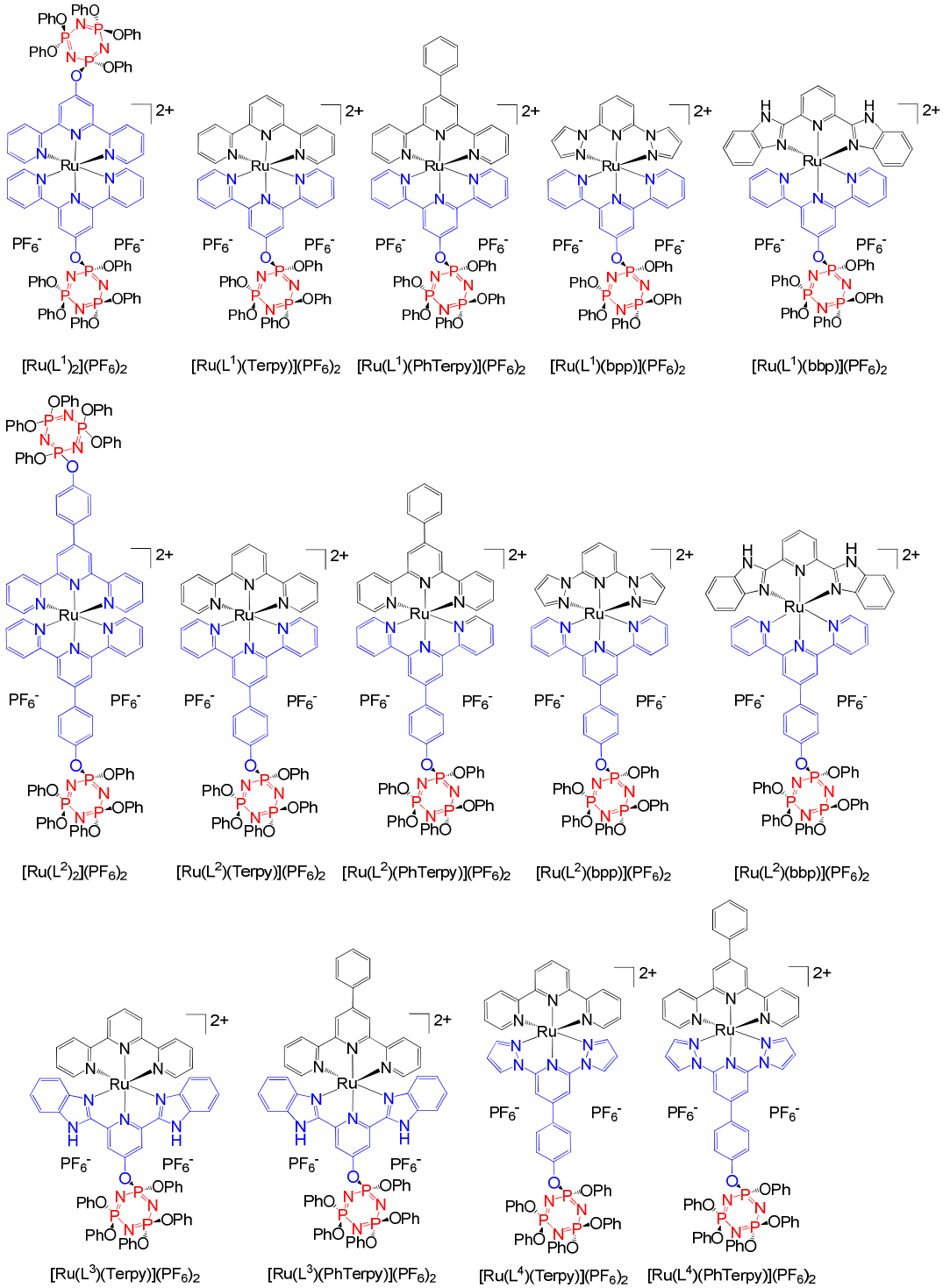

Figure 4.3.1 Ruthenium complexes synthesised in this chapter, hexafluorophosphate was used as the counter ion for each complex.

4.3.1 Homoleptic ruthenium(II) complexes

Homoleptic terpy complexes were formed by reacting two equivalents of each respective ligand with one equivalent of ruthenium trichloride, followed by the addition of ammonium hexafluorophosphate to precipitate out the pure product. N-ethylmorpholine was added to promote the reduction of ruthenium(III) to ruthenium(II); without its addition the yield was reduced by approximately 50%. Under the same conditions L^3 and L^4 only formed the respective ruthenium trichloride complexes, $Ru(L^3)Cl_3$ and $Ru(L^4)Cl_3$ (see Figure 4.3.1.1). This is consistent with the few literature examples available with bbp and bpp ligands.[17,18,26,27] Typically, refluxing in high temperature solvents such as ethylene glycol or DMF is required to form the homoleptic complexes.

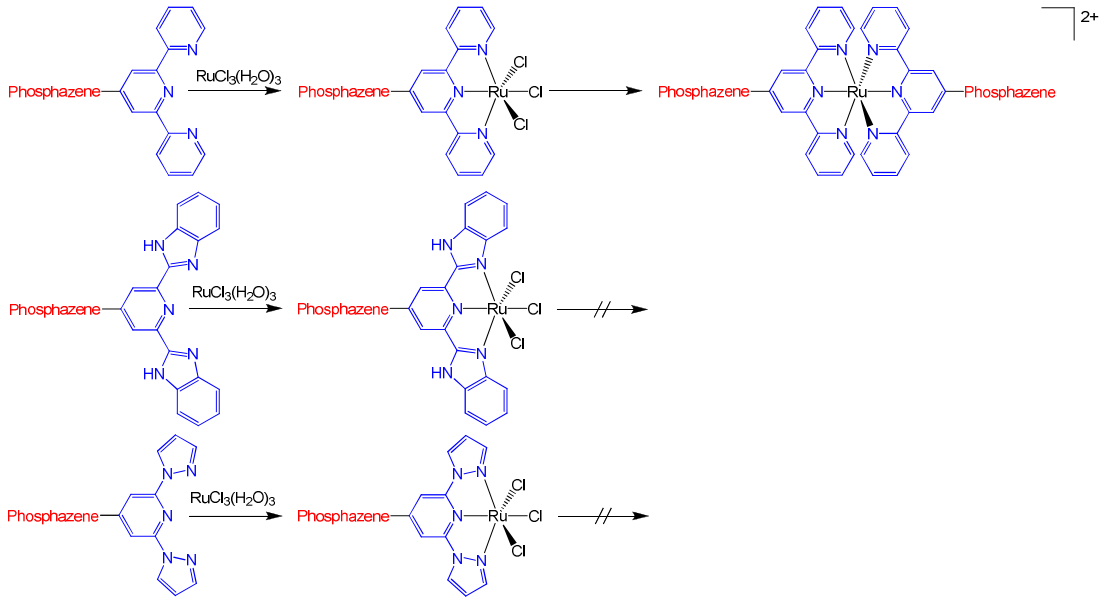

Figure 4.3.1.1 Homoleptic reaction schemes for L^1, L^2, L^3 and L^4.

4.3.2 Heteroleptic ruthenium(II) complexes

Ruthenium(II) heteroleptic complexes could be formed by two different methods:

A. reacting ruthenium trichloride with one equivalent of each phosphazene ligand forming the ruthenium trichloride complex, followed by reacting that complex with the respective co-ligand.
B. reacting one equivalent of the phosphazene ligand with one equivalent of the ruthenium trichloride complex of the respective co-ligand, e.g. $Ru(Terpy)Cl_3$ or $Ru(PhTerpy)Cl_3$.

For the terpy-terpy heteroleptic complexes either method produced the same product with approximately the same yield. However, for both L^3 and L^4 method A gave the ruthenium trichloride complex ($Ru(L^3)Cl_3$ and $Ru(L^4)Cl_3$) respectively which would not react with any co-ligand to form a ruthenium(II) complex. $Ru(DMSO)_4Cl_2$ could not be used for the formation of heteroleptic L^3 complexes because the reaction proceeded to the homoleptic species too rapidly. When method B was used only $Ru(Terpy)Cl_3$ and $Ru(PhTerpy)Cl_3$ reacted with the ligands. This is because both $Ru(bbp)Cl_3$ and $Ru(bpp)Cl_3$ require reactions to be carried out at high temperatures to proceed and this often forms mixtures of products.

When producing bbp complexes, care was necessary with the addition of N-ethylmorpholine; if too much was added a mixture of the protonated and deprotonated species were formed which could not be readily separated. By reducing the amount of N-ethylmorpholine, approximately half of the reactants remained unreacted, however, only the protonated species was formed. The addition of an excess of N-ethylmorpholine or triethylamine resulted in a large ratio of the deprotonated species being formed, however, the product still contained a mixture of the protonated species. This is likely due to an equilibrium forming as a result of a weak base reacting with a weak acid; if a stronger base was used it may drive the equilibrium to the deprotonated species. However, this increases the chance of damaging the phosphazene (see Figure 4.3.2.1).

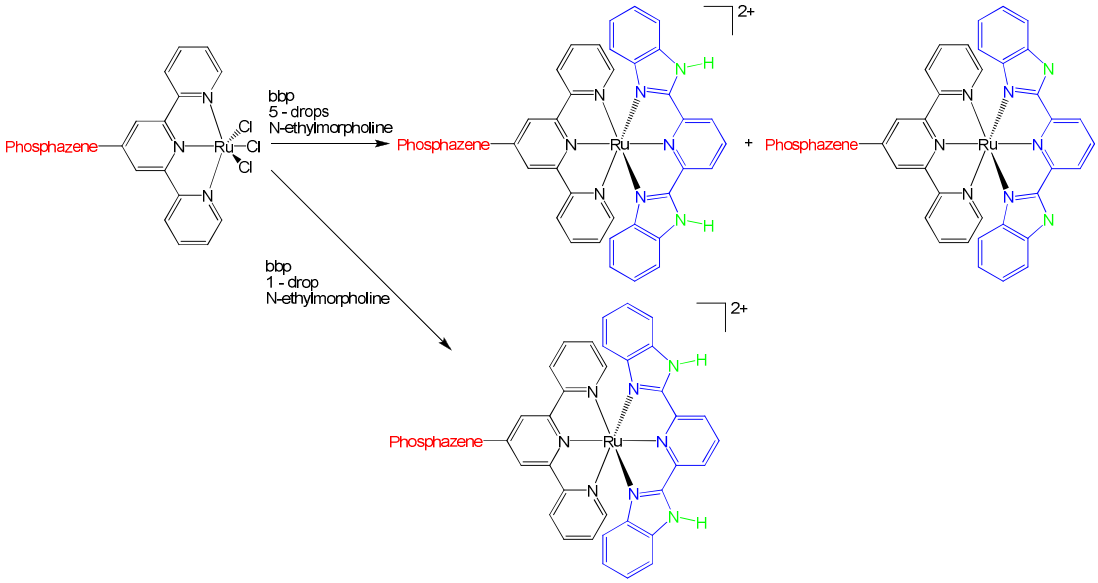

Figure 4.3.2.1 Controlled synthesis of both the protonated and deprotonated bbp complexes.

Such behaviour was not observed for L^3 based complexes. When the same ratio of N-ethylmorpholine was added to the reaction no deprotonated species were produced. This is possibly due to electronic effects or steric effects due to the ligand core being held close to the phosphazene unit (see Figure 4.3.2.2).

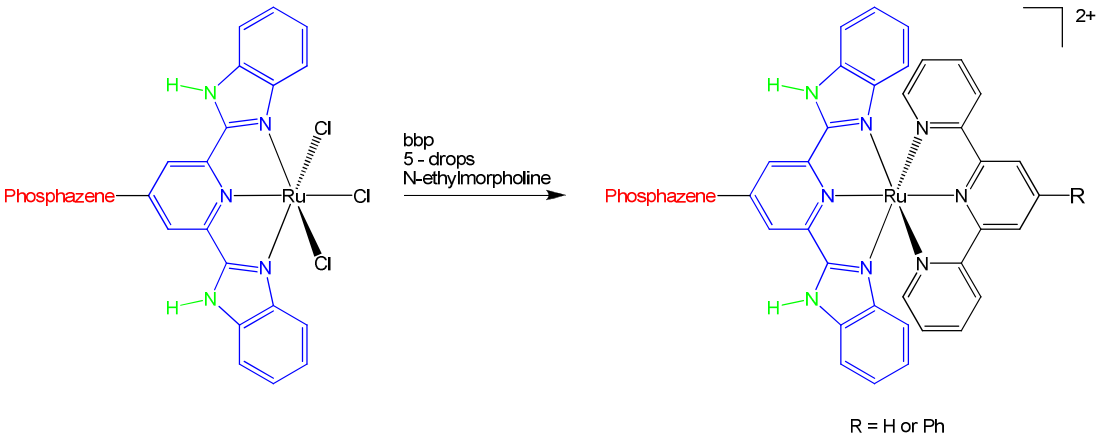

Figure 4.3.2.2 Synthetic scheme for the synthesis of L^3 complexes.

4.4 Crystallography

The X-ray data were collected at low temperature with a Rigaku-Spider X-ray diffractometer, comprising a Rigaku MM007 microfocus copper rotating-anode generator, high-flux Osmic monochromating and focusing multilayer mirror optics (Cu K radiation, λ = 1.5418 Å), and a curved image-plate detector. *CrystalClear*[28] was utilised for data collection and *FSProcess* in *PROCESS-AUTO* for cell refinement and data reduction.

The structures were solved by direct methods and refined using both the *SHELX*[29] and *OLEX*[2] [30] programs. Hydrogen atoms were calculated at ideal positions. Crystal refinement data are given in Table 4.4.1.1. CIF files are included on the accompanying compact disc for reference. On conducting an online CIF check, all significant alerts have been explained in the CIF file.

4.4.1 L^1 based complexes

Refinement data for the X-ray crystal structures are given in Table 4.4.1.1.

Table 4.4.1.1 Crystallographic and refinement data for complexes.

Compound	**$[Ru(L^1)_2](PF_6)_2 \cdot CH_3CN$**	**$[Ru(L^1)(Terpy)](PF_6)_2 \cdot CH_3CN$**
Molecular formula	$C_{92}H_{73}F_{12}N_{13}O_{12}P_8Ru$	$C_{62}H_{49}F_{12}N_{10}O_6P_5Ru$
M (g mol^{-1})	2129.51	1514.03
Temperature (K)	143 (2)	163 (2)
Crystal system	Triclinic	Triclinic
Space group	$P\bar{1}$	$P\bar{1}$
a(Å)	15.022 (3)	14.249 (3)
b(Å)	16.380 (3)	14.389 (3)
c(Å)	21.000 (4)	17.779 (4)
α(°)	102.50 (3)	111.43 (3)
β(°)	100.80 (3)	90.67 (3)
γ(°)	91.59 (3)	109.85 (3)
V(Å^3)	4944.1 (17)	3153.0 (16)
Z	2	2
μ(Cu Kα) mm^{-1}	3.266	4.062
ρ_{calc} (g cm^{-3})	1.430	1.595
$2\theta_{max}$(°)	124.76	130.16
Number of unique reflections	15176	10242
Data/restrains/ parameters	15176/90/1244	10242/0/866
Final R indices [I>2σ(I)]	$R1$ = 0.0534	$R1$ = 0.0424
	$wR2$ = 0.1478	$wR2$ = 0.1213
R indices (all data)	$R1$ = 0.0604	$R1$ = 0.0508
	$wR2$ = 0.1539	$wR2$ = 0.1302
Goodness-of-fit on F^2	1.041	0.923

Table 4.4.1.1 Continued. Crystallographic and refinement data for complexes.

Compound	**$[Ru(L^1)(PhTerpy)](PF_6)_2$**	**$[Ru(L^1)(bpp)](PF_6)_2 \cdot CH_3CN$**	**$[Ru(L^1)(bbp)](PF_6)_2$**
Molecular formula	$C_{66}H_{50}F_{12}N_9O_6P_5Ru$	$C_{56}H_{44}F_{12}N_{12}O_6P_5Ru$	$C_{70}H_{60}F_{12}N_{11}O_8P_5Ru$
M (g mol^{-1})	1549.09	1450.94	1667.21
Temperature (K)	163 (2)	173 (2)	123 (2)
Crystal system	Monoclinic	Monoclinic	Triclinic
Space group	$P2_1/c$	$C2/c$	$P\bar{1}$
a(Å)	9.7822 (2)	37.525 (8)	9.8217 (2)
b(Å)	17.6621 (3)	15.032 (3)	19.6815 (4)
c(Å)	37.307 (3)	23.974 (5)	20.6624 (15)
α(°)	90.00	90.00	81.567 (6)
β(°)	96.182 (7)	110.81 (3)	76.696 (5)
γ(°)	90.00	90.00	80.709 (6)
V(Å^3)	6408.2 (5)	12641 (4)	3810.6 (3)
Z	4	8	2
μ(Cu Kα) mm^{-1}	4.009	4.029	3.440
ρ_{calc} (g cm^{-3})	1.606	1.525	1.453
$2\theta_{max}$(°)	130.16	144.18	117.88
Number of unique reflections	10872	12210	10729
Data/restrains/parameters	10872/194/933	12210/331/910	10729/754/1093
Final R indices [I>2σ(I)]	$R1$ = 0.0773	$R1$ = 0.0527	$R1$ = 0.0723
	$wR2$ = 0.1846	$wR2$ = 0.1550	$wR2$ = 0.2054
R indices (all data)	$R1$ = 0.1042	$R1$ = 0.0648	$R1$ = 0.0790
	$wR2$ = 0.2028	$wR2$ = 0.1653	$wR2$ = 0.2152
Goodness-of-fit on F^2	1.071	1.077	1.103

Crystal structure of $[Ru(L^1)_2](PF_6)_2 \cdot CH_3CN$

Triclinic $[Ru(L^1)_2](PF_6)_2 \cdot CH_3CN$ crystallises in space group $P\bar{1}$ with one molecule of acetonitrile. 48 electrons per cell were removed via *PLATON/SQUEEZE*[31] corresponding to 1.14 molecules of diethyl ether. The structure refines with one cationic complex and two hexafluorophosphate anions per unit cell (see Figure 4.4.1.1).

The complex shows a ruthenium(II) bis-terpy arrangement, with each of the terpy nitrogens coordinating to the ruthenium atom, confirming the spectroscopic data collected. The phosphazene rings sit in two different positions, one pointing away from the central terpy complex, while the other folds over due to π-H interactions between the terpy hydrogen and non-geminal pendant phenol rings (3.347(3) Å), forming a pocket. This complex forms an isomorph of its iron analogue ($[Fe(L^1)_2](PF_6)_2 \cdot CH_3CN$).

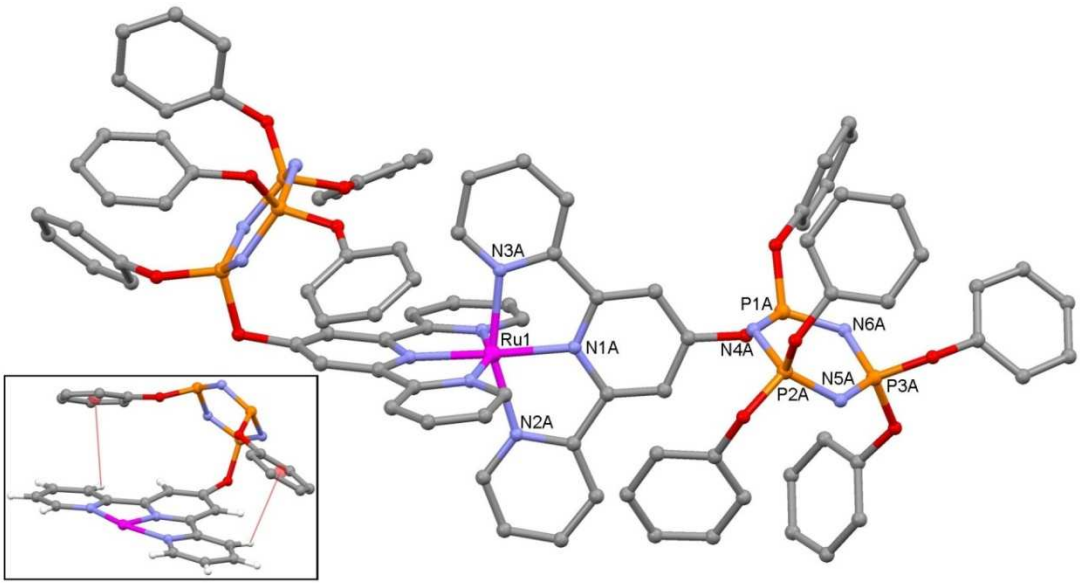

Figure 4.4.1.1 Unit cell of $[Ru(L^1)_2](PF_6)_2 \cdot CH_3CN$ (hydrogen atoms, solvents and anions removed for clarity). Insert: Red lines indicate π-H interactions.

The ruthenium-nitrogen axial bond lengths (Ru1–N1A and –N1B) are 1.977(3) and 1.980(3) Å respectively; the equatorial bond lengths (Ru1 –N2A, –N3A, –N2B and –N3B) are 2.053(3) – 2.074(3) Å (see Appendix C). These are typical bond lengths for ruthenium(II) bis-terpy complexes,[32,33] which is consistent with the orange colour of the complex. The phosphazene bond lengths are also of typical size for phenoxy-substituted cyclotriphosphazene[34] (see Appendix C).

Crystal structure of $[Ru(L^1)(Terpy)](PF_6)_2 \cdot CH_3CN$

Triclinic $[Ru(L^1)(Terpy)](PF_6)_2 \cdot CH_3CN$ crystallises in space group $P\,\bar{1}$ with one molecule of acetonitrile. The structure refines with one cationic complex and two hexafluorophosphate anions per unit cell (see Figure 4.4.1.2).

This heteroleptic complex shows two terpy units coordinating to the ruthenium centre, with each of the terpy nitrogens coordinating to the ruthenium atom, confirming the spectroscopic data collected. The phosphazene ring folds over the terpy oxygen with two of the non-geminal pendant phenoxy groups, showing a face to face π-H interaction with the proton of the terpy group (3.245(3) Å). The phosphazene substituted terpy ruthenium-nitrogen bonds lengths are (Ru1–N1, –N2 and –N3) 1.982(3), 2.072(3) and 2.079(3) Å respectively. The non-phosphazene ruthenium-nitrogen terpy bond lengths are (Ru1–N4, –N5 and –N6) 1.980(3), 2.080(3) Å and 2.095(3) Å respectively (Appendix C), showing that the phosphazene terpy is slightly more electron donating than the unsubstituted terpy.

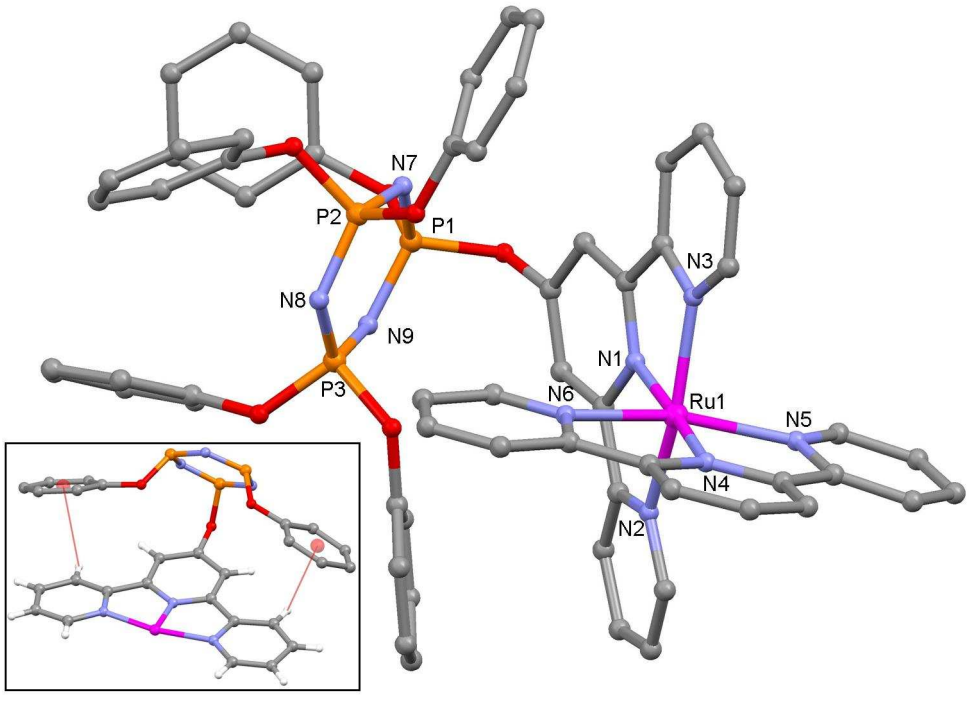

Figure 4.4.1.2 Unit cell of $[Ru(L^1)(Terpy)](PF_6)_2 \cdot CH_3CN$ (hydrogen atoms removed for clarity). Insert: Red lines indicate π-H interactions.

Crystal structure of [Ru(L^1)(PhTerpy)](PF_6)$_2$

Monoclinic [Ru(L^1)(PhTerpy)](PF_6)$_2$ crystallises in space group $P2_1/c$. The structure refines with one cationic complex and two hexafluorophosphate anions per unit cell (see Figure 4.4.1.3).

This heteroleptic complex shows two terpy units coordinating to the ruthenium centre, with each of the terpy nitrogens coordinating to the ruthenium atom, confirming the spectroscopic data collected. No interactions were observed between the terpy unit and the phosphazene. The phosphazene substituted terpy ruthenium-nitrogen bonds lengths are (Ru1–N1, –N2 and –N3) 1.980(4), 2.092(6) and 2.055(6) Å respectively. The PhTerpy ruthenium-nitrogen bond lengths are (Ru1–N4, –N5 and –N6) 1.965(4), 2.072(5) and 2.066(5) Å respectively (see Appendix C), showing phenyl-substituted terpy is slightly more electron donating than the phosphazene-substituted terpy unit; however, this difference is less significant than for the non-substituted terpy. See Chapter 6 for further investigations.

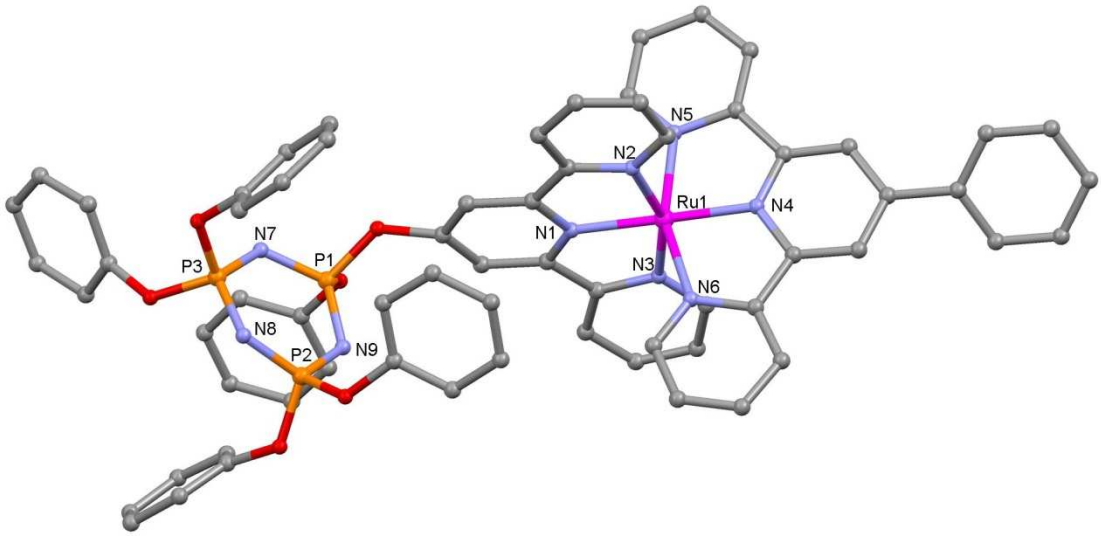

Figure 4.4.1.3 Unit cell of [Ru(L^1)(PhTerpy)](PF_6)$_2$ (hydrogen atoms and anions removed for clarity).

Crystal structure of $[Ru(L^1)(bpp)](PF_6)_2 \cdot CH_3CN$

Monoclinic $[Ru(L^1)(bpp)](PF_6)_2 \cdot CH_3CN$ crystallises in space group *C*2/*c*. The structure refines with one cationic complex, one acetonitrile molecule and two hexafluorophosphate anions per unit cell (see Figure 4.4.1.4).

This heteroleptic complex shows one terpy and bpp units coordinating to the ruthenium centre, with each of the terpy and pyrazole nitrogens coordinating to the ruthenium atom, confirming the spectroscopic data collected. The phosphazene ring folds over the oxygen terpy, with two of the non-geminal pendant phenoxy groups showing a face to face π-H interaction with the proton of the terpy group (2.883(3) Å). The ruthenium-nitrogen bonds of terpy are (Ru1–N1, –N2 and –N3) 1.972(3), 2.071(3) and 2.069(3) Å respectively. The bpp bond lengths are (Ru1–N4,–N6 and –N7) 1.997(3), 2.060(3) and 2.071(3) Å respectively (see Appendix C). The longer bpp bond lengths are typical of the ruthenium terpy-bpp complex.[26]

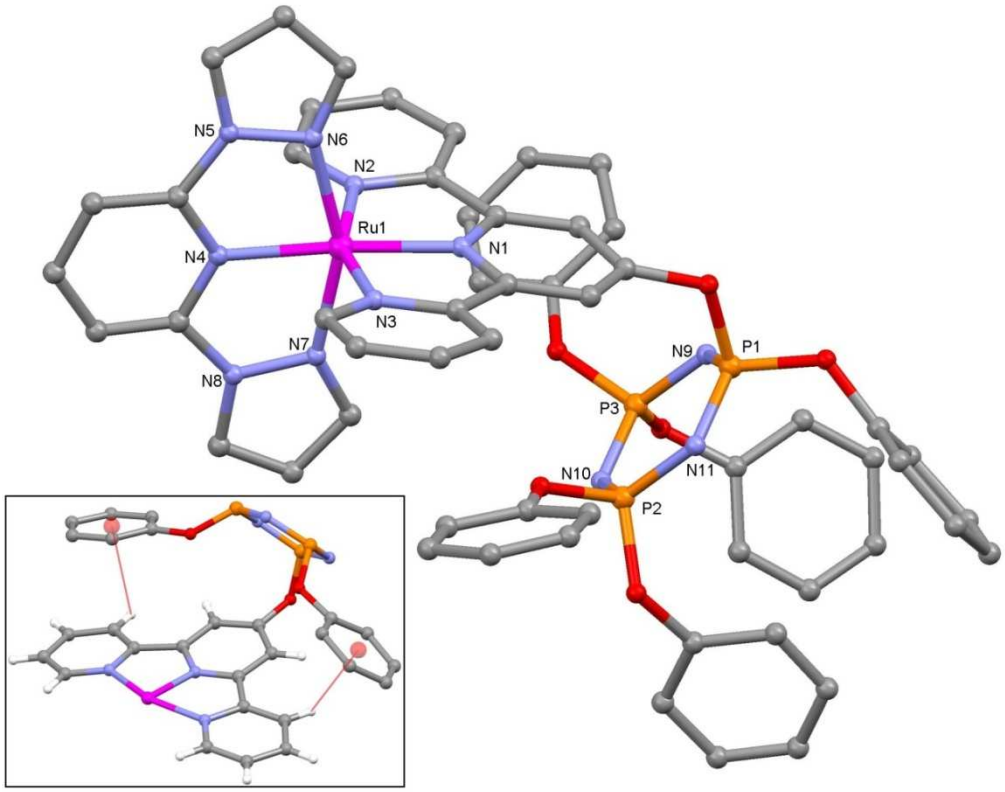

Figure 4.4.1.4 Unit cell of $[Ru(L^1)(bpp)](PF_6)_2 \cdot CH_3CN$ (hydrogen atoms, solvents and anions removed for clarity). Insert: Red lines indicate π-H interactions.

Crystal structure of $[Ru(L^1)(bbp)](PF_6)_2 \cdot C_3H_5O$

Triclinic $[Ru(L^1)(bbp)](PF_6)_2 \cdot C_3H_5O$ crystallises in space group $P\bar{1}$. The structure refines with one cationic complex, one acetone molecule and two hexafluorophosphate anions per unit cell (see Figure 4.4.1.5). 50 electrons per cell were removed via *PLATON/SQUEEZE*[31] corresponding to 1.56 molecules of acetone.

This heteroleptic complex shows one terpy and bbp units coordinating to the ruthenium centre, with each of the terpy and imidazole nitrogens coordinating to the ruthenium atom, confirming the spectroscopic data collected. The phosphazene ring folds over the oxygen terpy. However, unlike $[Ru(L^1)(bpp)](PF_6)_2 \cdot CH_3CN$ the non-geminal pendant phenoxy groups do not display π-π interactions, possibly due to the different crystallisation conditions. The ruthenium-nitrogen bonds lengths of terpy are (Ru1–N1, –N2 and –N3) 1.968(4), 2.063(4) and 2.074(4) Å respectively. The ruthenium-nitrogen bond lengths of bbp are (Ru1–N4, –N6 and –N8) 2.007(4), 2.069(4) and 2.065(4) Å respectively (see Appendix C), the longer bbp bond lengths are typical of the ruthenium terpy-bbp complex.[19,27]

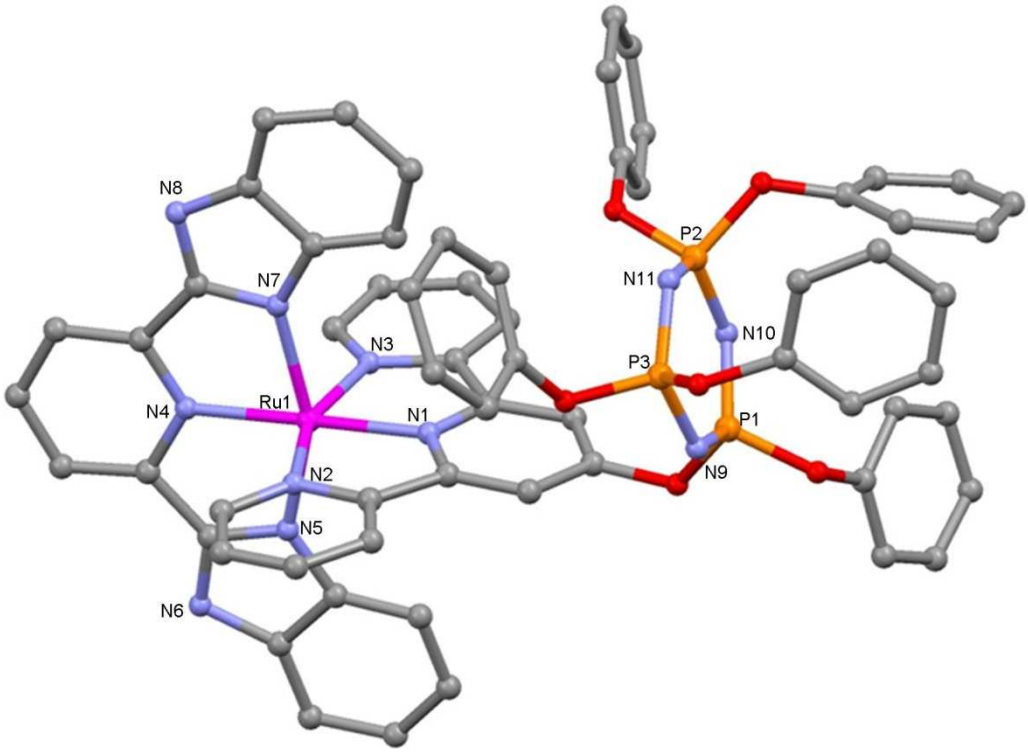

Figure 4.4.1.5 Unit cell of $[Ru(L^1)(bbp)](PF_6)_2 \cdot C_3H_5O$ (hydrogen atoms, solvents and anions removed for clarity).

4.4.2 Packing of the L^1 based complexes

For $[Ru(L^1)_2](PF_6)_2$ both the hexafluorophosphate anions show hydrogen bonding with the protons of the terpy units of the cationic complex, forming a channel of anions between the cationic complexes. The localised acetonitrile fills in the voids formed between the phenol and terpy groups (see Figure 4.4.2.1).

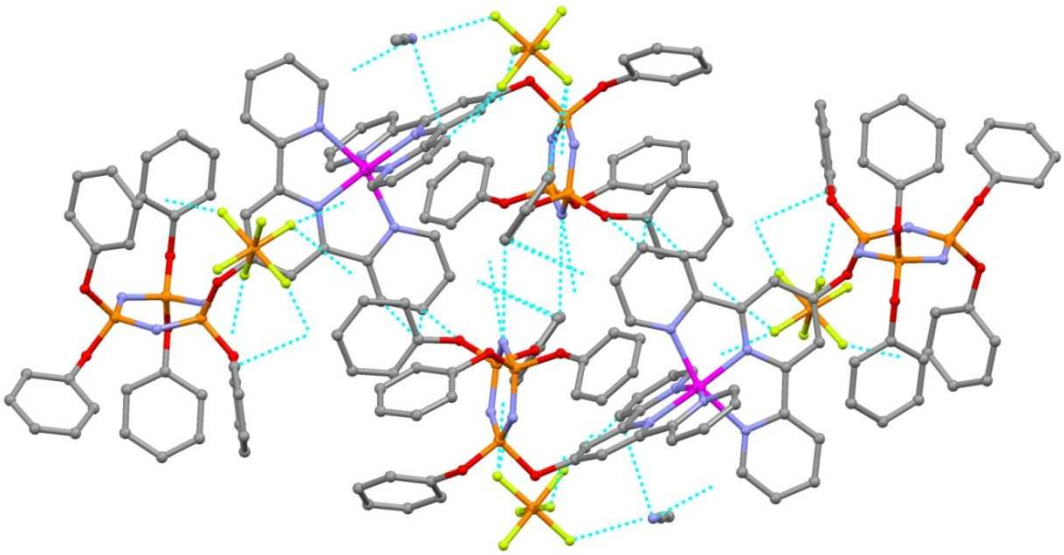

Figure 4.4.2.1 Packing of $[Ru(L^1)_2](PF_6)_2 \cdot CH_3CN$, dotted lines indicate bonding interactions.

Both $[Ru(L^1)(Terpy)](PF_6)_2 \cdot CH_3CN$ and $[Ru(L^1)(bpp)](PF_6)_2 \cdot CH_3CN$ packed via a combination of hexafluorophosphate anions hydrogen bonding with the protons of the terpy units and the phenyl rings, forming a channel of anions between the cationic complexes, with the acetonitrile hydrogen bonding with the unsubstituted terpy proton and the hexafluorophosphate anion filling the cavity (see Figure 4.4.2.2).

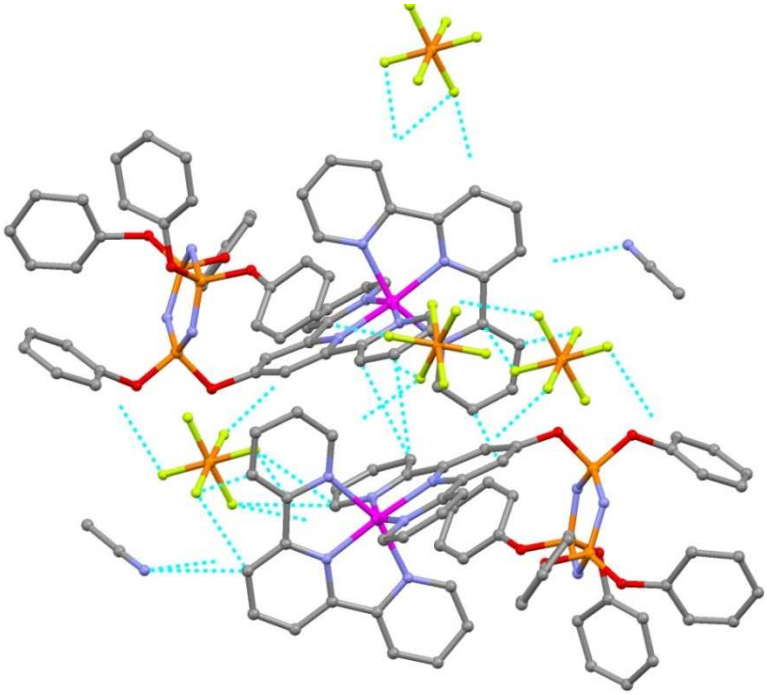

Figure 4.4.2.2 Packing of $[Ru(L^1)(Terpy)](PF_6)_2 \cdot CH_3CN$. Dotted lines indicate bonding interactions.

$[Ru(L^1)(PhTerpy)](PF_6)_2$ crystallises with the absence of any solvent molecules in the matrix. The cationic complexes are hydrogen bonded between terpy protons with the hexafluorophosphate anions, forming a zig-zag channel between the terpy units (see Figure 4.4.2.3).

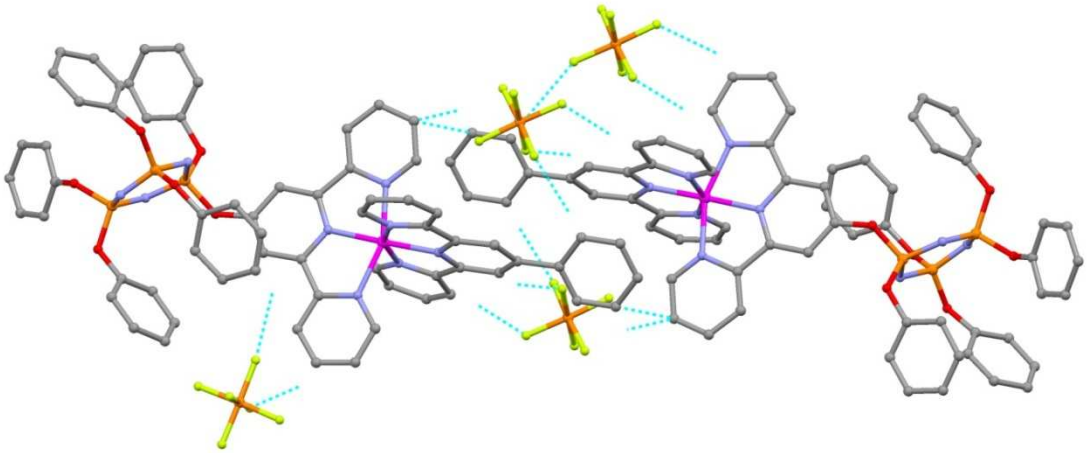

Figure 4.4.2.3 Packing of $[Ru(L^1)(PhTerpy)](PF_6)_2$, dotted lines indicate bonding interactions.

$[Ru(L^1)(bbp)](PF_6)_2 \cdot C_3H_5O$ packed via a combination of hexafluorophosphate anions hydrogen bonding with the protons of the terpy and bbp units and the phenyl rings, forming a channel of anions between the cationic complexes, with the acetone hydrogen bonding with the protons of both the terpy and bbp protons (see Figure 4.4.2.4).

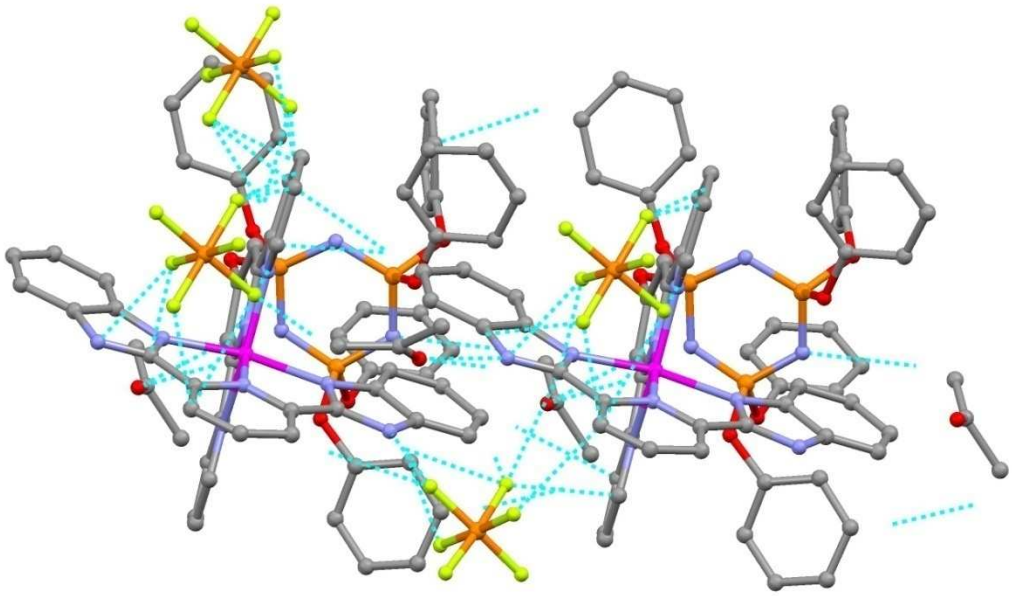

Figure 4.4.2.4 Packing of $[Ru(L^1)(bbp)](PF_6)_2 \cdot C_3H_5O$, dotted lines indicate bonding interactions.

4.4.3 L^2 based complexes

Refinement data for the $[Ru(L^2)_2](PF_6)_2$ crystal structure are given in Table 4.4.3.1.

Table 4.4.3.1 Crystallographic and refinement data for the complex.

Compound	**$[Ru(L^2)_2](PF_6)_2$**
Molecular formula	$C_{102}H_{78}F_{12}N_{12}O_{12}P_8Ru$
M (g mol^{-1})	2240.60
Temperature (K)	143 (2)
Crystal system	Triclinic
Space group	$P\bar{1}$
a(Å)	9.8601 (2)
b(Å)	20.8653 (5)
c(Å)	25.0464 (18)
α(°)	85.942 (6)
β(°)	83.704 (6)
γ(°)	87.947 (4)
V(Å^3)	5106.9 (4)
Z	2
μ(Cu Kα) mm^{-1}	3.190
ρ_{calc} (g cm^{-3})	1.457
$2\theta_{max}$(°)	130.16
Number of unique reflections	17091
Data/restrains/parameters	17091/1045/1330
Final R indices [I>2σ(I)]	$R1$ = 0.0722
	$wR2$ = 0.2004
R indices (all data)	$R1$ = 0.0871
	$wR2$ = 0.2324
Goodness-of-fit on F^2	1.048

Crystal structure of $[Ru(L^2)_2](PF_6)_2$

Triclinic $[Ru(L^2)_2](PF_6)_2$ crystallises in space group $P\bar{1}$. 44 electrons per cell were removed via *PLATON/SQUEEZE*[31] corresponding to 2 molecules of acetonitrile. The structure refines with one cationic complex and two hexafluorophosphate anions per unit cell (see Figure 4.4.3.1).

The complex shows a ruthenium(II) bis-terpy arrangement, with each of the terpy nitrogens coordinating to the ruthenium atom, confirming the spectroscopic data collected. The phosphazene rings are in two identical positions with each ruthenium(II)-bis-terpy unit pointing away from the phosphazene ring. No interactions are observed between the phosphazene rings and phenyl rings and the ruthenium-terpy complex. The compound is isomorphous with its iron analogue ($[Fe(L^2)_2](PF_6)_2 \cdot CH_3CN$, see Chapter 3). The axial ruthenium-nitrogen bonds lengths are (Ru1–N1A and –N1B) 1.976(4) Å, 1.974(4) Å and the equatorial (Ru1–N2A, –N2B, –N3A and –N3B) 2.066(4) - 2.083(4) Å (see Appendix C), consistent with ruthenium(II)-bis-terpy complexes and the orange colour of the complex.

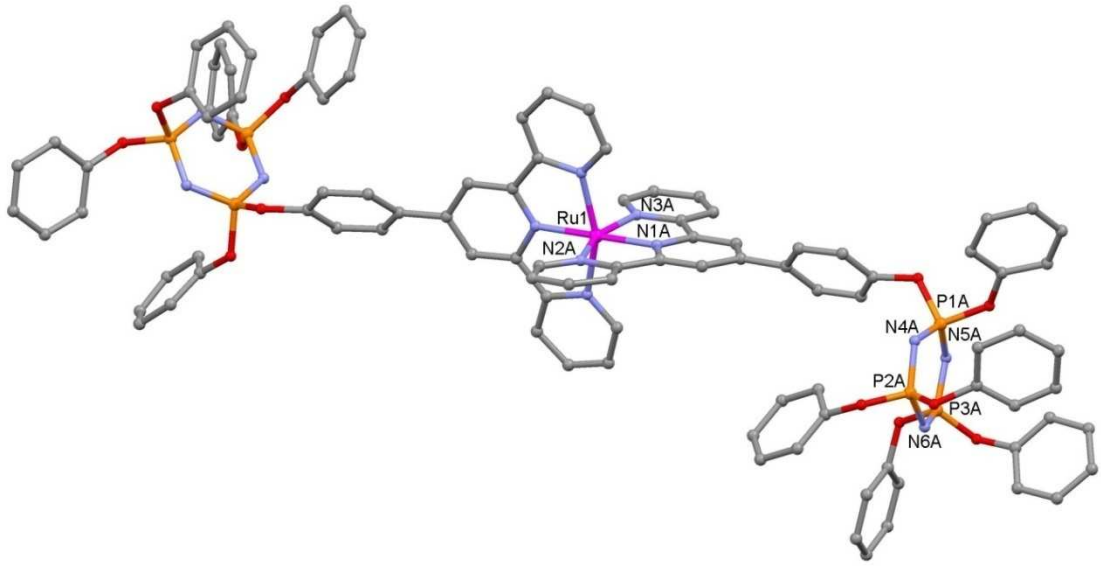

Figure 4.4.3.1 Unit cell of $[Ru(L^2)_2](PF_6)_2$ (hydrogen atoms and anions removed for clarity).

4.4.4 $[Ru(L^2)_2](PF_6)_2$ packing

As with the other ruthenium complexes the cationic complex $[Ru(L^2)_2](PF_6)_2$ packs via hydrogen bonding between the terpy protons and the hexafluorophosphate anions. No observable interactions are evident between the phosphazene ring and any of the substituents (see Figure 4.4.4.1).

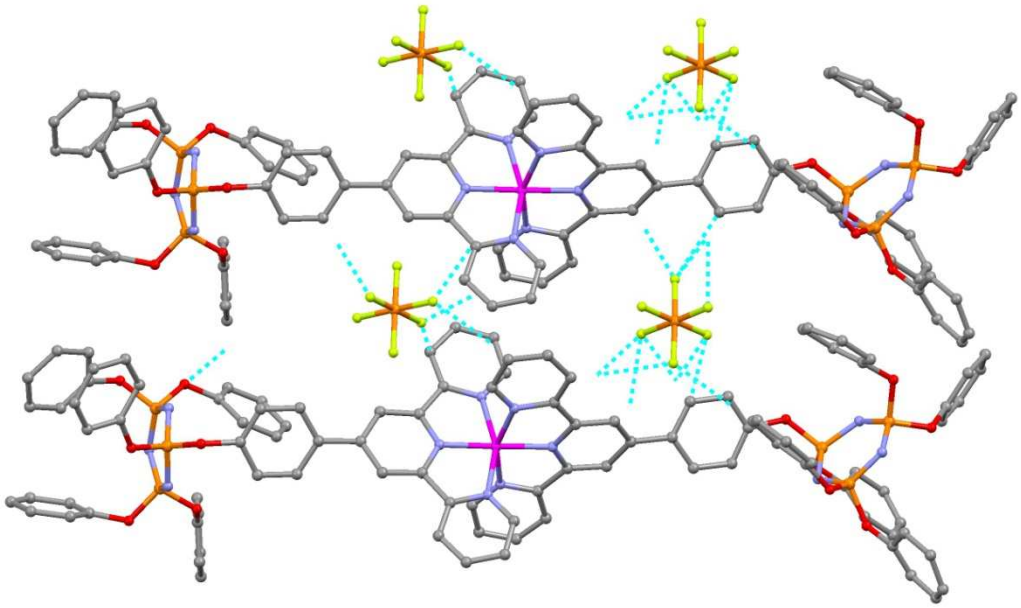

Figure 4.4.4.1 Packing of $[Ru(L^2)_2](PF_6)_2$, dotted lines indicate closest contacts.

4.4.5 L^3 based complexes

Refinement data for the X-ray crystal structures are given in Table 4.4.5.1.

Table 4.4.5.1 Crystallographic and refinement data for complexes.

Compound	**$[Ru(L^3)(Terpy)](PF_6)_2 \cdot 2CH_3CN$**	**$[Ru(L^3)(PhTerpy)](PF_6)_2 \cdot CH_3CN$**
Molecular formula	$C_{66}H_{51}F_{12}N_{12}O_6P_5Ru$	$C_{72}H_{55}F_{12}N_{12}O_6P_5Ru$
M (g mol^{-1})	1592.12	1668.20
Temperature (K)	163 (2)	123 (2)
Crystal system	Triclinic	Triclinic
Space group	$P\bar{1}$	$P\bar{1}$
a(Å)	13.7659 (3)	15.0162 (8)
b(Å)	15.1173 (3)	15.7753 (10)
c(Å)	18.5931 (13)	18.5730 (13)
α(°)	70.493 (5)	98.702 (7)
β(°)	76.535 (5)	109.897 (8)
γ(°)	75.639 (5)	95.212 (7)
V(Å^3)	3485.2 (3)	4041.2 (4)
Z	2	2
μ(Cu Kα) mm^{-1}	3.715	3.214
ρ_{calc} (g cm^{-3})	1.517	1.371
$2\theta_{max}$(°)	130.16	117.86
Number of unique reflections	11366	11249
Data/restrains/parameters	11366/401/920	11249/390/1039
Final R indices [I>2σ(I)]	$R1$ = 0.0689	$R1$ = 0.0865
	$wR2$ = 0.1813	$wR2$ = 0.2262
R indices (all data)	$R1$ = 0.0840	$R1$ = 0.1077
	$wR2$ = 0.2164	$wR2$ = 0.2489
Goodness-of-fit on F^2	1.185	1.091

Crystal structure of $[Ru(L^3)(Terpy)](PF_6)_2 \cdot CH_3CN$

Triclinic $[Ru(L^3)(Terpy)](PF_6)_2 \cdot CH_3CN$ crystallises in space group $P\bar{1}$. The structure refines with one cationic complex, one acetonitrile molecule and two hexafluorophosphate anions per unit cell (see Figure 4.4.5.1).

This heteroleptic complex shows one terpy and bbp units coordinating to the ruthenium centre, with each of the pyridine and imidazole nitrogens coordinating to the ruthenium atom, confirming the spectroscopic data collected. The ruthenium-nitrogen bond lengths of terpy are (Ru1–N6, –N7 and –N8) 1.979(5), 2.071(4) and 2.063(4) Å respectively. The ruthenium-nitrogen bond lengths of bbp are (Ru1–N1, –N2 and –N4) 1.999(5), 2.063(4) and 2.073(4) Å respectively (see Appendix C). The longer bbp bond lengths are typical of the ruthenium(II) terpy-bbp complex.[19,27]

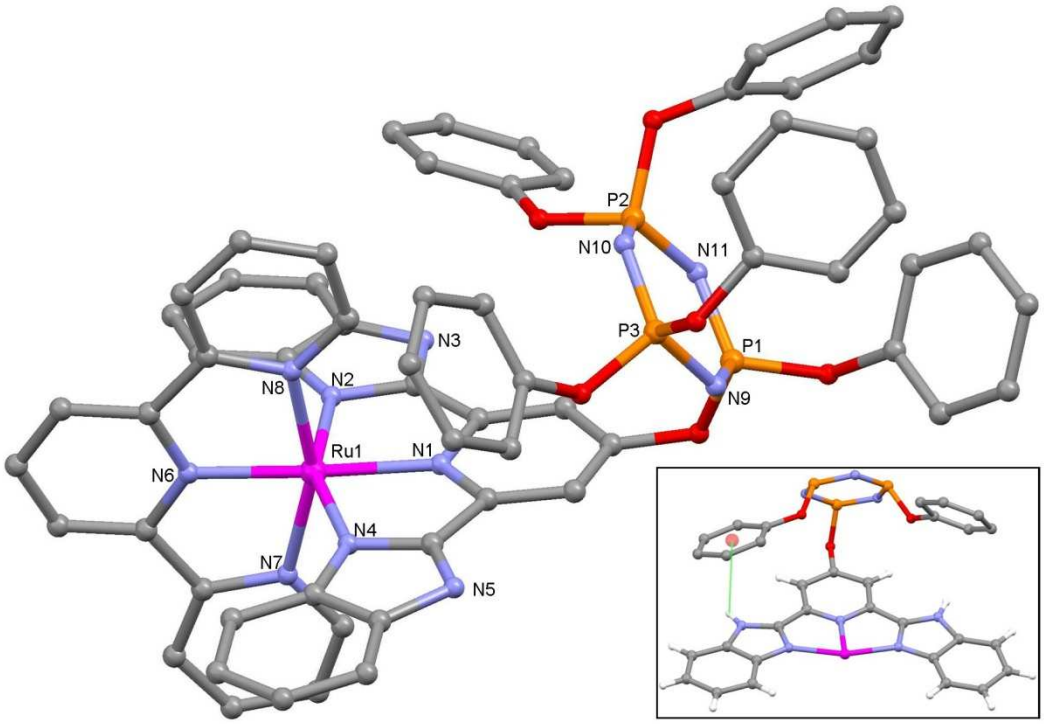

Figure 4.4.5.1 Unit cell of $[Ru(L^3)(Terpy)](PF_6)_2 \cdot CH_3CN$ (hydrogen atoms, solvents and anions removed for clarity). Insert: Red lines indicate π-H interactions.

Crystal structure of $[Ru(L^3)(PhTerpy)](PF_6)_2 \cdot CH_3CN$

Triclinic $[Ru(L^3)(PhTerpy)](PF_6)_2 \cdot CH_3CN$ crystallises in space group $P\,\bar{1}$. The structure refines with one cationic complex, one acetonitrile molecule and two hexafluorophosphate anions per unit cell (see Figure 4.4.5.2).

This heteroleptic complex shows one PhTerpy and bbp units coordinating to the ruthenium centre, with each of the pyridine and imidazole nitrogens coordinating to the ruthenium atom, confirming the spectroscopic data collected. The phosphazene ring folds over the oxygen terpy, with two of the non-geminal phenoxy groups showing a facing imidazole ring but only one was close enough for a π-H interactions (3.179 (5) Å). The ruthenium-nitrogen bond lengths of terpy are (Ru1–N6, –N7 and –N8) 1.939(5), 2.064(5) and 2.075(5) Å respectively. The ruthenium-nitrogen bond lengths of bbp are (Ru1–N1, –N2 and –N4) 1.985(6), 2.059(5) and 2.066(5) Å respectively (see Appendix C). The longer bbp bond lengths are typical of the ruthenium terpy-bbp complex. The phenyl group is at a 25(8)° torsional angle with respect to the terpy group.[19,27]

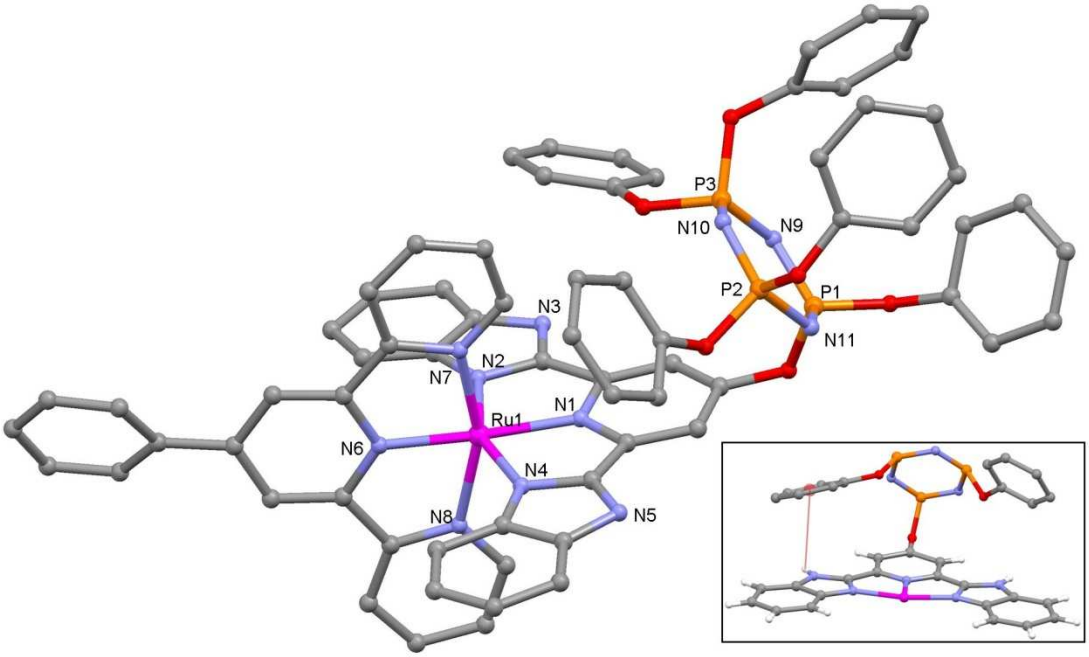

Figure 4.4.5.2 Unit cell of $[Ru(L^3)(PhTerpy)](PF_6)_2 \cdot CH_3CN$ (hydrogen atoms, solvents and anions removed for clarity). Insert: Red lines indicate π-H interactions.

4.4.6 Packing of L^3 based complexes

Both $[Ru(L^3)(Terpy)](PF_6)_2 \cdot CH_3CN$ and $[Ru(L^3)(PhTerpy)](PF_6)_2 \cdot CH_3CN$ complexes pack via hydrogen bonding between the hexafluorophosphate anions and the hydrogen atoms of terpy and bbp groups. In addition, hydrogen bonding is observed between the acetonitrile group and the hydrogen atoms of the imidazole and phenoxy groups (see Figure 4.4.6.1).

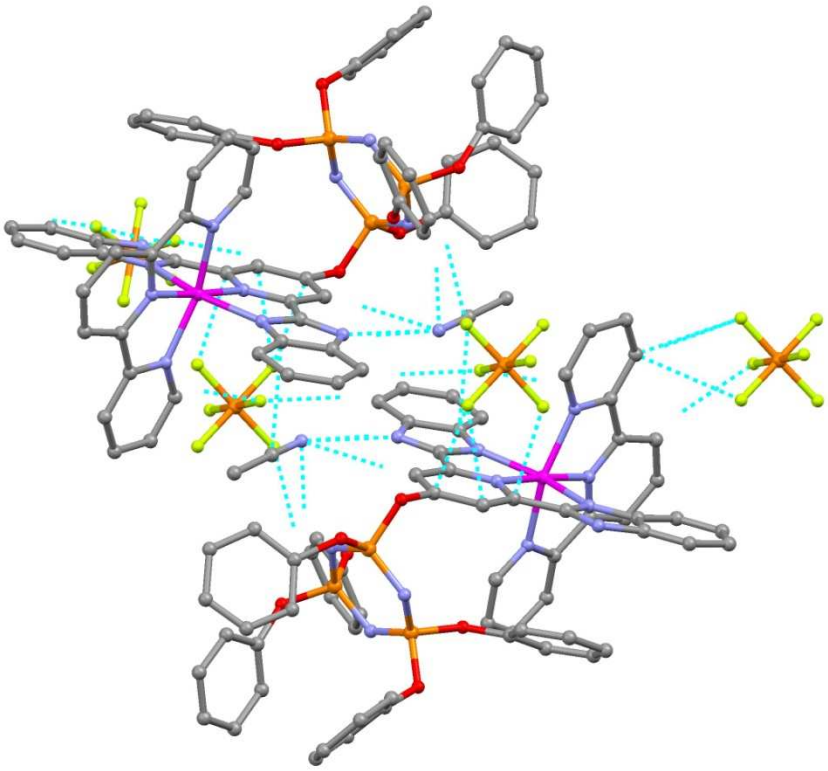

Figure 4.4.6.1 Packing of $[Ru(L^3)(Terpy)](PF_6)_2 \cdot CH_3CN$, dotted lines indicate bonding interactions.

4.5 Conclusion

Two homoleptic and 15 heteroleptic ruthenium(II) complexes were synthesised by reacting the ligands produced in Chapter 2 (L^1, L^2, L^3 and L^4). The homoleptic complexes were synthesised by reacting the ligands with either $RuCl_3 \cdot 3H_2O$. The heteroleptic complexes were synthesised by two methods. Method A was to make the ruthenium trichloride complex of the respective ligand and react it with the co-ligand. Method B was to react the respective ligand with the ruthenium trichloride complex of the co-ligand. This method was limited to only using the terpy based co-ligands.

The crystal structures of both the L^1 and L^2 homoleptic complexes were isomorphs of the iron analogues discussed in Chapter 3 which is consistent with the orange colours of the complexes. Each crystal structure of the heteroleptic complexes displayed the expected coordination of the two different tridentate ligands to one ruthenium centre. Each of the bond lengths measured were similar to that of the reported non-phosphazene analogues. In addition none of the crystal structure displayed significant interactions between the ruthenium complex centres and the rest of the molecule, suggesting that the physical behaviour will remain the same as the non-phosphazene analogues, however, this will be thoroughly investigated in Chapter 7.

From these small molecule models it can be assumed that the same coordination behaviour will be observed in the polymer, as the phosphazene rings displayed no interaction with the coordination centre.

4.6 References

1. Cotton, F. A.; Wilkinson, G. *Advanced Inorganic Chemistry*; 4th ed.; John Wiley & Sons: Toronto, **1980**.

2. Suzuki, A. *Journal of Organometallic Chemistry* **1999**, *576*, 147-168.

3. Constable, E. C. *Chemical Society Reviews* **2007**, *36*, 246-253.

4. Andres, P. R.; Schubert, U. S. *Advanced Materials* **2004**, *16*, 1043-1068.

5. Thompson, A. *Coordination Chemistry Reviews* **1997**, *160*, 1-52.

6. Shklover, V.; Nazeeruddin, K.; Gratzel, M.; Ovchinnikov, Y. E. *Applied Organometallic Chemistry* **2002**, *16*, 635-642.

7. Lee, Y. G.; Jang, S. R.; Vittal, R.; Kim, K. J. *New Journal of Chemistry* **2007**, *31*, 2120-2126.

8. Nazeeruddin, M. K.; Pechy, P.; Renouard, T.; Zakeeruddin, S. M.; Humphry-Baker, R.; Comte, P.; Liska, P.; Cevey, L.; Costa, E.; Shklover, V., *et al. Journal of the American Chemical Society* **2001**, *123*, 1613-1624.

9. Medlycott, E. A.; Hanan, G. S. *Chemical Society Reviews* **2005**, *34*, 133-142.

10. Kohle, O.; Ruile, S.; Gratzel, M. *Inorganic Chemistry* **1996**, *35*, 4779-4787.

11. Nusbaumer, H.; Zakeeruddin, S. M.; Moser, J. E.; Gratzel, M. *Chemistry-A European Journal* **2003**, *9*, 3756-3763.

12. Mishra, L.; Sinha, R.; Itokawa, H.; Bastow, K. F.; Tachibana, Y.; Nakanishi, Y.; Kilgore, N.; Lee, K. H. *Bioorganic & Medicinal Chemistry* **2001**, *9*, 1667-1671.

13. Yu, S. C.; Hou, S. J.; Chan, W. K. *Macromolecules* **1999**, *32*, 5251-5256.

14. Singh, A.; Prarnanik, A.; Das, G.; Mondal, B. *Organometallics* **2008**, *27*, 6403-6404.

15. Chen, Z. F.; Concepcion, J. J.; Jurss, J. W.; Meyer, T. J. *Journal of the American Chemical Society* **2009**, *131*, 15580-15581.

16. Concepcion, J. J.; Jurss, J. W.; Norris, M. R.; Chen, Z. F.; Templeton, J. L.; Meyer, T. J. *Inorganic Chemistry* **2010**, *49*, 1277-1279.

17. Haga, M.; Takasugi, T.; Tomie, A.; Ishizuya, M.; Yamada, T.; Hossain, M. D.; Inoue, M. *Dalton Transactions* **2003**, 2069-2079.

18. Hossain, M. D.; Ueno, R.; Haga, M. *Inorganic Chemistry Communications* **2000**, *3*, 35-38.

19. Singh, A.; Das, G.; Mondal, B. *Polyhedron* **2008**, *27*, 2563-2568.

20. Singh, A.; Chetia, B.; Mobin, S. M.; Das, G.; Iyer, P. K.; Mondal, B. *Polyhedron* **2008**, *27*, 1983-1988.

21. Jameson, D. L.; Blaho, J. K.; Kruger, K. T.; Goldsby, K. A. *Inorganic Chemistry* **1989**, *28*, 4312-4314.

22. Philippopoulos, A. I.; Terzis, A.; Raptopoulou, C. P.; Catalano, V. J.; Falaras, P. *European Journal of Inorganic Chemistry* **2007**, 5633-5644.

23. Jo, D. H.; Yeo, H. J. *Bulletin of the Korean Chemical Society* **1993**, *14*, 682-686.

24. Beach, N. J.; Spivak, G. J. *Inorganica Chimica Acta* **2003**, *343*, 244-252.

25. Fung, W. H.; Yu, W. Y.; Che, C. M. *Journal of Organic Chemistry* **1998**, *63*, 7715-7726.

26. Schramm, F.; Chandrasekar, R.; Zevaco, T. A.; Rudolph, M.; Gorls, H.; Poppitz, W.; Ruben, M. *European Journal of Inorganic Chemistry* **2009**, 53-61.

27. Bhaumik, C.; Das, S.; Saha, D.; Dutta, S.; Baitalik, S. *Inorganic Chemistry* **2010**, *49*, 5049-5062.

28. Rigaku; Version 1.4.0 ed.; Rigaku Americas Corp: The Woodlands, **2007**, p program for area detector data collection.

29. Sheldrick, G. M. *Acta Crystallographica Section A* **2008**, *64*, 112-122.

30. Dolomanov, O. V.; Bourhis, L. J.; Gildea, R. J.; Howard, J. A. K.; Puschmann, H. *Journal of Applied Crystallography* **2009**, *42*, 339-341.

31. Vandersluis, P.; Spek, A. L. *Acta Crystallographica Section A* **1990**, *46*, 194-201.

32. Beves, J. E.; Dunphy, E. L.; Constable, E. C.; Housecroft, C. E.; Kepert, C. J.; Neuburger, M.; Price, D. J.; Schaffner, S. *Dalton Transactions* **2008**, 386-396.

33. Constable, E. C.; Housecroft, C. E.; Medlycott, E. A.; Neuburger, M.; Reinders, F.; Reymann, S.; Schaffner, S. *Inorganic Chemistry Communications* **2008**, *11*, 805-808.

34. Horvath, R.; Otter, C. A.; Gordon, K. C.; Brodie, A. M.; Ainscough, E. W. *Inorganic Chemistry* **2010**, *49*, 4073-4083.

Chapter 5

Synthesis and reactions of polyphosphazenes with iron(II) perchlorate and ruthenium complexes.

5.0 Abbreviations used in Chapter 5

ROP	Ring opening polymerization
MOF	Metal organic framework
NMR	Nuclear magnetic resonance
GPC	Gel permeation chromatography
SEC	Size exclusion column
DSC	Differential scanning calorimetry
T_g	Glass transition temperature
SCO	Spin crossover
TFE	Trifluoroethoxy
OPhTerpy	4-(2,6-di{pyridin-2-yl}-pyridine-4-yl)phenolate
OTerpy	2,6-bis(2-pyridyl)-4(1*H*)-pyridonate
Obpp	2,6-bis(benzimidazole)-4(1*H*)-pyridonate
OPhbpp	4-(2,6-(pyraz-1-yl)-pyridine-4-yl)phenolate
Terpy	2,2':6',2''-terpyridine
PhTerpy	4-phenyl-2,2':6',2''-terpyridine
^{t}Bu	Tert-butyl
OPh^{tBu}	4-tert-butylphenolate
TBAN	Tetra(butyl)ammonium nitrate
TBAB	Tetra(butyl)ammonium bromide
THF	Tetrahydrofuran
M_n	Number average molecular weight
	$M_n = \frac{\sum_i N_i M_i}{\sum_i N_i}$ where N_i is the number of molecules of M_{weight}
M_i	
M_w	Weight average molecular weight
	$M_W = \frac{\sum_i N_i M_i^2}{\sum_i N_i M_i}$
PDI	Polydispersity index

5.1 Introduction

5.1.1 Polyphosphazenes and metals

Polyphosphazenes have shared a long history of coordinating metal ions via substituents ranging from pyridines to phosphines.[1-6] These coordination compounds have been used for a variety of applications such as luminescence materials,[1] metal extraction,[2] catalysts and nano-particle precursors.[3-5] However, until recently the substituents used have only been mono-dentate, relying on the phosphazene scaffold to hold the substituents close enough to form multidentate ligands (see Figure 5.1.1.1).

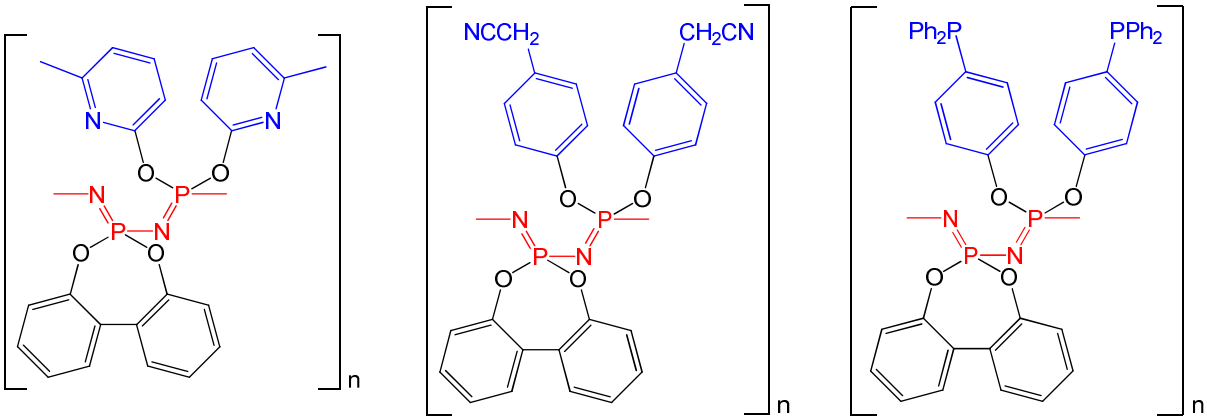

Figure 5.1.1.1 Examples of phosphazene polymers with metal coordinating substituents.[6-11]

Multidentate substituents were not reported until Ainscough *et al.* attached 4-(6-phenyl-2,2'-bipyridin-4-yl)phenolate (OPhBipyPh) to a polyphosphazene backbone.[1] These OPhBipyPh polymers were subsequently coordinated to a selection of metals to produce luminescent polymers[1] (see Figure 5.1.1.2). It was found through physical measurements and computational models that the addition of these groups to the polyphosphazene had no effect on the optical behaviour of these complexes in the solution phase.

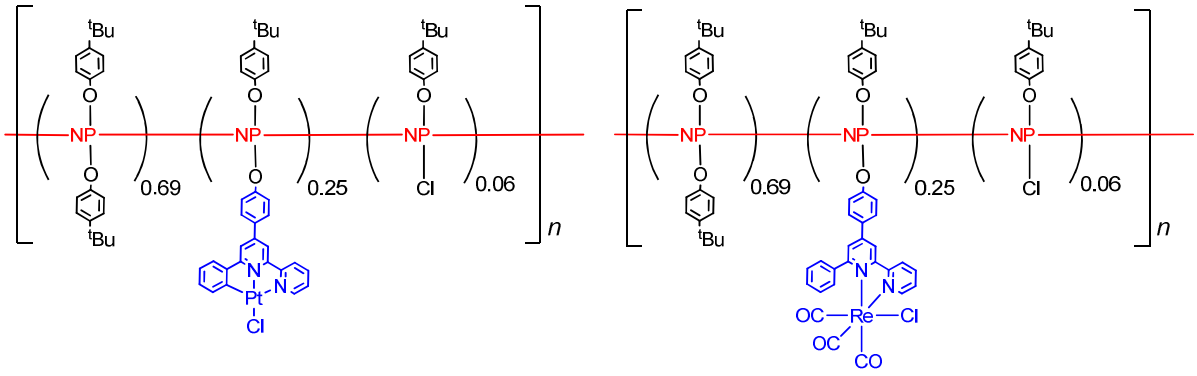

Figure 5.1.1.2 Examples of multidentate ligands attached to polyphosphazene backbones forming luminescent polymers.[1]

5.1.2 Cross-linked polyphosphazenes

The first polyphosphazenes, which were made by Stokes,[12-17] were suspected to be cross-linked as they were described as an inorganic rubber that would only swell in a solvent, not dissolve. In addition, any substitution reactions that were attempted resulted in only partial completion. Both observations are signs of cross-linking.

It was not until 1965 that Allcock discovered the ring opening polymerisation (ROP) method of forming linear high molecular weight polymers.[18,19] These polymers were readily soluble in some solvents; as such numerous substitution reactions could be performed on them, spawning a new branch of polymer science.

After such a heroic effort to make linear polyphosphazenes one has to wonder why anyone would return to cross-linked polymers. The reason being the discovery that cross-linked polymers have a range of properties different to that of linear polymers, making them useful for a range of applications. Three examples of cross-linked polyphosphazenes are described below:

i) Scaffolds for tissue growth.

Structural biopolymers are all cross-linked rather than linear; this is because the cross-linked polymers are very strong but flexible, ideal for organs. With this in mind polyphosphazenes have been modified to be integrated with tissue to form scaffolds, allowing tissue to be grown on it. Polyphosphazenes are ideal for this as they are able to be hydrolysed into phosphates and ammonia which can be dealt with by biological systems. Such polymers have already been used as bone scaffolds, facilitating rapid

bone repair.[20-23] An example of bone starting to grow between polyphosphazene beads is shown in Figure 5.1.2.1.

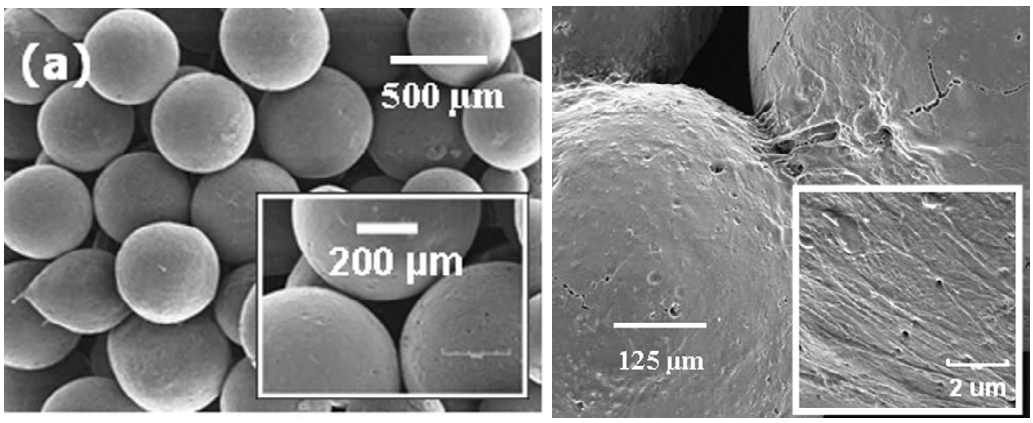

Figure 5.1.2.1 Left: Example of polyphosphazene beads for the use of bone growth. Right: Cell growth between polyphosphazene beads.[23]

ii) Hydrogels.

As was earlier discovered, when cross-linked phosphazenes are soaked in solvent they swell (see Figure 5.1.2.2) because the solvent molecules are filling the cavities between the polymer chains.[22] Such behaviour can be used to form hydrogels[24,25] which can be designed to hold specific drugs that can be released at specific parts of the body. The hydro-gels can then be further modified to be preferentially absorbed by specific body parts,[26] where the slow breakdown of the phosphazene can release a steady amount of a drug.[27]

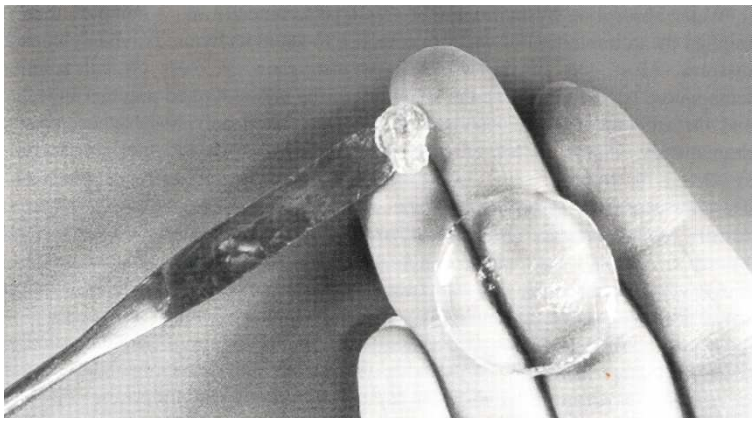

Figure 5.1.2.2 Example of a hydrogel (MEEP), dried and solvent absorbed.[22]

Both of these examples are based on organic substituents cross-linking either via the formation of radicals or hydrogen bonding (see Figure 5.1.2.3).[22]

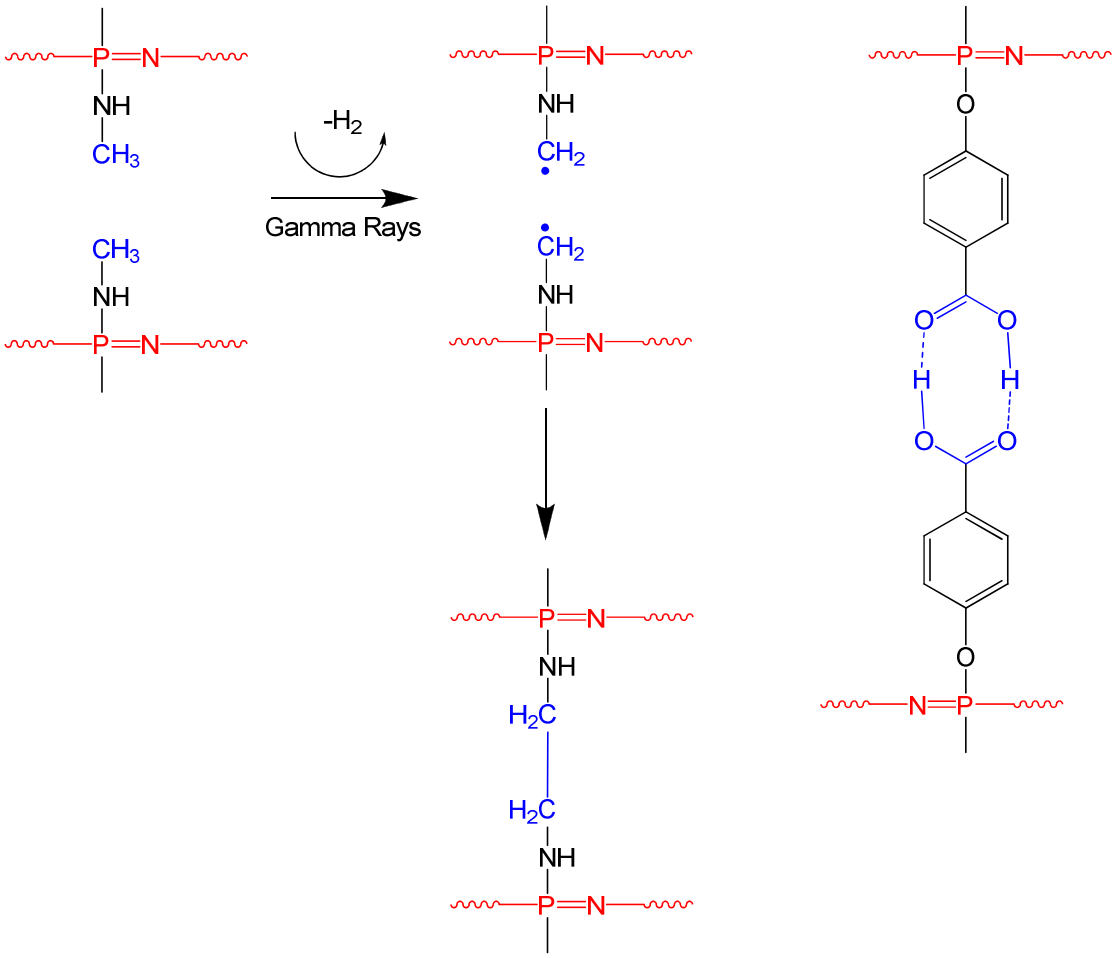

Figure 5.1.2.3 Left: Suggested mechanism for cross-linking via radical formation. Right: Cross-linking via hydrogen bonding.[22]

iii) Metal coordination cross-linking

There are only a handful of examples where metal ions are used to cross-link polyphosphazenes. One comes from Díaz *et al.* whose work focused on coordinating metal ions to the polymer backbone via benzyl-nitrile substituents.[28] Typically counter ligands were chosen such that cross-linking is prevented. However, in one case when diphenyl phosphine ethylene was used, unexpected cross-linking occurred via a transition metal. A proposed structure for the cross-linking is shown in Figure 5.1.2.4.

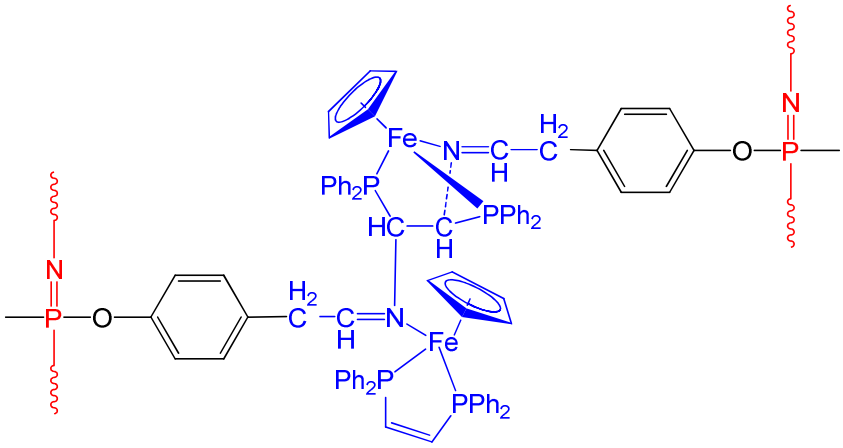

Figure 5.1.2.4 A proposed structure for the cross-linking of polyphosphazene chains via a metal ion.[28]

A second group, Carriedo *et al.*, has focused on the production of polymeric metal organic framework (MOF).[29] MOFs have drawn a great deal of attention in recent years due to their high porosity and the potential to be functionalised for catalysis, gas storage, etc. Carriedo's MOF was formed via gold coordinating to phosphine substituents attached to the phosphazene backbone (see Figure 5.1.2.5).

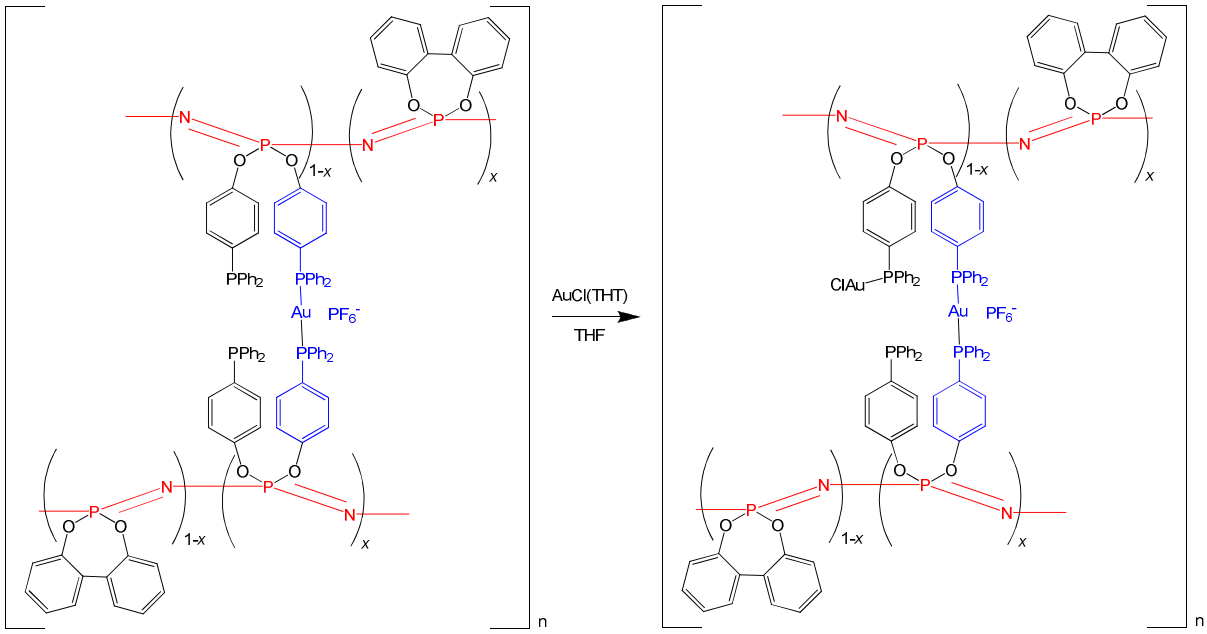

Figure 5.1.2.5 Carriedo's MOF based on polyphosphazenes cross-linked via gold.[29]

These cross-linked polymers formed large solvent cavities. Once the cavities were evacuated by heating the sample, it left them available to be filled with other molecules for catalytic reactions or gas storage.[29]

5.2 Polymer characterisation

Polyphosphazenes like all other materials have their own methods for characterisation. Unlike small molecules it is impossible to obtain crystals for single crystal X-ray diffraction, and elemental analysis is subject to large errors (up to 4%).[6] However, an assortment of spectroscopic techniques can be applied. The key methods for characterising the composition and physical behaviour are nuclear magnetic resonance (NMR), gel permeation chromatography (GPC) and differential scanning calorimetry (DSC).[22]

5.2.1 NMR spectroscopy

Polyphosphazenes like many other compounds can be characterised using NMR spectroscopy of its respective nuclei. As the phosphazene backbone contains phosphorus they can be studied directly by ^{31}P NMR spectroscopy. It provides a clear indication of a reaction's progress by the disappearance or appearance of a particular peak. In addition, by observing the ^{31}P NMR signal width, the distribution of the substituents can be determined, i.e. in blocks or randomly with other substituents (see Figure 5.2.1.1).

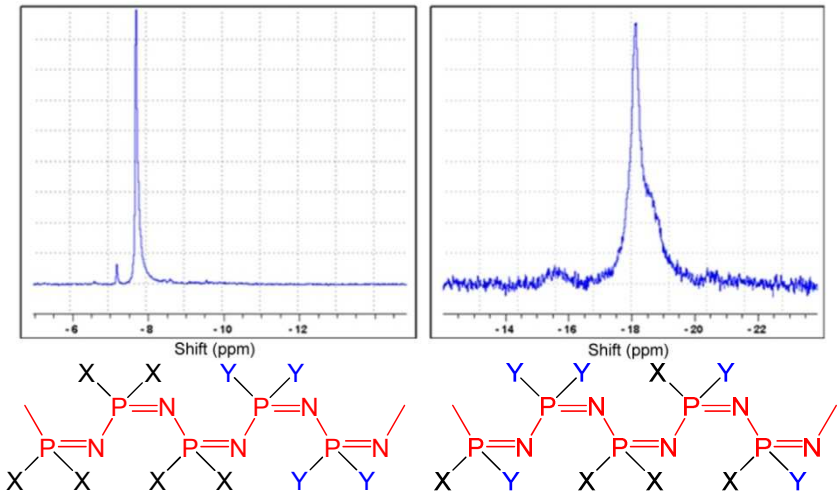

Figure 5.2.1.1 Left: Example ^{31}P NMR of a blocky distributed substitution polyphosphazene ([NP(O-2-Py-6-Me)$_2$]$_n$).[6] Right: Example ^{31}P NMR of a randomly distributed substitution polyphosphazene ([{NP(OPh^{tBu})$_2$}$_{0.75}${NP(OPh^{tBu})(OPh-4-Bipy-2-Ph)}$_{0.25}$]$_n$).[1]

As observed in Figure 5.2.1.1 the signal for each phosphorus atom is sharp for the blocky distributed, but broad and less resolved for the randomly distributed substituents on the polyphosphazene backbone.

^{1}H NMR is also useful when the substituents have chemically distinct protons, although due to the broadening of the signal, distinguishing the difference between chemically similar protons becomes very difficult.

5.2.2 Gel permeation chromatography

Gel permeation chromatography (GPC) is a method of measuring the size and distribution of sizes for the polymers. This works by passing the polymer through a size exclusion column (SEC). Contained in this column is gel that allows small particles to interact with them while allowing the larger particles to pass by, shown in Figure 5.2.2.1, resulting in the larger polymers passing through the column faster than the smaller ones. By the calibration of the column it becomes possible to relate the retention time to the size of the polymer.

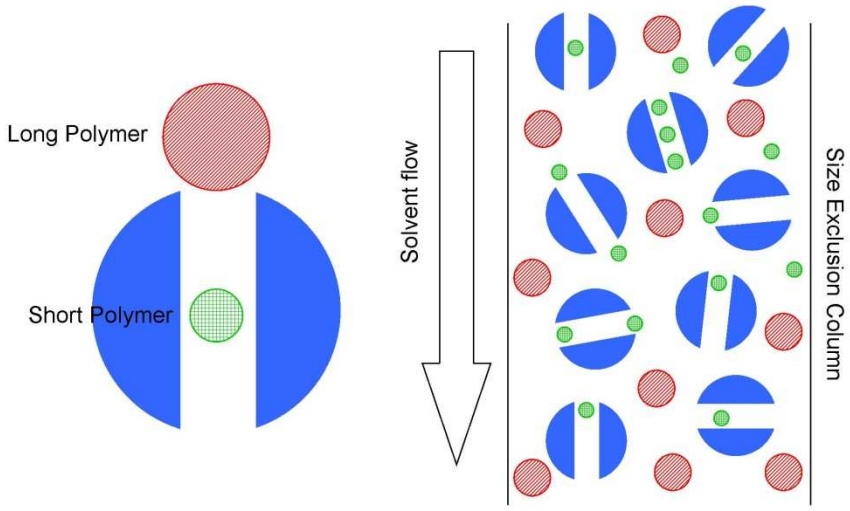

Figure 5.2.2.1 Left: A schematic view of the size exclusion gel. Right: A schematic view of a size exclusion column in action.

From the width of the peak the polydispersity index (PDI) can be determined. This is a measure of the size distribution of the polymer, it is defined as follows (Formulas 5.2.2.1 – 3):

$$\mathrm{PDI} = \frac{M_w}{M_n} \quad \text{where} \quad M_W = \frac{\sum_i N_i M_i^2}{\sum_i N_i M_i} \quad \text{and} \quad M_n = \frac{\sum_i N_i M_i}{\sum_i N_i}$$

Formulas 5.2.2.1 - 3 respectively

M_w is the weight average molecular weight and M_n is the number average molecular weight. N_i is the number of polymer chains with the mass W_i.

For a polymer where all molecules have the exact same weight the PDI = 1; however, in reality all polymers have PDIs >1.

In addition, in 1987 Nielson *et al.* found it was necessary to include a salt 'tetra(butyl)ammonium nitrate' (TBAN) to obtain reproducible results.[30] While no definite explanation has been determined it has been suggested that the addition of the salt prevents the polymer from either folding in on itself giving a different size or it prevents the small polymers from building up into the column. As a result is has become a standard method for GPC analysis of polyphosphazenes.

5.2.3 Differential scanning calorimetry

The third most common technique used for the characterisation of polymers is differential scanning calorimetry (DSC). This is a measure of the thermal transition of materials. These transitions are measured by heating two samples, one a control and the other a sample, monitoring the amount of heat required to increase the temperature.[22]

For polymers the key feature is the glass transition temperature (T_g), which describes the temperature at which the polymer switches from being microcrystalline (ordered regions) to completely amorphous. The sample can be further heated to show the

breakdown temperature of the polymers, an example of a DSC curve is shown in Figure 5.2.3.1.

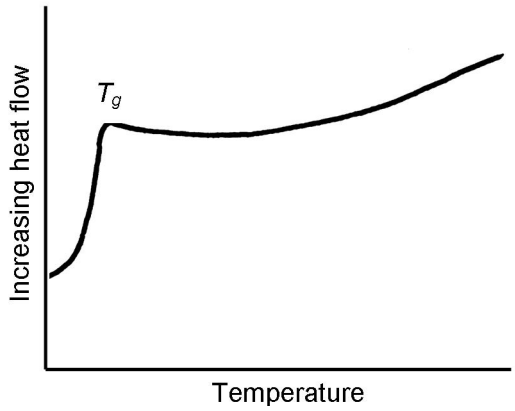

Figure 5.2.3.1 An example of a DSC curve.

The T_g temperature is primarily affected by six different factors:[6]

i) Torsion energy of the =P-N=P-N- bond. While the nature of the bond is now well understood, the calculated torsion energy of the bond is still under debate. Recent publications put the theoretical value at 0.4 kJ bond^{-1}.[31]

ii) Distribution of substituents. Unlike some organic polymers the substituents are attached to alternating atoms rather than every atom, making it less dense. In addition when dealing with hetero-substituted phosphazenes the distribution of each substituent along the polymer backbone can prevent the formation of microcrystalline regions.

iii) The nature of the substituent itself can have an effect via its intramolecular interactions and its intermolecular interactions.

iv) Cross-linking of the polymer increases T_g. This is because cross-linking forms rigid networks preventing polymer chains from sliding over each other.

v) The architecture of the polymer backbone (whether it is an idealised linear polymer, collinear or has side branches) has the largest effect.

vi) Solvents and impurities also affect the T_g. Although samples are purified and extensively dried it is often impossible to completely remove solvents and impurities from the polymer.

Shown in Table 5.2.3.1 are examples of how a variation in substituents varies the T_g temperature:[32]

Table 5.2.3.1 Examples of T_g temperature for different substituents.[32]

Polymer	T_g (^{o}C)
$[NP(OPh)_2]_n$	-8
$[NP(OPhMe)_2]_n$	2
$[NP(OPhEt)_2]_n$	-19
$[NP(OPh^nPr)_2]_n$	-34
$[NP(OPh^iPr)_2]_n$	-0.1
$[NP(OPh^sBu)_2]_n$	-16
$[NP(OPh^tBu)_2]_n$	44

The general trend observed for these polymers and others is that as the bulkiness of the pendant is increased the T_g increases. However, this is offset by the tendency for the T_g to decrease as the pendant group becomes longer (i.e. a discrete chainlike structure). T_g values remain similar no matter what co-substituents are added, assuming the primary substituent forms the bulk of the polymer.[32]

Shown in Table 5.2.3.2 is a comparison of T_g values for cross-linked polymers based on Carriedo's gold coordinating polymers, shown in Figure 5.2.3.2.[29]

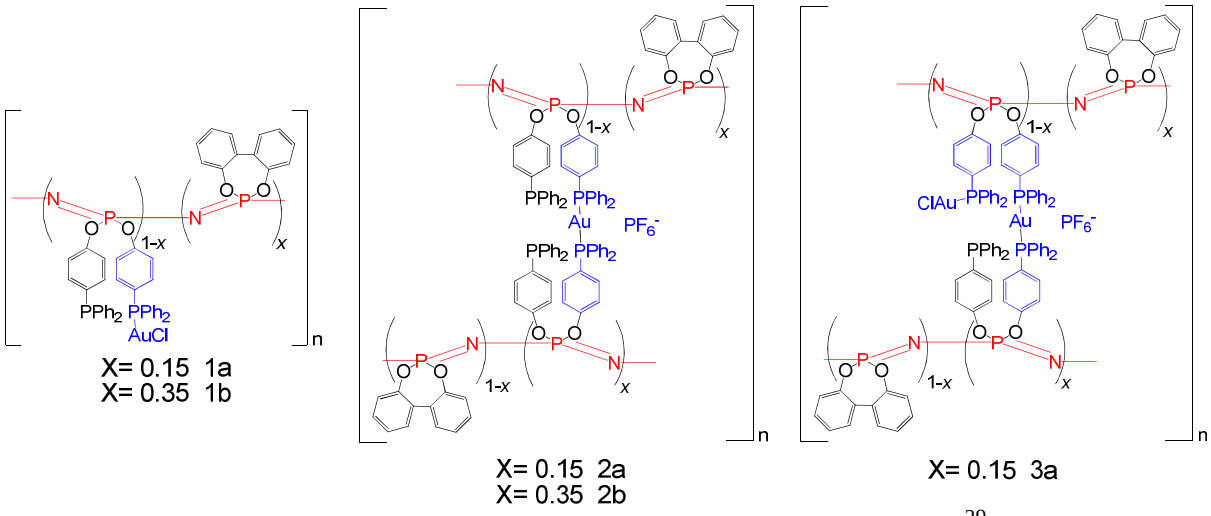

Figure 5.2.3.2 Carriedo's gold cross-linked polyphosphazenes.[29]

Table 5.2.3.2 T_g values for Carriedo's gold cross-linked polyphosphazenes.[29]

Polymer	T_g (^{o}C)
1a	176
1b	Not visible
2a	159
2b	170
3a	176

The most interesting result from the T_g values are found from Carriedo et al[29] where cross-linking caused a relatively small increase in T_g values for the polymers. Even when the cross-linking is increased the T_g value does not increase in comparison. This can be explained if the cross-linking has only a small effect on the flexibility of the polymer backbone, particularly when coordinating a soft metal to a soft ligand resulting in a flexible metal-ligand bond.[29] However, this may change once the ratio of cross-linking is greatly increased, although no one has explored this yet.

5.2.4 Polyphosphazene standard

A standard is used for each of the measurements of the polyphosphazenes. The common standard used is the trifluoroethanoxypolyphosphazene ($[NP(TFE)_2]_n$) (see Figure 5.2.4.1), it is synthesised by reacting the sodium salt of trifluoroethanol with $NPCl_2$.[22]

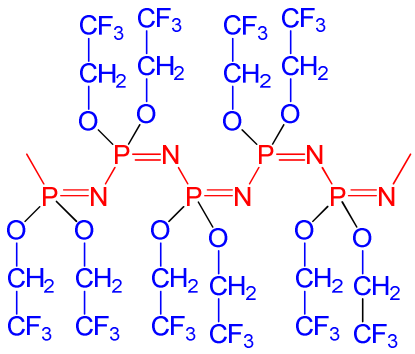

Figure 5.2.4.1 $[NP(TFE)_2]_n$, used as a phosphazene polymer standard.[22]

$[NP(TFE)_2]_n$ is used as a standard because it is very stable to hydrolysis and any other potential sources of degradation during synthesis and storage. In addition, $[NP(TFE)_2]_n$ has been one of the most extensively characterised polyphosphazenes; therefore, all of its properties are known (T_g = -66 °C, ^{31}P NMR = -7.60 ppm).[22]

5.3 Synthesis of polymers

This chapter describes the synthesis and characterisation of the polyphosphazenes containing the substituent's described in Chapter 2 (see Figure 5.3.1) and their respective iron(II) and ruthenium(II) complexes.

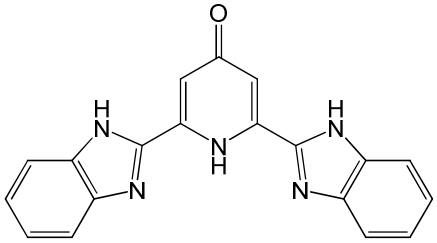

2,6-di(1*H*-benzoimidazol-2-yl)pyridin-4(1*H*)-one
HObbp

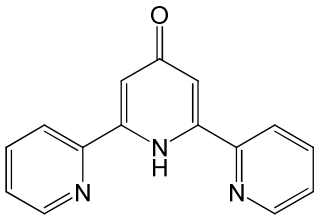

2,6-di(pyridin-2-yl)pyridin-4(1*H*)-one
HOTerpy

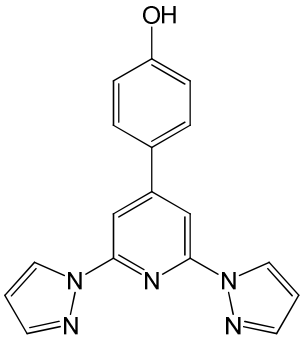

4-(2,6-di(1*H*-pyrazol-1-yl)pyridin-4-yl)phenol
HOPhbpp

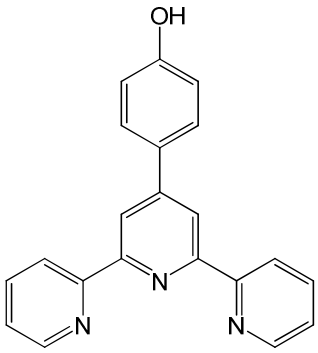

4-(2,6-di(pyridin-2-yl)-pyridine-4-yl)phenol
HOPhTerpy

Figure 5.3.1 Ligands attached to the polyphosphazene backbone.[33-36]

Chapter 2 proved that both HOPhbpp and HOPhTerpy readily react within a day to completely substitute the cyclicphosphazene chlorides; however, both HObbp and HOTerpy require 3-5 days reaction time. In addition for HObbp, a carbonate base was required to prevent side reactions that could occur if a hydride base was used as with the other substituents.

Chapter 3 proved that when reacting iron(II) salts the reaction occurred rapidly forming homoleptic complexes with each of the ligands, requiring only stirring at room temperature. Each of the anions displayed the same weak interaction with the iron centre of the cationic complex. No interactions were seen between the phosphazene ring or its substituents with the complex core. It is assumed that the same behaviours will be observed for the polymeric analogues.

Chapter 4 proved that the ligands could react with a selection of ruthenium complexes to either form homoleptic or heteroleptic complexes. The homoleptic complexes were achieved by reacting two equivalents of the ligands with one equivalent of ruthenium trichloride trihydrate, however, this only produced clean products with terpy based ligands.

Heteroleptic complexes could be synthesised by two possible means, either by forming the ruthenium trichloride complex of the ligand then subsequently reacting it with the respective co-ligand; again this only works for the terpy based ligands. The other method that can be used is the reaction of the ruthenium trichloride co-ligand with the respective ligand. For each of the ruthenium complexes the anions weakly interacted with the ruthenium centre. No interactions were observed between the phosphazene ring or its substituents with the complex core. It is assumed as for iron that the same behaviours will be observed for the polymeric analogues.

Each of the ligand substituents were intended to be added in a 0.20 ratio. By comparison to the polymers produced by Ainscough *et al.*[1], a ratio of 0.20-0.25 results in a polymer that remains soluble and displays no interaction between metal centres while maintaining a high enough ratio of the metal complex to detect. The experimental data for the polymers are described in Appendix D.

5.4 Observations from polymer syntheses

Each of the polymers was synthesised by initially reacting $[NPCl_2]_n$ with a 10% ratio of the $NaOPh^{tBu}$, to maintain the solubility of the polymer while the other substituent was reacted. Toluene was added to the solution because the OPh^{tBu} substituted polymer is more soluble in toluene than tetrahydrofuran (THF). The next step in the reaction was to add the sodium salt of the respective substituent (or potassium salt of 2,6-di(1*H*-benzimidazol-2-yl)pyridine-4(1*H*)-onate). Once all of the substituent had reacted with the phosphazene polymer, an excess of $NaOPh^{tBu}$ was added to replace the remaining chlorines (see Appendix D), producing the polymers shown in Figure 5.4.1.

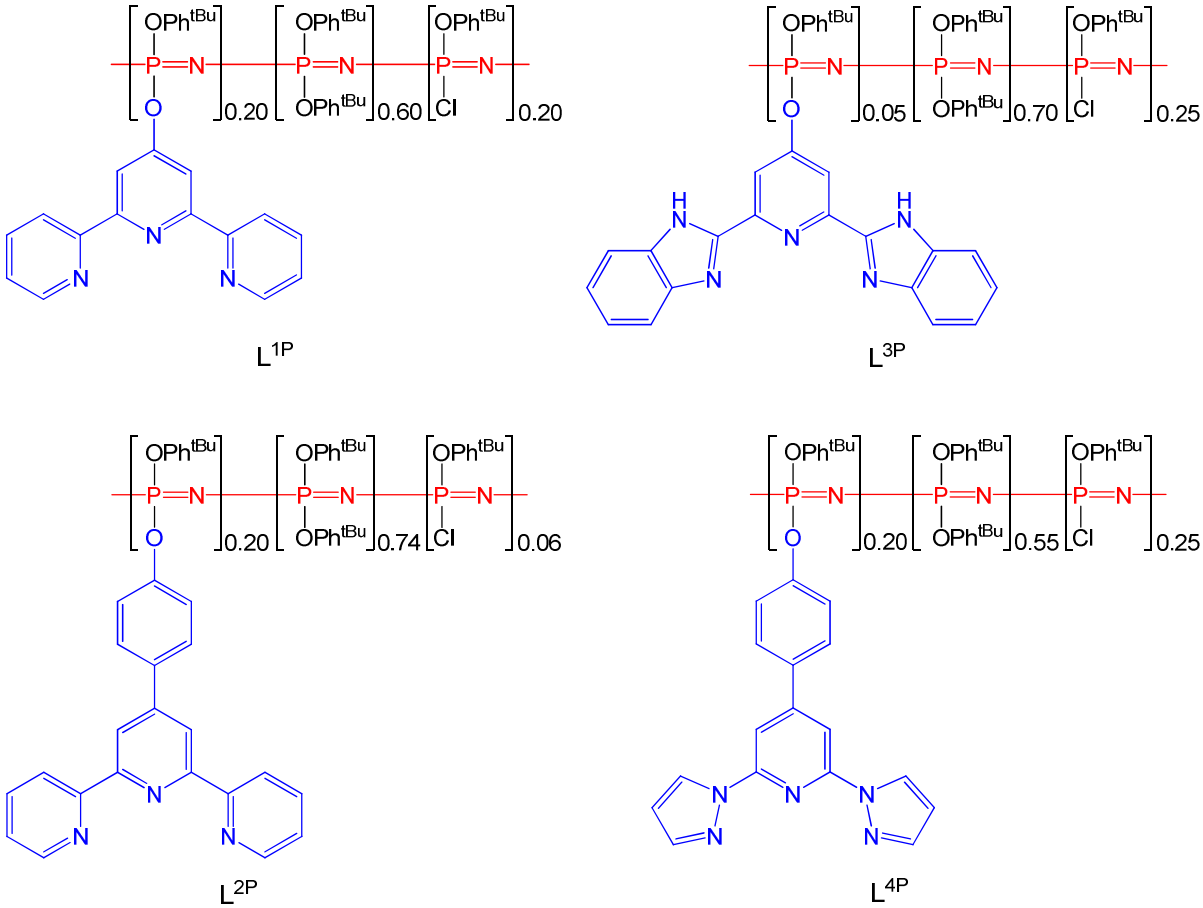

Figure 5.4.1 Metal-free polymers synthesised.

5.4.1 Unreacted P-Cl units

The first feature that arises when looking at the molecular formula of each polymer is the large amount of unreacted P-Cl units that remain. This occurs commonly when attempting to attach 'bulky' substituents, such as OPh^{tBu} to a polyphosphazene backbone. Attempts were made to change the ratios of the reactants, choice of base, and

addition of promoters and solvents with higher boiling points; however, none of these variations improved the completeness of the reaction and in some cases promoted the decay of the polymer. Each of the reactions left similar amounts of unreacted chlorines showing that it is reproducible. Despite the incomplete substitution the remaining P-Cl units were stable in water and in all other solvents the polymers were exposed to, which was satisfactory for the purposes of this investigation. A possible reason for the low reactivity of the chlorine can be explained by looking at a space-filling model of a polymer segment (see Figure 5.4.1.1). The chlorine is enclosed by the other substituents preventing reactants from reaching that centre.

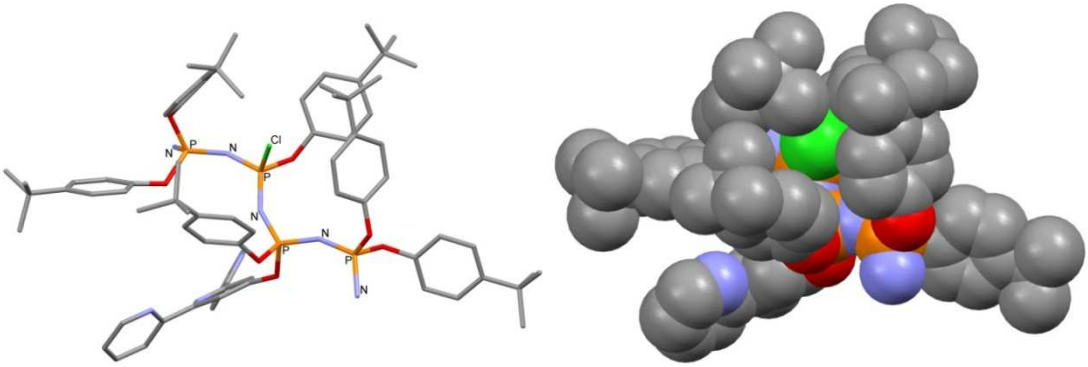

Figure 5.4.1.1 Left: Schematic diagram displaying the unreacted P-Cl unit found on the polyphosphazene backbone (hydrogens removed for clarity). Right: Space-filling model displaying the unreacted chlorines found on the polyphosphazene backbone (hydrogens removed for clarity).

5.4.2 2,6-bis(2-pyridyl)-4(1*H*)-pyridonate based polymer (L^{1P})

2,6-bis(2-pyridyl)-4(1*H*)-pyridonate (OTerpy) reacted with the chloropolymer with a similar rate to the small molecule analogues (see Chapter 2). However, during the course of the reaction polymer degradation was observed using ^{31}P NMR spectroscopy. This was determined by the appearance of peaks near 15 and 20 ppm (see Figure 5.4.2.1).

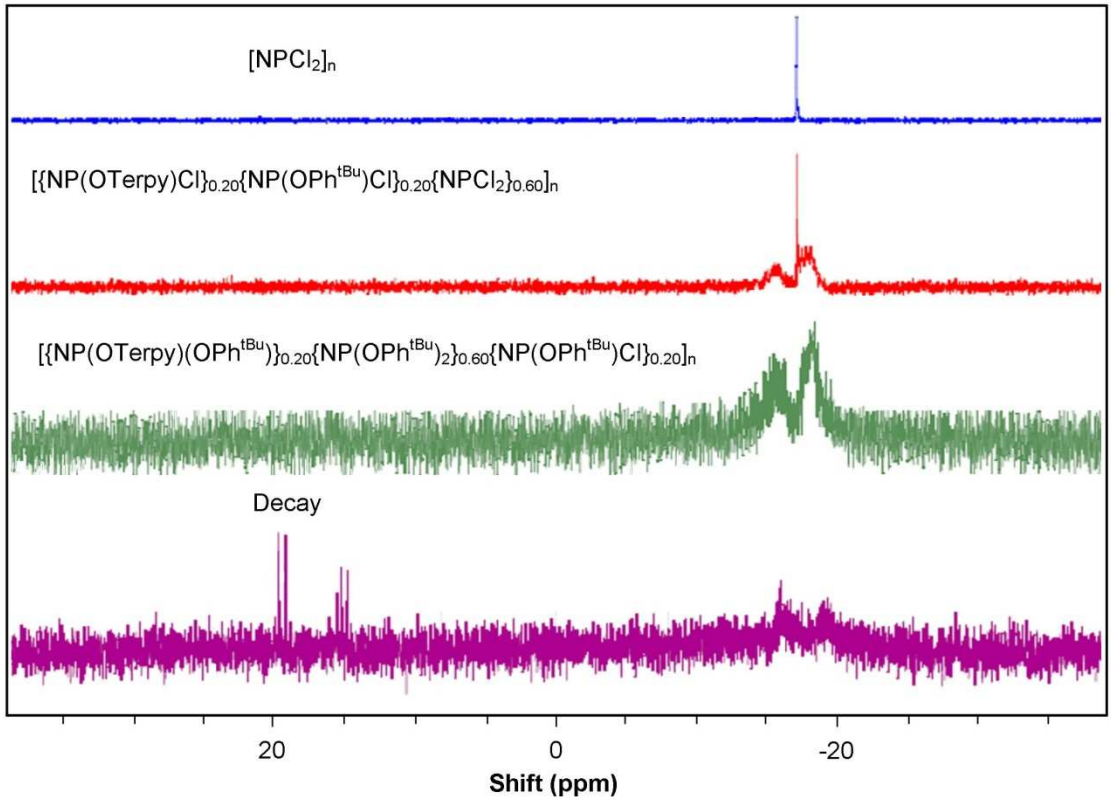

Figure 5.4.2.1 ^{31}P NMR spectra of L^{1P} during the course of its synthesis, showing the decay.

It was suggested by Kirk *et al.*[6] that the pyridine nitrogen of 2-pyridoxy attacked the -P=N- bond during its synthesis breaking the polymer into oligomers because peaks observed at 15 and 20 ppm are typical of the trimeric species. By comparison to Kirk *et al.*[6] an analogous mechanism for this decay of the OTerpy polymer is shown in Figure 5.4.2.2.

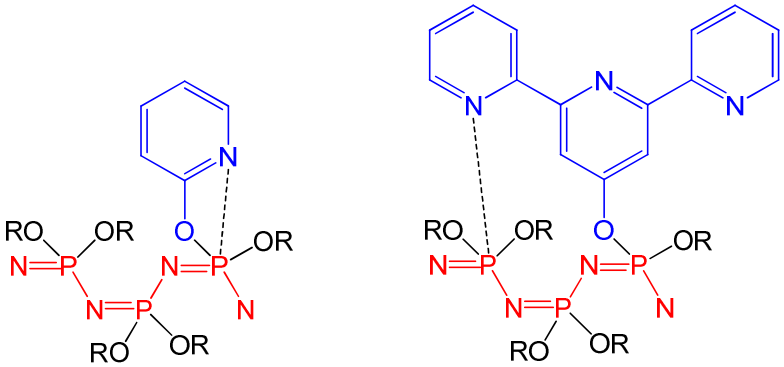

Figure 5.4.2.2 Left: 2-Pyridoxy interactions with the polyphosphazene backbone. Right: Proposed decay mechanism of the OTerpy based polymers.

The molecular weights described in Section 5.6 show that the polymers are also shorter than the parent polymer. This suggests that the polymer is breaking down but not as significantly as the pyridine ones; which is most likely due to the geometry of the terpy substituents. The aromatic nitrogens are held close to the polymer backbone but not to the same extent as for the 2-pyridoxy polymer.

5.4.3 2,6-di(1*H*-benzimidazol-2-yl)pyridine-4(1*H*)-onate based polymer (L^{3P})

2,6-di(1*H*-benzimidazol-2-yl)pyridine-4(1*H*)-one (HObbp) was insoluble in all viable solvents except acetone, in which it was only sparingly soluble. Acetone was used for the small molecule analogues (see Chapter 2), as it provided no problems with the phosphazene starting material and product. However, both the chloro- and tert-butylphenol substituted polyphosphazenes are not soluble in acetone; therefore, only small amounts could be added to the THF/toluene reaction solution to prevent the polymer from precipitating. The amount of acetone limited the amount of HObbp that could be added to the polymer. One possible solution is to extend the reaction time. However, this results in another problem, typically polyphosphazene halogen substitution reactions only run for 7–10 days before hydrolysis becomes a significant problem. As adding 0.05 ratio of 2,6-di(1*H*-benzimidazol-2-yl)pyridine-4(1*H*)-onate (Obbp) takes 3 days (ignoring the additional time required to substitute $HOPhBu^t$), further addition would take longer increasing the amount of hydrolytic decay.

5.4.4 4-(2,6-di{pyridin-2-yl}-pyridine-4-yl)phenolate and 4-(2,6-di{1*H*-pyrazol-1-yl}pyridine-4-yl)phenolate based polymers (L^{2P} and L^{4P})

The phenol groups in the 4-(2,6-di{pyridin-2-yl}-pyridine-4-yl)phenol (HOPhTerpy) and 4-(2,6-di{1*H*-pyrazol-1-yl}pyridine-4-yl)phenol (HOPhbpp) ligands were more acidic than that of the HObbp and HOTerpy substituents. This allowed for a more rapid nucleophilic substitution of the chlorine (consistent with the small molecule analogues), with no evidence of hydrolytic decay (see Figure 5.5.4). In addition, the phenyl spacer reduced steric hindrance, further accelerating the reaction. This reaction behaviour was the same as the small molecule analogues.

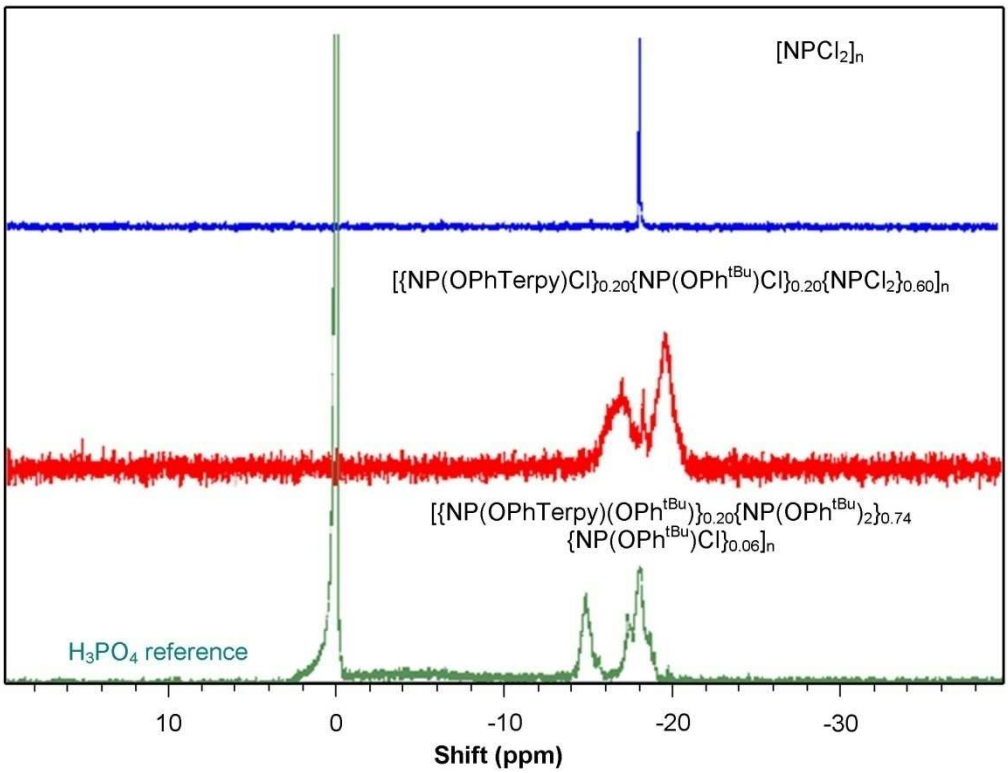

Figure 5.4.4.1 ^{31}P NMR spectra of the reaction progress of L^{2P}.

5.5 Molecular weights of the metal-free polyphosphazenes

As described in Section 5.2.2, GPC is the standard method for determining the weight of a polymer. Shown in Figure 5.5.1 is a typical GPC spectrum recorded for a phosphazene.

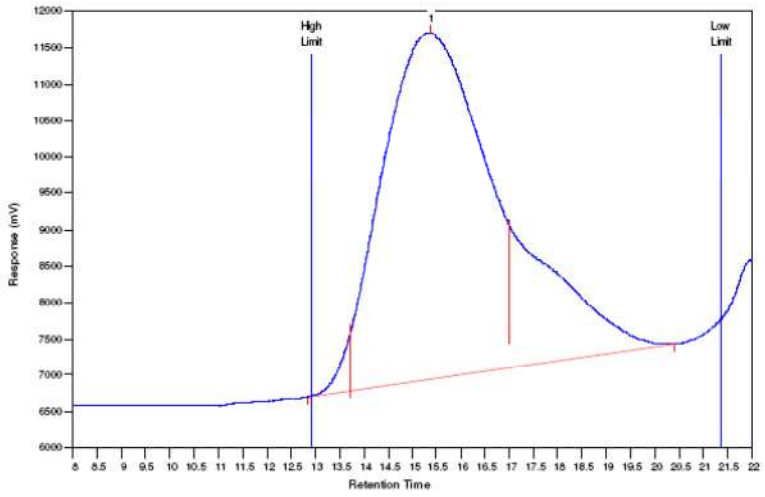

Figure 5.5.1 Example of a typical peak recorded on a GPC.

The retention time of the polymer corresponds to the molecular weight (M_w), i.e. large polymers have short retention times while small polymers have larger retention. From the width of the peak it becomes possible to determine the distribution of chain lengths (M_n). The distribution of polymer weights versus chain length is given by its PDI. $[NP(TFE)_2]_n$ is used as the reference to deduce the molecular weight of the parent polymer.

Shown in Table 5.5.1 are the molecular weights and PDIs of the TFE and metal-free polymers.

Table 5.5.1 Molecular weights and PDIs of the metal-free polyphosphazenes.

Polymer	Mw (10^3)	PDI	No. of Repeating units
$[NP(TFE)_2]_n$	256	1.53	1057
L^{1P}	399	2.97	234
L^{2P}	795	2.01	427
L^{3P}	820	1.66	126
L^{4P}	1,141	1.85	660

As seen in Table 5.5.1 the parent polymer is 1057 repeating units, this is smaller than produced by established labs such as Allcock's. However, its molecular weight and PDI are within the range for a TFE substituted phosphazene polymer formed using the ROP method. Each of the polymers displayed varying degrees of decay which relates to the length of reaction time. Both L^{2P} and L^{4P} have only 427–660 repeating units suggesting some decay during the reaction, however, as both L^{3P} and L^{1P} required significantly longer reaction times resulting in greater decay. The number of repeating units for L^{3P} is deceptive. This is because the repeating unit is based on the number of primary substituents. As L^{3P} has a low ratio of primary substituents the repeating unit is large.

The PDIs of L^{2P}, L^{3P} and L^{4P} are within a typical range of a substituted ROP polyphosphazene. They show some small variation due to the random distribution of substituents and decay that occurs with longer reaction times. L^{1P} suffered from a significant amount of decay causing a high PDI.

5.6 Observations from metal-coordinated polymer (metallo-polymer) syntheses

The homoleptic iron(II) metallo-polymers were synthesised by dissolving two equivalents of the polymer (see Figure 5.6.1) in chloroform under argon. Finally one equivalent of iron(II) perchlorate was added and the solution was stirred at room temperature, forming the metallo-polymers in Figure 5.6.1. Experimental data is given in Appendix D.

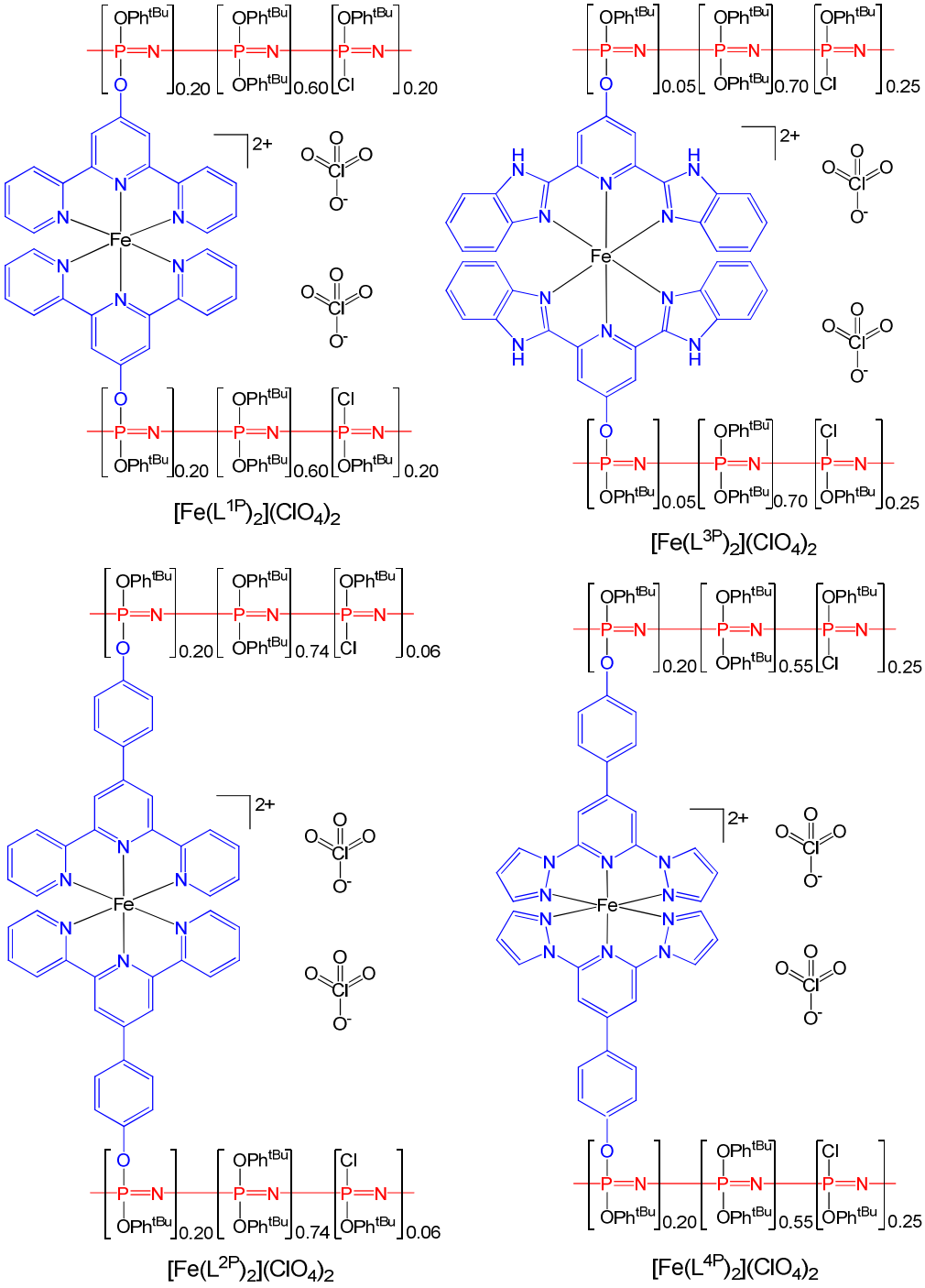

Figure 5.6.1 Iron(II) metallo-polymers synthesised.

5.6.1 Iron(II) metallo-polymers

As for the small molecule analogues (Chapter 3), one equivalent of $Fe(ClO_4)_2.6H_2O$ was added to two equivalents of the polymer's repeating unit dissolved in a chloroform: methanol (9:1) mixture under argon (see Figure 5.6.1.1). In the case of L^{1P}, L^{2P}, and L^{3P} the solutions rapidly turned purple. However, L^{4P} produced a yellow solution. Each of the solutions were stirred for an extended period of time to assure the reaction went to completion. The solution was cooled to precipitate excess iron salts from the solution followed by the precipitation of the polymer by the addition of methanol. Anion metathesis was not viable for the polymers as it was impossible to precipitate the salts produced during the reaction. In addition often unless reactions are stoichiometric a mixture of products will be formed during the reaction.

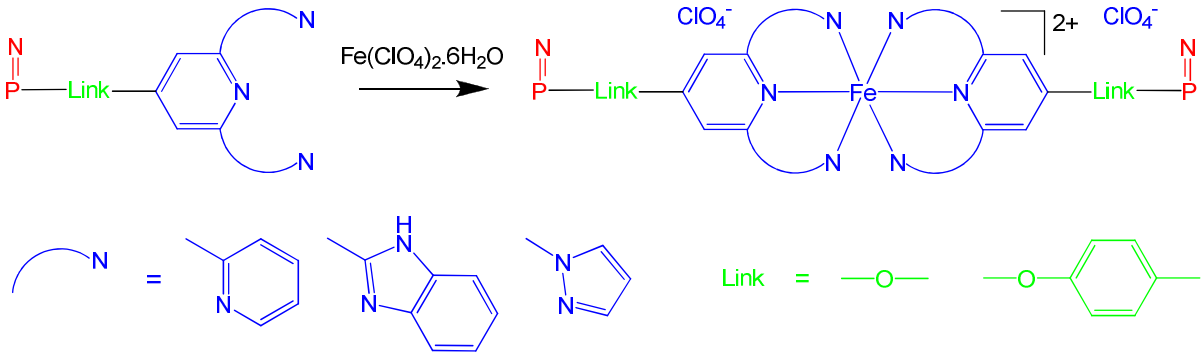

Figure 5.6.1.1 Schematic view of the iron(II) metallo-polymers synthesis.

If $Fe(ClO_4)_2.6H_2O$ was added to a concentrated (greater than 0.001 mol L^{-1}) solution of the polymer, the solution would rapidly form a purple elastic precipitate. However, if $Fe(ClO_4)_2.6H_2O$ was added gradually to a dilute solution (less than 0.0005 mol L^{-1}), the solution slowly turned purple over a period of hours. Once the complexation reaction had completed the solvent volume could be reduced forming a concentrated (~ 0.002 mol L^{-1}) solution; however, at this concentration a precipitate was not formed. As the polymer remained soluble it suggests that the polymer chains are not cross-linking; however, the colour is typical of the small molecule analogues which suggests an iron(II) bis-terpy complex. A possible explanation for this is that at low concentrations the polymer is unable to significantly cross-link between different polymer chains, rather it forms intra-chain cross-links (see Figure 5.6.1.2).

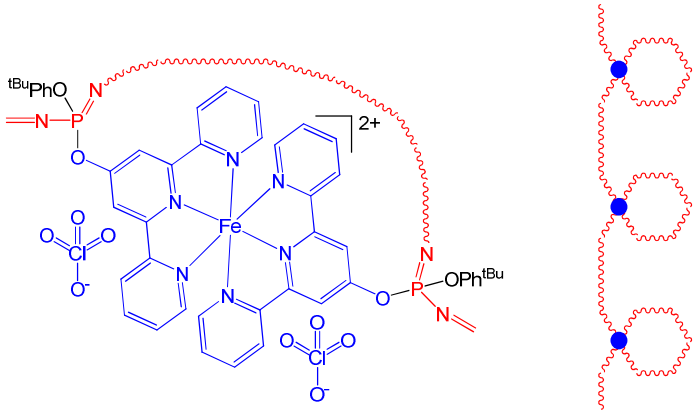

Figure 5.6.1.2 Left: Schematic diagram for the suggested intra-chain linkage. Right: An extended view of the looped polymer chain.

Once the soluble form of the polymer was made it only remained in solution for 2-7 days after which the elastic precipitate (see Figure 5.6.1.3) was formed which was insoluble in all solvents. The same result could be achieved by the addition of methanol; this is because the parent polymer is insoluble in methanol.

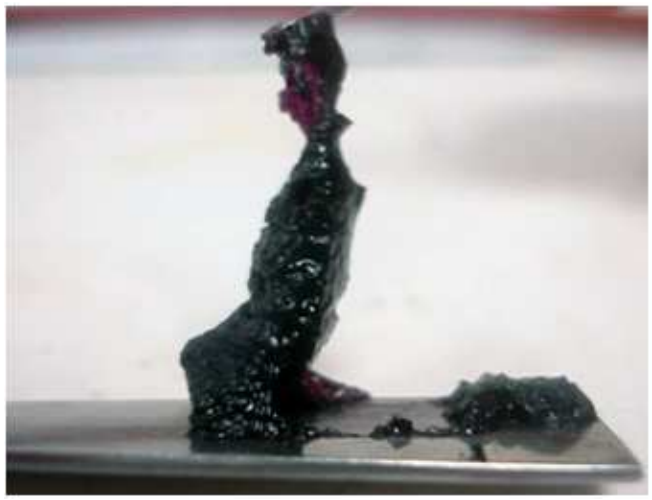

Figure 5.6.1.3 Example of the stretched cross-linked metallo-polymer ($[Fe(L^{1P})_2](ClO_4)$).

The metallo-polymer precipitate formed is insoluble in all solvents, but swells when exposed to solvents such as chloroform or THF. These properties suggest that inter-chain cross-linking was occurring (see Figure 5.6.1.4).

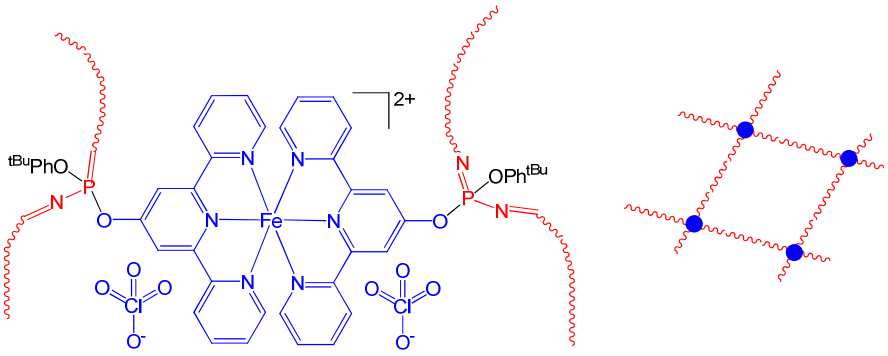

Figure 5.6.1.4 Left: schematic diagram of the suggested cross-linked polymer. Right: An extended view of the cross-linked polymer.

The soluble form slowly forms the precipitate because iron(II) is labile, thus intra-chain loops are able to convert to the entropically favourable inter-chain cross-links. Due to the insolubility of the metal complexed polymers it was impossible to obtain the molecular weights. It is therefore assumed that the addition of the metal has not affected the parent polymer chains integrity; it has simply coordinated to the substituent ligands. Such cross-linking behaviour was observed for L^{2P}, L^{3P} and L^{4P} based polymer complexes.

Although the colours of the polymers match the small molecule analogues, a thorough investigation is made in Chapter 7 to investigate the coordination site of the polymer and the physical properties (electronic, vibrational, electrochemical and magnetic).

5.7 Observations from metal-coordinated polymer (metallo-polymer) synthesis

The heteroleptic ruthenium(II) metallo-polymer was synthesised by dissolving one equivalent of the polymer in THF, followed by the addition of methanol. Finally, one equivalent of the ruthenium trichloride complex of the co-ligand was added and the solution was stirred at room temperature, forming the metallo-polymers in Figure 5.7.1. Experimental data is given in Appendix D.

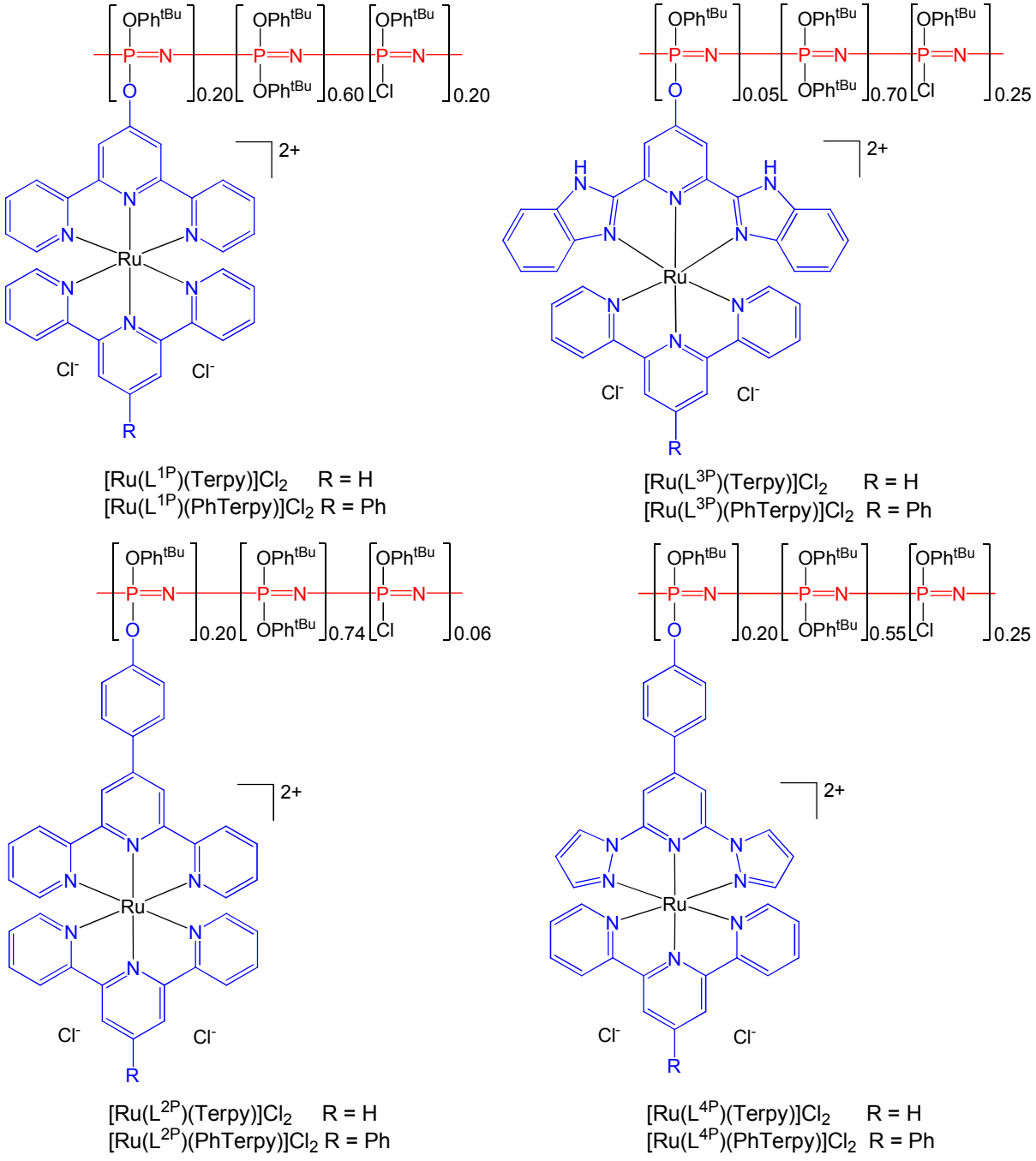

Figure 5.7.1 Ruthenium(II) metallo-polymers synthesised.

5.7.1 Ruthenium(II) metallo-polymers

Homoleptic complexes were attempted by reacting ruthenium trichloride with the free ligands L^{1P} and L^{2P}, as only the terpy based small molecule analogues cleanly formed homoleptic complexes. However, unlike with iron(II) the reactions were slow requiring refluxing to proceed. After three hours (the time required to coordinate as the ruthenium (III) complex) for each reaction, a precipitate formed that would not dissolve in any suitable solvents. This is likely due to some of the ruthenium coordination sites cross-linking; however, due to the high temperatures the reaction was driven towards the kinetically favourable product without froming the intermediate loops as with iron(II). As the precipitate could not be dissolved it prevented any means of purifying or characterising it by many techniques used for the iron polymers. In addition, as the precipitate formed in only three hours it is likely that only a small ratio of ruthenium(II) sites have formed, the rest would still be ruthenium(III). Not only did this precipitation prevent the formation of the homoleptic ruthenium metallo-polymers, but it also prevented the formation of heteroleptic ruthenium complexes by initially forming the ruthenium(III) trichloride complexes then reacting with the respective ligand.

The heteroleptic ruthenium(II) metallo-polymers were formed by reacting each ligand with the respective ruthenium(III) trichloride co-ligand complex. This resulted in the formation of soluble polymers. This reaction displayed no differences with the different ratios of substituents.

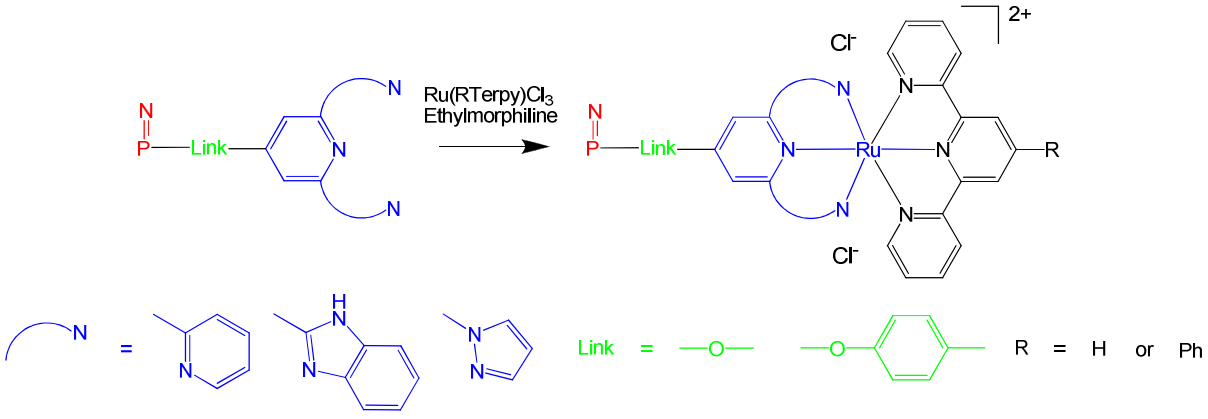

Figure 5.7.1.1 Schematic view of ruthenium(II) metallo-polymer synthesis.

The physical properties (electronic, vibrational and electrochemical) of the ruthenium small molecule and metallo-polymer complexes are fully compared in Chapter 6.

5.8 Differential scanning calorimetry

Shown in Table 5.8.1 are the T_g values obtained for each of the free and coordinated polymers. Four assumptions can be made for each of the polymers when comparing their T_g values:[6]

i) As each of the polymer backbones contains only =P-N=P-N- bonding the energy barrier for bond torsion will be the same.

As each of the polymers was made from the same parent polymer these assumptions can be made:

ii) The same degree of cross-linking is present for each metal-free parent polymer.

iii) The architecture of the metal-free polymers will be the same, i.e. linear, collinear or containing side branches.

iv) Finally, each of the polymers was prepared for measurements under the same conditions.

Table 5.8.1 T_g values for metal-free, iron(II) and ruthenium(II) complexes of the polyphosphazenes.

Polymer	**T_g (°C)**			
	Metal-Free	$Fe(ClO_4)_2$	$Ru(Terpy)Cl_2$	$Ru(PhTerpy)Cl_2$
$[NP(TFE)_2]_n$	-62.76	-	-	-
L^{1P}	38.52	not visible	42.33	29.67
L^{2P}	38.61	44.40	58.70	28.28
L^{3P}	44.31	42.70	34.18	30.43
L^{4P}	35.52	47.92	37.92	40.34

The T_g temperature for the $[NP(TFE)_2]_n$ is -62.76°C, this is typical of a fully substituted linear $[NP(TFE)_2]_n$ polymer, therefore it can be assumed that the parent chloro polymer is linear. The free polymers also display similar T_g values for that of Ainscough's polymers (43 -47°C).[1]

For $[Fe(L^{2P})_2](ClO_4)_2$ and $[Fe(L^{4P})_2](ClO_4)_2$ the T_g values have slightly increased (5.79 and 12.4°C respectively) relative to the free polymers. While one may expect a large increase due to the reduced flexibility of the system, this is neither observed in the current work nor with Carriedo's gold cross-linked systems.[29] These may well be typical increases for transition metal cross-linked systems; however, there are few

examples to compare. $[Fe(L^{1P})_2](ClO_4)_2$ shows no discernable glass transition point, the most likely reason for this is that the transition is too gradual to observe. The decrease of T_g for $[Fe(L^{3P})_2](ClO_4)_2$ relative to the free polymer is difficult to explain, one theory for this is that a certain amount of cross-linking occurs at the unreacted chlorine sites; however, under the reaction conditions of the metal coordination some of the cross-linking is reduced.

The ruthenium metallo-polymers based on L^{1P}, L^{2P} and L^{4P} each displayed an increase in T_g relative to that of the free polymers. This can be explained by the addition of a larger charged group to the polymer backbone. Again the L^{3P} based complexes had lower T_g values most likely due to the reduction of cross-linking under the coordinating conditions. The effect may be greater for these polymers because the reaction times were longer than those for the iron reactions discussed in 5.6.

It can also be observed that the ruthenium metallo-polymers co-substituted with PhTerpy has lower T_g values than the terpy analogues. A possible reason for this behaviour is that the generally longer substituents lower it, although this usually applies to alkyl groups rather than aromatic ones.

5.9 Conclusion

Four polymers containing different tridentate substituents were successfully synthesised (L^{1P}, L^{2P}, L^{3P} and L^{4P}). The reactivity of each of the tridentate substituents (OTerpy, OPhTerpy, Obbp and OPhbpp) was similar to that of the small molecule analogues in Chapter 2. Each of the polymers had a high ratio of unreacted chlorines due to the presence of bulky substituents.

Each of the four metal-free polymers reacts with $Fe(ClO_4)_2.6H_2O$ to form a homoleptic iron(II) polymer, initially forming what was suspected to be an intra-chain cross-linked polymer but after precipitation formed inter-chain cross-linked polymer network. It is suspected that $[Fe(L^{1P})_2](ClO_4)_2$, $[Fe(L^{2P})_2](ClO_4)$ and $[Fe(L^{3P})_2](ClO_4)_2$ were low spin; however, $[Fe(L^{4P})_2](ClO_4)_2$ appears to be high spin due to its yellow colour, although these properties are thoroughly investigated in Chapter 7.

Eight heteroleptic ruthenium(II) metallo-polymers were synthesised by reacting either Ru(Terpy)Cl_3 or Ru(PhTerpy)Cl_3 with the free polymer. Due to an inability to perform anion metathesis on the polymers the anions remained as chlorides rather than hexafluorophosphates.

The reactions of $RuCl_3 \cdot 3H_2O$ with the four metal-free polymers produced solids that were insoluble in all suitable solvents, possibly due to some cross-linking. It is suspected due to the rate of the reaction only a small ratio of ruthenium(II) centers are formed, therefore, the remainder of metal centers remain ruthenium(III). These compounds could not be purified or characteriesed by normal techniques, so studies on them were abandoned.

Ruthenium trichloride complexes of the free polymers could not be synthesised and isolated, because the reaction readily formed an insoluble solid, possibly due to some cross-linking. Due to the insolubility of the precipitate it cannot be purified or characterised by many techniques. This also meant that the heteroleptic complexes could not be formed by reacting the co-ligand with the ruthenium trichloride complex.

Despite the limitations of the synthesis the reactions clearly demonstrate that it is possible to attach groups (a phenyl ring in these examples) to a polyphosphazene backbone under relatively mild conditions. The coordination behaviour and physical properties of these links will be thoroughly investigated in Chapter 6.

5.10 References

1. Horvath, R.; Otter, C. A.; Gordon, K. C.; Brodie, A. M.; Ainscough, E. W. *Unpublished results*.

2. Diefenbach, U.; Cannon, A. M.; Stromburg, B. E.; Olmeijer, D. L.; Allcock, H. R. *Journal of Applied Polymer Science* **2000**, *78*, 650-661.

3. Carriedo, G. A.; Alonso, F. J. G.; Soto, A. P. *Journal of Inorganic and Organometallic Polymers and Materials* **2007**, *17*, 399-406.

4. Spitaleri, A.; Pertici, P.; Scalera, N.; Vitulli, G.; Hoang, M.; Turney, T. W.; Gleria, M. *Inorganica Chimica Acta* **2003**, *352*, 61-71.

5. Diaz, C.; Valenzuela, M. L.; Spodine, E.; Moreno, Y.; Pena, O. *Journal of Cluster Science* **2007**, *18*, 831-844.

6. Kirk, S. *Cyclo- and Polyphosphazenes Containing 2-oxypyridine Moieties Coordinated to Selected Transition Metals*, Massey University, Palmerston North, **2008**.

7. Diaz, C.; Castillo, P. *Polymer Bulletin* **2003**, *50*, 123-129.

8. Diaz, C.; Carriedo, G. A.; Valenzuela, M. L. *Polymer Bulletin* **2009**, *63*, 829-835.

9. Carriedo, G. A.; Alonso, F. J. G.; Gonzalez, P. A.; Valenzuela, C. D.; Saez, N. Y. *Polyhedron* **2002**, *21*, 2579-2586.

10. Carriedo, G. A.; Alonso, F. J. G.; Gonzalez, P. A.; Gomez-Elipe, P. *Polyhedron* **1999**, *18*, 2853-2859.

11. Allcock, H. R.; Lavin, K. D.; Tollefson, N. M.; Evans, T. L. *Organometallics* **1983**, *2*, 267-275.

12. Stokes, H. N. *Chemische Berichte* **1895**, *28*, 437-439.

13. Stokes, H. N. *American Chemical Journal* **1896**, *18*, 629-663.

14. Stokes, H. N. *American Chemical Journal* **1896**, *18*, 780-789.

15. Stokes, H. N. *American Chemical Journal* **1897**, *19*, 782-796.

16. Stokes, H. N. *American Chemical Journal* **1898**, *20*, 740-760.

17. Stokes, H. N. *American Chemical Journal* **1895**, *1895*, 275.

18. Allcock, H. R.; Kugel, R. L. *Journal of the American Chemical Society* **1965**, *87*, 4216-4217.

19. Allcock, H. R.; Kugel, R. L. *Inorganic Chemistry* **1966**, *5*, 1716-1718.

20. El-Amin, S. F.; Kwon, M. S.; Starnes, T.; Allcock, H. R.; Laurencin, C. T. *Journal of Inorganic and Organometallic Polymers and Materials* **2006**, *16*, 387-396.

21. Greish, Y. E.; Sturgeon, J. L.; Singh, A.; Krogman, N. R.; Touny, A. H.; Sethuraman, S.; Nair, L. S.; Laurencin, C. T.; Allcock, H. R.; Brown, P. W. *Journal of Materials Science-Materials in Medicine* **2008**, *19*, 3153-3160.

22. Allcock, H. R. *Chemistry and Applications of Polyphosphazenes*; John Wiley & Sons Inc: Hoboken, **2003**.

23. Nukavarapu, S. P.; Kumbar, S. G.; Brown, J. L.; Krogman, N. R.; Weikel, A. L.; Hindenlan, M. D.; Nair, L. S.; Allcock, H. R.; Laurencin, C. T. *Biomacromolecules* **2008**, *9*, 1818-1825.

24. Andrianov, A. K.; Chen, J. P.; Payne, L. G. *Biomaterials* **1998**, *19*, 109-115.

25. Allcock, H. R.; Pucher, S. R.; Turner, M. L.; Fitzpatrick, R. J. *Macromolecules* **1992**, *25*, 5573-5577.

26. Potta, T.; Chun, C.; Song, S. C. *Biomacromolecules*, *11*, 1741-1753.

27. Qiu, L. Y. *Journal of Applied Polymer Science* **2003**, *87*, 986-992.

28. Diaz, C.; Valenzuela, M. L.; Barbosa, M. *Materials Research Bulletin* **2004**, *39*, 9-19.

29. Carriedo, G. A.; Presa, A.; Valenzuela, M. L.; Ventalon, M. *Journal of Organometallic Chemistry* **2009**, *694*, 249-252.

30. Neilson, R. H.; Hani, R.; Wisianneilson, P.; Meister, J. J.; Roy, A. K.; Hagnauer, G. L. *Macromolecules* **1987**, *20*, 910-916.

31. Mark, J. E.; Allcock, H. R.; West, R. *Inorganic Polymers*; 2nd ed.; Oxford Press: Oxford, **2005**.

32. Dieck, R. L.; Goldfarb, L. *Journal of Polymer Science Part A - Polymer Chemistry* **1977**, *15*, 361-369.

33. Constable, E. C.; Ward, M. D. *Journal of the Chemical Society-Dalton Transactions* **1990**, 1405-1409.

34. Spahni, W.; Calzaferri, G. *Helvetica Chimica Acta* **1984**, *67*, 450-454.

35. Drew, M. G. B.; Hill, C.; Hudson, M. J.; Iveson, P. B.; Madic, C.; Vaillant, L.; Youngs, T. G. A. *New Journal of Chemistry* **2004**, *28*, 462-470.

36. Madhu, N. T.; Salitros, I.; Schramm, F.; Klyatskaya, S.; Fuhr, O.; Ruben, M. *Comptes Rendus Chimie* **2008**, *11*, 1166-1174.

Chapter 6

Coordination site characterisation of the ruthenium(II) metallo polymer and the physical behaviour of both the cyclotriphosphazene and polyphosphazene ruthenium(II) metallo polymer.

6.0 Abbreviations used in Chapter 6

SMA	Small molecule analogue
Terpy	2,2':6',2''-terpyridine
PhTerpy	2,6-di(pyridin-2-yl)-4-phenylpyridine
bbp	2,6-di(1*H*- benzimidazol-2-yl)pyridine
bpp	2,6-di(1*H*-pyrazol-1-yl)pyridine
CV	Cyclic Voltammetry
IR	Infrared spectroscopy
UV/Vis	Ultraviolet/Visible
MLCT	Metal-to-ligand charge transfer
^{3}MC	Metal-centred triplet state
DFT	Density functional theory
TD-DFT	Time-dependent density functional theory
NEt_3	Triethylamine
σ^+	Cationic Hammett Parameter
rR	Resonace Raman

6.1 Introduction

6.1.1 Metallo-polymers

Metallo-polymers are gaining interest due to their potential uses as electroluminescent materials, photovoltaic materials, photocatalysts, etc.[1-4] They have been used for these applications because they combine the flexibility, solubility and ductility of the polymer with the desired optical, catalytic, magnetic, etc. properties of the metal complex.

Metallo-polymers fall into two different classes: i) coordination polymer and ii) grafted polymer. The coordination polymer is one in which the polymer consists of a repeating unit of two ligands with an organic linker, forming a link and each one coordinates to two metal ions forming a chain (see Figure 6.1.1.1). If a conjugated linker is used the metal centres can electronically interact with each other.

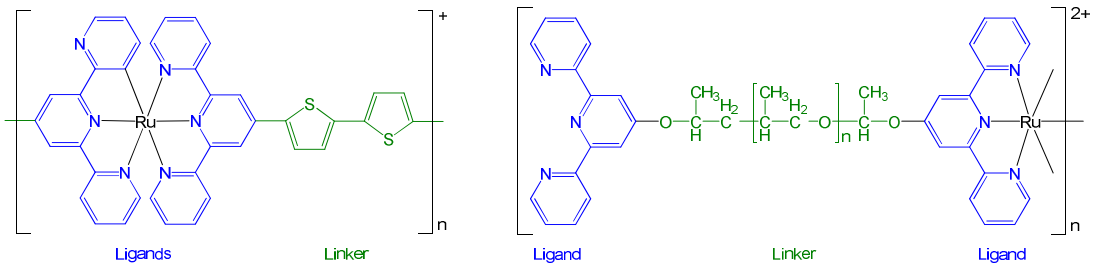

Figure 6.1.1.1 Two examples of coordination polymers. Left: an electronically active thiophene linker.[5] Right: an electronically mute polyether linker.[6]

The most pertinent metallo-polymers to this project are grafted polymers. These have a polymer backbone with the ligands attached as side chains. They have an advantage over the coordination polymers, in that they can either be polymerised first then the metal coordinated or the metal can be coordinated and then the monomer unit polymerised. Depending on the system either approach can be advantageous. In addition the use of grafting potentially allows the addition of complex groups, rather than just modifications of the polymer backbone, although to date this has not been investigated. As with the coordination polymers, the metals can electronically interact via the polymer; however, consideration about the linker as well as the polymer must be made (see Figure 6.1.1.2), i.e. even if the polymer backbone is conjugated the metals cannot interact via the polymer unless the linking groups are also conjugated.

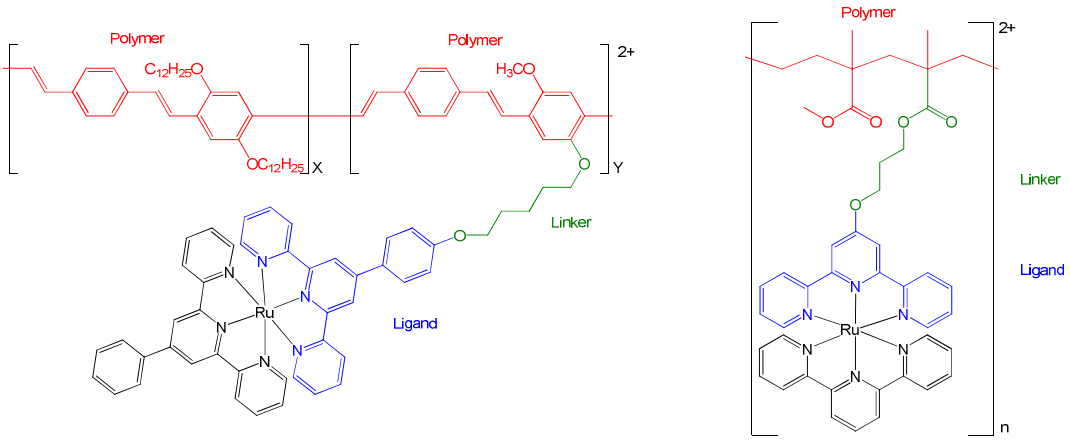

Figure 6.1.1.2 Two examples of grafted polymers. Left: an electronically active poly(phenylenevinylene) polymer with electronically mute ether linker.[7] Right: an electronically mute alkyl polymer with an electronically mute ester linker.[8]

While metal communication can provide new desirable properties by expanding the conjugation, metal communication is not always desirable. In some cases the properties of the metal complex were already suitable and the only polymer features required are the solubility and ductility of the polymer, for these cases electronically mute polymers are ideal, e.g. alkyl chains, polyethers, polypeptides, polyphosphazenes, etc.

In this study the feasibility of attaching groups to a polyphosphazene via metal coordination was investigated. Tridentate ligands were chosen as the ligands and linkers because when they are coordinated to certain metals they only form metal-bis-ligand complexes with an octahedral geometry. Although these groups are intended to act as a new linker to a phosphazene, they also have physical properties that are unique which needed to be examined to determine how they will behave before other substituents could be used. In this case a phenyl ring was used as a model for other groups. Each of the substituents chosen to act as ligands consisted of the following groups: 2,2':6',2''-terpyridine (Terpy); 4-phenyl-2,2':6',2''-terpyridine (PhTerpy); 2,6-di(1*H*-benzimidazol-2-yl)pyridine (bbp); and 2,6-di(1*H*-pyrazol-1-yl)pyridine (bpp). The physical behaviours of these complexes are described in turn.

6.1.2 Ruthenium(II) bis(2,2':6',2"-terpyridine) complexes

Ruthenium(II) bis(2,2':6,2"-terpyridine) ($[Ru(Terpy)_2]^{2+}$) complexes have been one of the most studied species of complex,[9,10] primarily due to their metal-to-ligand charge transfer (MLCT) bands.[11-14] While both $[Ru(Terpy)_2]^{2+}$ and Ruthenium(II) tris(2,2'-bipyridine) ($[Ru(Bipy)_3]^{2+}$) complexes have the MLCT band at approximately the same position, $[Ru(Terpy)_2]^{2+}$ has a very short excited state lifetime relative to that of $[Ru(Bipy)_3]^{2+}$, this occurs because the axial N-Ru-N angle is smaller (158.6°) that that of 2,2'-bipyridine (173.0°). This causes weaker ligand field strength, resulting in the metal centred triplet state (^{3}MC) energy being reduced. As a consequence the ^{3}MC is thermally accessible from the triplet excited state (^{3}MLCT), facilitating non-radiative decay back to the ground state (GS).[14]

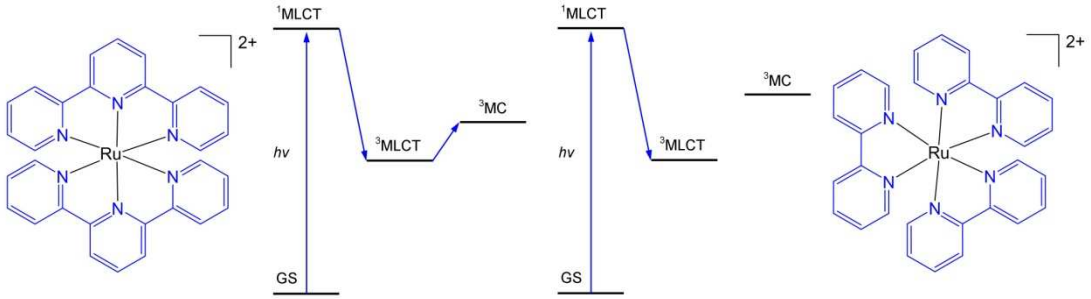

Figure 6.1.2.1 Molecular orbital diagrams of an MLCT transition. Left: $[Ru(Terpy)_2]^{2+}$. Right: $[Ru(Bipy)_3]^{2+}$.

The fluorescence can be altered by either lowering the singlet metal to ligand charge transfer (^{1}MLCT) energy level or by stabilising the ^{3}MLCT state. This is achieved by varying the electron donation of the substituents or by extending the aromaticity of the system.[14]

When increasing the aromaticity of a system by the addition of a phenyl ring via a single C-C bond rather than by forming a fused ring, co-planarity plays a significant role. The cationic Hammett parameter (σ^+)[15] (a measure of a substituent's withdrawing effect) of the phenyl ring is similar to hydrogen. However, in practice the MLCT band is shifted to 481 nm compared to 475 nm for $[Ru(Terpy)_2]^{2+}$, due to the stabilisation of

the ^{3}MLCT state. This occurs because at the GS geometry the phenyl ring twists away from the central pyridine to reduce steric hindrance; however, at the excited state the ring rotates becoming planar, stabilising the ^{3}MLCT state.[14]

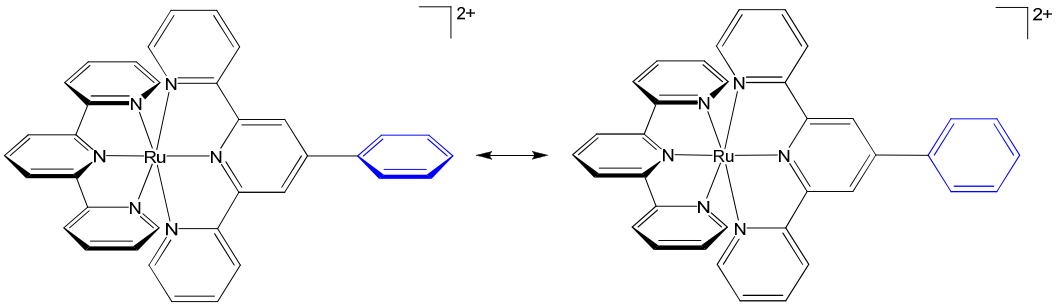

Figure 6.1.2.2 Rotation of the phenyl ring attached to the $[Ru(Terpy)_2]^{2+}$ complex.

In addition to the distinct optical properties $[Ru(Terpy)_2]^{2+}$ complexes show distinct electrochemical behaviour. They each have an oxidation peak that corresponds to the Ru^{II}/Ru^{III} couple, this shift is greatly dependent on the electron donation of substituents attached to the ligands. Constable et al.[16-18] determined the σ' value is directly related to the Ru^{II}/Ru^{III} couple (see Formula 6.1.2.1).

$$E^o\,(Ru) = 0.245\sigma' + 0.944 \quad \text{(Formula 6.1.2.1).}$$

Where σ' is the average of the substituent's cationic Hammett parameter (σ^+)

i.e. for $[Re(XTerpy)(YTerpy)]^{2+}$: $\sigma' = \frac{1}{2}(\sigma^+(X) + \sigma^+(Y))$ (Formula 6.1.2.1)

The σ^+ value was used rather than the Hammett parameter (σ) because the process is essentially the generation of a positively charged species, albeit on the metal centre rather than the organic ligand.

6.1.3 Ruthenium(II) (2,6-di{1*H*-benzimidazol-2-yl}pyridine)(2,2':6',2"-terpyridine) complexes

Ruthenium(II) (2,6-di{1*H*-benzimidazol-2-yl}pyridine)(2,2':6',2"-terpyridine) ([Ru(bbp)(Terpy)]$^{2+}$) complexes have not been as thoroughly studied as [Ru(Terpy)$_2$]$^{2+}$ complexes. Bbp's coordination behaviour is similar to that of terpy.[19] However, the imidazole nitrogens are poorer π-acceptors and better π-donors than pyridine nitrogen,[20] which causes a lowering of the ^{3}MLCT energy level. As a result the lifetimes and quantum yields are typically increased beyond that of the [Ru(Terpy)$_2$]$^{2+}$ complexes, although in most cases below practically useful levels.[21]

In addition to the difference in electronic properties the imidazole proton can hydrogen bond with anions, resulting in significant differences in the electronic spectra and electrochemical properties with different anions. Also, these protons can also be removed and substituted by other groups.[21] The systematic removal of the protons causes the imidazole group to become a stronger σ-donor subsequently lowering the ^{1}MLCT causing the MLCT band to be red shifted. This is also reflected in the Ru^{II}/Ru^{III} oxidisation potential as the complex is deprotonated.[22,23]

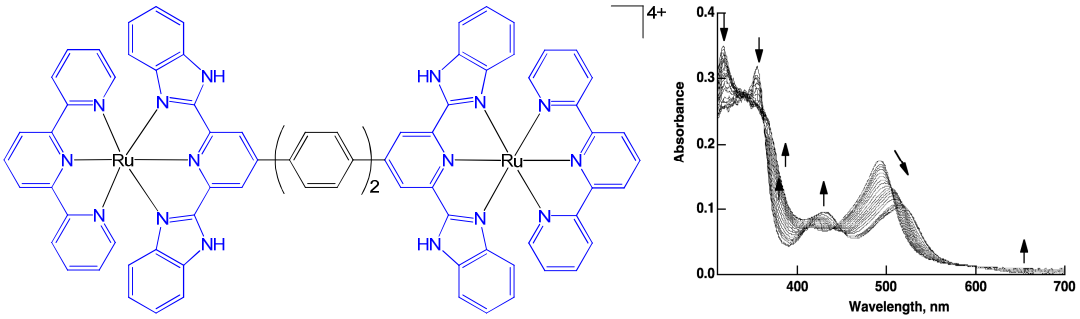

Figure 6.1.3.1 Left: Two [Ru(bbp)(Terpy)]$^{2+}$ complexes linked by a biphenyl spacer. Right: The absorbance spectra of the complex as the pH was gradually increased.[23]

6.1.4 Ruthenium(II) (2,6-di{1*H*-pyrazol-1-yl}pyridine)(2,2':6',2"-terpyridine) complexes

Ruthenium(II) (2,6-di{1*H*-pyrazol-1-yl}pyridine)(2,2':6',2"-terpyridine) ([Ru(bpp)(Terpy)]$^{2+}$) complexes are rare, only five have ever been reported.[24-26] In one such report, the complexes were shown to only be weakly fluorescent even at 77 K.[24] Based on other metal-bpp complexes it can be determined that the pyrazole group is a weaker σ-donor and π-acceptor than pyridine.[27] There are limited examples for electrochemical behaviour of [Ru(bpp)(Terpy)]$^{2+}$ based complexes; however, a series of [Ru(bpp)$_2$]$^{2+}$ based complexes provide insight into how the Ru^{II}/Ru^{III} oxidation potential is dependent on the pyrazole substitution. As the number of methyl groups added to the pyrazoles increased, the oxidation potential linearly decreased (see Figure 6.1.4.1).[28]

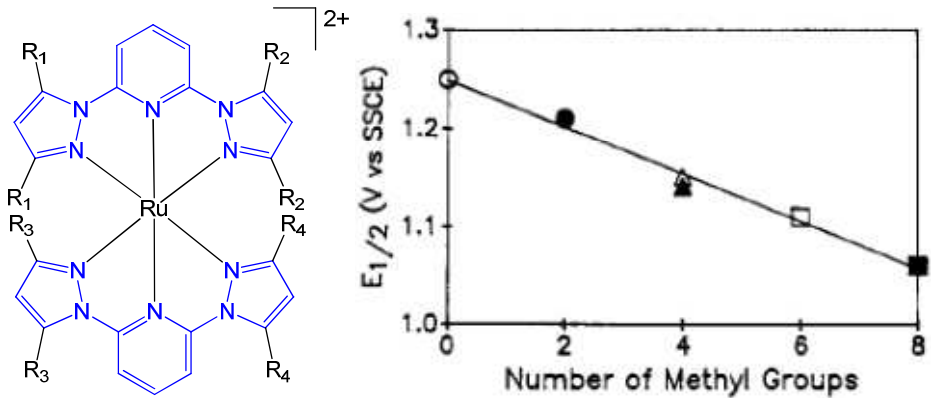

Figure 6.1.4.1 Left: [Ru(bpp)$_2$]$^{2+}$ based complex; No. methyl groups = 0 (R_1, R_2, R_3, R_4 = H), 2 (R_1 = Me, R_2, R_3, R_4 = H), 4 (R_1, R_2 = Me, R_3, R_4 = H), 6 (R_1, R_2, R_3 = Me, R_4 = H) and 8 (R_1, R_2, R_3, R_4 = Me). Right: Ru^{II}/Ru^{III} oxidation potential vs. methyl substitution number.[28]

6.2 Current research

This chapter describes the physical properties (electronic, vibrational and electrochemical) of the ruthenium complexes synthesised in Chapters 4 and 5 (see Figure 6.2.1). These measurements were used to determine if the addition of a phosphazene to the complex cores resulted in a change in their behaviour.

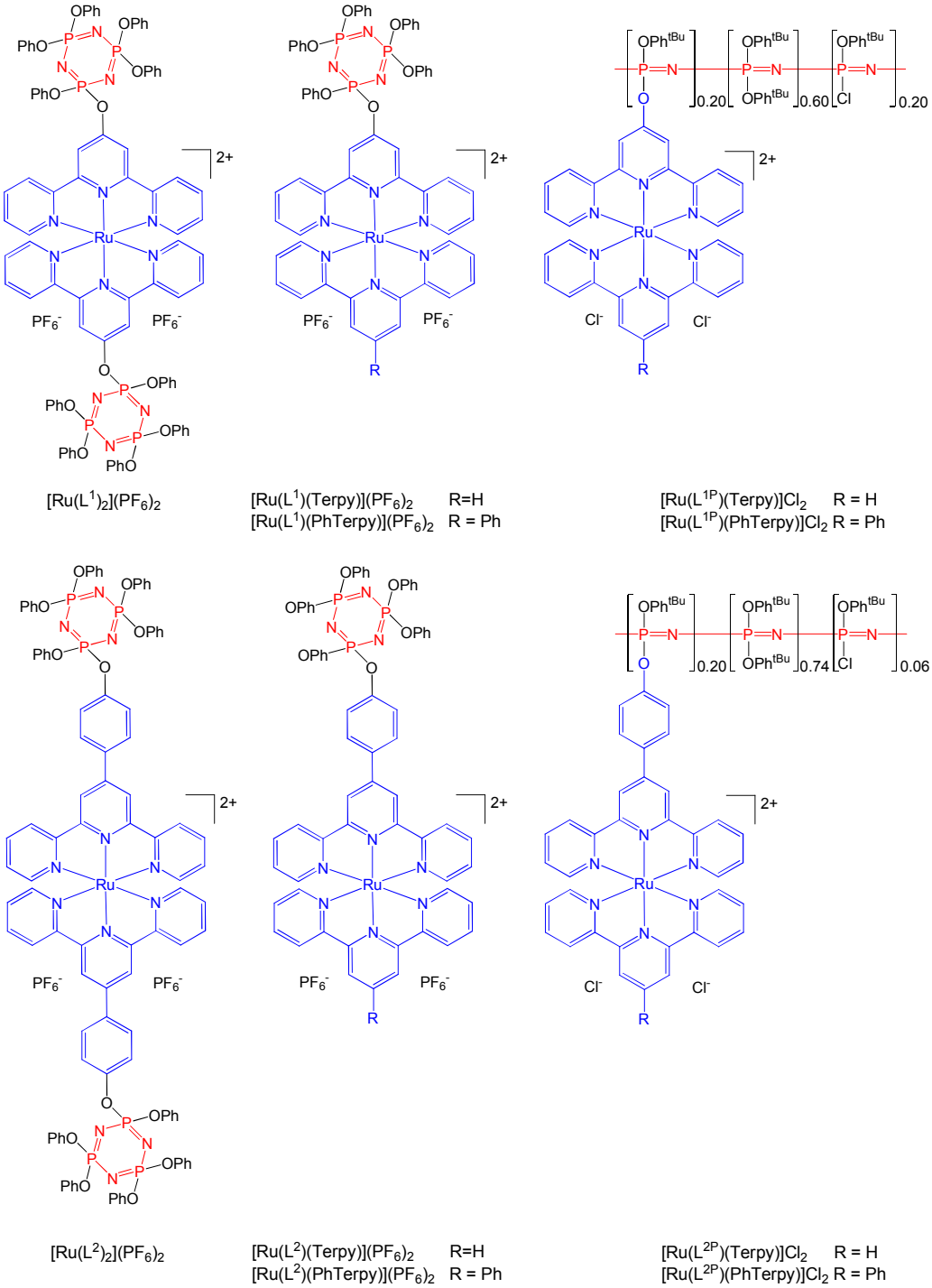

Figure 6.2.1 Ruthenium complexes investigated in this chapter.

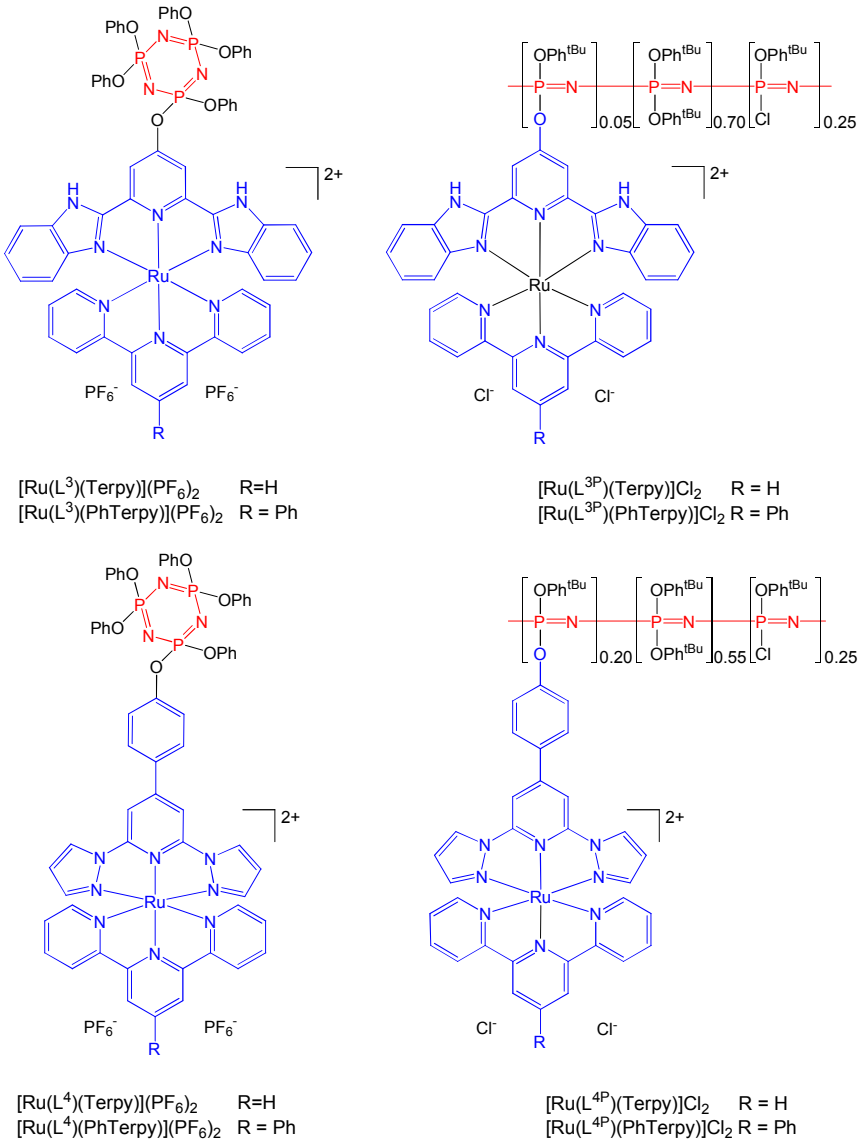

Figure 6.2.1 continued Ruthenium complexes investigated in this chapter.

Electronic absorbance, resonance Raman (rR) and electrochemical data were recorded in acetonitrile for the small molecule complexes and in chloroform for the polymers. IR data was recorded using KBr disks for both small molecule and polymeric complexes. Instrumental details and specific conditions are given in Appendix E.

Computational models of the respective cationic complexes were employed to aid the assignment of the electronic absorbance and vibrational spectra, using a DFT/B3LYP calculation with an SDD basis set. The time-dependent calculations were carried out in an acetonitrile solvent field using the PCM method.[29] All calculations were performed using the *Gaussian09*[30]/*GaussView5*[31] packages.

As a means of determining the accuracy of these models, the calculated bond lengths were compared to those obtained from crystallographic data (see Chapter 4). This gave a mean difference of 0.016 ($[Ru(L^1)(Terpy)]^{2+}$) – 0.073 Å ($[Ru(L^1)_2]^{2+}$); see Appendix E for all calculated values.

In addition to structural accuracy, the electronic accuracy of the models was measured by comparison of the calculated vibrational frequencies to the measured ones (see an example in Figure 6.2.2); the output frequencies were scaled by 0.96.[32] As these complexes did not contain unique vibrational modes, the mean average deviation (MAD) values were calculated using all assigned vibrational modes.[33] This gave values of 3.08 ($[Ru(L^1)(bbp)]^{2+}$) – 6.96 cm^{-1} ($[Ru(L^4)(Terpy)]^{2+}$) which is particularly accurate for this basis set with a large complex. See Appendix E for all calculated values.

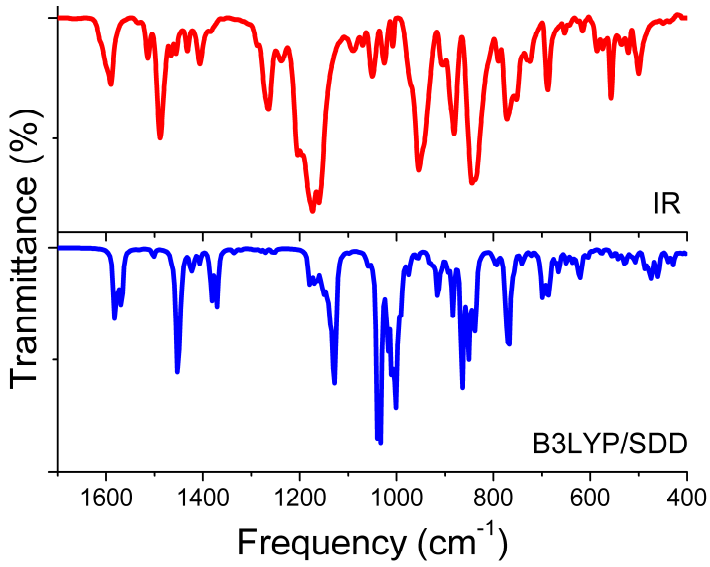

Figure 6.2.2 Comparison of the IR spectra for $[Ru(L^1)_2](PF_6)_2$ to the calculated IR spectra of $[Ru(L^1)_2]^{2+}$.

6.3 Electronic absorbance spectroscopy

6.3.1 Ruthenium(II) bis(2,2':6',2"-terpyridine) complexes

The electronic absorbance spectra of each of the 4-(2,2':6',2"-terpyridine)-4'-yl-phenolate (OPhTerpy) based complexes display an MLCT band at 483–489 nm characteristic of a $[Ru(Terpy)_2]^{2+}$ complex. Each of the small molecule L^2 based complexes—$[Ru(L^2)_2](PF_6)_2$, $[Ru(L^2)(Terpy)](PF_6)_2$ and $[Ru(L^2)(PhTerpy)](PF_6)_2$—show approximately a 1–4 nm red shift relative to $[Ru(PhTerpy)_2](PF_6)_2$[34] (see Table 6.3.1.1).

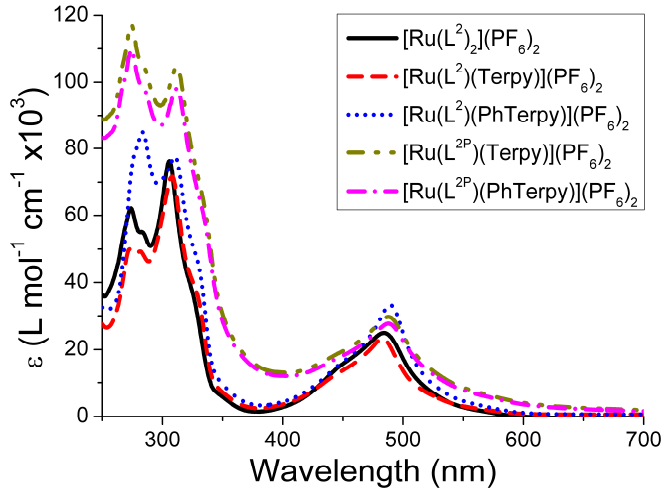

Figure 6.3.1.1 Electronic absorbance spectra of the compounds. OPhTerpy based complexes $[Ru(L^2)_2](PF_6)_2$, $[Ru(L^2)(Terpy)](PF_6)_2$, $[Ru(L^2)(PhTerpy)](PF_6)_2$, $[Ru(L^{2P})(Terpy)]Cl_2$ and $[Ru(L^{2P})(PhTerpy)]Cl_2$.

Table 6.3.1.1 Extinction coefficients of MLCT bands for the OPhTerpy based complexes.

Complex	λ_{max} / nm (ε / 10^3 L mol^{-1} cm^{-1})
$[Ru(PhTerpy)_2](PF_6)_2$ [a 34]	487 (26)
$[Ru(L^2)_2](PF_6)_2$ [a]	484 (25)
$[Ru(L^2)(Terpy)](PF_6)_2$ [a]	483 (23)
$[Ru(L^2)(PhTerpy)](PF_6)_2$ [a]	489 (33)
$[Ru(L^{2P})(Terpy)]Cl_2$ [b]	489 (29)
$[Ru(L^{2P})(PhTerpy)]Cl_2$ [b]	488 (28)

Recorded in: [a] acetonitrile and [b] chloroform.

The slight red shift proves that the substitution of the phosphazene had only a weak electron-withdrawing effect indicated by almost no effect on the MLCT band. DFT calculations support this by showing no contribution from the phosphazene in the orbitals involved in the MLCT (see Appendix E), an example of $[Ru(L^2)_2]^{2+}$ orbitals are shown in Figure 6.3.1.2.

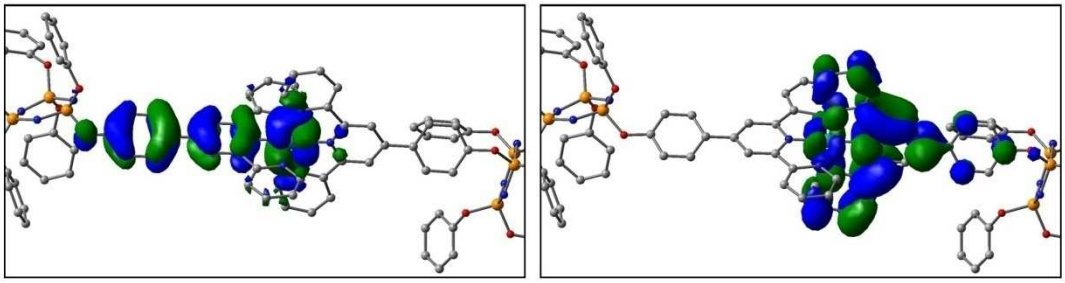

Figure 6.3.1.2 Highest occupied molecular orbital (HOMO) and lowest unoccupied molecular orbital (LUMO) of $[Ru(L^2)_2]^{2+}$.

The phenyl spacer acts to increase the distance between the terpy unit and phosphazene, thereby reducing any contribution the phosphazene may have otherwise made. In addition, because of the 'bulk' surrounding the phenyl spacer it is probable that its rotation in the excited state is hindered. This would reduce the stabilisation of the ^{3}MLCT state accounting for the absence of fluorescence at room temperature.

The polymeric analogues $[Ru(L^{2P})(Terpy)]Cl_2$ and $[Ru(L^{2P})(PhTerpy)]Cl_2$ display almost identical MLCT λ_{max} positions to that of their small molecule analogues (SMA) (see Figure 6.3.1.1), with the slight differences potentially being explained by the difference in the solvent environment as the SMA were recorded in acetonitrile and the polymers in chloroform. The π-π^* transitions (220-350 nm) are notably different due to the difference in co-substituent. Also, extinction coefficients of each of the polymers show a difference compared to the SMA, it is possible that the change in environment could alter this; however, the most likely reason is that the molecular weight of the complex may not be exact, as is often the problem with polyphosphazenes (see Chapter 5).

The 2,6-di(pyridine-2-yl)pyridine-4(1*H*)-onate (OTerpy) based complexes—$[Ru(L^1)_2](PF_6)_2$, $[Ru(L^1)(Terpy)](PF_6)_2$, $[Ru(L^1)(PhTerpy)](PF_6)_2$, $[Ru(L^{1P})(Terpy)](PF_6)_2$ and $[Ru(L^{1P})(PhTerpy)](PF_6)_2$—also displayed the characteristic MLCT bands associated with $[Ru(Terpy)_2]^{2+}$ complexes (see Figure 6.3.1.2). However, they displayed a greater range of λ_{max} (474–490 nm) than the OPhTerpy complexes. The larger differences occurred because there is a greater variation in electron-withdrawing effects of the terpy substituents. This effect was larger for these complexes than OPhTerpy, because the terpy centre was isolated due to the phenyl spacer. $[Ru(L^1)(PhTerpy)](PF_6)_2$ has a 485 nm λ_{max} showing that the MLCT is dominated by the PhTerpy group. $[Ru(L^1)(Terpy)](PF_6)_2$ has a 477 nm λ_{max} red shifted by 3 nm relative to $[Ru(Terpy)_2](PF_6)_2$[34], suggesting that the phosphazene is acting as an electron-withdrawing group. The electron-withdrawing effect was greatly enhanced for $[Ru(L^1)_2](PF_6)_2$ because two electron-withdrawing substituents were attached.

Unlike $[Ru(L^{2P})(Terpy)]Cl_2$ and $[Ru(L^{2P})(PhTerpy)]Cl_2$ the polymer analogues $[Ru(L^{1P})(Terpy)]Cl_2$ and $[Ru(L^{1P})(PhTerpy)]Cl_2$ are red shifted compared to that of the SMA. This suggests that a $[Ru(Terpy)_2]^{2+}$ complex is formed, but the environment has changed enough to alter the electronic spectra. As observed with the OPhTerpy complexes, a variation between the SMA extinction coefficients and the polymers was seen; again, possibly due to the typical errors associated with the molecular weight of the polymer.

Finally, significant differences occur for the π-π^* (220-350 nm) bands of the polymers relative to the SMA. As for the OPhTerpy based complexes, the OTerpy based polymers have a different ratio and type of co-substituent to that of the SMA.

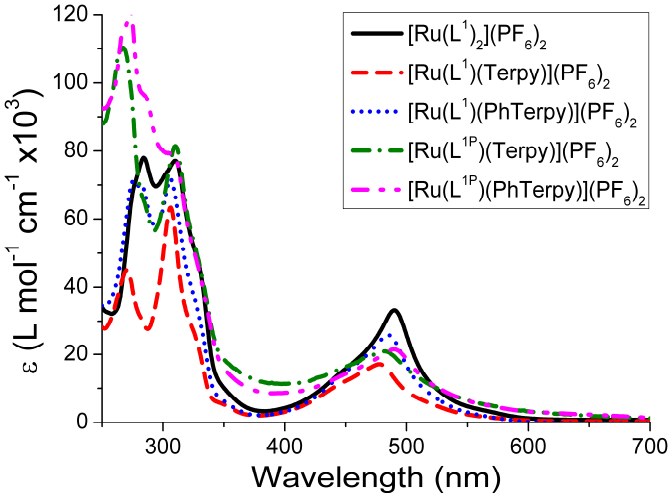

Figure 6.3.1.3 Electronic absorbance spectra of the compounds. OTerpy based complexes $[Ru(L^1)_2](PF_6)_2$, $[Ru(L^1)(Terpy)](PF_6)_2$, $[Ru(L^1)(PhTerpy)](PF_6)_2$, $[Ru(L^{1P})(Terpy)]Cl_2$ and $[Ru(L^{1P})(PhTerpy)]Cl_2$.

Table 6.3.1.2 Extinction coefficients of MLCT bands for the OTerpy based complexes.

Complex	λ_{max} / nm (ε / 10^3 L mol^{-1} cm^{-1})
$[Ru(Terpy)_2](PF_6)_2$ [a 34]	474 (10)
$[Ru(L^1)_2](PF_6)_2$ [a]	490 (33)
$[Ru(L^1)(Terpy)](PF_6)_2$ [a]	477 (17)
$[Ru(L^1)(PhTerpy)](PF_6)_2$ [a]	485 (26)
$[Ru(L^{1P})(Terpy)]Cl_2$ [b]	482 (21)
$[Ru(L^{1P})(PhTerpy)]Cl_2$ [b]	490 (21)

Recorded in: [a] acetonitrile and [b] chloroform.

6.3.2 Ruthenium(II) (2,6-di{1*H*-benzimidazol-2-yl}pyridine)(2,2':6',2"-terpyridine) complexes

Each of the ruthenium(II) (2,6-di{1*H*-benzimidazol-2-yl}pyridine)(2,2':6',2"-terpyridine) $[Ru(bbp)(Terpy)]^{2+}$ complexes—$[Ru(L^3)(Terpy)](PF_6)_2$, $[Ru(L^3)(PhTerpy)](PF_6)_2$, $[Ru(L^1)(bbp)](PF_6)_2$ and $[Ru(L^2)(bbp)](PF_6)_2$—exhibit MLCT transitions at 479–489 nm (see Figure 6.3.2.1), red shifted 0–4 nm from those observed for non-phosphazene analogues ($[Ru(bbp)(Terpy)](ClO_4)_2$[22] and $[Ru(bbp)(MePhTerpy)](PF_6)_2$[35]) (see Table 6.3.2.1). The small differences are associated with the electron-withdrawing effects of the phosphazene.

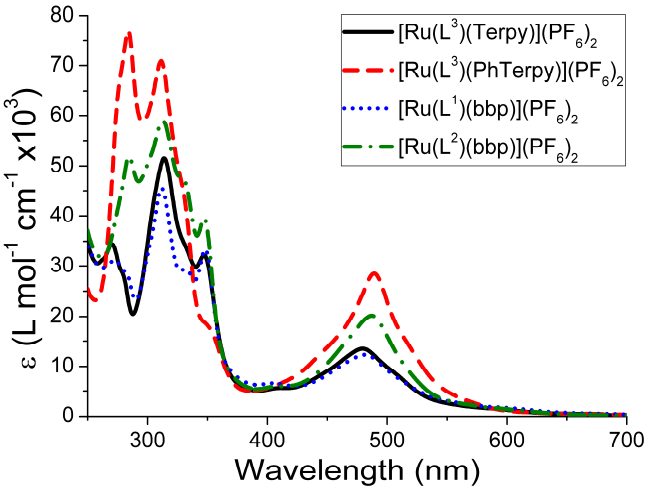

Figure 6.3.2.1 Electronic absorbance spectra of the compounds; bbp based complexes $[Ru(L^3)(Terpy)](PF_6)_2$, $[Ru(L^3)(PhTerpy)](PF_6)_2$, $[Ru(L^1)(bbp)](PF_6)_2$ and $[Ru(L^2)(bbp)](PF_6)_2$.

DFT calculations indicate small contributions to the MLCT orbitals from the phosphazene ring for $[Ru(L^3)(Terpy)](PF_6)_2$, $[Ru(L^3)(PhTerpy)](PF_6)_2$ and $[Ru(L^1)(bbp)](PF_6)_2$. However, calculations of $[Ru(L^2)(bbp)](PF_6)_2$ show no such contribution; this is again due to the presence of the phenyl spacer separating the phosphazene and complex centre (see Appendix E), an example orbitals of $[Ru(L^3)(Terpy)]^{2+}$ and $[Ru(L^2)(bbp)]^{2+}$ are shown in Figure 6.3.2.2.

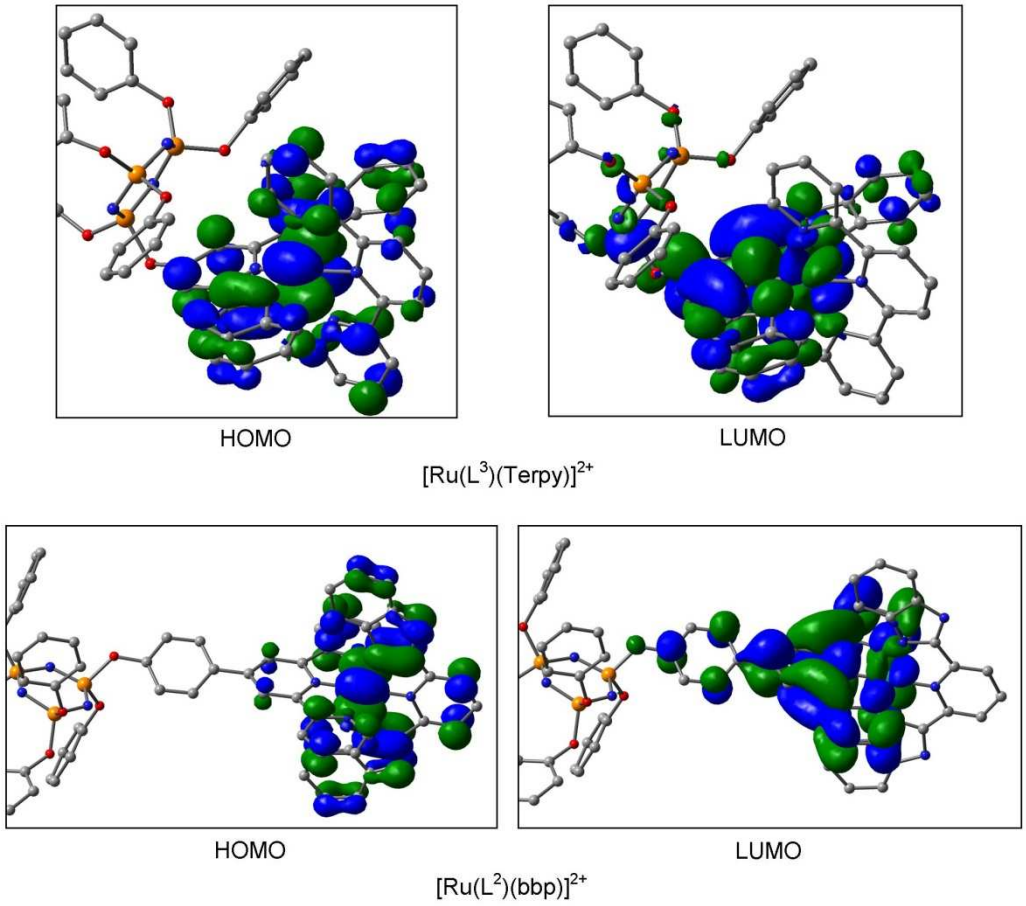

Figure 6.3.2.2 HOMO and LUMO orbitals of $[Ru(L^3)(Terpy)]^{2+}$ and $[Ru(L^2)(bbp)]^{2+}$.

The polymeric complexes $[Ru(L^{3P})(Terpy)]Cl_2$ and $[Ru(L^{3P})(PhTerpy)]Cl_2$ displayed a low signal-to-noise ratio showing that at 5% substitution of Obbp UV/Vis spectroscopy became impractical.

Each of the small molecule complexes was systematically deprotonated by the addition of triethylamine (NEt_3). As the complexes were deprotonated the MLCT λ_{max} was red shifted (see Table 6.3.2.1), e.g. $[Ru(L^3)(Terpy)](PF_6)_2$: 479 nm (0 eq NEt_3) → 499 nm (1 eq NEt_3) → 508 nm (2 eq NEt_3). By comparison to DFT models and literature the species formed with 1eq of NEt_3 is likely to be the mono-protonated complex previously observed by Mondal.[22] Upon the further addition of NEt_3 the completely deprotonated species was formed. However, the MLCT band for eq $NEt_3 \geq 2$ remains broader than observed in similar literature examples (see Figure 6.3.2.1) and is likely

due to an equilibrium being formed between the completely and mono-deprotonated complexes. This occurs because a weaker base (NEt_3) was used. The equilibria could be shifted by using a much stronger base, but such a base would likely hydrolyse the phosphazene in the process.

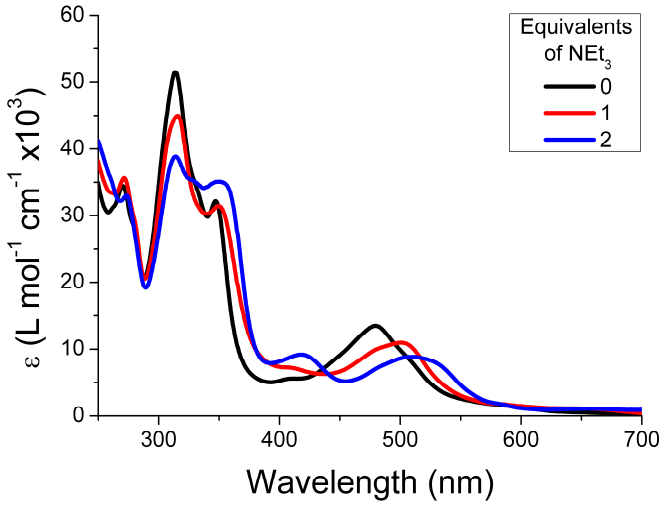

Figure 6.3.2.2 Electronic spectra of $[Ru(L^3)(Terpy)](PF_6)_2$ as NEt_3 was sequentially added to the solution.

Table 6.3.2.1 Peak MLCT absorption wavelengths and extinction coefficient of the bbp based complexes as NEt_3 was sequentially added.

Complex	**λ_{max} / nm (ε / 10^3 L mol^{-1} cm^{-1}) eq NEt_3**		
	0 eq	**1 eq**	**2 eq**
$[Ru(L^3)(Terpy)](PF_6)_2$	479 (13)	499 (11)	417 (9), 508 (9)
$[Ru(L^3)(PhTerpy)](PF_6)_2$	489 (20)	492 (19)	420 (11), 494 (15)
$[Ru(L^1)(bbp)](PF_6)_2$	481 (12)	488 (10)	408 (8), 509 (8)
$[Ru(L^2)(bbp)](PF_6)_2$	487 (20)	504 (9)	409 (8), 509 (8)

6.3.3 Ruthenium(II) (2,6-di{1*H*-pyrazol-1-yl}pyridine)(2,2':6',2"-terpyridine) complexes

Each of the bpp based small molecule complexes—$[Ru(L^4)(Terpy)](PF_6)_2$, $[Ru(L^4)(PhTerpy)](PF_6)_2$, $[Ru(L^1)(bpp)](PF_6)_2$ and $[Ru(L^2)(bpp)](PF_6)_2$—displayed an MLCT band at 432–440 nm, with a second less distinguished MLCT band at 355–387 nm observed for $[Ru(L^4)(Terpy)](PF_6)_2$ and $[Ru(L^4)(PhTerpy)](PF_6)_2$ (see Figure 6.3.3.1). In similar literature examples, the highest energy MLCT was concluded to primarily involve the bpp ligand and the lower energy one primarily involved the terpy ligand.[24,26] However, for both $[Ru(L^4)(Terpy)](PF_6)_2$ and $[Ru(L^4)(PhTerpy)](PF_6)_2$ the two MLCT bands are broader than the other literature examples. DFT calculations suggest the orbitals involved in the transitions do not solely involve individual ligands; rather, they involve varying contributions from each ligand—the mixture of ligand orbitals causes the broadening of the observed peaks (see Appendix E).

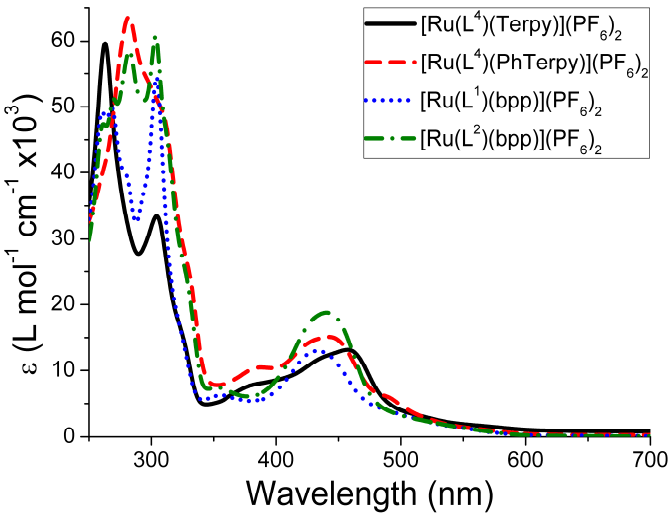

Figure 6.3.3.1 Electronic absorbance spectra of the compounds: $[Ru(L^4)(Terpy)](PF_6)_2$, $[Ru(L^4)(PhTerpy)](PF_6)_2$, $[Ru(L^1)(bpp)](PF_6)_2$ and $[Ru(L^2)(bpp)](PF_6)_2$.

Table 6.3.3.1 Extinction coefficients of MLCT bands for the bpp based complexes recorded in acetonitrile.

Complex	λ_{max} / nm (ε / 10^3 L mol^{-1} cm^{-1})
[Ru((Me)$_4$bpp)(MePhTerpy)](PF$_6$)$_2$[26]	359 (3), 457 (10)
[Ru(bpp-Ph-bpp)(Terpy)](PF$_6$)$_2$[24]	366 (9), 443 (25)
[(Terpy)Ru(bpp-Ph-bpp)Ru(Terpy)](PF$_6$)$_4$[24]	371 (13), 453 (45)
[Ru(L^4)(Terpy)](PF$_6$)$_2$	387 (8), 458 (13)
[Ru(L^4)(PhTerpy)](PF$_6$)$_2$	387 (10), 443 (15)
[Ru(L^1)(bpp)](PF$_6$)$_2$	357 (6), 440 (15)
[Ru(L^2)(bpp)](PF$_6$)$_2$	355 (7), 432 (19)

The polymer analogues [Ru(L^{4P})(Terpy)]Cl$_2$ and [Ru(L^{4P})(PhTerpy)]Cl$_2$ displayed significantly different absorbance spectra to that of the SMA. They had a broad absorbance with no clearly defined peaks, these differences suggest a different in coordination behaviour. In previous work by Ruben *et al.*,[24] it was necessary to remove a chloride from the ruthenium trichloride complex prior to reacting it with the bpp in order to produce a clean product. This was not necessary for the synthesis of the SMA as the reaction was performed in neat methanol; however, the polymer reactions were performed in a solution of methanol and THF (50:50). As a result the solution had a lower boiling temperature; in addition, the absence of anion metathesis may have resulted in the reactions not going to completion.

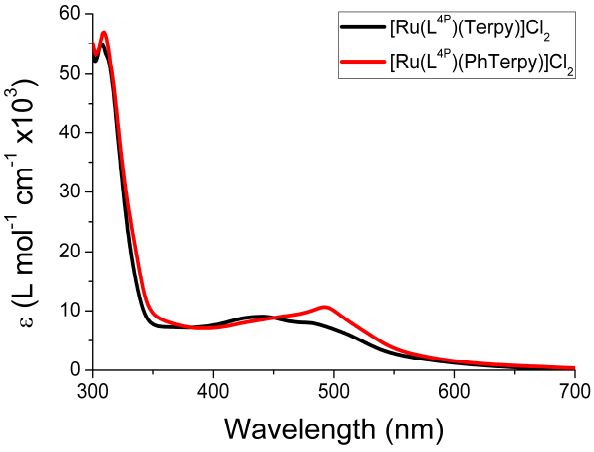

Figure 6.3.3.2 Electronic absorbance spectra of the compounds [Ru(L^{4P})(Terpy)]Cl$_2$ and [Ru(L^{4P})(PhTerpy)]Cl$_2$.

Based on comparisons to other similar complexes in the literature it was suggested that a chloride remains coordinated to the ruthenium atom and only one of the pyrazole rings coordinates (see Figure 6.3.3.3).[36-40]

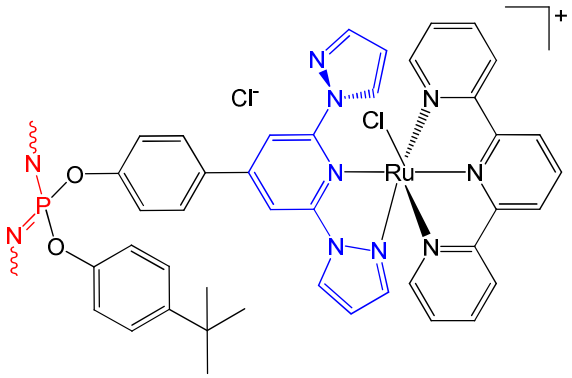

Figure 6.3.3.3 Proposed complex formed on the polymer.

Time dependent-DFT (TD-DFT) calculations were used to simulate the electronic spectra of the proposed structure. This provides a fair approximation for the recorded spectra, but is not conclusive. The coordination behaviour of $[Ru(L^{4P})(Terpy)]Cl_2$ and $[Ru(L^{4P})(Terpy)]Cl_2$ was further investigated using rR spectroscopy (see Section 6.4.3).

6.4 Vibrational spectroscopy

6.4.1 Ruthenium(II) bis(2,2':6',2"-terpyridine) complexes

The IR data collected was dominated by aromatic ring deformations and thus were similar for all of the compounds, therefore rR proved to be a more definitive technique. This is because it shows selective enhancement of modes within active chromophores, where the excitation wavelength (λ_{ex}) determines which particular chromophores are being probed. Each of the complexes were excited by wavelengths at 488 and 514 nm, which correspond to the MLCT band. TD-DFT calculations indicated that these transitions are localised on the $[Ru(Terpy)_2]^{2+}$ centres. Both 488 and 514 nm excitations displayed similar results; as such, the 488 nm excitations are shown in Figure 6.4.1.1 and all vibrational data is tabulated and assigned using DFT calculations in Appendix E. Both sets of complexes displayed vibrational modes that were localised predominantly on the $[Ru(Terpy)_2]^{2+}$ centre. However, each of them displayed low energy vibrational modes (below 675 cm^{-1}) delocalised through the entire ligand including the phosphazene ring.

The heteroleptic complexes displayed additional bands due to the asymmetry of the complex. This is reflected in the splitting of the bands at 1329, 1351 cm^{-1} ($[Ru(L^1)(Terpy)]^{2+}$) compared to 1356 cm^{-1} ($[Ru(L^1)_2]^{2+}$), and 1473, 1487 cm^{-1} ($[Ru(L^1)(Terpy)]^{2+}$) compared to 1473 cm^{-1} ($[Ru(L^1)_2]^{2+}$) corresponding to the terpy stretching modes (see an example in Figure 6.4.1.1). It is much less significant for the OPhTerpy based complexes only showing a difference at 1329 cm^{-1}. This is due to the phenyl group localising the enhanced vibrational modes. The effect is increased for the OTerpy based complexes, due to the greater difference in mass and electronegativity.

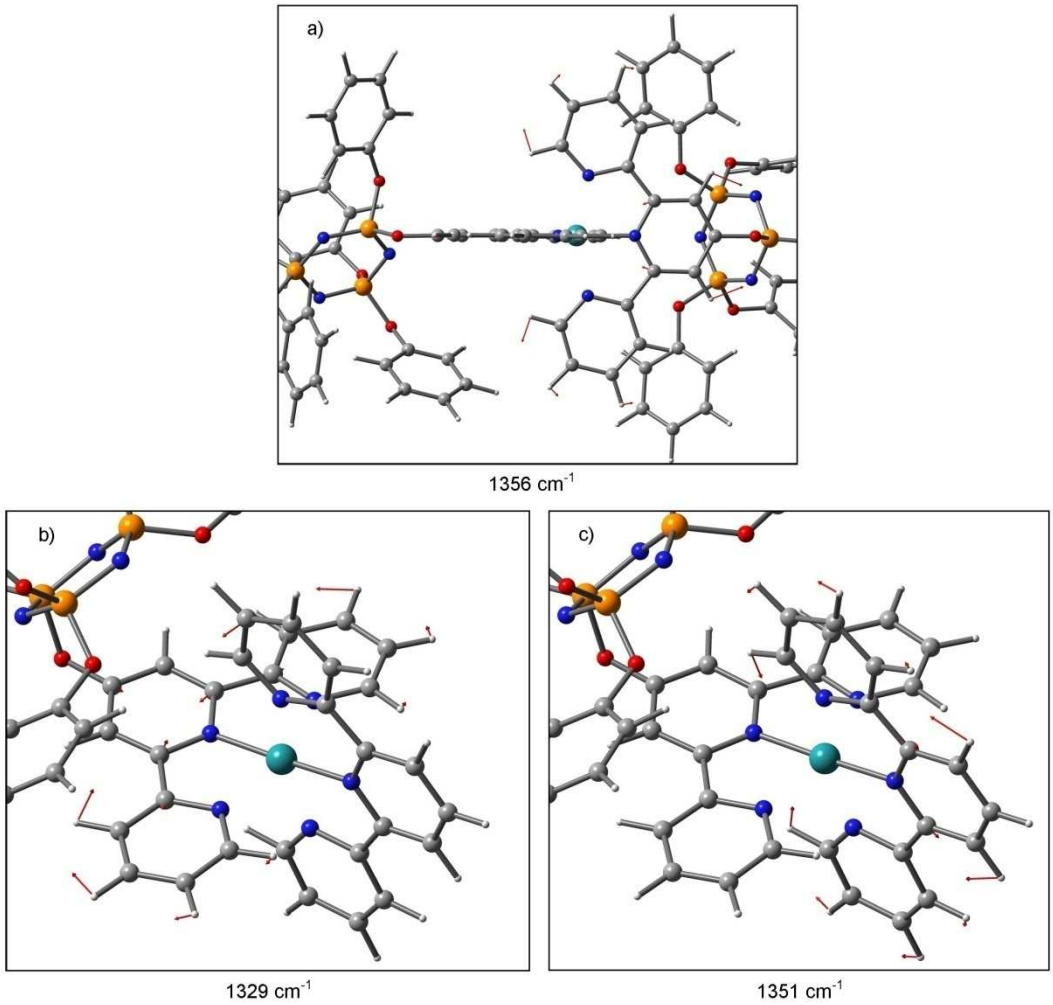

Figure 6.4.1.1 Example of additional vibrational modes due to the asymmetry of a heteroleptic complex (red arrows indicate displacement vectors). a) $[Ru(L^1)_2]^{2+}$, b) and c) $[Ru(L^1)(Terpy)]^{2+}$.

The polymeric complexes displayed almost identical rR spectra to the SMA (see Figure 6.4.1.2), small differences can be attributed to the use of chloroform rather than acetonitrile, due to solubility. However, the spectra are so similar that it can be determined that the ruthenium coordination sites on the polymer are very similar to that of the SMA.

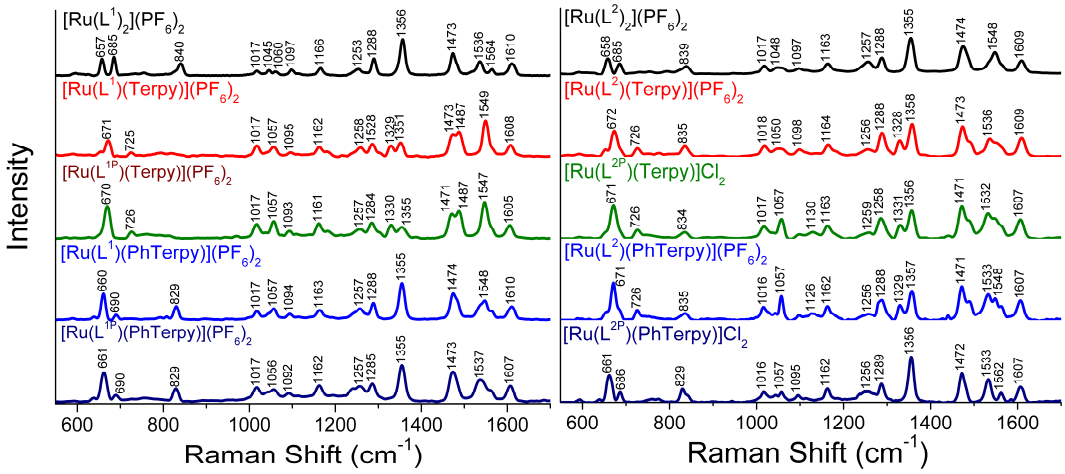

Figure 6.4.1.2 rR spectra recorded using a 488 nm excitation. Left: OTerpy based complexes $[Ru(L^1)_2](PF_6)_2$, $[Ru(L^1)(Terpy)](PF_6)_2$, $[Ru(L^1)(PhTerpy)](PF_6)_2$, $[Ru(L^{1P})(Terpy)]Cl_2$ and $[Ru(L^{1P})(PhTerpy)]Cl_2$. Right: OPhTerpy based complexes $[Ru(L^2)_2](PF_6)_2$, $[Ru(L^2)(Terpy)](PF_6)_2$, $[Ru(L^2)(PhTerpy)](PF_6)_2$, $[Ru(L^{2P})(Terpy)]Cl_2$ and $[Ru(L^{2P})(PhTerpy)]Cl_2$.

6.4.2 Ruthenium(II) (2,6-di{1*H*-benzimidzol-2-yl}pyridine)(2,2':6',2"-terpyridine) complexes

Each of the complexes containing bbp moiety displayed rR enhancement of the vibrational modes associated with the $[Ru(bbp)(Terpy)]^{2+}$ centre as the λ_{ex} of 514 and 488 nm was used corresponding to the MLCT band (see Figure 6.4.2.1).

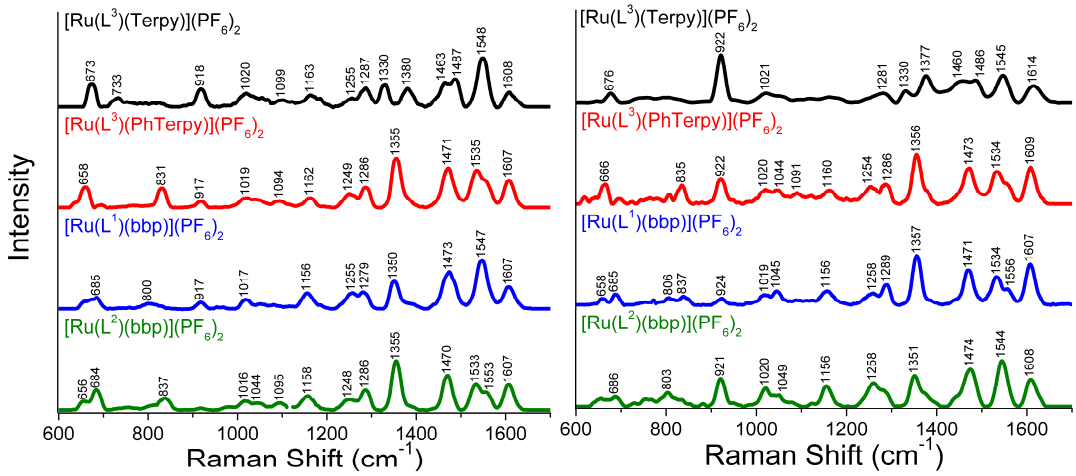

Figure 6.4.2.1 rR spectra of $[Ru(L^3)(Terpy)](PF_6)_2$, $[Ru(L^3)(PhTerpy)](PF_6)_2$, $[Ru(L^1)(bbp)](PF_6)_2$ and $[Ru(L^2)(bbp)](PF_6)_2$. Left: λ_{ex} 488 nm, right: λ_{ex} 514 nm.

For each of the complexes the phosphazene was shown to contribute to the delocalised vibrational modes below 845 cm^{-1}; however, it has no involvement in the higher energy vibrations simulated by DFT calculations (see Appendix E).

The spectra of the complexes can be divided into two groups:

i) $[Ru(L^3)(Terpy)](PF_6)_2$ and $[Ru(L^1)(bbp)](PF_6)_2$;

ii) $[Ru(L^3)(PhTerpy)](PF_6)_2$ and $[Ru(L^2)(bbp)](PF_6)_2$.

Each of the groups have similar spectra, except those in group ii display differences associated with the phenyl terpy group, e.g. at 1535 and 1533 cm^{-1} respectively (see Figure 6.4.2.2).

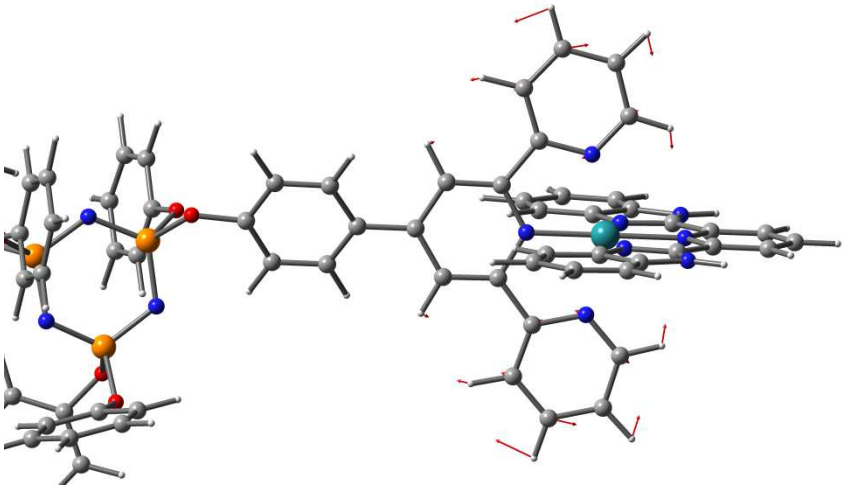

Figure 6.4.2.2 1533 cm^{-1} vibrational mode of $[Ru(L^2)(bbp)]^{2+}$ (red arrows indicate displacement vectors).

The polymers displayed poor signal-to-noise ratios due to the low ratio of the metal centre relative to the rest of the polymer. This means that rR could not be used to definitively determine whether the same complex had formed on the polymer.

rR spectra for the complexes were recorded as NEt_3 was sequentially added. Excitation wavelength of 488 and 514 nm were used as these both corresponded to the MLCT band. Shown in Figure 6.4.2.3 are the spectra for $[Ru(L^3)(Terpy)](PF_6)_2$ recorded with λ_{ex} 488 nm (data collected with λ_{ex} 514 nm is included in Appendix E).

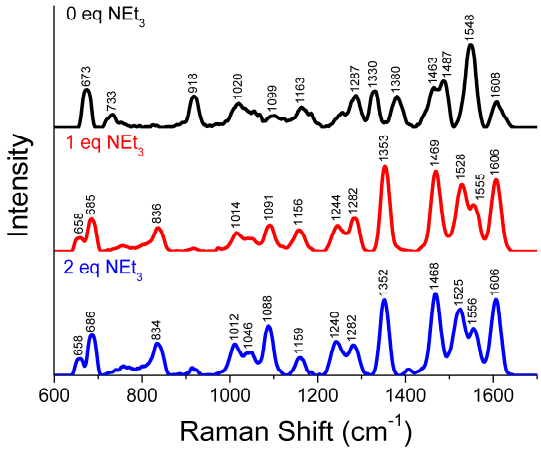

Figure 6.4.2.3 rR spectra of $[Ru(L^3)(Terpy)](PF_6)_2$ as triethylamine was sequentially added to the solution.

As NEt_3 was added, the vibrational bands associated with Obbp displayed both a shift and splitting. The shifts occurred because the removal of a proton from the imidazole ring made it a stronger σ-donor. This is best illustrated for the asymmetric N_{bbp}-Ru-N_{Terpy} stretching mode shifts from 1091 cm^{-1} (1 eq NEt_3) and 1088 cm^{-1}(2 eq NEt_3). The shift occurs because additional electron density is available to the metal centre resulting in the axial bonds increasing in length. 0 eq NEt_3 displayed the symmetric N_{bbp}-Ru-N_{Terpy} stretching mode but did not display the asymmetric one.

Splitting of the peaks could have occurred by two possible means:

i) the mono-protonated complex has both a protonated and a deprotonated imidazole ring, each has a different vibrational mode associated.

ii) an equilibrium is formed between the mono-protonated and completely deprotonated complexes (see Figure 6.4.2.3).

The observed splitting is likely a combination of both options as the DFT predicted spectra are similar for both species making a distinction between the two unreliable. The equilibrium occurs because of the use of a weak base.

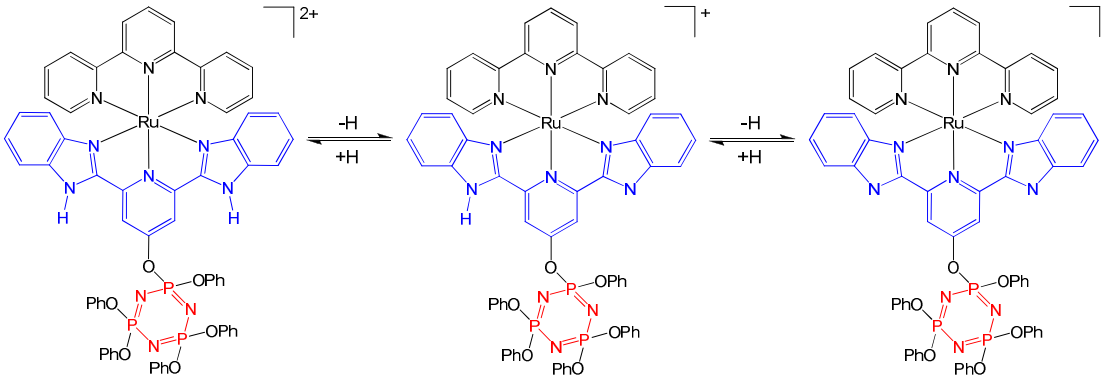

Figure 6.4.2.4 Equilibria formed by $[Ru(L^3)(Terpy)](PF_6)_2$.

6.4.3 Ruthenium(II) (2,6-di{1*H*-pyrazol-1-yl}pyridine)(2,2':6',2"-terpyridine) complexes

As with the previous complexes, IR provided limited information about each system; however, by using rR with a λ_{ex} of 488 and 514 nm, the $[Ru(bpp)(Terpy)]^{2+}$ centres could be specifically probed due to the MLCT band.

Due to the phenyl spacer for $[Ru(L^4)(Terpy)](PF_6)_2$, $[Ru(L^4)(PhTerpy)](PF_6)_2$ and $[Ru(L^2)(bpp)](PF_6)_2$ only the most delocalised low energy vibrations include the phosphazene ring. However, for $[Ru(L^1)(bpp)](PF_6)_2$ the complex is directly attached to the phosphazene ring resulting in an increased contribution by the phosphazene ring to the low energy vibrations (below 700 cm^{-1}) as indicated by DFT simulations (see Appendix E). The spectra are very similar with the only differences being associated with the vibrations of the terpy unit (see Figure 6.4.3.1).

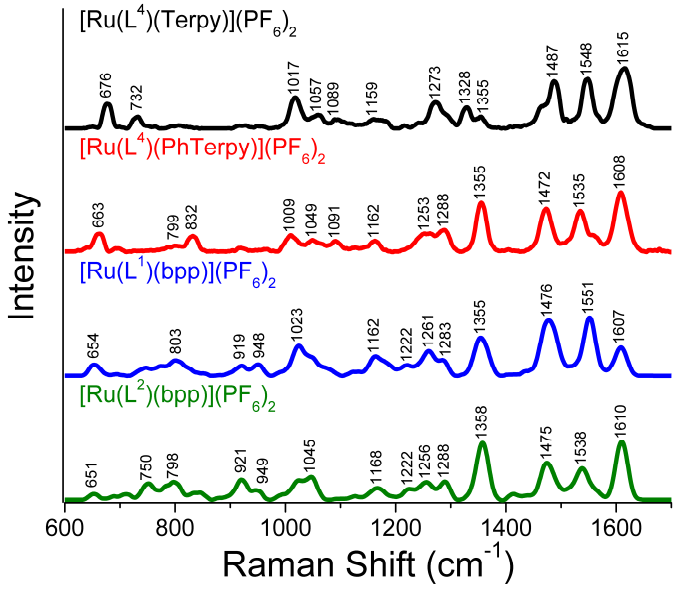

Figure 6.4.3.1 rR λ_{ex} 514 nm. $[Ru(L^4)(Terpy)](PF_6)_2$, $[Ru(L^4)(PhTerpy)](PF_6)_2$, $[Ru(L^1)(bpp)](PF_6)_2$ and $[Ru(L^2)(bpp)](PF_6)_2$.

The electronic spectra of the polymer analogues ($[Ru(L^{4P})(Terpy)]Cl_2$ and $[Ru(L^{4P})(PhTerpy)]Cl_2$) showed that the coordination sites are different to that of the SMAs ($[Ru(L^4)(Terpy)](PF_6)_2$ and $[Ru(L^4)(PhTerpy)](PF_6)_2$), see Section 6.3.3. It was suggested by comparison to DFT models that a [Ru(bpp)(Terpy)Cl]Cl species was formed, as the reaction could not go to completion under the reaction conditions.

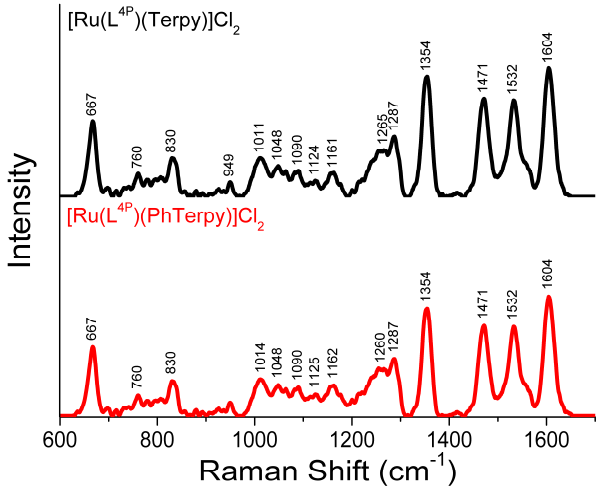

Figure 6.4.3.2 λ_{ex} 514 nm. $[Ru(L^{4P})(Terpy)]Cl_2$ and $[Ru(L^{4P})(PhTerpy)]Cl_2$.

An assignment of the polymer rR can be made based on the proposed structure in Figure 6.3.3.3. However, due to the inaccuracies observed for the other complexes it is not possible to confirm that this is the species formed.

While a comparison to a DFT model does not definitively identify the complex, ultimately, even if the suggested model proves to be incorrect, the rR confirms the polymer is behaving in a different manner to the SMA and therefore would be unsuitable to act as a grafting group to polyphosphazenes.

6.5 Electrochemistry

6.5.1 Ruthenium(II) bis(2,2':6',2"-terpyridine) complexes

Each of the small molecule complexes containing L^1 displayed a reversible metal-based oxidation (Ru^{II}/Ru^{III}) between 0.928 and 0.976 V and ligand based reductions between −1.490 and −1.656 V (all the relevant data is given in Table 6.5.1.1). The oxidation potentials are slightly higher than that of $[Ru(Terpy)_2](PF_6)_2$ (0.918 V)[16]. This increase shows that the phosphazene ether linkage acts as an electron-withdrawing group, consistent with the observations made for the electronic absorbance spectra of the complexes.

Table 6.5.1.1. Electrochemical data for the small molecule complexes, parentheses indicate ΔE_p (mV).

Complex	$E_{½ox}$/V Ru^{II}/Ru^{III}	$E_{½red}$/V 1st redn.	$E_{½red}$/V 2nd redn.
$[Ru(L^1)_2](PF_6)_2$	0.976 (61)	-1.490 (irr)	-1.705 (irr)
$[Ru(L^1)(Terpy)](PF_6)_2$	0.963 (92)	-1.656 (irr)	-1.788 (irr)
$[Ru(L^1)(PhTerpy)](PF_6)_2$	0.928 (73)	-1.522 (irr)	-1.765 (irr)
$[Ru(L^2)_2](PF_6)_2$	0.996 (86)	-1.530 (irr)	-1.760 (irr)
$[Ru(L^2)(Terpy)](PF_6)_2$	0.930 (53)	-1.640 (irr)	-1.769 (irr)
$[Ru(L^2)(PhTerpy)](PF_6)_2$	0.933 (47)	-1.494 (irr)	-1.702 (irr)

Using Formula 6.1.2.1 it was possible to determine the σ^+ value for the phosphazene ether bond for the following complexes: $[Ru(L^1)_2](PF_6)_2$ ($\sigma^+ = 0.13$), $[Ru(L^1)(Terpy)](PF_6)_2$ ($\sigma^+ = 0.15$) and $[Ru(L^1)(Terpy)](PF_6)_2$ ($\sigma^+ = -0.04$). The wide variation in values could be attributed to the confirmation changes occurring in the complex when oxidised. Such behaviour has been observed in the literature,[16] and this is possibly why this method is only used on relatively simple complexes.

The replacement of L^1 in $[Ru(L^1)_2](PF_6)_2$ by L^2 to give $[Ru(L^2)_2](PF_6)_2$ varies the $E_{½ox}$ (Ru^{II}/Ru^{III}) from 0.976 V to 0.996 V which is counterintuitive as L^1 is expected to be more electron withdrawing than L^2 given that the red shift in the MLCT bands of these complexes was less than the L^1 based complexes. This is possibly due to conformation

changes taking place either at the complex core or via interactions with the surrounding complex (see Figure 6.5.1.1). However, in the heteroleptic L^1 based complexes, $[Ru(L^1)(Terpy)](PF_6)_2$ and $[Ru(L^1)(PhTerpy)](PF_6)_2$, the $E_{½ox}$ decreases from 0.963 V to 0.928 V respectively consistent with the phenyl group of PhTerpy being a stronger electron donor group than the hydrogen of terpy. A comparison of $E_{½ox}$ for $[Ru(L^1)(Terpy)](PF_6)_2$ and $[Ru(L^1)(Terpy)](PF_6)_2$ is consistent with L^1 having a greater electron-withdrawing ability than L^2.

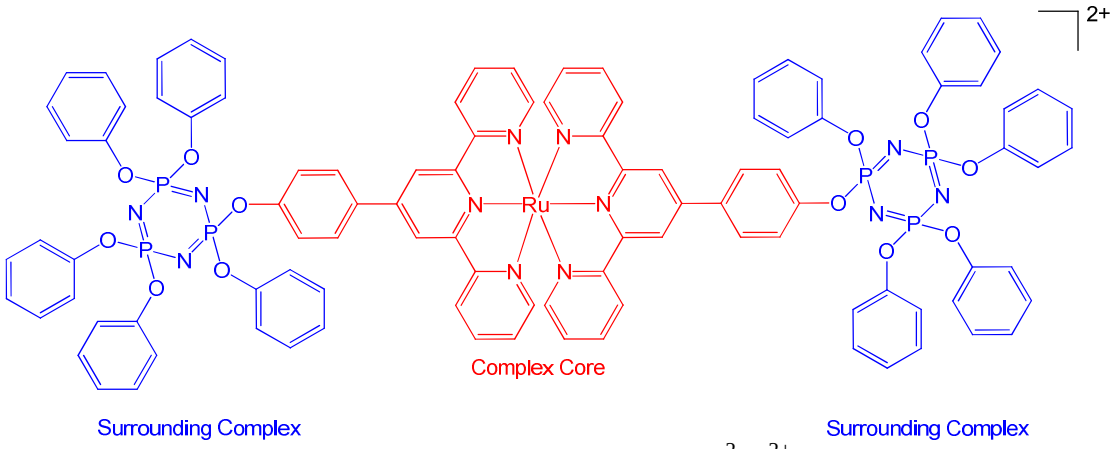

Figure 6.5.1.1 Components of the $[Ru(L^2)_2]^{2+}$ complex.

Reliable electrochemical data could not be obtained for the polymer analogues due to the low conductivity of the solution and the polymer's tendency to form films on the surface of the electrodes.

6.3.2 Ruthenium(II) (2,6-di{1*H*-benzimidazol-2-yl}pyridine)(2,2':6',2"-terpyridine) complexes

Electrochemical data were recorded for each of the $[Ru(bbp)(Terpy)]^{2+}$ based complexes. Each displayed a single oxidation corresponding to the Ru^{II}/Ru^{III} coupling. Two other reductions are also observed corresponding to the reduction of the ligands, although it cannot be unambiguously assigned (see Table 6.3.2.1).

As with the electronic and rR spectroscopy each of the complexes shows a shift in the electrochemical potential to a more negative value as they were deprotonated (see Table 6.3.2.1). The cyclic voltammetry data was collected in neat acetonitrile, as any significant amounts of water caused precipitation, this prevented the determination of pH. In addition, only a weak organic base, triethylamine (NEt_3), could be used because a stronger base would degrade the phosphazene.

Table 6.3.2.1 Electrochemical data for the $[Ru(bbp)(Terpy)]^{2+}$ based complexes, parentheses indicate ΔE_p (mV).

Complex	0 Eq NEt_3			2 Eq NEt_3		
	Ru^{II}/Ru^{III} (V)	**1^{st} redn. (V)**	**2^{nd} redn. (V)**	**Ru^{II}/Ru^{III} (V)**	**1^{st} redn. (V)**	**2^{nd} redn. (V)**
$[Ru(L^3)(Terpy)]$ $(PF_6)_2$	1.171 (65)	-0.896 (irr)	-1.454 (irr)	0.521 (53)	-1.056 (irr)	-1.398 (irr)
$[Ru(L^3)(PhTerpy)]$ $(PF_6)_2$	1.133 (34)	-1.082 (irr)	-1.456 (irr)	0.494 (85)	-1.077 (irr)	-1.306 (irr)
$[Ru(L^1)(bbp)]$ $(PF_6)_2$	1.140 (38)	-0.897 (irr)	-1.193 (irr)	0.591 (89)	-1.069 (irr)	-1.324 (irr)
$[Ru(L^2)(bbp)]$ $(PF_6)_2$	1.018 (83)	-0.881 (irr)	-1.584 (irr)	0.522 (64)	-1.427 (irr)	-1.539 (irr)

As NEt_3 was sequentially added the complexes changed from the protonated ligand to deprotonated ligand complex. This corresponded to an anodic shift, which occurs

because the deprotonated imidazole is a stronger σ-donor than the protonated one; as a result the metal centre required a lower oxidation potential (see Figure 6.5.2.1). Although the electronic spectra displays the presence of the signally deprotonated species, no intermediate step was observed that would support the involvement of the singly protonated complex. This behaviour has been observed for similar examples by Bond[41] and Mondal[22].

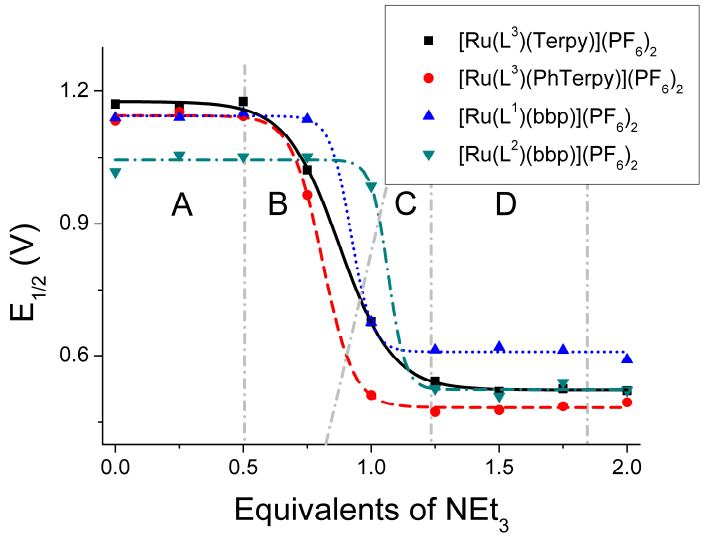

Figure 6.5.2.1 $E_{½}$ of the Ru^{II}/Ru^{III} oxidation vs. NEt_3 addition for: $[Ru(L^3)(Terpy)](PF_6)_2$ (black squares), $[Ru(L^3)(PhTerpy)](PF_6)_2$ (red circles), $[Ru(L^1)(bbp)](PF_6)_2$ (blue triangles) and $[Ru(L^2)(bbp)](PF_6)_2$ (green diamonds).

The complexes displayed the same dependence on solution basicity as the hydrogen substituted complexes. Therefore, it was assumed that the same processes occur; these are described in the following:[22]

For section A the process only involves the protonated complex and a single electron transfer:

$$[Ru^{II}(Terpy)(LH_2)]^{2+} \leftrightarrow [Ru^{III}(Terpy)(LH_2)]^{3+} + e^-$$

For section B a one electron/proton process occurs:

$$[Ru^{II}(Terpy)(LH_2)]^{2+} \leftrightarrow [Ru^{III}(Terpy)(LH)]^{+} + H^+ + e^-$$

For section C a two proton/one electron process occurs:

$$[Ru^{II}(Terpy)(LH_2)]^{2+} \leftrightarrow [Ru^{III}(Terpy)(L)]^{+} + 2H^{+} + e^{-}$$

For section D a one electron/proton process occurs:

$$[Ru^{II}(Terpy)(LH)]^{+} \leftrightarrow [Ru^{III}(Terpy)(L)]^{+} + H^{+} + e^{-}$$

Finally beyond 2 equivalents NEt_3 the process only involves the deprotonated species; however, the distinction difference was not obvious; therefore, it may be that a weak base such as NEt_3 is not strong enough to completely deprotonate the complex and an equilibrium is formed as suggested in the vibrational study.

In the protonated state, $[Ru(L^3)(Terpy)](PF_6)_2$, $[Ru(L^3)(PhTerpy)](PF_6)_2$ and $[Ru(L^1)(bbp)](PF_6)_2$ had a similar Ru^{II}/Ru^{III} oxidation potential (1.133 – 1.171 V), higher than the unsubstituted analogue ($[Ru(bbp)(Terpy)](ClO_4)_2$, 0.99 V). This is because both L^3 and L^1 have the ligands (Obbp and OTerpy respectively) directly attached to the phosphazene ring, which is electron-withdrawing. $[Ru(L^2)(bbp)](PF_6)_2$ (1.018 V) has a lower oxidation potential due to the phenyl spacer reducing the electron-withdrawing effects.

Once deprotonated, $[Ru(L^3)(Terpy)](PF_6)_2$, $[Ru(L^3)(PhTerpy)](PF_6)_2$ and $[Ru(L^2)(bbp)](PF_6)_2$ have similar oxidation potentials (0.494 – 0.522 V) but $[Ru(L^1)(bbp)](PF_6)_2$ (0.591 V) has a higher one. The difference occurs because the deprotonated imidazole rings are less aromatic and more electron-donating, reducing the effects of the phosphazene making the oxidation potential similar to the phenyl spacer. However, $[Ru(L^1)(bbp)](PF_6)_2$ has the OTerpy ligand directly attached.

6.5.3 Ruthenium(II) (2,6-di{1*H*-pyrazol-1-yl}pyridine)(2,2':6',2"-terpyridine) complexes

The electrochemical data for the $[Ru(bpp)(Terpy)]^{2+}$ complexes were collected using cyclic voltammetry. Each of the complexes displayed a reversible oxidation, associated with the Ru^{II}/Ru^{III} couple, and two irreversible reductions associated with the ligands although these cannot be unambiguously assigned (see Table 6.5.3.1).

The Ru^{II}/Ru^{III} oxidation potential of $[Ru(L^1)(bpp)](PF_6)_2$ (0.993 V) was slightly lower than that of $[Ru(L^1)(Terpy)](PF_6)_2$ (0.963 V) but $[Ru(L^2)(bpp)](PF_6)_2$ (0.939 V) was almost the same as $[Ru(L^2)(Terpy)](PF_6)_2$ (0.930 V). $[Ru(L^4)(Terpy)](PF_6)_2$ (0.961 V) and $[Ru(L^4)(PhTerpy)](PF_6)_2$ (0.994 V) both displayed a slight increase in potential relative to $[Ru(L^2)(Terpy)](PF_6)_2$ (0.930 V) and $[Ru(L^2)(PhTerpy)](PF_6)_2$ (0.933 V).

Bpp is more electron-donating than terpy; as such, the potentials should be lower. However, as demonstrated by the ruthenium-bis-terpy complexes, conformational changes occurring upon oxidation could have a larger effect than substituents. This is further exhibited by the use of PhTerpy instead of Terpy for $[Ru(L^4)(PhTerpy)](PF_6)_2$. Phenyl groups are weakly electron-donating, therefore the oxidation potential should have been $\leq [Ru(L^4)(Terpy)](PF_6)_2$, yet an increase was shown, and this is likely associated with conformation changes.

Not many $[Ru(bpp)(Terpy)]^{2+}$ based complexes have been reported and few electrochemical studies have been performed. Compared to the reported values of the complexes studied by Ruben *et al*.,[24] these have high oxidation potentials largely due to the electron-withdrawing effects of the phosphazene ether unit.

Table 6.5.3.1 Electrochemical data for the small molecule complexes, parentheses indicate ΔE_p (mV).

Complex	$E_{½ox}$/V Ru^{II}/Ru^{III}	$E_{½red}$/V 1st redn.	$E_{½red}$/V 2nd redn.
$[Ru(L^4)(Terpy)](PF_6)_2$	0.961(89)	-1.552 (irr)	-1.806 (irr)
$[Ru(L^4)(PhTerpy)](PF_6)_2$	0.994 (92)	-1.580 (irr)	-1.803 (irr)
$[Ru(L^1)(bpp)](PF_6)_2$	0.933 (82)	-1.647 (irr)	-1.741 (irr)
$[Ru(L^2)(bpp)](PF_6)_2$	0.939 (90)	-1.569 (irr)	-1.759 (irr)

As observed for the other polymers reliable electrochemical data could not be obtained for the polymers $[Ru(L^{4P})(Terpy)]Cl_2$ and $[Ru(L^{4P})(PhTerpy)]Cl_2$.

6.6 Conclusion

The electronic, vibrational and electrochemical properties of both the polymers and their SMA were determined to access the viability of using these ruthenium complexes to attach other groups.

Through the use of electronic absorbance and rR spectroscopy it was determined that the complex cores of the $[Ru(Terpy)_2]^{2+}$ based polymers ($[Ru(L^{1P})(Terpy)]Cl_2$, $[Ru(L^{1P})(PhTerpy)]Cl_2$, $[Ru(L^{2P})(Terpy)]Cl_2$ and $[Ru(L^{2P})(PhTerpy)]Cl_2$) match that of the SMA ($[Ru(L^{1})(Terpy)]Cl_2$, $[Ru(L^{1})(PhTerpy)]Cl_2$, $[Ru(L^{2})(Terpy)]Cl_2$ and $[Ru(L^{2})(PhTerpy)]Cl_2$ respectively). The λ_{max} of the MLCT bands were red shifted relative to the hydrogen-substituted species due to the phosphazene ether bond being slightly electron-withdrawing.

A consistent σ^+ value for the phosphazene ether unit could not be determined, but each of the complexes displayed cathodic shifts of their oxidation potentials, consistent with the phosphazene ether unit being electron-withdrawing.

The $[Ru(bbp)(Terpy)]^{2+}$ based complexes ($[Ru(L^{3})(Terpy)](PF_6)_2$, $[Ru(L^{3})(PhTerpy)](PF_6)_2$, $[Ru(L^{1})(bbp)](PF_6)_2$ and $[Ru(L^{2})(bbp)](PF_6)_2$) displayed the electron-withdrawing effects observed with the $[Ru(Terpy)_2]^{2+}$ based complexes, slightly red shifting λ_{max} and increasing the oxidation potential. Due to only a 5% loading, the polymer produced poor physical data, therefore it was not possible to assess if the polymer had the same metal centres as the SMA.

Despite having a phosphazene attached to the $[Ru(bbp)(Terpy)]^{2+}$ based complexes, they displayed the same dependence of the basicity of the solution. As NEt_3 was added the imidazole protons were systematically removed, causing a red shift of the MLCT band, providing evidence that both the singly and completely deprotonated species were present. Even at high concentrations of NEt_3, rR suggested the presence of both the singly and completely deprotonated species existing in equilibrium, likely due to the use of a weak base.

The oxidation potential of the complexes displayed the same dependence on the bascity; as the complex was deprotonated the oxidation potential greatly decreased due to the

increased σ-donor behaviour of the imidazole nitrogen. However, the pure deprotonated species were not observed due to the use of the weak base.

The $[Ru(bpp)(Terpy)]^{2+}$ based complexes displayed a difference between the polymer ($[Ru(L^{4P})(Terpy)]Cl_2$ and ($[Ru(L^{4P})(Terpy)]Cl_2$) and the SMA ($[Ru(L^4)(Terpy)](PF_6)_2$, $[Ru(L^4)(PhTerpy)](PF_6)_2$, $[Ru(L^1)(bpp)](PF_6)_2$ and $[Ru(L^4)(Terpy)](PF_6)_2$). The SMA displayed the characteristic MLCT bands and matches the predicted vibrational spectra. However, the polymers have a broad absorbance in the MLCT band range and the rR spectra did not match that of the SMA. A possible explanation for this is that under the reaction conditions it did not go to completion, leaving a chloride attached to the ruthenium atom.

For the purposes of using a metal complex to attach groups to a polyphosphazene the terpy substituents are ideal. The polymers reacted in an identical fashion to the SMA with only slight variations in physical behaviour due to the grafted phosphazene. As only a 5% loading of bbp could be achieved for the polymer, the data obtained was poor, and the inability to vary the ratios of the substituent also makes it unsuitable for grafting other groups.

Bpp polymers proved to be unsuitable for the grafting groups given that the same complex was not formed on the polymer as the SMA. However, their absorbance spectra should warrant further investigation for a range of other potential applications.

6.7 References

1. Eloi, J. C.; Chabanne, L.; Whittell, G. R.; Manners, I. *Materials Today* **2008**, *11*, 28-36.

2. Whittell, G. R.; Manners, I. *Advanced Materials* **2007**, *19*, 3439-3468.

3. Leung, A. C. W.; Chong, J. H.; MacLachlan, M. J. *Macromolecular Symposia* **2003**, *196*, 229-234.

4. Wong, W. Y. *Dalton Transactions* **2007**, 4495-4510.

5. Hjelm, J.; Constable, E. C.; Figgemeier, E.; Hagfeldt, A.; Handel, R.; Housecroft, C. E.; Mukhtar, E.; Schofield, E. *Chemical Communications* **2002**, 284-285.

6. Schubert, U. S.; Schmatloch, S.; Precup, A. A. *Designed Monomers and Polymers* **2002**, *5*, 211-221.

7. Wong, C. T.; Chan, W. K. *Advanced Materials* **1999**, *11*, 455-459.

8. Schubert, U. S.; Hofmeier, H. *Macromolecular Rapid Communications* **2002**, *23*, 561-566.

9. Gohy, J. F.; Lohmeijer, B. G. G.; Schubert, U. S. *Chemistry-A European Journal* **2003**, *9*, 3472-3479.

10. Hofmeier, H.; Schubert, U. S. *Chemical Communications* **2005**, 2423-2432.

11. Suen, H. F.; Wilson, S. W.; Pomerantz, M.; Walsh, J. L. *Inorganic Chemistry* **1989**, *28*, 786-791.

12. Puntoriero, F.; Campagna, S.; Stadler, A. M.; Lehn, J. M. *Coordination Chemistry Reviews* **2008**, *252*, 2480-2492.

13. Sauvage, J. P.; Collin, J. P.; Chambron, J. C.; Guillerez, S.; Coudret, C.; Balzani, V.; Barigelletti, F.; Decola, L.; Flamigni, L. *Chemical Reviews* **1994**, *94*, 993-1019.

14. Medlycott, E. A.; Hanan, G. S. *Chemical Society Reviews* **2005**, *34*, 133-142.

15. Hansch, C.; Leo, A.; Taft, R. W. *Chemical Reviews* **1991**, *91*, 165-195.

16. Constable, E. C.; Thompson, A.; Tocher, D. A.; Daniels, M. A. M. *New Journal of Chemistry* **1992**, *16*, 855-867.

17. Constable, E. C.; Neuburger, M.; Smith, D. R.; Zehnder, M. *Inorganica Chimica Acta* **1998**, *276*, 359-365.

18. Constable, E. C.; Harverson, P.; Smith, D. R.; Whall, L. *Polyhedron* **1997**, *16*, 3615-3623.

19. Singh, A.; Mondal, B. *Inorganica Chimica Acta* **2010**, *363*, 3145-3150.

20. Nazeeruddin, M. K.; Muller, E.; Humphry-Baker, R.; Vlachopoulos, N.; Gratzel, M. *Journal of the Chemical Society-Dalton Transactions* **1997**, 4571-4578.

21. Bhaumik, C.; Das, S.; Saha, D.; Dutta, S.; Baitalik, S. *Inorganic Chemistry*, *49*, 5049-5062.

22. Singh, A.; Chetia, B.; Mobin, S. M.; Das, G.; Iyer, P. K.; Mondal, B. *Polyhedron* **2008**, *27*, 1983-1988.

23. Haga, M.; Takasugi, T.; Tomie, A.; Ishizuya, M.; Yamada, T.; Hossain, M. D.; Inoue, M. *Dalton Transactions* **2003**, 2069-2079.

24. Schramm, F.; Chandrasekar, R.; Zevaco, T. A.; Rudolph, M.; Gorls, H.; Poppitz, W.; Ruben, M. *European Journal of Inorganic Chemistry* **2009**, 53-61.

25. Zhu, X. J.; Holliday, B. J. *Macromolecular Rapid Communications*, *31*, 904-909.

26. Laemmel, A. C.; Collin, J. P.; Sauvage, J. P. *Comptes Rendus De L Academie Des Sciences Serie Ii Fascicule C-Chimie* **2000**, *3*, 43-49.

27. Halcrow, M. A. *Coordination Chemistry Reviews* **2005**, *249*, 2880-2908.

28. Jameson, D. L.; Blaho, J. K.; Kruger, K. T.; Goldsby, K. A. *Inorganic Chemistry* **1989**, *28*, 4312-4314.

29. Tomasi, J.; Mennucci, B.; Cammi, R. *Chemical Reviews* **2005**, *105*, 2999-3093.

30. M. J. Frisch; G. W. Trucks; H. B. Schlegel; G. E. Scuseria; M. A. Robb; J. R. Cheeseman; G. Scalmani; V. Barone; B. Mennucci; G. A. Petersson, *et al.*; A.1 ed.; Gaussian, Inc: Wallingford CT, **2009**.

31. Dennington, R.; Keith, T.; Millam, J.; Version 5 ed.; Semichem Inc.: Shawnee Mission KS, **2009**.

32. Johnson, R. D.; April 2010 ed.; NIST Computational Chemistry Comparison and Benchmark Database: **2010**.

33. Horvath, R.; Otter, C. A.; Gordon, K. C.; Brodie, A. M.; Ainscough, E. W. *Inorganic Chemistry* **2010**, *49*, 4073-4083.

34. Amouyal, E.; Mouallembahout, M.; Calzaferri, G. *Journal of Physical Chemistry* **1991**, *95*, 7641-7649.

35. Bhaumik, C.; Das, S.; Saha, D.; Dutta, S.; Baitalik, S. *Inorganic Chemistry* **2010**, *49*, 5049-5062.

36. Sivakumar, R.; Marcelis, A. T. M.; Anandan, S. *Journal of Photochemistry and Photobiology A-Chemistry* **2009**, *208*, 154-158.

37. Philippopoulos, A. I.; Terzis, A.; Raptopoulou, C. P.; Catalano, V. J.; Falaras, P. *European Journal of Inorganic Chemistry* **2007**, 5633-5644.

38. Stergiopoulos, T.; Karakostas, S.; Falaras, P. *Journal of Photochemistry and Photobiology A-Chemistry* **2004**, *163*, 331-340.

39. Chryssou, K.; Catalano, V. J.; Kurtaran, R.; Falaras, P. *Inorganica Chimica Acta* **2002**, *328*, 204-209.

40. Catalano, V. J.; Kurtaran, R.; Heck, R. A.; Ohman, A.; Hill, M. G. *Inorganica Chimica Acta* **1999**, *286*, 181-188.

41. Bond, A. M.; Haga, M. *Inorganic Chemistry* **1986**, *25*, 4507-4514.

Chapter 7

Coordination site characterisation of the iron(II) metallo polymer and the physical behaviour of both the cyclotriphosphazene and polyphosphazene iron(II) metallo polymer

7.0 Abbreviations used in Chapter 7

SCO	Spin Crossover
HS	High Spin
LS	Low Spin
SQUID	Superconducting Quantum Interference Device
δ_{iso}	Isomer shift
ΔE_Q	Quadrupole Coupling
UV/Vis	Ultraviolet Visible
MLCT	Metal Ligand Charge Transfer
FT-IR	Fourier Transform Infrared
rR	Resonance Raman
DFT	Density Function Theory
OPhTerpy	4-(2,6-di{pyridin-2-yl}-pyridine-4-yl)phenolate
OTerpy	2,6-bis(2-pyridyl)-4(1*H*)-pyridonate
Obpp	2,6-bis(benzimidazole)-4(1*H*)-pyridonate
OPhbpp	4-(2,6-(pyraz-1-yl)-pyridine-4-yl)phenolate
Terpy	2,2':6',2''-terpyridine
PhTerpy	2,6-di(pyridin-2-yl)-4-phenylpyridine
bbp	2,6-di(1*H*- benzimidazol-2-yl)pyridine
bpp	2,6-di(1*H*-pyrazol-1-yl)pyridine

7.1 Introduction

Spin Crossover (SCO) is a phenomenon that results in a metal complex changing its magnetism because of an external influence, such as heat[1], pressure[2], and light[3]. This only occurs in the first row transition metals with a cation electron configuration of 4–7 d electrons. The most common example of this is iron(II)[4] which has a d^6 electron configuration; the complex changes from diamagnetic to paramagnetic (see Figure 7.1). There are other examples of Fe(III)[5], Co(II)[6], Mn(II), Mn(III), Co(II), and Fe(III)[7] complexes undergoing SCO; however, each of these examples are paramagnetic for both spin states.

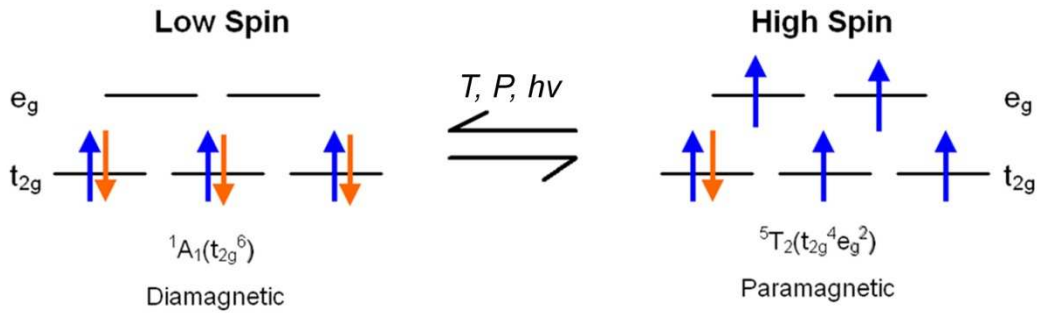

Figure 7.1 Schematic view of SCO for an octahedral Fe(II) complex.

7.1.1 Preparative concepts

In order to explain thermally induced spin crossover, some basic concepts must be covered first. To make things simple, an octahedral iron(II) complex will be used as the example. The d electrons of any transition metal can be broken down into two groups based on their symmetry: the t_{2g} orbitals, consisting of the d_{xy}, d_{xz}, d_{yz}, all non-bonding orbitals; and the e_g orbitals, consisting of $d_{x^2-y^2}$ and d_{z^2}, which are weakly anti-bonding.

Using ligand field theory, if these two groups of orbitals have an energy difference (10Dq or Δ_o) less than the electron pairing energy (Π), the electrons will follow Hunds rule[8] (this occurs with weak field ligands) and will occupy all available orbitals before pairing, resulting in a paramagnetic complex. However, if 10Dq > Π, the electrons will remain paired in the t_{2g} orbitals (this occurs with strong field ligands), see Figure 7.1.1.1.

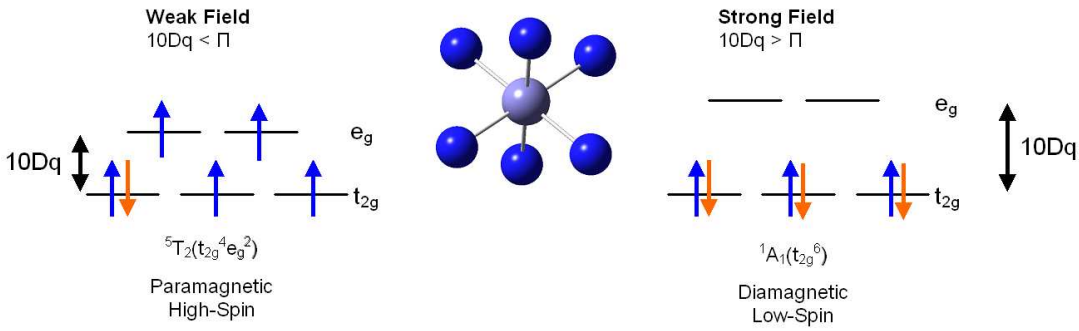

Figure 7.1.1.1 The electron arrangement of strong field and weak field complexes.

By varying the metal ion, the ligand, and the metal-ligand distance 10Dq can be altered, as described by Jørgenson's spectrochemical series[8].

7.1.2 The occurrence of thermal SCO

As an iron(II) SCO complex changes from LS to HS, the M-L bond length typically increases by ~0.2 Å. This is a result of electron density being removed from the non-bonding orbitals and going into the weakly anti-bonding orbitals. The change in bond length helps explain how SCO occurs. Since the change in bond length is not gradual, it suggests that there are two potential wells: one corresponding to LS, and the other to HS (see Figure 7.1.2.1). A vibrational mode links these two potential wells; more specifically, the symmetrical stretching mode.[1]

A simplistic view of it consists of a two-level thermally accessible system (see Figure 7.1.2.1), the population of electron density follows a distribution. This distribution is affected by two variables: Δr_{HL} (the difference in the bond lengths) and ΔE_{HL} (the difference in potential energy wells). These factors are both governed by the metal ion and the ligands attached.

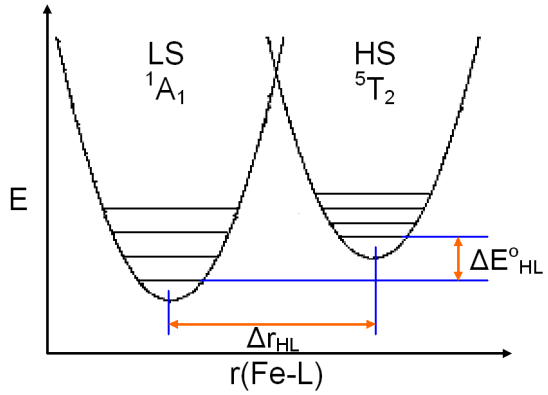

Figure 7.1.2.1 Potential wells of the HS and LS states.

The dependence of thermal SCO on temperature proves that the process is driven by entropy. The initial assumption was that entropy was generated by the increase of degeneracy formed by the change of electron spin, as has been displayed in the previous models. However, due to Jahn-Teller effects much of the degeneracy is lost. The largest contribution comes from the change in vibrational mode density due to the almost 0.20 Å difference in bond lengths between the HS and LS states.[9]

10Dq also changes as the spin state changes because of the bond lengthening. This change results in a much smaller energy gap, with a ratio difference of approximately 1.7 (see Formula 7.1.2.1). The change in 10Dq can result in a dramatic colour change, e.g. from purple to colourless for aromatic N donor ligands bound to Fe(II).

$$\frac{10Dq^{LS}}{10Dq^{HS}} = \left(\frac{r_{HS}}{r_{LS}}\right)^n \qquad \textbf{Formula 7.1.2.1}$$

($10D_q$ is the respective energy gap, r_{HS} is the bond length for the HS state, r_{LS} is the bond length for the LS state, and n is typically 5–6).[10]

7.1.3 The occurrence of optical excitation

While similar principles apply for optically induced SCO, the mechanism is quite different.[3] In the case of an optical excitation, there is an inversion of the population of states. It is possible to have no occupancy in the low spin state while the high spin state is fully occupied, in contrast to distribution observed for thermal excitation.

The electrons of a complex can be excited into the ligand's orbitals (a metal ligand charge transfer). As the electron relaxes, it can fall into either the HS or LS potential wells and, as the complex absorbs more photons, the entire population can be converted to HS (see Figure 7.1.3.1).

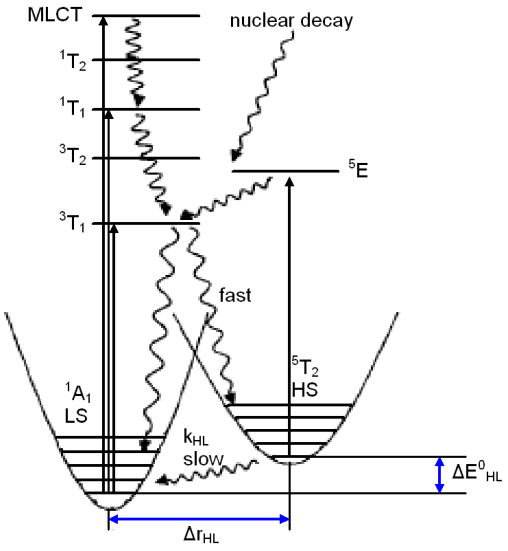

Figure 7.1.3.1 A schematic mechanism for optical excitation.

At room temperature, the relaxation of the complex from HS to LS is within the range of nano-micro seconds. However, Decurtins[11] discovered that, at cryogenic temperatures, the relaxation could be considerably slowed to such a degree that it could take weeks to occur. This meant that, at these temperatures, the electron was essentially trapped in the HS state – this phenomenon was called Light Induced Excited State Spin Trapping (LIESST).

Two of the most thoroughly studied systems are ferrous tris(1-propyl-tetrazole) bis-tetrafluoroborate $[Fe(Ptz)_3](BF_4)_2$[12] and ferrous tris-2-(amino-methyl)pyridine bis-chloride $[Fe(Pic)_3]Cl_2 \cdot EtOH$[13], both were known to display thermal SCO with respective SCO temperatures of 130 K and 120 K. For light excitation, each of these complexes was cooled to 50 K, then excited with light. This resulted in a bleaching of the crystals' colour – evident in the absorption spectra, where the peaks that relate to the low spin state are reduced when bleached (see Figure 7.1.3.2).

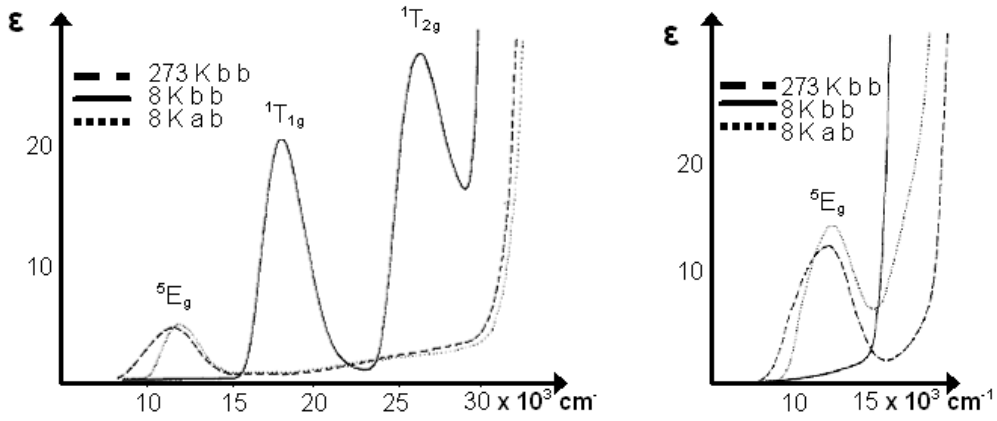

Figure 7.1.3.2 UV/Vis spectra for the before bleaching (b b) and after bleaching (a b) Left: $[Fe(Ptz)_3](BF_4)_2$.[12] Right: $[Fe(Pic)_3]Cl_2 \cdot EtOH$.[13]

The SCO behaviour is also displayed in the magnetic moment of the complex. As the complex is cooled, the magnetic moment decreases. However, when excited by radiation, the magnetic moment dramatically jumps.[12] Magnetic measurements were not performed for $[Fe(Pic)_3]Cl_2 \cdot EtOH$ crystals, which were irreversibly fractured on bleaching.[13] However, $[Fe(Ptz)_3](BF_4)_2$ was stable during the bleaching process, possibly as a result of the cooperativity effects, allowing the magnetic moment to be measured (see Figure 7.1.3.3).[12]

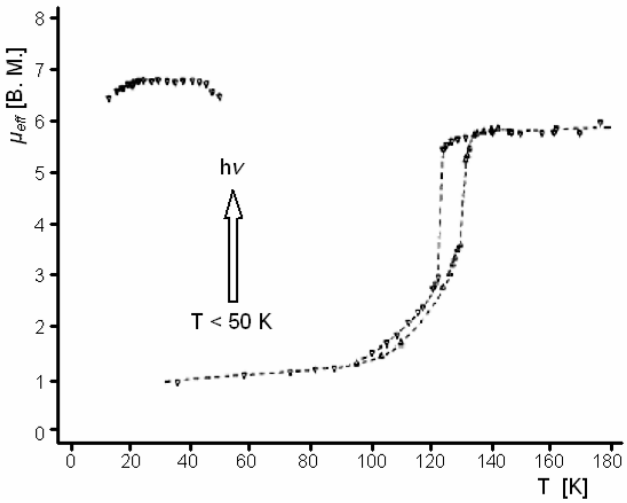

Figure 7.1.3.3 Magnetic moment vs. temperature, and magnetic moment before bleaching and after-bleaching for $[Fe(Ptz)_3](BF_4)_2$.[12]

At low temperatures, the excited state will remain stable almost indefinitely, but once warmed the vibration of the molecule will relax the complex to its ground state once again. The stability of the excited state is dependent on the ligand field strength with weaker field ligands: if ΔE^{o}_{HL} is small, the excited state lifetime is increased; having a larger Δr_{HL} also increases the excited state lifetime.[14] Furthermore, it was discovered that by exciting the HS complex with a lower energy photon the complex could be relaxed to the LS state. This was the result of the lower energy photon providing sufficient energy to cross the energy barrier between the HS and LS energy well, without providing sufficient energy to cause further excitation to the HS state. This is of particular interest for optical electronics as it is a system that can be turned ‘on’ and ‘off’ optically.

7.1.4 Spin crossover grafted polymers

SCO materials have long been suggested to be useful for memory storage or atomic switches, but they are typically crystals or powders limiting their use for applications. To this end SCO gels,[15,16] liquid crystals,[17-21] resins,[22] Langmuir-Blodgett films[23-25] and hetero-polymer blends[26,27] have been used. The gels, liquid-crystals, resins and Langmuir-Blodgett films are all made by taking an existing SCO complex and substituting it with groups such as long alkyl chains making the material amorphous. The heterogeneous polymers are made by blending a polymer such as PMMA with an SCO complex, allowing it to be spread by an assortment of techniques. The properties of this material were enhanced by including hydrogen donors and acceptors on the metal complex and the polymer backbone, resulting in the metal complex being hydrogen-bonded to the polymer backbone,[28] which is not removed by solvent (see Figure 7.1.5.1).

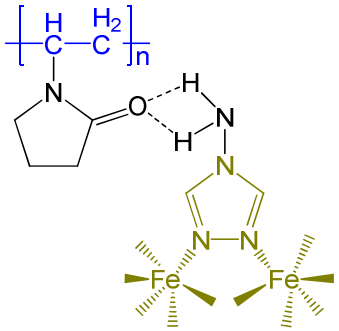

Figure 7.1.5.1 Example of an iron triazole complex hydrogen-bonded to a polymer backbone.[28]

SCO grafted polymers are a rare field, there are two examples of attempts of producing SCO polymers: thiophene and terthiophene. At this stage these examples can only be regarded as attempts because the polymers were not characterised (e.g. molecular weight). The thiophene and terthiophene examples were based on an iron(III) quinoline-salene (OQSal) unit (see Figure 7.1.5.2).[29,30] It was shown that the polymer analogue had similar magnetic behaviour to the small molecule analogue. Because the molecular weights were not reported, it is difficult to determine if a polymer or oligomer had been formed, although the electronic spectrum did provide a rough indication as to how long the polymer is.

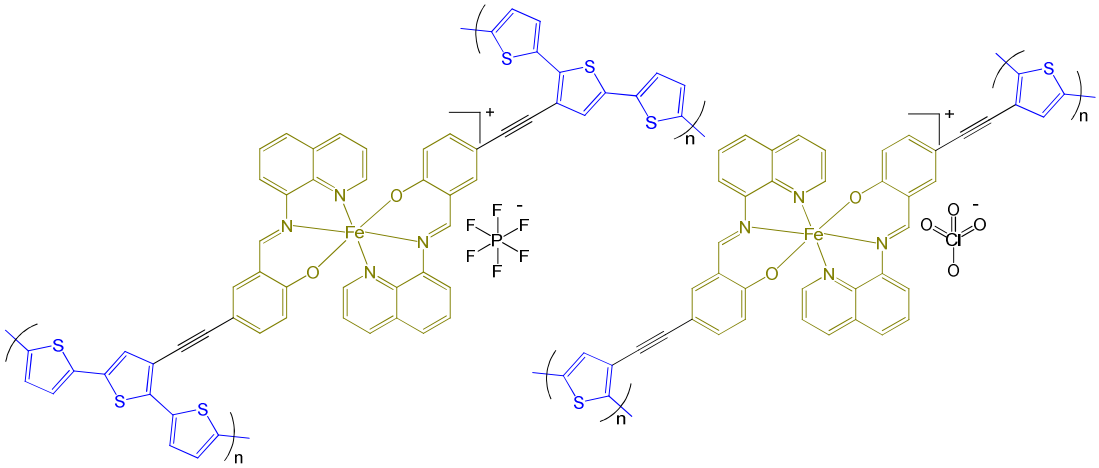

Figure 7.1.5.2 Left: Terthiophene OQSal based metallo-complex. Right: Thiophene OQSal based metallo-complex.[29,30]

7.2 Detection methods

7.2.1 Magnetic susceptibility

There are a variety of methods that have been used to identify SCO systems. As this is a magnetic phenomenon, the most extensively used instruments are magnetometers. Many exist such as Faraday balance, Gouy balance, Foner-type vibrating sample and finally a superconducting quantum interference device (SQUID)[31], which is the most sensitive and versatile magnetometer. SQUIDs are based on Josephson junctions, which are formed by two superconductors being separated by a non-conducting barrier. In the absence of magnetic flux the current is distributed equally between two superconductors; however, once one is induced the current between each of them varies. This difference can be used to determine the magnetic flux. Using this, the magnetic susceptibility of a solid sample can be measured as a function of temperature, pressure and for some systems, light. A SQUID is often used for studying SCO systems because it is able to clearly show the transition from the LS state to the HS state and, in some systems, intermediate states. An example of the magnetic moment versus temperature is shown below in Figure 7.2.1.1. In fact, it is from such a curve that the SCO temperature is determined: it is defined as the temperature at which the sample is half-way between HS and LS.

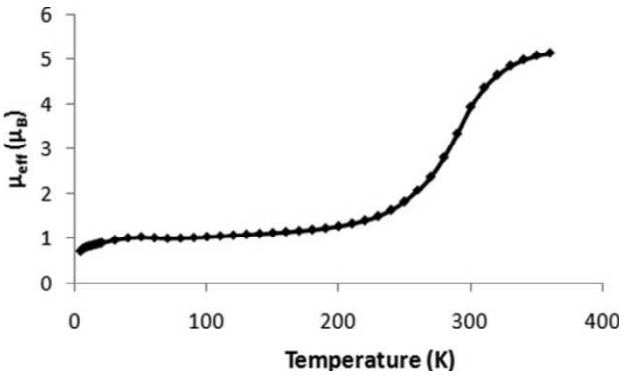

Figure 7.2.1.1 An SCO curve for iron(II) complex of a dipyridyltriazole ligand.[23]

7.2.2 Mössbauer spectroscopy

Another frequently used technique is Mössbauer spectroscopy.[32] This technique uses γ-radiation to excite the nucleus of an atom. In order to achieve measurable results a fluorescence resonance must be achieved.

The energies required to measure the hyperfine interactions are so small they can be achieved using the Doppler effect. This is achieved by oscillating a radiation source at a speed within the range of mm/s. As the energy differences in the nuclei are small the recoil of the photon hitting the nucleus is enough to affect them. Therefore, Mössbauer determined that by measuring the sample in the solid state with low enough energy of γ-rays that the recoil becomes insignificant.

Two key features that can be obtained from the Mössbauer spectra are the isomer shift (δ_{iso}) and the quadrupole coupling (ΔE_Q). These values can be computationally predicted for known structures, therefore they can be compared to the measured data to determine the coordination behaviour, oxidation state, etc.

δ_{iso} occurs because the nucleus and electron charge density (from the 1s-orbital electrons) have a non-zero volume. This causes a coulomb interaction, thereby altering the nuclear energy levels. Thus any changes in the 1s orbital electrons, source or absorber will change the δ_{iso}. The shift cannot be measured directly, therefore it is measured relative to a known absorber, e.g. iron-57 is measured relative to α-iron. As the δ_{iso} is affected by coulombic effects on the 1s orbitals, the oxidation state of a metal can be determined, e.g. Fe^{3+} and Fe^{2+}. The ferrous ions have less s-electrons at the nucleus due to the greater screening of the d-electrons. Thus ferrous ions will have a larger positive δ_{iso} than ferric ions.[32]

ΔE_Q occurs in nuclei with an angular momentum quantum number $I > ½$, this produces a non-spherical charge distribution. This results in a nuclear quadrupole moment. In the presence of an asymmetric electric field (produced by a ligand arrangement) the nuclear energy levels are split. In the case of iron-57 ($I = {}^3/_2$) the excited state splits into two: $m_i \pm ½$ and $m_i \pm {}^3/_2$. As such δ_{iso} can be related to the ligands attached.[32]

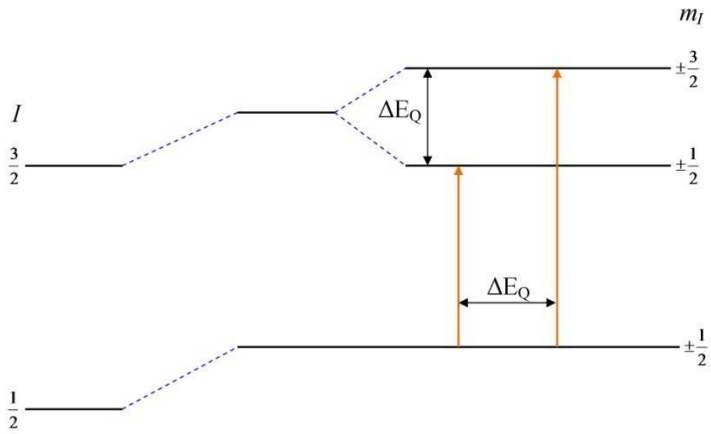

Figure 7.2.2.1 Nuclei energy splitting responsible for quadrapole splitting.

The orbitals can in turn be split further via an external magnetic field, this is called the Zeeman effect; which is not explored for this study.

As both δ_{iso} and ΔE_Q are indirectly dependent on the d-orbital behaviour and bond lengths, both change as the complex crosses over from LS → HS. In addition, if the area of the Mössbauer peaks for the HS and LS species are equal then it is possible to calculate the relative amounts of each species (see Figure 7.2.2.2).

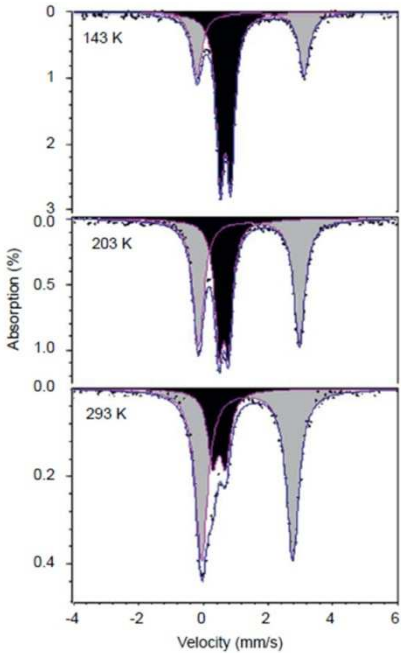

Figure 7.2.2.2 Example Mössbauer spectra of an SCO complex, [Fe(3-Br-phen)$_2$(NCS)$_2$]·0.5MeOH (black = LS, grey = HS).[33]

While this is a versatile and powerful technique it has significant limitations. The relative number of suitable Mössbauer absorption and emission of γ-rays are dependent on the γ-ray energy, therefore the effect is only detected in isotopes with low lying excited states. In order to achieve the resolution required, long lifetime excited states are necessary, greatly restricting the elements and their isotopes that can be detected. Iron-57, cobalt-57 and a small selection of other nuclei satisfy both requirements. As SCO complexes are dominated by iron this provides a powerful technique for analysing SCO.[32]

7.2.3 Ultraviolet/Visible absorption spectroscopy

SQUID and Mössbauer spectroscopies are the two most common methods used to measure the magnetism of the system and the state of the metal centre respectively. However, there are many other methods that are able to measure SCO in systems. Variable-temperature Ultraviolet/Visible absorption spectroscopy (UV/Vis) has been used to monitor the absorption of light specific to the metal centre, i.e. the MLCT and d-d transitions. As the HS state's occupancy increases, the LS state's occupancy decreases, leaving fewer electrons to absorb the light and thereby decreasing absorbance. This is a convenient method for monitoring LIESST, as many UV/visible spectrometers are capable of taking readings as a laser is pulsed – an example is shown in Figure 7.2.3.1 for ferrous tris(2-methyl-1,10-phenanthroline)[34] $[Fe(2\text{-mephen})_3]^{2+}$.

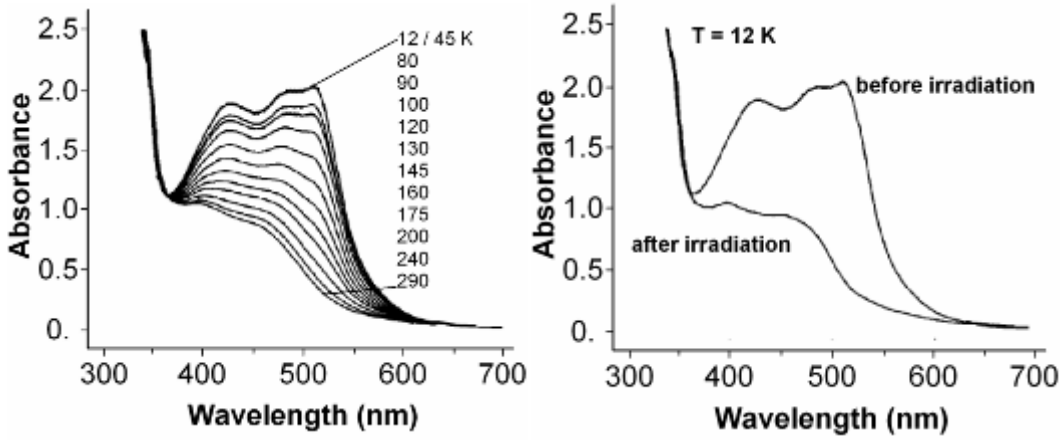

Figure 7.2.3.1 $[Fe(2\text{-mephen})_3]^{2+}$ Left: variable temperature UV/Vis. Right: irradiated sample.[34]

Although a powerful technique, care must be taken to assure SCO and not another process causes the changes in electronic spectra. It is possible for compounds to decay while being heated, that is why it is rare to find studies exclusively using UV/Vis to identify SCO.

7.2.4 Vibrational spectroscopy

Vibrational spectroscopy is also a powerful technique in studying SCO. This is because the bond lengthening associated with the transition results in differences in the vibrational modes associated with the ligand and metal centre.

Three possible techniques are available: infrared (IR) and fourier transform Raman spectroscopy (FT-R) and resonance Raman (rR). IR spectroscopy involves passing IR light through a given sample. As the vibrational energies of the bonds fall within the range of IR (4000 – 400 cm^{-1}), specific vibrational modes will absorb at specific wavelengths. In the case of SCO a disappearance of peaks corresponding to the metal-ligand bonds associated with LS species and the increase of the HS species. See an example in Figure 7.2.4.1.

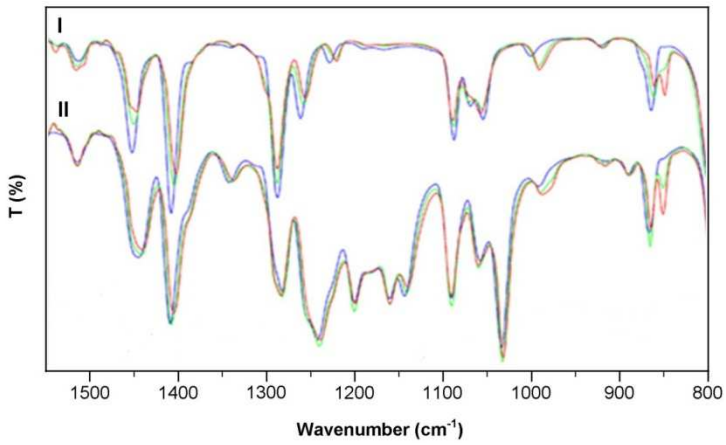

Figure 7.2.4.1 Example IR spectra of SCO compounds. I $[Fe\{HC(pz)_3\}_2]SiF_6$, II $[Fe\{HC(pz)_3\}_2]_2$(TCAS). $HC(pz)_3$ (tris(pyrazol-1-yl)methane) and TCAS (p-sulfonatothiacalix[4]arene). Blue line (room temperature), green lines (373 K) and red lines (433 K).[35]

Using FT-IR to follow SCO is limited to observing distinctive bonds in simple complexes. This is because FT-IR detects all vibrational modes at once often resulting in many peaks overlapping. Even if the peaks do not overlap the spectra is often filled with peaks having no relation to the metal centre.

FT-Raman suffers from similar problems to FT-IR; however, rR provides a solution to this. As previously discussed in Chapter 6, it uses a laser with a wavelength

corresponding to a chromophore's peak electronic absorbance. This results in an enhancement of the vibrational modes associated with the said chromophore. Typically iron(II) SCO complexes have distinct MLCT bands. This makes it possible to specifically excite the iron-ligand centre despite the surrounding complex thus resulting in a less cluttered spectrum. That, as with IR, displays the disappearance and appearance of HS and LS species. An example of this is shown for a $Fe(Pyrazine)Pt(CN)_4$ (see Figure 7.2.4.2). The peaks associated with Pt-CN bending and Fe-N stretching modes, 349 and 233 cm^{-1} respectively for the HS state, and LS contributed to the band at 1238 cm^{-1}.

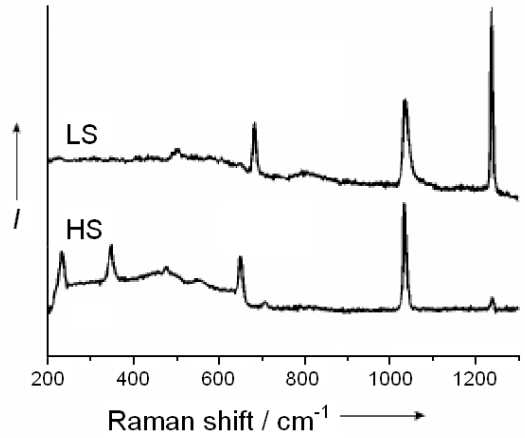

Figure 7.2.4.2 Example of a change in Raman spectra as a result of SCO for a $Fe(Pyrazine)Pt(CN)_4$ complex.[36]

7.3 Current research

In this chapter the coordination and magnetic behaviour of a selection of small molecule and polymeric complexes were investigated to determine if grafting SCO groups to a polymer alters their behaviour. The synthetic details for the small molecule complexes are given in Chapter 3 and the polymeric species in Chapter 5 (see Figure 7.3.1).

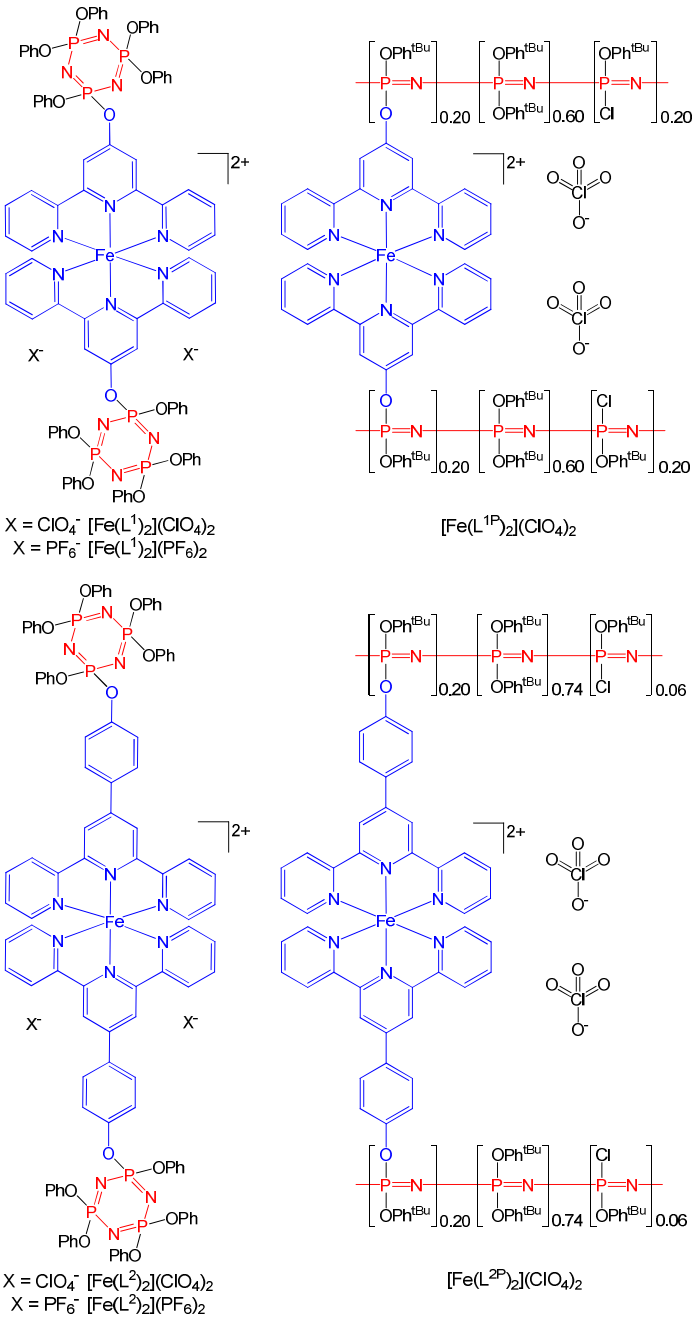

Figure 7.3.1 Small molecule and polymeric complexes studied in this chapter. OPh (Phenoxy), OPh^{tBu} (tert-butylphenoxy).

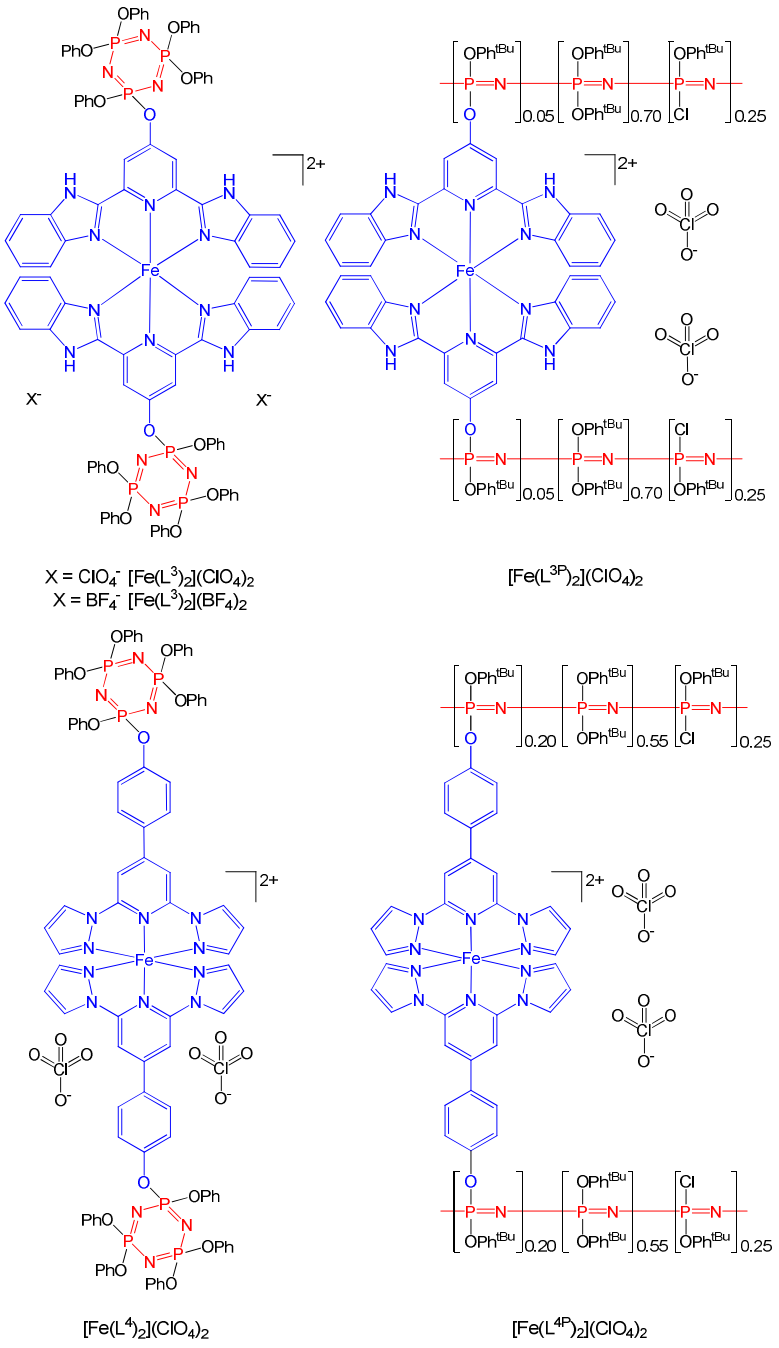

Figure 7.3.1 Continued Small molecule and polymeric complexes studied in this chapter. OPh (Phenoxy), OPh^{tBu} (tert-butylphenoxy).

Only the phenoxy (OPh) substituted phosphazene complexes were studied because they each grew crystals even if they were not diffractable, leading to a high reproducibility of crystal packing and purity. The 2,2'-biphenol substituted phosphazene complexes could be purified; however, as none of them grew crystals the packing would not be reproducible. Differences in packing or phases have proven to alter the SCO behaviour

of complexes. In addition OPh substituted phosphazene complexes provide a more accurate analogue to that of the tert-butylphenol substituted polymer.

Due to the polymers being synthesised with perchlorate salts each of the perchlorate small molecule analogues were studied in addition to the anions of the diffractable complexes. Based on the crystal data obtained in Chapter 5 the anions reside in the same position relative to the cationic complex, therefore it can be assumed that this will occur for all complexes.

Electronic absorbance and electrochemical data were recorded in acetonitrile for the small molecule complexes, unless otherwise stated, and the polymers in chloroform. IR data was recorded using KBr disks for both the small molecule and polymeric complexes. The magnetic, resonance Raman (rR) and Mössbauer data were recorded in solid-state for all complexes. Instrumental details and specific conditions are given in Appendix F.

Computational models of the respective cationic complexes were employed to aid the assignment of the electronic absorbance and vibrational spectra. DFT calculations were performed with both the B3LYP and OLYP levels using the 6-31G(d) basis set, available in the *Gaussian09*[37]/*GaussView5*[38] packages. The calculated bond lengths and vibrational frequencies were compared to the measured data to determine the most accurate model.

Using the available crystallographic data in Chapter 3, the OLYP models were shown to have only a 0.003 ($[Fe(L^3)_2]^{2+}$) – 0.006 Å ($[Fe(L^2)_2]^{2+}$) mean deviation in bond length while B3LYP had a 0.021 Å deviation for all of its models.

For the vibrational comparisons, the B3LYP frequencies were scaled by 0.9613[39] and the OLYP ones by 0.9782[40]. As these complexes did not contain unique vibrational modes, the mean average deviation (MAD) values were calculated using all assigned vibrational modes (see Appendix F for all calculated values).[41] Both OLYP and B3LYP produced similar MAD values of 4.08 – 4.52 cm^{-1} for the $[Fe(L^1)_2]^{2+}$ and $[Fe(L^2)_2]^{2+}$ complexes. However, for $[Fe(L^3)_2]^{2+}$ OLYP had a 5.36 cm^{-1} value while B3LYP had 7.70 cm^{-1}. Although there was only a small improvement in vibrational accuracy the significant increase in structural accuracy proved that OLYP produced the most accurate models of these systems.

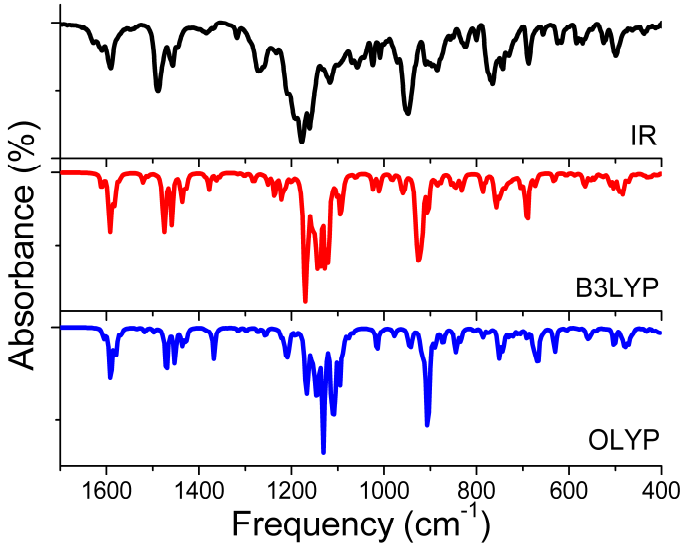

Figure 7.3.2 Comparison of IR spectrum for $[Fe(L^3)_2](ClO_4)_2$ with the B3LYP and OLYP predicted spectra for $[Fe(L^3)_2]^{2+}$.

The time-dependent (TD) calculations were carried out in an acetonitrile solvent field using the PCM method.[42]

7.4 Electrochemistry

Each of the iron complexes displayed the characteristic Fe^{II}/Fe^{III} oxidation coupling and reductions associated with the ligands. The L^1 ($[Fe(L^1)_2](ClO_4)_2$ and $[Fe(L^1)_2](PF_6)_2$) and L^2 ($[Fe(L^2)_2](ClO_4)_2$ and $[Fe(L^2)_2](PF_6)_2$) based complexes did not display a difference in oxidation potential with a change in anions, suggesting no significant interaction between the cationic complex and the anions. However, by changing from perchlorate for $[Fe(L^3)_2](ClO_4)_2$ (0.575 V) to tetrafluoroborate for $[Fe(L^3)_2](BF_4)_2$ (0.550 V) the oxidation potential was anodically shifted 25 mV, indicating a significant interaction between the cationic complex and anion in solution.

A comparison of $E_{½OX}$ of each of the complexes to their hydrogen substituted analogues show they are cathodically shifted, e.g. $[Fe(L^1)_2](PF_6)_2$ (0.854 V) and $[Fe(Terpy)_2](PF_6)_2$ (0.77 V);[43] $[Fe(L^3)_2](ClO_4)_2$ (0.575 V) and $[Fe(bbp)_2](ClO_4)_2$ (0.415 V);[44] and no published data is available to compare $[Fe(L^4)_2](ClO_4)_2$. This behaviour is consistent with the ruthenium analogues (see Chapter 6) and proves that the phosphazene ether acts as an electron-withdrawing group. $[Fe(L^2)_2](ClO_4)_2$ (0.940 V) displayed a difference the $E_{½ox}$ value is anodically shifted relative to $[Fe(PhTerpy)_2](ClO_4)_2$ (1.105).[45,46] This difference can be attributed to the phenyl group to functions as a weak electron donor and acceptor via resonance coupling to the terpy ring system.[45] Attempts were made to calculate the cationic Hammett parameter but as with the ruthenium analogues, it was not possible to obtain a consistent value, possibly due to conformation changes upon oxidation.

Table 7.4.1 Electrochemical data in CH_3CN at 293 K

Complex	**$E_{½ox}$ (V)**	**$E_{½red}$ (V)**	**$E_{½red}$ (V)**
$[Fe(L^1)_2](ClO_4)_2$	0.854 (65)	-1.234 (irr)	
$[Fe(L^1)_2](PF_6)_2$	0.854 (68)	-1.237 (irr)	
$[Fe(L^2)_2](ClO_4)_2$	0.940 (83)	-1.259 (irr)	-1.514 (irr)
$[Fe(L^2)_2](PF_6)_2$	0.940 (83)	-1.259 (irr)	-1.514 (irr)
$[Fe(L^3)_2](ClO_4)_2$	0.575 (98)	-0.930 (irr)	-1.474 (irr)
$[Fe(L^3)_2](BF_4)_2$	0.550 (96)	-0.912 (irr)	-1.556 (irr)
$[Fe(L^4)_2](ClO_4)_2$	1.262 (75)	-0.812 (irr)	-1.179 (irr)

Reliable data could not be obtained for the polymers due to the low conductivity of the solution and the tendency of the polymer to form insulative layers. Therefore, it can only be assumed that the polymers have the same electrochemical behaviour.

7.5 Electronic absorbance spectroscopy

As previously discussed electronic absorbance spectroscopy provides insight into SCO behaviour, but it also provides an indication of coordination behaviour. By comparisons between electronic spectra it can be determined if the same metal-ligand configuration has been formed.

7.5.1 Iron(II) bis(2,2':6',2''-terpyridine) based complexes

Shown in Figure 7.5.1.1 are the electronic absorbance spectra of the 2,6-di(pyridine-2-yl)pyridine-4(1*H*)-onate (OTerpy) based complexes ($[Fe(L^{1})_2](ClO_4)_2$, $[Fe(L^{1})_2](PF_6)_2$ and $[Fe(L^{1P})_2](ClO_4)_2$), and the 4-(2,2':6',2''-terpyrdine)-4'-yl-phenolate (OPhTerpy) based complexes ($[Fe(L^{2})_2](ClO_4)_2$, $[Fe(L^{2})_2](PF_6)_2$ and $[Fe(L^{2P})_2](ClO_4)_2$). In each case an MLCT band consistent with the formation of a $[Fe(Terpy)_2]^{2+}$ species was observed (see Figure 7.5.1.1).

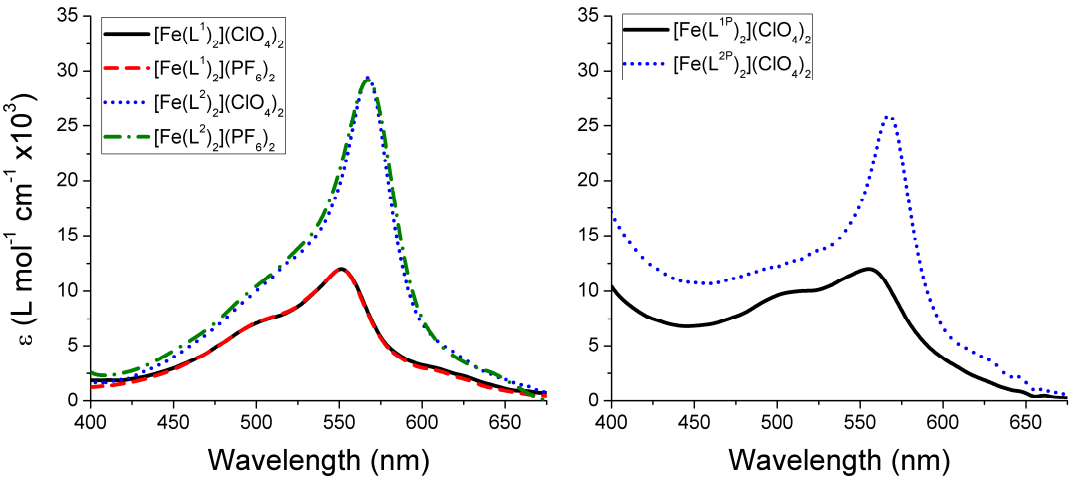

Figure 7.5.1.1 Electronic absorption spectra. Left: $[Fe(L^{1})_2](ClO_4)_2$, $[Fe(L^{1})_2](PF_6)_2$, $[Fe(L^{2})_2](ClO_4)_2$ and $[Fe(L^{2})_2](PF_6)_2$. Right: $[Fe(L^{1P})_2](ClO_4)_2$ and $[Fe(L^{2P})_2](ClO_4)_2$.

The absorption spectra of $[Fe(L^{1})_2](ClO_4)_2$ and $[Fe(L^{1})_2](PF_6)_2$ are identical showing no significant anion interaction in the solution phase. In addition, the spectra are almost identical to that of the unsubstituted terpy complex ($[Fe(Terpy)](ClO_4)_2$);[47] however, the λ_{max} of the MLCT (556 nm) is red shifted by 4 nm relative to it (552 nm) (see Table

7.5.1.1). This behaviour is consistent with the slight electron-withdrawing effects of phosphazene ether observed for the ruthenium analogue (see Chapter 6).

Based on time-dependent-DFT (TD-DFT) calculations the major contributor to the MLCT is the transition from (HOMO, HOMO-2) → (LUMO, LUMO+1) transition at 549 nm. These orbitals are localised to the $[Fe(Terpy)_2]^{2+}$ centre with only small contributions from the P-O bond (see Figure 7.5.1.2), assignments of the first 10 transitions are included in the Appendix F.

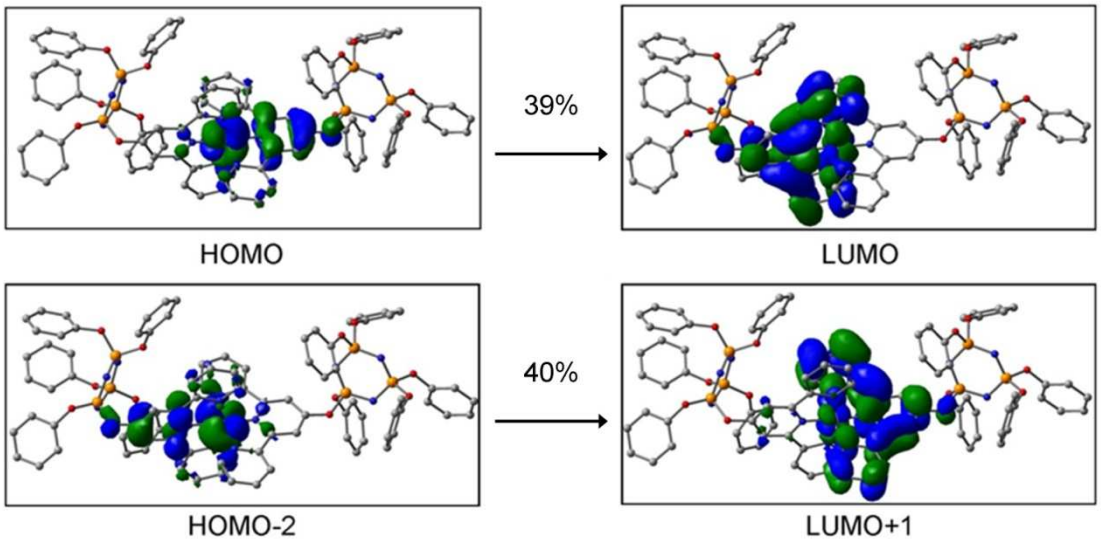

Figure 7.5.1.2 Molecular orbitals associated with the 549 nm transition.

$[Fe(L^{1P})_2](ClO_4)_2$ (555 nm) displays an identical MLCT band to $[Fe(L^1)_2](ClO_4)_2$ but is only shifted by 1 nm (see Table 7.5.1.1), this shift within the range of error but could be accounted for by solvochromic effects. However, this provides strong evidence $[Fe(L^{1P})_2](ClO_4)_2$ contains the same $[Fe(Terpy)_2]^{2+}$ core as $[Fe(L^1)_2](ClO_4)_2$.

The electronic spectra of $[Fe(L^2)_2](ClO_4)_2$ and $[Fe(L^2)_2](PF_6)_2$ were also identical, once again showing no anion interactions. As with the complexes $[Fe(L^1)_2](ClO_4)_2$ and $[Fe(L^1)_2](PF_6)_2$, the λ_{max} (568 nm) of the MLCT band was red shifted relative to $[Fe(PhTerpy)_2](ClO_4)_2$,[48] although only by 2 nm (see Table 7.5.1.1). The reduction of red shifting is due to the phenyl ring of L^2 increasing the distance between the phosphazene ether bond and the $[Fe(Terpy)_2]^{2+}$ core. This is consistent with the TD-DFT calculations; there is still a small contribution from the P-O bond in the relevant orbitals, although this contribution is greatly reduced compared to the $[Fe(L^1)_2]^{2+}$

complexes. In addition, no contributions from the phosphazene are observed (see Appendix F).

Like $[Fe(L^{1P})_2](ClO_4)_2$ and $[Fe(L^{1})_2](ClO_4)_2$, $[Fe(L^{2P})_2](ClO_4)_2$ (568 nm) display an identical MLCT band with $[Fe(L^{2})_2](ClO_4)_2$ except the extinction coefficient is slightly lower for $[Fe(L^{2P})_2](ClO_4)_2$ which is likely due to the inherent inaccuracy in the molecular formula of a polyphosphazene (see Chapter 5). However, this similarity of MLCT bands is strong evidence that the $[Fe(Terpy)_2]^{2+}$ core for $[Fe(L^{2P})_2](ClO_4)_2$ is the same as $[Fe(L^{2})_2](ClO_4)_2$.

Table 7.5.1.1 Peak MLCT absorption wavelengths and extinction coefficient.

Complex	**λ_{max} / nm (ε / 10^3 L mol^{-1} cm^{-1})**
$[Fe(Terpy)_2](ClO_4)_2$ [a]	552[47]
$[Fe(PhTerpy)_2](ClO_4)_2$ [a]	566[48]
$[Fe(L^{1})_2](ClO_4)_2$ [a]	556 (12)
$[Fe(L^{1})_2](PF_6)_2$ [a]	556 (12)
$[Fe(L^{2})_2](ClO_4)_2$ [a]	568 (29)
$[Fe(L^{2})_2](PF_6)_2$ [a]	568 (30)
$[Fe(L^{1P})_2](ClO_4)_2$ [b]	555 (12)
$[Fe(L^{2P})_2](ClO_4)_2$ [b]	568 (26)

[a] Recorded in acetonitrile, [b] in chloroform.

Variable temperature measurements were performed on each of the small molecule complexes from 243–343 K and 243–323 K for the polymeric analogues. None of the complexes displayed a variation in spectra as a function of temperature.

7.5.2 Iron(II) bis(2,6-di{1*H*-benzimidazol-2-yl)pyridine) based complexes

Both $[Fe(L^3)_2](ClO_4)_2$ and $[Fe(L^3)_2](BF_4)_2$ complexes display an MLCT, typical of an iron-bis(2,6-di{1*H*-benzimidazol-2-yl}pyridine) ($[Fe(bbp)_2]^{2+}$) complex, with λ_{max} of 560 and 561 nm respectively. Only a 1 nm difference was seen between the complexes but it was reproducible, which suggests that there is a weak interaction between the cationic complex and the anion. The λ_{max} of each of the complexes are red shifted by 8–9 nm relative to the hydrogen substituted complex $[Fe(bbp)_2](ClO_4)_2$ (λ_{max} 552 nm in acetonitrile).[49] This is explained by the slight electron-withdrawing effects of the phosphazene ether unit observed in the previous examples.

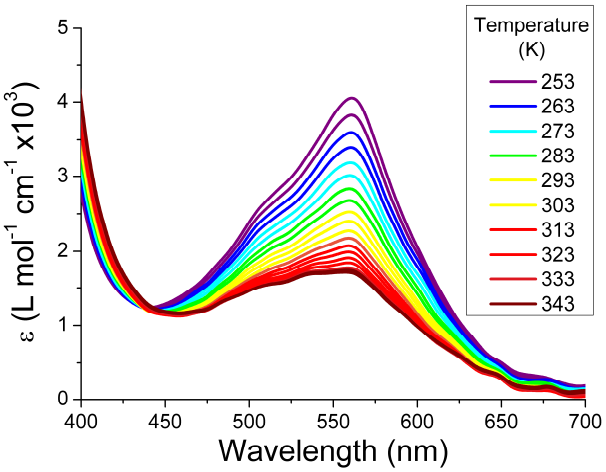

Figure 7.5.2.1 MLCT band absorbance as a function of temperature for $[Fe(L^3)_2](ClO_4)_2$ (recorded in benzonitrile).

The extinction coefficient of the MLCT band decreased as the temperature was increased. A notable difference was observed between the tetrafluoroborate and perchlorate analogues. Based on the ruthenium bbp complexes the anion hydrogen-bonds with the imidazole proton altering the optical and electrochemical properties of the complex.[50] It is possible that enough of an interaction is observed to affect the SCO behaviour in solution (see Figure 7.5.2.2). Variable temperature measurements were recorded in both acetonitrile and benzonitrile, no differences in behaviour were observed between the solvents. Therefore, the data was collected in benzonitrile due to its high boiling point. Due to the limitations of the equipment it was not possible to

record the data to either higher or lower temperatures, preventing the determination of the thermodynamic parameters.

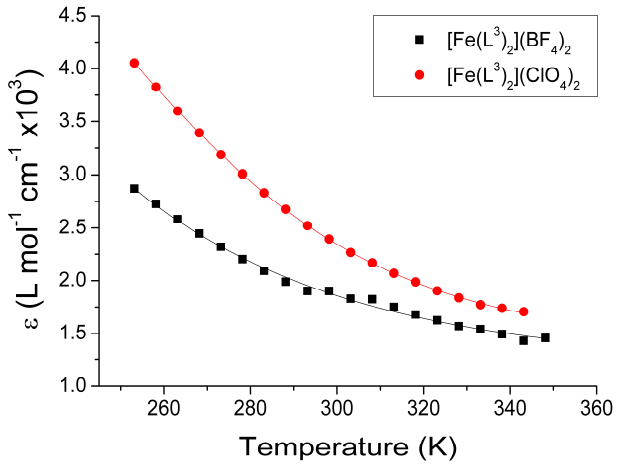

Figure 7.5.2.2 Extinction coefficient vs. temperature for $[Fe(L^3)_2](ClO_4)_2$ and $[Fe(L^3)_2](BF_4)_2$ (recorded in benzonitrile).

The curve could also be very gradual because the complex breaks down as a result of an equilibria formed with coordinating solvents (acetonitrile or benzonitrile). Linert *et al.*[49] determined that in coordinating solvents the mono- and bis-coordinated complexes form an equilibria with the metal ion.

$$[FeL_2]^{2+} \rightleftharpoons [FeL(solvent)_3]^{2+} + L \rightleftharpoons [Fe(solvent)_6]^{2+} + 2L$$

Titrations of L^3 with iron salts in acetonitrile (see Appendix F) did display peaks that could be attributed to the $[Fe(L^3)(CH_3CN)_3]^{2+}$ species. However, no evidence of this complex was observed in the recorded mass-spectrum, although it could be a contributing factor to the temperature dependence of the extinction coefficient in addition to SCO.

The polymer analogue did not display an MLCT band at any temperature; this is inconclusive as it could be due to the polymer being in the HS state or it could be that the metal concentration is too low to be detected, as occurred in the similar ruthenium complexes.

7.5.3 Iron(II) bis(2,6-di{1*H*-pyrazol-1-yl}pyridine) based complexes

A significant difference is observed between complexes $[Fe(L^{4})_2](ClO_4)_2$ and $[Fe(L^{4P})_2](ClO_4)_2$. $[Fe(L^{4})_2](ClO_4)_2$ only displays absorbance between 300 and 200 nm, associated with $\pi \rightarrow \pi^*$ transitions, with no observable MLCT bands for all accessible temperatures. Such an electronic spectrum is indicative of an HS complex. However, complex $[Fe(L^{4P})_2](ClO_4)_2$ shows a different behaviour. In addition to the $\pi \rightarrow \pi^*$ transitions it also displays an MLCT band which consists of two peak transitions at 524 nm (1550 L mol^{-1} cm^{-1}) and 491 nm (1316 L mol^{-1} cm^{-1}) (see Figure 7.5.3.1). This is significantly shifted compared to that of $[Fe(bpp)_2](BF_4)_2$ with λ_{max} of 418 and 380 nm,[51] but it is consistent with that of the TD-DFT calculations, which show the excitations are localised to the $[Fe(bpp)_2]^{2+}$ core, due to the phenyl spacer preventing the phosphazene from contributing. With the possibility of SCO occurring it is impossible to determine if the same metal-ligand configuration has been formed for both the polymer and SMA.

The variable temperature measurements show that the MLCT band of $[Fe(L^{4P})_2](ClO_4)_2$ decreased as the temperature was increased, characteristic of SCO (see Figure 7.5.3.1). However, the polymer was only soluble in chloroform if the temperature range was limited. As neither a pure HS nor LS solution could be obtained, the thermodynamic parameters could not be determined.

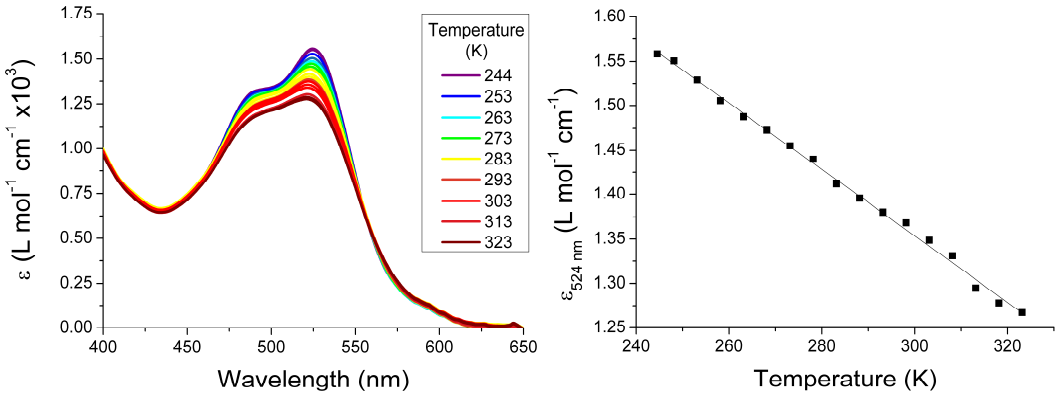

Figure 7.5.3.1 Left: Absorbance spectra of $[Fe(L^{4P})_2](ClO_4)_2$ collected at a range of temperatures. Right: the extinction coefficient of $[Fe(L^{4P})_2](ClO_4)_2$ at 524 nm as a function of temperature.

7.6 Vibrational spectroscopy

FT-IR spectroscopy was initially used to study the vibrational behaviour of the complexes; however, all the spectra were dominated by the aromatic vibrational modes, thereby showing little difference between each complex. Solution rR was also attempted. While the small molecule complexes produced a high signal-to-noise ratio, the polymers did not, due to the cross-linked polymers forming precipitates that scattered the light. Therefore, solid-state rR was employed, allowing the vibrational modes of the iron-ligand centre to be observed, which afforded a greater range of temperatures to be measured than in the solution phase (data collected by R. Horvath and K. Gordon, University of Otago).

7.6.1 Iron(II) bis(2,2':6',2"-terpyridine) based complexes

RR data was collected using a λ_{ex} of 568, 514 and 457 nm (exciting the MLCT). Excitations at 568 nm displayed the greatest signal-to-noise ratio due to it being closest to the peak absorbance; however, 514 nm and 457 nm displayed similar results. By comparison to DFT models the enhanced vibrational modes primarily consisted of the terpy ring distortions and iron-nitrogen bond stretching (see Appendix F for assignments). It was noted that $[Fe(L^1)_2]^{2+}$ complexes displayed contributions from the phosphazene ring for the low energy delocalised vibrational modes; however, $[Fe(L^2)_2]^{2+}$ displayed little, providing further evidence that the addition of a phenyl spacer, specifically one that is not in-plane with the chromophore, prevents any contributions from the phosphazene ring.

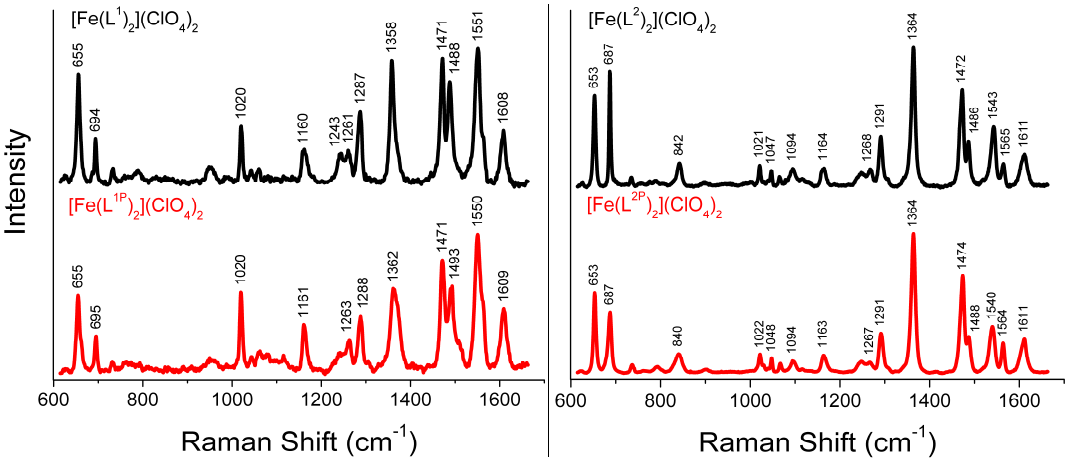

Figure 7.6.1.1 Solid-state rR spectra recorded using 568 nm excitation. Left: $[Fe(L^{1})_2](ClO_4)_2$ and $[Fe(L^{1P})_2](ClO_4)_2$. Right: $[Fe(L^{2})_2](ClO_4)_2$ and $[Fe(L^{2P})_2](ClO_4)_2$.

$[Fe(L^{2P})_2](ClO_4)_2$ displayed an almost identical rR spectra to $[Fe(L^{2})_2](ClO_4)_2$ with differences in Raman shift less than 2 cm^{-1} (see Figure 7.6.1.1). Confirming that the same $[Fe(Terpy)_2]^{2+}$ core has been formed in the polymer and SMA. $[Fe(L^{1P})_2](ClO_4)_2$ displays a similar correlation between the polymer and SMA with the exception of two peaks. The peaks (1358 and 1488 cm^{-1}) are shifted by 4–5 cm^{-1} relative to the polymer. These vibrational modes correspond to the OTerpy ring deformations (see Figure 7.6.1.2). As with each of the other vibrational modes the same $[Fe(Terpy)_2]^{2+}$ cores are formed in the polymer and SMA; the shifting of the two peaks are due to matrix effects.

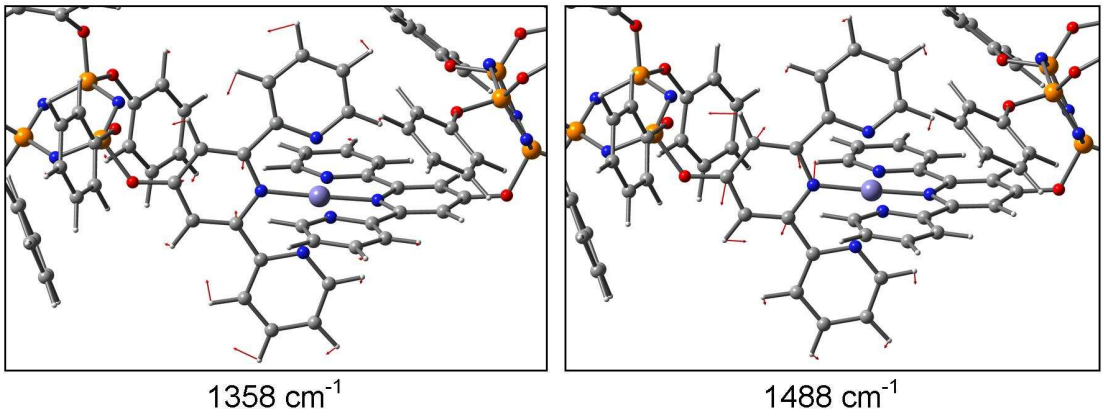

Figure 7.6.1.2 Two different vibrational modes of $[Fe(L^{1})_2]^{2+}$, Red arrows indicate displacement vectors.

The spectra were recorded at 79, 298 and 362 K. No changes in vibrational modes were observed, suggesting the absence of SCO.

7.6.2 Iron(II) bis(2,6-di{1*H*-benzimidazol-2-yl}pyridine) based complexes

As for the OTerpy and OPhTerpy based complexes rR was collected at 514, 568 and 457 nm. Both 568 and 514 nm produced a suitable signal-to-noise ratio. As such the spectra were collected at a range of temperatures. λ_{ex} 568 nm is shown in Figure 7.6.2.1 and λ_{ex} 514 nm is included in Supplementary S7.

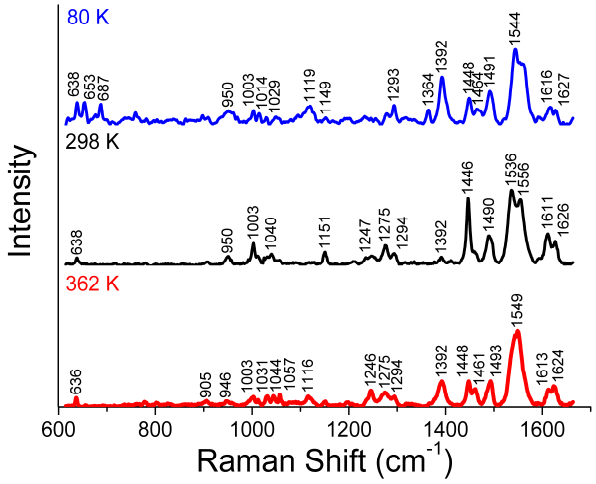

Figure 7.6.2.1 Solid-state rR collected for $[Fe(L^3)_2](BF_4)_2$. λ_{ex} 568 nm.

Assignments of the vibrational modes were again based on DFT calculations, in this case they were only based on the low temperature as this guaranteed they were of the LS species. The IR data was collected at room temperature; these were not used for the initial assignment. The vibrational modes enhanced by rR corresponded to those localised to the $[Fe(bbp)_2]^{2+}$ core with contributions from the phosphazene for the low energy delocalised vibrations.

As the temperature was increased, significant differences were observed, e.g. additional peaks were observed at 1556 cm^{-1} (see Figure 7.6.2.2). By comparison to the HS DFT model, it can be tentatively assigned as the HS species.

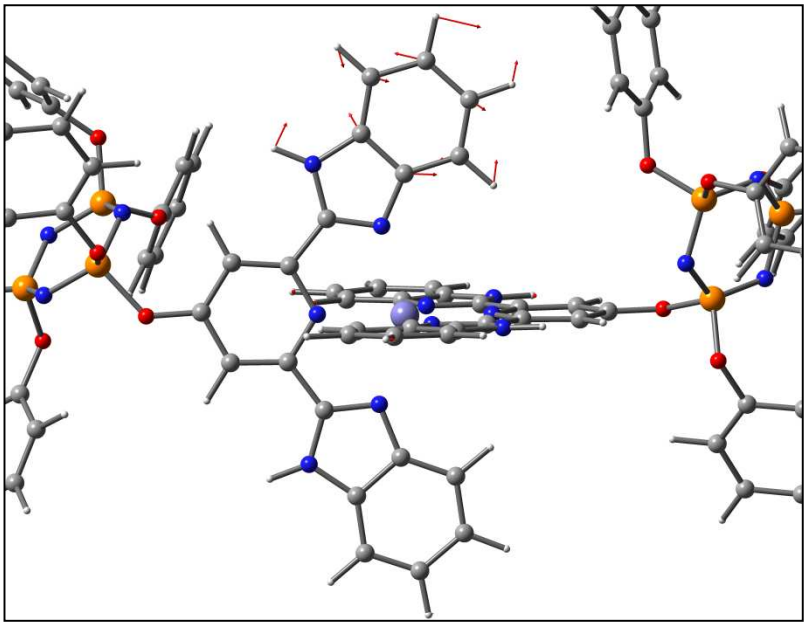

Figure 7.6.2.2 Vibrational mode assigned to 1556 cm^{-1} for HS-$[Fe(L^{3})_2]^{2+}$, red arrows indicate displacement vectors (exaggerated for clarity).

The rR of the polymeric analogue ($[Fe(L^{3P})_2](ClO_4)_2$) was recorded under the same conditions as the SMA; however, as with the similar ruthenium polymers the metal concentration was too low to give suitable data.

7.6.3 Iron(II) bis(2,6-di{1*H*-pyrazol-1-yl}pyridine) based complexes

It was not possible to obtain rR data for $[Fe(L^{4})_2](ClO_4)_2$ due to the absence of strong absorbance associated with the metal centre. Also, as previously observed with the other compounds, the IR spectra were dominated by aromatic ring distortions, making it unsuitable for studying the metal centre. Despite the MLCT band observed for $[Fe(L^{4P})_2](ClO_4)_2$ it was also too fluorescent to obtain high quality rR data. Therefore, this result is inconclusive for both complexes.

7.7 Magnetic moments

As a definite means of determining the SCO behaviour of the complexes a SQUID was used to measure the magnetic moments of the complexes as a function of temperature (data collected by B. Moubaraki and K. Murray, Monash University). It is important to note that for safety reasons the perchlorate complexes could not be heated.

7.7.1 Iron(II) bis(2,2':6',2"-terpyridine) based complexes

Shown in Figure 7.7.1.1 are the magnetic moments of $[Fe(L^1)_2](ClO_4)_2$, $[Fe(L^1)_2](PF_6)_2$, $[Fe(L^2)_2](ClO_4)_2$ and $[Fe(L^2)_2](PF_6)_2$. Although $[Fe(L^1)_2](PF_6)_2$ has a higher magnetic moment (1.35 μ_B) than $[Fe(L^1)_2](ClO_4)_2$ (0.83 μ_B), at low temperature both are within the typical range of values for LS octahedral iron complexes, consistent with the other data collected for these complexes.

$[Fe(L^2)_2](ClO_4)_2$ and $[Fe(L^2)_2](PF_6)_2$ display a difference in behaviour. $[Fe(L^2)_2](PF_6)_2$ remains LS (0.58 μ_B) below 294 K; however, once heated beyond this temperature the magnetic moment begins to increase. $[Fe(L^2)_2](ClO_4)_2$ remained LS (1.09 μ_B) for all available temperatures, while its magnetic moment remained higher than that of $[Fe(L^2)_2](PF_6)_2$ (see Figure 7.7.1.1), which could be due to the presence of a minute amount of paramagnetic impurity or simply the difference in anion has slightly altered the magnetic behaviour, which has been shown to occur in many literature examples.[23,52,53]

The change in magnetic moment for $[Fe(L^2)_2](PF_6)_2$ could have also been caused by the loss of solvent on heating; but such behaviour would have been observed in all of the complexes as they each contain acetonitrile. Therefore it is likely that this complex displays the start of SCO. The reason $[Fe(L^2)_2](PF_6)_2$ displays the start of SCO and $[Fe(L^1)_2](PF_6)_2$ does not is due to the phenyl spacer in L^2 increasing the length of the complex, thereby increasing the strain on the metal centre (see Chapter 3 for the crystal structure). The increase is similar to that observed in the banana-shaped terpy complexes of Hayami et al.,[54] but to a far lesser extent. Unfortunately, the magnetic moment could not be collected beyond 340 K due to the limitations of the equipment.

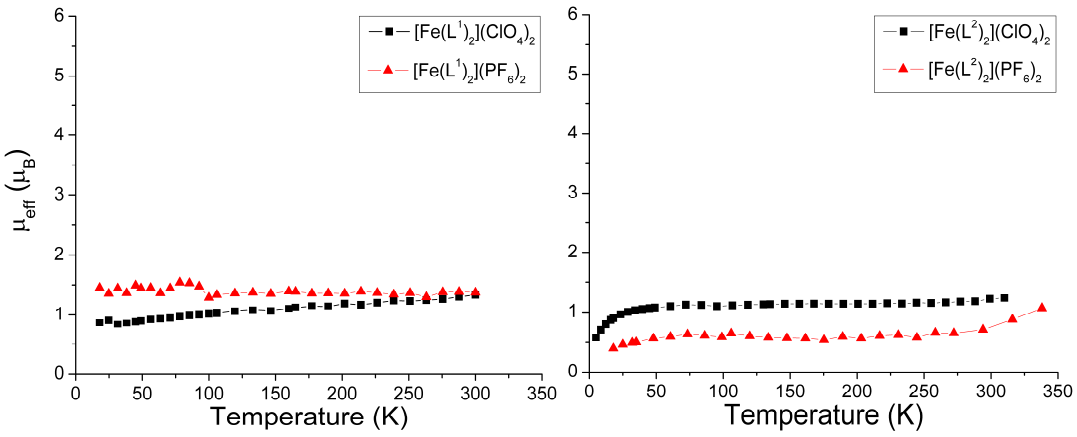

Figure 7.7.1.1 Variable temperature magnetic moments. Left: $[Fe(L^1)_2](ClO_4)_2$ and $[Fe(L^1)_2](PF_6)_2$. Right: $[Fe(L^2)_2](PF_6)_2$.

Optical excitations were also attempted for these complexes, but displayed no transitions to the HS state.

Magnetic moment data was collected for each of the polymer analogues ($[Fe(L^{1P})_2](ClO_4)_2$ and $[Fe(L^{2P})_2](ClO_4)_2$); these displayed the presence of a paramagnetic impurity. This impurity could have originated from excess $Fe(ClO_4)_2$ remaining in the polymer matrix, an iron species coordinating to the polymer backbone or residual OPh^{tBu} reacting with the iron to form an iron(III) species. The impurity occurred in significant enough amounts to invalidate the data for the polymers.

7.7.2 Iron(II) bis(2,6-di{1*H*-benzimidazol-2-yl}pyridine) based complexes

Shown in Figure 7.7.2.1 are the magnetic moments vs. temperature for $[Fe(L^3)_2](ClO_4)_2$ and $[Fe(L^3)_2](BF_4)_2$. Each of the complexes displayed an increase in magnetic moment as the temperature was increased. Due to the danger of heating a perchlorate salt, $[Fe(L^3)_2](ClO_4)_2$ could only be heated to 317 K. Therefore, only the initial SCO curve was observed. For $[Fe(L^3)_2](BF_4)_2$, the complex was safe to heat to 400 K. In this temperature range an almost full SCO curve was observed with a $T_{1/2}$ at 336 K (1st run). After heating, solvent was lost from the lattice, greatly altering the behaviour of the complex. Once the solvent was lost the complex could not be cooled low enough to form the LS species (2nd run). Successive heating resulted in a further loss of solvent, further altering the magnetic behaviour, trapping it in the mid-spin state (3rd run).

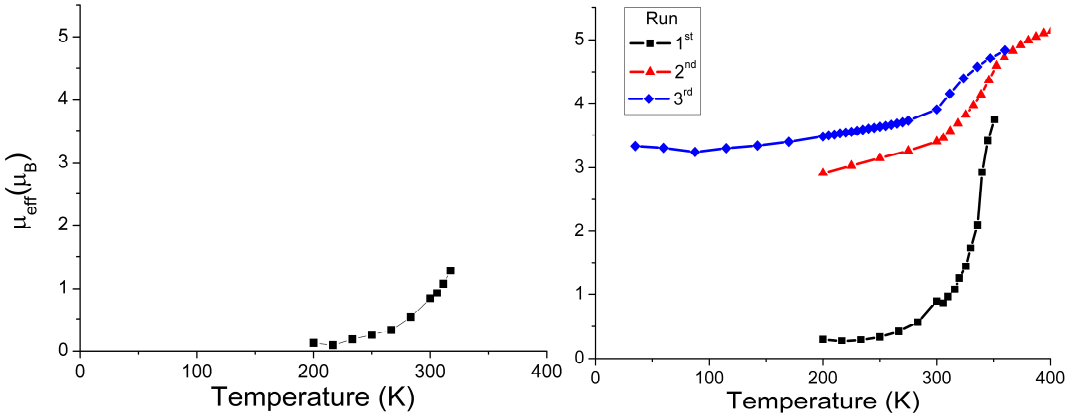

Figure 7.7.2.1 Magnetic moment vs. temperature. Left: $[Fe(L^3)_2](ClO_4)_2$. Right: $[Fe(L^3)_2](BF_4)_2$.

Magnetic data was not collected for $[Fe(L^{3P})_2](ClO_4)_2$ as the metal concentration is too low to detect in the diamagnetic polymer matrix. While many physical properties can be assumed to be the same between polymers and SMA, this assumption may not hold true for SCO because it tends to be environmentally dependent.

7.7.3 Iron(II) bis(2,6-di{1*H*-pyrazol-1-yl}pyridine) based complexes

Shown in Figure 7.7.3.1 is the magnetic moment of $[Fe(L^4)_2](ClO_4)_2$ recorded over a temperature range of 4 to 300 K. Between 50–300 K the complex displayed Curie-Weiss behaviour with a magnetic moment of 5.2 μ_B, a typical value for an octahedral HS iron complex. Below 50 K there is a reduction in magnetic moment down to a value of 3.75 μ_B at 4 K. This behaviour is associated with zero-field splitting of the spin quintet state. The complex being in the HS state is consistent with the absence of an MLCT band in the UV/Vis absorbance spectra and the inability to obtain rR and NMR data.

As was observed for the OPhTerpy based complexes the addition of a phosphazene provides enough strain on the metal centre to induce SCO behaviour. However, $[Fe(bpp)_2]^{2+}$ systems already display SCO, and increased strain due to the bulk of the attached phosphazene results in the HS species being dominant. It is possible that substituent effects (i.e. electron donation) also contribute, but it is impossible to say to what degree.

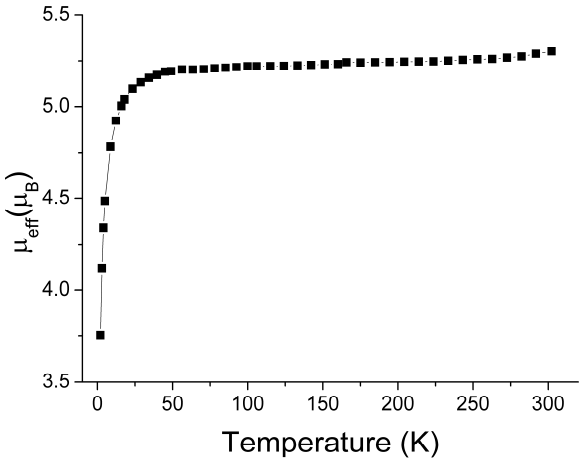

Figure 7.7.3.1 Magnetic moment of $[Fe(L^4)_2](ClO_4)_2$.

The magnetic moments of $[Fe(L^{4P})_2](ClO_4)_2$ were not recorded because both $[Fe(L^{1P})_2](ClO_4)_2$ and $[Fe(L^{2P})_2](ClO_4)_2$ displayed the presence of a paramagnetic impurity, therefore it is likely the same would occur for this polymer.

7.8 Mössbauer spectroscopy

Mössbauer spectroscopy was used to complement each of the previous techniques. It was used to identify the coordination behaviour of the polymers and compare it to the SMA; in addition, the spin states of all of the complexes were investigated. While the small molecule complexes have sufficient natural iron to give a suitable signal, the polymer complexes required iron-57 enrichment (data collected by G. Jameson, University of Otago). Only two Mössbauer studies have been performed on polyphosphazenes and on the cyclotriphosphazene.[55] The polymer studies focused on how iron(III) protoporphyrin coordinated to an imidazole substitute.[56,57] These studies had the advantage of being able to purify a stable iron species before reacting it with the polymer; this provides a significant difference to the polymers in this investigation.

7.8.1 Iron(II) bis(2,2':6',2"-terpyridine) based complexes

Shown in Figure 7.8.1.1 are the Mössbauer spectra of $[Fe(L^{1})_2](ClO_4)_2$ and $[Fe(L^{1P})_2](ClO_4)_2$ collected at 4 K. $[Fe(L^{1})_2](ClO_4)_2$ displays a doublet with δ_{iso} (0.27 mm s^{-1}) and ΔE_Q (0.96 mm s^{-1}), and $[Fe(L^{1P})_2](ClO_4)_2$ shows the presence of a doublet with δ_{iso} (0.30 mm s^{-1}) and ΔE_Q (1.15 mm s^{-1}). The slight difference could be attributed to matrix effects but both sets of values are within the range of an LS $[Fe(Terpy)_2]^{2+}$ complex.

In addition to the doublet, $[Fe(L^{1P})_2](ClO_4)_2$ also displayed a septuplet signal, this corresponds to an unknown slow relaxing paramagnetic impurity which was detected in the magnetic measurements. This impurity is not observed in $[Fe(L^{1})_2](ClO_4)_2$, although this may be due to it being purified by crystallisation. Polymers are a distribution of products rather than one pure species, it is possible other iron species are present, e.g. coordinating to non-specific sites or residing in the polymer matrix. It was observed that by reducing the amount of iron added that the ratio of this impurity was reduced but not eliminated.

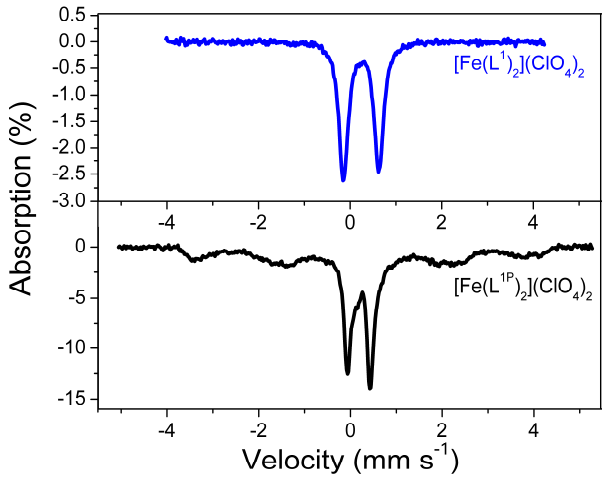

Figure 7.8.1.1 Mössbauer spectra of $[Fe(L^{1})_2](ClO_4)_2$ and $[Fe(L^{1P})_2](ClO_4)_2$ collected at 4 K. $[Fe(L^{1P})_2](ClO_4)_2$ enriched with iron-57.

Mössbauer data was collected at 4–298 K (the instrument limits), no significant differences were observed. This behaviour is consistent with the magnetic data collected for $[Fe(L^{1})_2](ClO_4)_2$. Therefore, it can be confirmed within the temperature range that both the SMA and the polymer remain LS.

Shown in Figure 7.8.1.2 are the Mössbauer spectra of $[Fe(L^{2})_2](ClO_4)_2$ and $[Fe(L^{2P})_2](ClO_4)_2$ collected at 4 K. $[Fe(L^{2})_2](ClO_4)_2$ displays a doublet signal with δ_{iso} (0.24 mm s^{-1}) and ΔE_Q (0.98 mm s^{-1}), consistent with an LS $[Fe(Terpy)_2]^{2+}$ complex. $[Fe(L^{2P})_2](ClO_4)_2$ may display a doublet consistent with an LS $[Fe(Terpy)_2]^{2+}$ species being present; however, an overlap of the paramagnetic species previously discussed prevents a definite identification. When recorded at 298 K the paramagnetic peaks shifted independent of the doublet, showing that the species were not linked.

The doublet of $[Fe(L^{2})_2](ClO_4)_2$ and the suspected doublet of $[Fe(L^{2P})_2](ClO_4)_2$ remain relatively unchanged when heated. This data confirms that within this temperature range $[Fe(L^{2})_2](ClO_4)_2$ remains LS consistent with the magnetic data. Based on the previous $[Fe(L^{1P})_2](ClO_4)_2$ it is likely that $[Fe(L^{2P})_2](ClO_4)_2$ is also LS but cannot be confirmed with the paramagnetic species overlapping. However, the presence of this species fits the electronic and rR data collected.

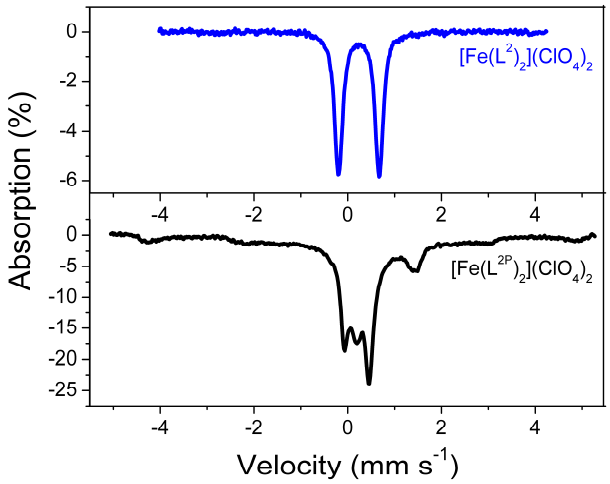

Figure 7.8.1.2 Mössbauer spectra of $[Fe(L^{2})_2](ClO_4)_2$ and $[Fe(L^{2P})_2](ClO_4)_2$ collected at 4 K ($[Fe(L^{2P})_2](ClO_4)_2$ enriched with iron-57).

7.8.2 Iron(II) bis(2,6-di{1*H*-benzimidzol-2-yl}pyridine) based complexes

Each of the Obbp based complexes ($[Fe(L^3)_2]X_2$, X = BF_4^- or ClO_4^-) displayed the characteristic doublet with δ_{iso} (0.35 mm s^{-1}) and ΔE_Q (0.47 mm s^{-1}) consistent with an LS $[Fe(bbp)_2]^{2+}$ complex.[58] Neither complex displayed a significant difference as the temperature was increased, although 294 K (the limiting temperature of the equipment) was below the temperature at which the SCO began to occur (see Figure 7.8.2.1).

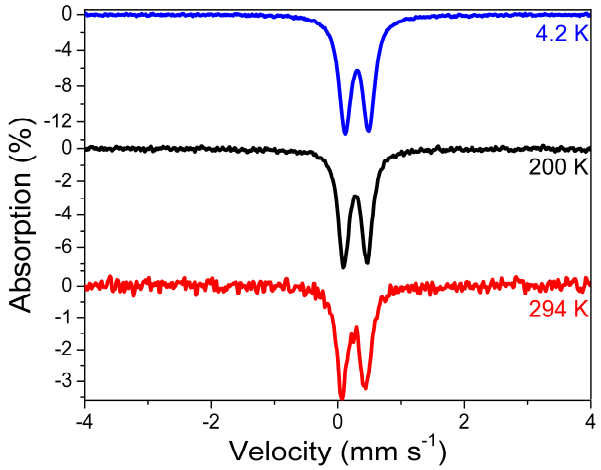

Figure 7.8.2.1 Mössbauer spectra of $[Fe(L^3)_2](ClO_4)_2$ recorded at 4.2 K, 200 K and 294 K.

Even with the use of 99% iron-57 the signal-to-noise ratio was too low to obtain suitable results, therefore no data was collected for the polymeric analogue $[Fe(L^{3P})_2](ClO_4)_2$.

7.8.3 Iron(II) bis(2,6-di{1*H*-pyrazol-1-yl}pyridine) based complexes

The OPhbpp based complexes displayed a striking difference. At 5.6 K, $[Fe(L^4)_2](ClO_4)_2$ displayed a doublet signal with δ_{iso} (1.38 mm s^{-1}) and ΔE_Q (3.16 mm s^{-1}), confirming that the complex is HS, consistent with the magnetic data and absence of MLCT. However, $[Fe(L^{4P})_2](ClO_4)_2$ displayed a doublet with δ_{iso} (0.55 mm s^{-1}) and ΔE_Q (0.50 mm s^{-1}) from 4.6–293 K consistent with an LS complex, in addition to a low level of the paramagnetic impurity (see Figure 7.8.3.1). This again was consistent with the presence of the MLCT.

A different complex being formed on the polymer may account for this difference; however, unless the polymer is substituted with electron-donating groups of substituents to direct coordination, the polymer backbone will not coordinate. As no coordinating solvents were used during the synthesis, solvent coordination was not possible. This means the only likely coordination species is the $[Fe(bpp)]^{2+}$ complex formed in the SMA; the only explanation is that the same complex core is in different spin states. This may occur because the rigid cyclotriphosphazene of $[Fe(L^4)_2](ClO_4)_2$ strains the core complex. The polymer backbone in $[Fe(L^{4P})_2](ClO_4)_2$ is far more flexible, reducing the strain on the core complex.

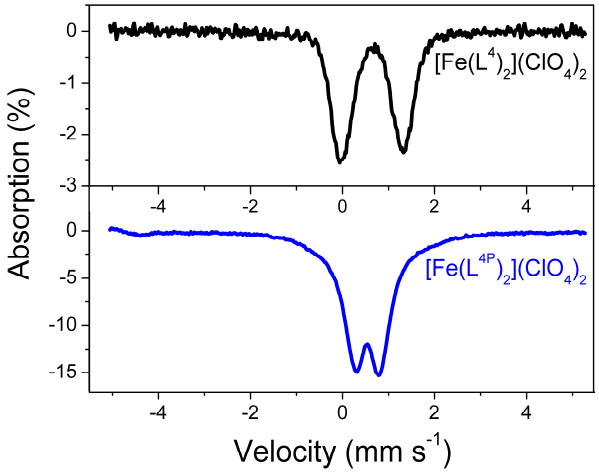

Figure 7.8.3.1 Mössbauer spectra of $[Fe(L^4)_2](ClO_4)_2$ and $[Fe(L^{4P})_2](ClO_4)_2$ collected at 5.6 K and 4.6 K respectively ($[Fe(L^{4P})_2](ClO_4)_2$ enriched with iron-57).

7.9 Conclusion

The electrochemical, electronic, vibrational and magnetic behaviours of the iron(II) metallo-polymers and their SMA were used to assess the coordination behaviour and physical properties of the complexes.

As with the ruthenium analogues, the oxidation potential of the SMA showed that the phosphazene ether groups act as electron-withdrawing groups causing the red shift of the MLCT maximum and cathodic shift of the Fe^{II}/Fe^{III} oxidation. Also, as with the ruthenium analogues, a consistent Hammett parameter could not be determined.

The vibrational and electronic spectra confirmed that $[Fe(L^{1P})_2](ClO_4)_2$ and $[Fe(L^{2P})_2](ClO_4)_2$ formed the same complex core as their SMA. However, with only 5% substitution it was not possible to obtain quality data from $[Fe(L^{3P})_2](ClO_4)_2$, and $[Fe(L^{4P})_2](ClO_4)_2$ displayed an MLCT band but the SMA did not. The difference did not necessarily preclude the existence of the same complex; rather SCO could play a role.

Using variable temperature magnetometry, rR and Mössbauer spectroscopy, it was determined that $[Fe(L^{1})_2](ClO_4)_2$, $[Fe(L^{1})_2](PF_6)_2$ and $[Fe(L^{1P})_2](ClO_4)_2$ were LS for all obtainable temperatures. $[Fe(L^{2})_2](PF_6)_2$ displayed the start of SCO beyond 294 K, while $[Fe(L^{2})_2](ClO_4)_2$ remained LS, and it is suspected that $[Fe(L^{2P})_2](ClO_4)_2$ remains LS but this is difficult to confirm due to the presence of a paramagnetic impurity.

$[Fe(L^{3})_2](BF_4)_2$ displayed an almost complete SCO curve between 200 K and 400 K. Through the course of the measurement, solvent was lost, trapping the complex in the mid spin-state. $[Fe(L^{3})_2](ClO_4)_2$ also displayed the start of SCO at 200 K but due to safety concerns could not be heated beyond 317 K. As with the other measurements, $[Fe(L^{3P})_2](ClO_4)_2$ did not contain enough iron to record either magnetic or Mössbauer data.

$[Fe(L^{4})_2](ClO_4)_2$ and $[Fe(L^{4P})_2](ClO_4)_2$ provided a striking difference in behaviour compared to the OTerpy and OPhTerpy based complexes. $[Fe(L^{4})_2](ClO_4)_2$ remained HS for all temperatures, accounting for the absence of an MLCT band. However, $[Fe(L^{4P})_2](ClO_4)_2$ remained LS for all measureable temperatures. The difference is possibly due to reduced strain on the complex due to a more flexible polymer backbone

rather than a rigid ring. This proves that while many physical properties of polymers can be modelled with SMA, SCO is not always one of them.

7.10 References

1. Hauser, A. In *Spin Crossover in Transition Metal Compounds I* **2004**; Vol. 233, p 49-58.

2. Gutlich, P.; Ksenofontov, V.; Gaspar, A. B. *Coordination Chemistry Reviews* **2005**, *249*, 1811-1829.

3. Hauser, A. In *Spin Crossover in Transition Metal Compounds II* **2004**; Vol. 234, p 155-198.

4. Gutlich, P.; Garcia, Y.; Goodwin, H. A. *Chemical Society Reviews* **2000**, *29*, 419-427.

5. van Koningsbruggen, P. J.; Maeda, Y.; Oshio, H. In *Spin Crossover in Transition Metal Compounds I* **2004**; Vol. 233, p 259-324.

6. Goodwin, H. A. In *Spin Crossover in Transition Metal Compounds II* **2004**; Vol. 234, p 23-47.

7. Garcia, Y.; Gutlich, P. In *Spin Crossover in Transition Metal Compounds II* **2004**; Vol. 234, p 49-62.

8. Shriver, D. F.; Atkins, P. W. *Inorganic Chemistry*; 3rd ed.; Springer: New York, **2002**.

9. Sorai, M. *Spin Crossover in Transition Metal Compounds III* **2004**, *235*, 153-170.

10. Hauser, A. *Spin Crossover in Transition Metal Compounds I* **2004**, *233*, 49-58.

11. Decurtins, S.; Gutlich, P.; Hasselbach, K. M.; Hauser, A.; Spiering, H. *Inorganic Chemistry* **1985**, *24*, 2174-2178.

12. Franke, P. L.; Haasnoot, J. G.; Zuur, A. P. *Inorganica Chimica Acta* **1982**, *59*, 5-9.

13. Sorai, M.; Ensling, J.; Gutlich, P. *Chemical Physics* **1976**, *18*, 199-209.

14. Gutlich, P.; Goodwin, H. A. In *Spin Crossover in Transition Metal Compounds I* **2004**; Vol. 233, p 1-47.

15. Rubio, M.; Lopez, D. *European Polymer Journal* **2009**, *45*, 3339-3346.

16. Roubeau, O.; Colin, A.; Schmitt, W.; Clerac, R. *Angewandte Chemie-International Edition* **2004**, *43*, 3283-3286.

17. Kuroiwa, K.; Kikuchi, H.; Kimizuka, N. *Chemical Communications*, *46*, 1229-1231.

18. Seredyuk, M.; Gaspar, A. B.; Ksenofontov, V.; Galyametdinov, Y.; Kusz, J.; Gutlich, P. *Advanced Functional Materials* **2008**, *18*, 2089-2101.

19. Jeong, S. H.; Kim, K. N.; Kang, J. S.; Hong, C. S.; Choi, D. H.; Jin, J. I.; Park, I. W.; Kim, M. G. *Molecular Crystals and Liquid Crystals* **2007**, *471*, 3-10.

20. Seredyuk, M.; Gaspar, A. B.; Ksenofontov, V.; Reiman, S.; Galyametdinov, Y.; Haase, W.; Rentschler, E.; Gutlich, P. *Chemistry of Materials* **2006**, *18*, 2513-2519.
21. Galyametdinov, Y.; Ksenofontov, V.; Prosvirin, A.; Ovchinnikov, I.; Ivanova, G.; Gutlich, P.; Haase, W. *Angewandte Chemie-International Edition* **2001**, *40*, 4269-4271.
22. Nakamoto, A.; Kojima, N.; Liu, X. J.; Moritomo, Y.; Nakamura, A. *Polyhedron* **2005**, *24*, 2909-2912.
23. Kitchen, J. A.; White, N. G.; Gandolfi, C.; Albrecht, M.; Jameson, G. N. L.; Tallon, J. L.; Brooker, S. *Chemical Communications* **2011**, *46*, 6464-6466.
24. Roubeau, O.; Natividad, E.; Agricole, B.; Ravaine, S. *Langmuir* **2007**, *23*, 3110-3117.
25. Soyer, H.; Dupart, E.; Mingotaud, C.; Gomez-Garcia, C. J.; Delhaes, P. *Colloids and Surfaces a-Physicochemical and Engineering Aspects* **2000**, *171*, 275-282.
26. Boillot, M. L.; Pillet, S.; Tissot, A.; Riviere, E.; Claiser, N.; Lecomte, C. *Inorganic Chemistry* **2009**, *48*, 4729-4736.
27. Lee, S. W.; Lee, J. W.; Jeong, S. H.; Park, I. W.; Kim, Y. M.; Jin, J. I. *Synthetic Metals* **2004**, *142*, 243-249.
28. Chen, Y.; Ma, J. G.; Zhang, J. J.; Shi, W.; Cheng, P.; Liao, D. Z.; Yan, S. P. *Chemical Communications*, *46*, 5073-5075.
29. Djukic, B.; Lemaire, M. T. *Inorganic Chemistry* **2009**, *48*, 10489-10491.
30. Djukic, B.; Dube, P. A.; Razavi, F.; Seda, T.; Jenkins, H. A.; Britten, J. F.; Lemaire, M. T. *Inorganic Chemistry* **2009**, *48*, 699-707.
31. Vulfson, S. G. *Molecular Magnetochemistry*; Nauka Publishers: Moscow, **1998**.
32. Parish, R. V. *NMR, NQR, EPR, and Mossbauer Spectroscopy in Inorganic Chemistry*; Ellis Horwood Limited: Chichester, **1990**.
33. Naik, A. D.; Tinant, B.; Muffler, K.; Wolny, J. A.; Schunemann, V.; Garcia, Y. *Journal of Solid State Chemistry* **2009**, *182*, 1365-1376.
34. Hauser, A. *Chemical Physics Letters* **1990**, *173*, 507-512.
35. Shakirova, O. G.; Lavrenova, L. G.; Daletsky, V. A.; Shusharina, E. A.; Griaznova, T. P.; Katsyuba, S. A.; Syakaev, V. V.; Skripacheva, V. V.; Mustafina, A. R.; Solovieva, S. E. *Inorganica Chimica Acta*, *363*, 4059-4064.
36. Bonhommeau, S.; Molnar, G.; Galet, A.; Zwick, A.; Real, J. A.; McGarvey, J. J.; Bousseksou, A. *Angewandte Chemie-International Edition* **2005**, *44*, 4069-4073.

37. M. J. Frisch; G. W. Trucks; H. B. Schlegel; G. E. Scuseria; M. A. Robb; J. R. Cheeseman; G. Scalmani; V. Barone; B. Mennucci; G. A. Petersson, *et al.*; A.1 ed.; Gaussian, Inc: Wallingford CT, **2009**.

38. Dennington, R.; Keith, T.; Millam, J.; Version 5 ed.; Semichem Inc.: Shawnee Mission KS, **2009**.

39. Alver, O.; Parlak, C.; Senyel, M. *Journal of Molecular Structure* **2009**, *923*, 120-126.

40. Tantirungrotechai, Y.; Phanasant, K.; Roddecha, S.; Surawatanawong, P.; Sutthikhum, V.; Limtrakul, J. *Journal of Molecular Structure-Theochem* **2006**, *760*, 189-192.

41. Horvath, R.; Otter, C. A.; Gordon, K. C.; Brodie, A. M.; Ainscough, E. W. *Inorganic Chemistry* **2010**, *49*, 4073-4083.

42. Tomasi, J.; Mennucci, B.; Cammi, R. *Chemical Reviews* **2005**, *105*, 2999-3093.

43. Hughes, M. C.; Macero, D. J.; Rao, J. M. *Inorganica Chimica Acta* **1981**, *49*, 241-245.

44. Addison, A. W.; Burman, S.; Wahlgren, C. G.; Rajan, O. A.; Rowe, T. M.; Sinn, E. *Journal of the Chemical Society-Dalton Transactions* **1987**, 2621-2630.

45. Rao, J. M.; Hughes, M. C.; Macero, D. J. *Inorganica Chimica Acta* **1976**, *16*, 231-236.

46. Rao, J. M.; Macero, D. J.; Hughes, M. C. *Inorganica Chimica Acta* **1980**, *41*, 221-226.

47. Fordsmith, M.; Sutin, N. *Journal of the American Chemical Society* **1961**, *83*, 1830-1834.

48. McMurtrie, J.; Dance, I. *Crystal engineering communication* **2009**, *11*, 1141-1149.

49. Linert, W.; Konecny, M.; Renz, F. *Journal of the Chemical Society-Dalton Transactions* **1994**, 1523-1531.

50. Bhaumik, C.; Das, S.; Saha, D.; Dutta, S.; Baitalik, S. *Inorganic Chemistry* **2010**, *49*, 5049-5062.

51. Holland, J. M.; McAllister, J. A.; Kilner, C. A.; Thornton-Pett, M.; Bridgeman, A. J.; Halcrow, M. A. *Journal of the Chemical Society-Dalton Transactions* **2002**, 548-554.

52. Boca, R.; Renz, F.; Boca, M.; Fuess, H.; Haase, W.; Kickelbick, G.; Linert, W.; Vrbova-Schikora, M. *Inorganic Chemistry Communications* **2005**, *8*, 227-230.

53. Baker, W. A.; Bobonich, H. M. *Inorganic Chemistry* **1964**, *3*, 1184-1188.

54. Hayami, S.; Urakami, D.; Kojima, Y.; Yoshizaki, H.; Yamamoto, Y.; Kato, K.; Fuyuhiro, A.; Kawata, S.; Inoue, K. *Inorganic Chemistry*, *49*, 1428-1432.

55. Allcock, H. R.; Suszko, P. R.; Wagner, L. J.; Whittle, R. R.; Boso, B. *Organometallics* **1985**, *4*, 446-457.

56. Allcock, H. R.; Neenan, T. X.; Boso, B. *Inorganic Chemistry* **1985**, *24*, 2656-2662.

57. Allcock, H. R.; Suszko, P. R.; Wagner, L. J.; Whittle, R. R.; Boso, B. *Journal of the American Chemical Society* **1984**, *106*, 4966-4977.

58. Enamullah, M.; Renz, F.; ElAyaan, U.; Wiesinger, G.; Linert, W. *Vibrational Spectroscopy* **1997**, *14*, 95-104.

Conclusion and final remarks

This investigation had two main objectives:

i) to determine the feasibility of a spin crossover (SCO) grafted polymer, and
ii) to use ruthenium(II) complexes to attach other groups to a polyphosphazene backbone.

To this end, four different tridentate ligands (2,6-di(pyridine-2-yl)pyridine-4(1*H*)-onate (OTerpy); 4-(2,6-di{pyridin-2-yl}-pyridine-4-yl)phenolate (OPhTerpy); 2,6-di(1*H*-benzoimidazol-2-yl)pyridine-4(1*H*)-onate (Obbp); and 4-(2,6-di{1*H*-pyrazol-1-yl}pyridine-4-yl)phenolate (OPhbpp)) were attached to both the polyphosphazene and cyclotri- and polyphosphazene ligands to act as small molecule analogues (SMA).

The synthesis of the ligands (L^1–$L^7$and L^{1P}–L^{4P}) demonstrated that for the substituents OTerpy and Obbp, the enone tautomer was favoured. As a result, only one ligand would attach per phosphorus atom and the reactions were typically slow. However, for the substituents containing a phenyl spacer (OPhTerpy and OPhbpp) the phenol tautomer was favoured, leading to rapid and complete reactions. Each of the polymers contained unreacted P-Cl units; this is predominately due to steric hindrance around the reactive site. In future projects, this could be improved by using either phenol or 4-methylphenol in place of 4-tert-butlyphenol.

When the ligands (L^1–L^7 and L^{1P}–L^{4P}) were reacted with iron(II) salts, homoleptic iron(II)-bis-ligand complexes were formed. For the polymers, this initially caused intra-chain linking possibly forming loops, but after time passed or solvent was removed inter-chain cross-linking occurred. This resulted in insoluble materials being formed. Through the use of electronic absorbance, resonance Raman (rR), magnetometry and Mössbauer spectroscopies it was determined that the polymers $[Fe(L^{1P})_2](ClO_4)_2$ and $[Fe(L^{2P})_2](ClO_4)_2$ had the same complex core as their SMA ($[Fe(L^1)_2](ClO_4)_2$ and $[Fe(L^2)_2](ClO_4)_2$). With the exception of $[Fe(L^2)_2](PF_6)_2$ each of the OTerpy and OPhTerpy based iron complexes was determined to be low spin (LS) for all measureable temperatures. $[Fe(L^2)_2](PF_6)_2$ displayed the start of SCO beyond 294 K,

but a full SCO curve could not be obtained within the instrument temperature range (4 – 400 K).

The low ratio of iron complex for $[Fe(L^{3P})_2](ClO_4)_2$ prevented the acquisition of high quality data. Its SMA ($[Fe(L^{3})_2](ClO_4)_2$) displayed the start of SCO but due to safety concerns it could not be heated further, but $[Fe(L^{3})_2](BF_4)_2$, being safer to heat, displayed an almost complete SCO curve between 200 K and 400 K. Once heated the solvent was also lost, trapping the complex in the medium-spin state.

The iron-OPhbpp based complexes ($[Fe(L^{4})_2](ClO_4)_2$ and $[Fe(L^{4P})_2](ClO_4)_2$) displayed a difference compared to that of the OPhTerpy and OTerpy based complexes. It is assumed that the polymer forms the same homoleptic iron(II)-bis-ligand complex core that the SMA does. However, the polymer remained LS for all measureable temperatures, but the SMA remained high spin (HS) for all temperatures. This difference is possible due to the flexible polymer backbone reducing the strain on the complex core that may have occurred with the rigid phosphazene rings of the SMA.

While this investigation may not have produced an ideal SCO grafted polymer, the difficulties encountered and fundamental behaviour required for such a system to work have been determined. Ideally, when using a polyphosphazene backbone, a coordinating substituent should be chosen to have: i) a phenyl spacer between the coordination centre and the attaching nucleophile (e.g. phenol) to allow a fast and complete reaction, ii) SCO of the groups should be relatively independent of its environment and tolerant to some strain induced by attaching a phosphazene similar to the Obbp based complexes. Additionally, to prevent cross-linking, thereby improving solubility of the metallopolymer, higher dentate ligands could be used as the substituent, i.e. macrocycles or by attaching to each phosphorous atom forming a pseudo-tetradentate ligand.

The OTerpy (L^{1} and L^{1P}) and OPhTerpy (L^{2} and L^{2P}) based ligands proved to be an effective basis for attaching groups to a polyphosphazene backbone via ruthenium complexes. Due to ruthenium (II) kinetic inertness, the complexes could be formed in a stepwise fashion in relatively mild conditions. Through the use of electronic absorbance and rR spectroscopy it was possible to determine that the polymers ($[Ru(L^{1P})(Terpy)]Cl_2$, ($[Ru(L^{1P})(PhTerpy)]Cl_2$, $[Ru(L^{2P})(Terpy)]Cl_2$ and ($[Ru(L^{2P})(PhTerpy)]Cl_2$) had the same core complex as the SMA

([Ru(L^1)(Terpy)](PF_6)$_2$, ([Ru(L^1)(PhTerpy)](PF_6)$_2$, [Ru(L^2)(Terpy)](PF_6)$_2$ and ([Ru(L^2)(PhTerpy)](PF_6)$_2$). Although rR determined that the enhanced vibrational modes of the metal-to-ligand charge transfer (MLCT) band were predominantly independent of the phosphazene ring, the oxidation potentials of the complexes were cathodically shifted and the MLCT band was bathochromically shifted relative to the hydrogen-substituted analogues. This confirmed that the phosphazene ether bond was acting as an electron-withdrawing group.

As with the iron complexes, both [Ru(L^{3P})(Terpy)]Cl_2 and [Ru(L^{3P})(PhTerpy)]Cl_2 had a low complex ratio; this meant quality data could not be obtained. As previously discussed, the addition of a phenyl spacer for this substituent would make it possible to improve the ratio. The SMA ([Ru(L^3)(Terpy)](PF_6)$_2$, [Ru(L^3)(PhTerpy)](PF_6)$_2$, [Ru(L^1)(bbp)](PF_6)$_2$ and [Ru(L^1)(bbp)](PF_6)$_2$) displayed a dependence solution basicity; as it increased, the imidazole protons were removed, forming an equilibrium between the mono-protonated and deprotonated complexes. This change in protonation caused a bathochromic shift of the MLCT bands, vibrational modes and oxidation potentials, similar to the behaviour of [Fe(2,6-di{1*H*-benzoimidazol-2-yl}pyridine)(2,2':6',2''-terpyridine)](ClO_4).

The small molecule complexes based on the Ru-2,6-di(1*H*-pyrazol-1-yl)pyridine-2,2':6',2''-terpyridine moiety demonstrated a new way of synthesising this class of complex using relatively mild conditions. However, the electronic absorption and rR spectra of their polymer analogues ([Ru(L^{4P})(Terpy)]Cl_2 and [Ru(L^{4P})(PhTerpy)]Cl_2) determined that they did not contain the same metal coordination centre; rather it was suggestive, but not conclusive, that one of the chloride atoms remained coordinated to the ruthenium atom. This behaviour made it unsuitable for attaching groups to the polymer backbone but may warrant further investigation for other purposes.

For the purpose of attaching groups to a polyphosphazene backbone via metal coordination, the OTerpy and OPhTerpy substituents coordinated to ruthenium(II) were effective, although OPhTerpy has the advantage of a more rapid and complete synthesis of the polymer ligand. With these substituents established as the most suitable in future research, the ratio of coordination centres could be varied to assess the effect and longer alkyl groups attached to the co-substituents to improve solubility without increasing the

steric hindrance of branched alkyl groups. With the groundwork established, more complex groups other than phenyl will no doubt be added in future investigations.

Appendix

Appendix A: Chapter 2 Supplementary

A.1 Ligand Synthesis

A.1.1 General Experimental

Analytical grades of solvents were used, except tetrahydrofuran (THF), which was dried over an alumina column. 2,2,3,3-bis(2,2′-biphenoxy)-1,1-bischlorocyclotriphosphazene[1] ($P_3N_3(Biphen)_2Cl_2$), 1,2,2,3,3-pentakis(phenoxy)-1-chlorocyclotriphosphazene[2] ($P_3N_3(OPh)_5Cl$) 2,6-Bis(2-pyridyl)-4(1*H*)-pyridone (HOTerpy)[3], 4-(2,6-di{pyridin-2-yl}-pyridine-4-yl)phenol (HOPhTerpy)[4], 2,6-di(1*H*-benzoimidazol-2-yl)pyridine-4(1*H*)-one (HObbp)[5], 4-phenol-2,6-bis(1-pyrazolyl)pyridine (HOPhbpp)[6], 4-methoxy-2,6-di(1*H*-pyrazol-1-yl)pyridine[7] were synthesised by literature methods. K_2CO_3, NaH (60% dispersed in mineral oil), phenol, 2,2′-Biphenol (Biphen), tetrabutylammonium bromide (TBAB), quinolin-8-amine, 2,5-dihydroxybenzaldehyde and 1,1,2,2,3,3,4,4,4-nonafluorobutane-1-sulfonyl fluoride (NfF) were all sourced from Aldrich. All manipulations were carried out under an argon atmosphere, using standard Schlenk techniques. Microanalysis was performed at the Campbell Micro-analytical Laboratory, University of Otago after samples were dried under vacuum at 50°C for at least 24 hours. Phosphorus and fluorine NMR data was recorded on a Bruker Avance A400 spectrometer, and proton NMR data was recorded on a Bruker Avance A500 spectrometer. Proton data was internally referenced to tetramethyl silane (TMS), phosphorus data were referenced to an external sample of 80% ortho phosphoric acid and fluorine data were referenced to an external reference of trifluoroethanol. NMR data were assigned using 2D NMR and Density Functional Theory (DFT) simulations. ESMS were obtained from an acetonitrile solution on a micromass ZMD spectrometer run in the positive ion mode. Listed peaks correspond to the most abundant isotope. Assignments were made by comparison of observed and measured spectra. All values stated in this section were recorded at room temperature.

A.1.2 Experimental Details

A.1.2.1 $N_3P_3(OPh)_5(OTerpy)$ (L^1)

$N_3P_3(OPh)_5Cl$ (100 mg, 0.16 mmol) was added to a solution containing HOTerpy (40 mg, 0.16 mmol) and NaH (9 mg, 0.22 mmol) in THF (30 mL). After stirring at reflux for three days the solvent was removed under reduced pressure, leaving a white oil which was washed with CH_2Cl_2/water and dried over $MgSO_4$. The oil was purified by column chromatography on silica gel with CH_2Cl_2/hexane (1:1) as the eluent, producing a colourless viscous oil. Yield: 73 mg (54%).

ESMS: m/z 849 $[N_3P_3(OPh)_5(OTerpy)H]^+$. $^{31}P\{^1H\}$ NMR ($CDCl_3$): δ 8.9 ppm (s, 3P). ^1H NMR ($CDCl_3$): δ 8.68 ppm (d (5 Hz), 2H), 8.62 (d (8), 2H), 8.38 (s, 2H), 7.85 (t (8), 2H), 7.32 (t (8), 2H), 7.28 (t (8), 2H), 7.20 (d (8), 10H), 7.16 (t (8), 8H), 7.05 (d (8), 5 H). Anal. Calc. for $C_{45}H_{36}N_6O_6P_3.CH_2Cl_2.2C_6H_{14}$: C, 62.93; H, 6.01; N, 7.59%. Found: C, 63.34; H, 5.95; N, 7.30%.

A.1.2.2 $N_3P_3(OPh)_5(OPhTerpy)$ (L^2)

$N_3P_3(OPh)_5Cl$ (100 mg, 0.16 mmol) was added to a solution containing HOPhTerpy·3HCl (75 mg, 0.17 mmol) and NaH (34 mg, 0.85 mmol) in THF (30 mL). After stirring at reflux overnight the solvent was removed under reduced pressure, leaving a white oil which was washed with CH_2Cl_2/water and dried over $MgSO_4$. The oil was purified by column chromatography on silica gel with CH_2Cl_2:hexane (1:1) as the eluent, producing a colourless viscous oil. Yield: 130 mg (88 %).

ESMS: m/z 926 $[N_3P_3(OPh)_5(OPhTerpy)H]^+$. $^{31}P\{^1H\}$ NMR ($CDCl_3$): δ 9.50 ppm. ^1H NMR ($CDCl_3$): δ 8.76 ppm (d (6 Hz), 2H), 8.72 (s, 2H), 8.70(d (8), 2H), 7.89 (t (8), 2H), 7.69 (d (8), 2H), 7.36 (t (8), 2H), 7.27-7.20 (m, 10H), 7.17-7.16 (m, 5H), 7.08 (d (8), 2H), 7.04-6.97 (m, 10H). Anal. Calc. for: $C_{51}H_{39}N_6O_6P_3 \cdot {}^2/_3C_6H_{14}$: C, 67.25; H, 4.96; N, 8.56 %. Found: C, 67.16; H, 4.98; N, 8.23 %.

A.1.2.3 $N_3P_3(OPh)_5(Obbp)$ (L^3)

$N_3P_3(OPh)_5Cl$ (195 mg, 0.31 mmol) was added to a solution containing HObbp (100 mg, 0.31 mmol) and K_2CO_3 (45 mg, 0.33 mmol) in acetone (50 mL). After stirring at reflux for five days the solvent was removed under reduced pressure, leaving a pink solid that was washed with $CHCl_3$/water and dried over $MgSO_4$. A minimal amount of hexane was added to the solution to form a white precipitate. The precipitate was filtered and dried under vacuum. Colourless crystals were grown via a slow evaporation of an acetone solution. Yield: 140 mg (51%).

ESMS: m/z 927 $[N_3P_3(OPh)_5(Obbp)H]^+$, 965$[N_3P_3(OPh)_5(Obbp)K]^+$. $^{31}P\{^1H\}$ NMR ($CDCl_3$): δ 9.6 ppm (s, 3P). ^1H NMR ($CDCl_3$): δ 8.02 ppm (s, 2H), 7.40 (s, 2H), 7.05-7.00 (m, 10H), 6.95 (d (8 Hz), 10H), 6.81 (t (8), 8H), 6.77 (d (8), 5H). Anal. Calc. for $C_{49}H_{37}N_8O_6P_3 \cdot {}^2/_3CHCl_3$: C, 59.28; H, 3.77; N, 11.13%. Found: C, 59.18; H, 3.76; N, 11.06%.

A.1.2.4 $N_3P_3(OPh)_5(OPhbpp)$ (L^4)

The same procedure as OPhTerpy-1 was used except HOPhbpp (51 mg, 0.17 mmol) was used in place of HOPhTerpy·3HCl, producing a colourless viscous oil. Yield: 100 mg (70 %).

ESMS: m/z 904 $[N_3P_3(OPh)_5(OPhbpp)H]^+$. $^{31}P\{^1H\}$ NMR ($CDCl_3$): δ 9.32 ppm. ^1H NMR ($CDCl_3$): δ 8.51 ppm (d (3 Hz), 2H), 8.34 (s, 2H), 7.76 (s, 2H), 7.60 (d (8), 2H), 7.35-7.32 (m, 4H), 7.29 (s, 2H), 7.25 (t (8), 2H), 7.16 (d (8), 6H), 7.13 (t (3), 4H), 6.94 (d (8), 6H), 6.86 (d (8), 2H), 6.49 (d (8), 2H). Anal. Calc. for $C_{47}H_{37}N_8O_6P_3 \cdot 2C_6H_{14} \cdot {}^1/_3CHCl_3$: C, 63.94; H, 5.91; N, 10.05 %. Found: C, 63.95; H, 5.67; N, 9.79 %.

A.1.2.5 $N_3P_3(Biphen)_2(OPh)(OTerpy)$ (L^5)

$N_3P_3(Biphen)_2Cl_2$ (200 mg, 0.35 mmol) was added to a solution containing HOTerpy (86 mg, 0.35 mmol) and NaH (28 mg, 0.70 mmol) in THF (30 mL). After refluxing for three days, phenol (32 mg, 0.35 mmol) was added. Refluxing was continued for an additional day before the solvent was removed under reduced pressure, leaving a white solid. The white solid was washed with CH_2Cl_2/water and dried over $MgSO_4$. A minimal amount of hexane was added to form a white precipitate, which was filtered and dried under vacuum. Colourless crystals were grown via a slow evaporation of a CH_2Cl_2/hexane solution. Yield: 200 mg (66%).

ESMS: m/z 845 $[N_3P_3(Biphen)_2(OPh)(OTerpy)H]^+$. $^{31}P\{^1H\}$ NMR ($CDCl_3$): δ 9.4 ppm (t (92 Hz), 1P), 25.3 (d (92), 2P). ^1H NMR ($CDCl_3$): δ 8.74 ppm (d (5 Hz), 2H), 8.66 (d (8), 2H), 8.58 (s, 2H), 7.86 (t (8), 2H), 7.49 (d (7), 4H), 7.43 (t (8), 2H), 7.36 (t (8), 4H), 7.28 (m, 9H), 7.21 (t (8), 2H), 7.15 (d (8), 2H). Anal. Calc for $C_{45}H_{31}N_6O_6P_3 \cdot 2½H_2O$: C, 60.75; H, 4.08; N, 9.45%. Found: C, 60.69; H, 4.19; N, 9.42%.

A.1.2.6 $N_3P_3(Biphen)_2(OPh)(OPhTerpy)$ (L^6)

$N_3P_3(Biphen)_2Cl_2$ (100 mg, 0.17 mmol) was added to a solution containing HOPhTerpy·3HCl (75 mg, 0.17 mmol) and NaH (35 mg, 0.85 mmol) in THF (30 mL). After refluxing for a day phenol (32 mg, 0.35 mmol) was added. Refluxing was continued for an additional day before the solvent was removed under reduced pressure, leaving a white solid. The white solid was washed with CH_2Cl_2/water and dried over $MgSO_4$. A minimal amount of hexane was added to form a white precipitate, which was filtered and dried under vacuum. Yield: 126 mg (81 %).

ESMS: m/z 921 $[N_3P_3(Biphen)_2(OPh)(OPhTerpy)H]^+$. $^{31}P\{^1H\}$ NMR ($CDCl_3$): δ 10.25 ppm (t (90 Hz), 1P), 26.26 (d (90), 2P). ^1H NMR ($CDCl_3$): δ 8.75 ppm (d (6 Hz), 2H), 8.73 (s, 2H), 8.69 (d (8), 2H), 7.90 (t (8), 4H), 7.52 (d (8), 2H), 7.45-7.33 (m, 13H), 7.32 (t (8), 4H), 7.28 (t (8), 2H), 7.07 (d (8), 2H), 7.05 (d (8), 2H). Anal. Calc. for $C_{51}H_{35}N_6O_6P_3 \cdot {}^3/_4H_2O$: C, 64.63; H, 4.04; N, 8.87 %. Found: C, 64.97; H, 4.34; N, 8.50%.

A.1.2.7 $N_3P_3(Biphen)_2(OPh)(Obbp)$ (L^7)

$N_3P_3(Biphen)_2Cl_2$ (175 mg, 0.30 mmol) was added to a solution containing HObbp (100 mg, 0.31 mmol) and K_2CO_3 (45 mg, 0.33 mmol) in acetone (50 mL). After refluxing for five days, sodium phenoxide (40 mg, 0.33 mmol) was added. Refluxing was continued for an additional day before the solvent was removed under reduced pressure, leaving a pink solid. The solid was washed with CH_2Cl_2/water and dried over $MgSO_4$. A minimal amount of hexane added to form a white precipitate, which was filtered and dried. Colourless crystals were grown by the slow evaporation of an acetone solution. Yield: 150 mg (54%).

ESMS: m/z 923 $[P_3N_3(Biphen)_2(OPh)(Obbp)H]^+$, 961 $[P_3N_3(Biphen)_2(OPh)(Obbp)K]^+$. $^{31}P\{^1H\}$ NMR ($CDCl_3$): δ 9.4 ppm (t (95 Hz), 1P), 25.1 (d (95), 2P). ^1H NMR ($CDCl_3$): δ 8.24 ppm (s, 2H), 7.59 (s, 2H), 7.51 (d (8 Hz), 4H), 7.23 (t (8), 8H), 7.12-7.35 (m, 13H), 6.90 (d (8), 4H). Anal. Calc. for $C_{49}H_{33}N_8O_6P_3.3H_2O$: C, 60.25; H, 4.02; N, 11.47%. Found: C, 59.66; H, 4.07; N, 11.38%.

A.1.2.8 2-((quinolin-8-ylimino)methyl)benzene-1,4-diol (HOQSal)

To a solution of quinolin-8-amine (500 mg, 4.33 mmol) in ethanol (50 mL) 2,5-dihydroxybenzaldehyde (597 mg, 4.33 mmol). The solution was refluxed for five days, before the solvent was removed under vacuum, producing a red solid. The solid was dissolved in acetone and filtered. The filtrate was dried under vacuum leaving a pure product. Yield: 1g (90%).

ESMS: m/z 265 $[HOQSalH]^+$. ^1H NMR ($CDCl_3$): δ 8.97 ppm (s, 1H), 8.96 (d (5 Hz), 1H), 8.42 (d (8), 1H), 7.90 (d (8), 1H), 7.69 (m, 2H), 7.61 (d (8), 1H), 7.07 (s, 1H), 6.91 (d (8), 1H), 6.84 (d (8), 1H), 3.36 (s, 2H). ^{13}C NMR ($CDCl_3$): δ 164.76 ppm, 154.24, 150.97, 149.94, 145.88, 142.28, 136.66, 129.19, 127.28, 126.82, 122.54, 121.81, 119.86, 118.77, 117.82, 117.45. Anal. Calc. for $C_{16}H_{12}N_2O_2 \cdot H_2O$: C, 68.08; H, 5.00; N, 9.92 %. Found: C, 68.79; H, 4.62; N, 10.08 %.

A.1.2.9 2,6-di(1*H*-benzoimidazol-2-yl)pyridin-4-yl 1,1,2,2,3,3,4,4,4-nonfluorobutane-1-sulfonate (NfObbp)

HObbp (500mg, 1.53 mmol) was dispersed in THF (100 mL). NfF (465 mg, 1.54 mmol) and NaH (65 mg, 1.60 mmol) were added, the solution was stirred for 8 hours before being filtered; the filtrate solvent was removed under reduced pressure. The solid was dissolved in dichloromethane and washed with water; the organic layer was dried with magnesium sulphate before the solvent was removed under vacuum leaving a pink solid, that was washed with diethyl ether and left to dry. Yield: 744 mg (80 %).
ESMS: m/z 610 $[NfObbpH]^+$. $^{19}F\{^1H\}$ NMR (C_4D_8O): δ -82.3 ppm (s, 3F), -109.2 (s, 2F), -115.9 (s, 2F), -122.1 (s, 2F), -126.8 (s, 2F), ^1H NMR (C_4D_8O): δ 7.81 ppm (s, 2H), 7.68 (d (J = 8 Hz), 4H), 7.29 (t (8), 4H), 4.65(s, broad, 2H). ^{13}C NMR (C_4D_8O): δ 172.9 ppm (s), 150.5 (s), 146.2 (s), 119.9 (s), 119.3 (t (J = 27 Hz)), 117.2 (t (34)), 114.4 (t (34)), 112.3 (t (34)), 111.3 (s), 108.9 (pent (34)), 107.9 (pent (34)). Anal. Calc. for $C_{23}H_{12}F_9N_5O_3S \cdot 3OC_4H_8 \cdot ½H_2O$: C, 50.00; H, 5.15; N, 8.33 %. Found: C, 49.92; H, 4.62; N, 7.78 %.

A.1.2.10 4-(2,6-di(1*H*-benzoimidazol-2-yl)pyridin-4-yl)phenol (HOPhbbp)

NfObbp (400mg, 0.66 mmol), 4-hydroxyphenylboronic acid (91 mg, 0.66 mmol) and $Pd(0)(PPh_3)_4$ (10 mol %) were suspended in argon-flushed solvents of methanol and toluene (1:1, 100 mL) and 2M Na_2CO_3 (8 mL). The mixture was heated to 70°C for two days under an argon atmosphere. The reaction mixture was dried under reduced pressure, leaving a white solid. Water (100 mL) was added to the remaining solid, forming a suspension; this was filtered and the solid was washed with dichloromethane leaving a white solid. Yield: 188 mg (71 %).
ESMS: m/z 404 $[HOPhbbpH]^+$.

A.2 Selected bond lengths

Table A.2.1 Selected bond lengths (Å) of $L^3 \cdot 3H_2O \cdot C_3H_6O$, $L^5 \cdot 2CH_2Cl_2$ and $L^7 \cdot C_3H_6O \cdot H_2O$.

$L^3 \cdot 3H_2O \cdot C_3H_6O$		$L^5 \cdot 2CH_2Cl_2$		$L^7 \cdot C_3H_6O \cdot H_2O$	
P(1) – N(1)	1.584 (4)	P(1) – N(1)	1.587 (3)	P(1) – N(1)	1.623 (3)
P(1) – N(3)	1.582 (4)	P(1) – N(3)	1.582 (3)	P(1) – N(3)	1.581 (3)
P(2) – N(1)	1.589 (4)	P(2) – N(1)	1.580 (3)	P(2) – N(1)	1.529 (3)
P(2) – N(2)	1.572 (4)	P(2) – N(2)	1.577 (3)	P(2) – N(2)	1.586 (3)
P(3) – N(2)	1.585 (5)	P(3) – N(2)	1.582 (3)	P(3) – N(2)	1.625 (3)
P(3) – N(3)	1.581 (4)	P(3) – N(3)	1.579 (3)	P(3) – N(3)	1.510 (3)

A.3 References

1. Carriedo, G. A.; Alonso, F. J. G.; Soto, A. P. *Journal of Inorganic and Organometallic Polymers and Materials* **2007**, *17*, 399-406.

2. McBee, E. T.; Okuhara, K.; Morton, C. J. *Inorganic Chemistry* **1966**, *5*, 450-457.

3. Constable, E. C.; Ward, M. D. *Journal of the Chemical Society-Dalton Transactions* **1990**, 1405-1409.

4. Spahni, W.; Calzaferri, G. *Helvetica Chimica Acta* **1984**, *67*, 450-454.

5. Drew, M. G. B.; Hill, C.; Hudson, M. J.; Iveson, P. B.; Madic, C.; Vaillant, L.; Youngs, T. G. A. *New Journal of Chemistry* **2004**, *28*, 462-470.

6. Chandrasekar, R.; Schramm, F.; Fuhr, O.; Ruben, M. *European Journal of Inorganic Chemistry* **2008**, 2649-2653.

7. Rodriguez-Ubis, J. C.; Sedano, R.; Barroso, G.; Juanes, O.; Brunet, E. *Helvetica Chimica Acta* **1997**, *80*, 86-96.

Appendix B: Chapter 3 Supplementary

B.1 Iron(II) Complex Synthesis

B.1.1 General Experimental

Analytical grades of solvents were used, each of which was bubbled with argon prior to use. $Ag(CH_3CN)_4PF_6$[1] and $Ag(CH_3CN)_4BF_4$[1] were synthesised by literature methods. $Fe(ClO_4)_2 \cdot 4H_2O$, $Fe(BF_4)_2 \cdot 6H_2O$ and $FeCl_2 \cdot 4H_2O$ were all sourced from Aldrich. All manipulations were carried out under an argon atmosphere, using standard Schlenk techniques. Microanalysis was performed at the Campbell Microanalytical Laboratory, University of Otago after samples were dried under vacuum at 50°C for at least 24 hours. Phosphorus nuclear magnetic resonance (NMR) data were recorded on a Bruker Avance A400 spectrometer, and proton NMR data were recorded on a Bruker Avance A500 spectrometer. Proton data were internally referenced to TMS, phosphorus data were referenced to an external sample of 80% ortho phosphoric acid. NMR data were assigned using 2D NMR and density function theory (DFT) simulations. Electrospray mass spectra were obtained from an acetonitrile solution on a micromass ZMD spectrometer run in the positive ion mode. Listed peaks correspond to the most abundant isotopmer. Assignments were made by comparison of observed and measured spectra. All values stated in this section were recorded at room temperature.

Caution! Perchlorate salts with organic ligands are potentially explosive and should be handled with the necessary precautions

B.1.2 Experimental Details

B.1.2.1a $[Fe(L^1)_2](ClO_4)_2$

To a stirred solution of L^1 (100 mg, 0.11 mmol) in MeOH:$CHCl_3$ (1:1, 8 mL), $Fe(ClO_4)_2 \cdot 6H_2O$ (4.0 mg, 0.066 mmol) was added, immediately turning the solution purple. Stirring was continued for 30 minutes before the solvent was removed under reduced pressure. The solid was dissolved in $CHCl_3$ and filtered through celite. The filtrate was dried under reduced pressure, leaving a purple solid. Crystals were grown by dissolving the solid in acetonitrile and vapour diffusion of diethyl ether, producing thin needles. Yield: 78 mg (68 %).

ESMS: m/z 876 $[Fe(L^1)_2]^{2+}$. $^{31}P\{^1H\}$ NMR (CD_3CN): δ 11.1 ppm (m, 6P), ^1H NMR (CD_3CN): δ 8.70 ppm (s, 4H), 8.18 (d (8 Hz), 4H), 7.68 (t (8), 4H), 7.42 (t (8), 4H), 7.36-7.15 (m, 42H), 7.04 (t (8), 4H), 6.98 (d (6), 4H), 6.93 (d (8), 4H). Anal. Calc. for $C_{90}H_{70}Cl_2FeN_{12}O_{20}P_6 \cdot 2½C_4H_{10}O \cdot 2H_2O$: C, 55.16; H, 4.77; N, 7.72 %. Found: C, 55.31; H, 4.60; N, 7.68 %.

B.1.2.1b $[Fe(L^1)_2](PF_6)_2$

To a stirred solution of L^1 (100 mg, 0.11 mmol) in MeOH:$CHCl_3$ (1:1, 8 mL), $FeCl_2 \cdot 4H_2O$ (22 mg, 0.11 mmol) was added immediately turning the solution purple. Stirring was continued for 30 minutes before the solvent was removed under reduced pressure, leaving a purple solid. The solid was dissolved in $CHCl_3$ and filtered through celite. The filtrate was dried under reduced pressure leaving a purple solid. This solid was dissolved in CH_3CN (5 mL) and $Ag(CH_3CN)_4(PF_6)$ (85 mg, 0.33 mmol) was added, immediately forming a white precipitate. The solution was stirred for 30 minutes before the solvent was removed under reduced pressure. The solid was dissolved in $CHCl_3$ and filtered through celite. The filtrate was dried under reduced pressure leaving a purple solid. The purple solid was dissolved in $CHCl_3$ and precipitated with hexane for analysis. Crystals were grown by dissolving the compound in CH_3CN and precipitated by vapour diffusion of diethyl ether, to produce thin needles. Yield: 76 mg (64 %).

ESMS: m/z 876 $[Fe(L^1)_2]^{2+}$. $^{31}P\{^1H\}$ NMR (CD_3CN): δ 10.6 ppm (m, 6P), -143.1 (sep (792 Hz), 2P). ^1H NMR (CD_3CN): δ 8.70 ppm (s, 4H), 8.17 (d (8 Hz), 4H), 7.78 (t (8),

4H), 7.39 (t (8), 4H), 7.32-7.12 (m, 42 H), 7.04 (t (8), 4H), 7.02 (d (6), 4H), 6.93 (d (8), 4H). Anal. Calc. for $C_{90}H_{70}F_{12}FeN_{12}O_{12}P_8 \cdot 3^1/_4CHCl_3$: C, 46.07; H, 3.04; N, 6.91 %. Found: C, 46.09; H, 3.09; N, 6.96.

B.1.2.1c $[Fe(L^1)_2](BF_4)_2$

The same procedure as for $[Fe(L^1)_2](PF_6)_2$ was used, except $Ag(CH_3CN)_4BF_4$ was used in place of $Ag(CH_3CN)_4PF_6$ producing a purple solid. The purple solid was dissolved in $CHCl_3$ and precipitated with hexane for analysis. Yield: 70 mg (66 %).

ESMS: m/z 876 $[Fe(L^1)_2]^{2+}$. $^{31}P\{^1H\}$ NMR (CD_3CN): δ 10.35 ppm (m, 6P). ^1H NMR (CD_3CN): δ 8.70 ppm (s, 4H), 8.17 (d (8 Hz), 4H), 7.78 (d (8), 4H), 7.39 (t (8, 4 H), 7.32-7.12 (m, 42H), 7.04 (t (8), 4H), 7.02 (d (6), 4H), 6.93 (d (8), 4H). Anal. Calc. $C_{90}H_{70}B_2F_8FeN_{12}O_{12}P_6 \cdot 3½C_6H_{14}$: C, 59.83; H, 5.38; N, 7.54 %. Found: C, 59.84; H, 4.97; N, 7.26 %.

B.1.2.2a $[Fe(L^2)_2](ClO_4)_2$

The procedure as for $[Fe(L^1)_2](ClO_4)_2$ was used; however, L^2 was used in place of L^1, forming a purple solid. Non-diffractable purple crystals were formed by vapour diffusion of diethyl ether into acetonitrile. The solid was dissolved in chloroform and precipitated with hexane for analysis. Yield: 60 mg (53%).

ESMS: m/z 953 $[Fe(L^2)_2]^{2+}$. $^{31}P\{^1H\}$ NMR (CD_3CN): δ 10.3 ppm (s, 6P). ^1H NMR (CD_3CN): 9.14 ppm (s, 4H), 8.65 (d (8 Hz), 4H), 8.25 (d (8), 4H), 7.59 (t (8), 4H), 7.42-7.29 (m, 26H), 7.24 (d (8), 4H), 7.13 (t (8), 12H), 7.04 (d (8), 4H), 6.98 (d (8), 8H). Anal. Calc. for $C_{102}H_{78}Cl_2FeN_{12}O_{20}P_6 \cdot {}^1/_2CHCl_3$. C, 56.89; H, 3.66; N, 7.77 %. Found: C, 56.76; H, 3.41; N, 7.76 %.

B.1.2.2b $[Fe(L^2)_2](PF_6)_2$

The procedure as for $[Fe(L^1)_2](PF_6)_2$ was used; however, L^2 was used in place of L^1. The purple solid was dissolved in $CHCl_3$ and precipitated with hexane for analysis. Purple crystals were grown via vapour diffusion of Et_2O into a CH_3CN solution. Yield: 72 mg (59 %).

ESMS: m/z 953 $[Fe(L^2)_2]^{2+}$. $^{31}P\{^1H\}$ NMR (CD_3CN): δ 10.3 ppm (s, 6P), -143.2 (sep (708 Hz), 2P). ^1H NMR (CD_3CN): 9.14 ppm (s, 4H), 8.65 (d (8 Hz), 4H), 8.25 (d (8), 4H), 7.59 (t (8), 4H), 7.42-7.29 (m, 26H), 7.24 (d (8), 4H), 7.13 (t (8), 12H), 7.04 (d (8), 4H), 6.98 (d (8), 8H). Anal. Calc. for: $C_{102}H_{78}F_{12}FeN_{12}O_{12}P_8 \cdot 1½CHCl_3$: C, 52.33; H, 3.37; N, 7.07 %. Found: C, 52.26, H, 3.63; N, 7.18 %.

B.1.2.3a $[Fe(L^3)_2](ClO_4)_2$

The same procedure as for $[Fe(L^1)_2](ClO_4)_2$ was used, except L^3 was used in place of L^1. Non-diffractable purple crystals were grown from dissolving in acetone, and vapour diffusion of tert-butyl methyl ether. Yield: 72 mg (62 %).

ESMS: m/z 955 $[Fe(L^3)_2]^{2+}$. $^{31}P\{^1H\}$ NMR (CD_3CN): δ11.28 ppm (d (93 Hz), 4P), -44.09 (t (93), 2P). ^1H NMR (CD_3CN): δ 14.48 ppm (4H), 9.00 (4H), 8.06 (4H), 7.85 (20H), 7.67 (10H), 7.57 (20H), 6.73 (4H), 6.32 (4H), 6.17 (4H).[a] Anal. Calc. $C_{98}H_{74}Cl_2FeN_{16}O_{20}P_6 \cdot C_5H_{12}O \cdot 2H_2O$: C, 55.41, H, 4.06; N, 10.04. Found: C, 55.26; H, 4.01; N, 10.01 %.

[a] NMR proton coupling data unavailable for $[Fe(L^3)_2](ClO_4)_2$ due to the complex being slightly paramagnetic.

B.1.2.3b $[Fe(L^3)_2](BF_4)_2$

The same procedure as for $[Fe(L^1)_2](ClO_4)_2$ was used, except L^3 was used in place of L^1 and $Fe(BF_4)_2 \cdot 6H_2O$. Purple crystals were grown from dissolving in acetone by vapour diffusion of tert-butyl methyl ether. Yield: 70 mg (63 %).

ESMS: m/z 955 $[Fe(L^3)_2]^{2+}$. $^{31}P\{^1H\}$ NMR (CD_3CN): δ11.6 ppm (d (93 Hz), 4P), -41.9 (t (93), 2P) ^1H NMR (CD_3CN): δ 14.60 ppm (4H), 8.94 (4H), 8.04 (4H), 7.84 (20H), 7.61 (10H), 7.57 (20H), 6.84 (4H), 6.64 (4H), 6.11 (4H).[b] Anal. Calc. $C_{98}H_{74}Cl_2FeN_{16}O_{20}P_6 \cdot {}^3/_4C_5H_{12}O \cdot H_2O$: C, 56.39; H, 3.95; N, 10.34 %. Found: C, 56.34; H, 4.02: N, 10.39 %.

B.1.2.4a $[Fe(L^4)_2](ClO_4)_2$

L^4 (100 mg, 0.12 mmol) was dissolved in 30 mL of CH_3CN. $Fe(ClO_4)_2.6H_2O$ (22 mg, 0.06 mmol) was added to this solution immediately forming a yellow colour. The solution was stirred for a further 30 minutes before diethyl ether was allowed to diffuse into the solution producing crystals of excess iron perchlorate, the solution was decanted and the process was repeated until no more iron perchlorate crystals formed. Non-diffractable yellow crystals were formed by vapour diffusing diethyl ether into an acetonitrile solution. Yield: 86 mg (70%).

Anal. Calc. for: $C_{94}H_{74}Cl_2FeN_{16}O_{20}P_6.3H_2O$: C, 53.40; H, 3.81; N, 10.60. Found: C, 53.16; H, 4.08; N, 10.50 %. m/z 931 $[Fe(L^4)_2]^{2+}$.[c]

[b] NMR proton coupling data unavailable for $[Fe(L^3)_2](BF_4)_2$ due to the complex being slightly paramagnetic.
[c] NMR proton coupling data unavailable for $[Fe(L^4)_2](ClO_4)_2$ due to the complex being paramagnetic.

B.1.2.5a $[Fe(L^5)_2](ClO_4)_2$

The procedure as for $[Fe(L^1)_2](ClO_4)_2$ was used; however, L^5 was used in place of L^1, producing a purple solid. The purple solid was dissolved in $CHCl_3$ and precipitated with hexane for analysis. Yield: 53 mg (49%).

ESMS: m/z 872 $[Fe(L^5)_2]^{2+}$. $^{31}P\{^1H\}$ NMR (CD_3CN): δ 10.8 ppm (t (95 Hz), 2P), 25.3 (d (95), 4P). ^1H NMR (CD_3CN): δ 9.00 ppm (s, 4H), 8.42 (d (8 Hz), 4H), 7.80 (t (8), 4H), 7.69 (d (8), 8H), 7.65 (t (8), 8H), 7.57 (t (8), 4H), 7.50 (d (8), 2H), 7.38 (t (8), 8H), 7.21 (d (8), 8H), 7.16 (d (6), 4H), 6.95 (d (8), 4H), 6.94 (t (8), 4H). Anal. Calc. for $C_{88}H_{60}Cl_2FeN_{12}O_{20}P_6 \cdot 3CHCl_3$: C, 48.02; H, 2.79 N, 7.38%. Found: C, 48.35; H, 3.14; N, 7.52%.

B.1.2.5b $[Fe(L^5)_2](PF_6)_2$

The same procedure as for $[Fe(L^1)_2](PF_6)_2$ above was used, except L^5 was used in place of L^1, producing a purple solid. The purple solid was dissolved in $CHCl_3$ and precipitated with hexane for analysis. Yield: 74 mg (66 %).

ESMS: m/z 872 $[Fe(L^5)_2]^{2+}$. $^{31}P\{^1H\}$ NMR (CD_3CN): δ 12.3 ppm (t (93 Hz), 2P), 26.9 (d (93), 4P), -143.2 (sep (696), 2P). ^1H NMR (CD_3CN): δ 9.00 ppm (s, 4H), 8.41 (d (8 Hz), 4H), 7.79 (t (8), 4H), 7.68 (d (8), 8H), 7.64 (t (8), 8H), 7.57 (t (8), 4H), 7.49 (d (8), 2H), 7.38 (t (8), 8H), 7.22 (d (8), 8H), 7.15 (d (6), 4H), 6.93 (d (8), 4H), 6.91 (t (8), 4H). Anal. Calc. $C_{90}H_{62}F_{12}FeN_{12}O_{12}P_8 \cdot 3C_6H_{14}$: C, 56.55; H, 4.57, N, 7.33% Found: C, 56.60; H, 4.96; N, 7.43 %

B.1.2.5c $[Fe(L^5)_2](BF_4)_2$

The same procedure as for $[Fe(L^5)_2](PF_6)_2$ was used, except $Ag(CH_3CN)_4BF_4$ was used in place of $Ag(CH_3CN)_4PF_6$, producing a purple solid. The purple solid was dissolved in $CHCl_3$ and precipitated with hexane for analysis. Yield: 60 mg (56 %).

ESMS: m/z 872 $[Fe(L^5)_2]^{2+}$. $^{31}P\{^1H\}$ NMR (CD_3CN): δ 12.1 ppm (t (91 Hz), 2P), 26.2 (d (91), 4P). ^1H NMR (CD_3CN): δ 9.00 ppm (s, 4H), 8.42 (d (8 Hz), 4H), 7.80 (t (8), 4H), 7.70 (d (8), 8H), 7.64 (t (8), 8 H), 7.56 (d (8), 2H), 7.50 (d (8), 4H), 7.38 (t (8), 8H), 7.21 (d (8), 8H), 7.15 (d (6), 4H), 6.95 (d (8), 4H), 6.92 (t (8), 4H). Anal. Calc. $C_{90}H_{62}B_2F_8FeN_{12}O_{12}P_6$: C, 56.33; H, 3.26; N, 8.76 %. Found: C, 55.99; H, 3.31; N, 8.74 %.

B.1.2.6a $[Fe(L^6)_2](ClO_4)_2$

The same procedure as for $[Fe(L^2)_2](ClO_4)_2$ above was used, except L^6 was used in place of L^2, producing a purple amorphous powder. The purple powder was dissolved in $CHCl_3$ and precipitated with hexane for analysis. Yield: 66 mg (59 %).

ESMS: m/z 949 $[Fe(L^6)_2]^{2+}$. $^{31}P\{^1H\}$ NMR (CD_3CN): δ 12.2 ppm (t (89 Hz), 2P), 27.2 (d (89), 4P). ^1H NMR (CD_3CN): δ 9.22 ppm (s, 4H), 8.62 (d (8 Hz), 4H), 8.50 (d (8), 4H), 7.92 (t (6), 4H), 7.85 (d (8), 4H), 7.68 (m, 8H), 7.62-7.54 (m, 12H), 7.51-7.44 (m, 14H), 7.32 (d (8), 4H), 7.21 (d (8), 4H), 7.16 (d (8), 4H), 7.11 (d (8), 4H). Anal. Calc. for $C_{102}H_{70}Cl_2FeN_{12}O_{20}P_6 \cdot 2½CHCl_3$: C, 52.14; H, 3.05; N, 7.02 %. Found: C, 52.01; H, 3.28; N, 7.30%.

B.1.2.6b $[Fe(L^6)_2](PF_6)_2$

The same procedure as for $[Fe(L^6)_2](PF_6)_2$ above was used, except L^6 was used in place of L^2, producing a purple solid. The purple solid was dissolved in $CHCl_3$ and precipitated with hexane for analysis. Yield 72 mg (60 %).
ESMS: m/z 949 $[Fe(L^6)_2]^{2+}$. $^{31}P\{^1H\}$ NMR (CD_3CN): δ 11.8 ppm (t (89 Hz), 2P), 26.7 (d (89), 4P), -143.2 (sep (708), 2P). ^1H NMR (CD_3CN): δ 9.21 ppm (s, 4H), 8.61 (d (8 Hz), 4H), 8.48 (d (8), 4H), 7.92 (t (8), 4H), 7.83 (d (8), 4H), 7.69-7.67 (m, 8H), 7.63-7.52 (m, 12H), 7.50-7.43 (m, 14H), 7.31 (d (8), 4H), 7.21 (d (8), 4H), 7.15 (d (8), 4H), 7.10 (t (8), 4H). Anal. Calc. for $C_{102}H_{70}F_{12}FeN_{12}O_{12}P_8.½C_6H_{14}$: C, 56.54; H, 3.48; N, 7.54 %. Found: C, 56.48; H, 4.53; N, 7.76 %.

B.1.2.7a $[Fe(L^7)_2](ClO_4)_2$

The same procedure as for $[Fe(L^5)_2](ClO_4)_2$ was used, except L^7 was used in place on L^5, producing a purple amorphous powder. The purple powder was dissolved in $CHCl_3$ and precipitated with hexane for analysis. Yield: 64 mg (54 %).

ESMS: m/z 950 $[Fe(L^7)_2]^{2+}$. $^{31}P\{^1H\}$ NMR (CD_3CN): δ 26.8 ppm (d (96 Hz), 4P), triplet not observed. ^1H NMR (CD_3CN): δ 13.60 ppm (4H), 9.13 (4H), 8.71 (4H), 7.95-7.48 (42H), 6.80 (4H), 6.54 (4H), 6.17 (4H).[d] Anal. Calc. $C_{98}H_{66}Cl_2FeN_{16}O_{20}P_6 \cdot 3CHCl_3 \cdot 4H_2O$: C, 47.94; H, 3.07; N, 8.86 %. Found: C, 47.89; H, 3.28; N, 8.46 %.

[d] NMR proton coupling data unavailable for $[Fe(L^7)_2](ClO_4)_2$ due to the complex being slightly paramagnetic.

B.1.2.7b $[Fe(L^7)_2](BF_4)_2$

The same procedure as for $[Fe(L^7)_2](ClO_4)_2$ was used, except $Fe(BF_4)_2(H_2O)_6$ was used in place of $Fe(ClO_4)_2(H_2O)_6$, producing a purple amorphous powder. The purple powder was dissolved in acetone and precipitated with tert-butyl methyl ether for analysis. Yield: 66 mg (56 %).

ESMS: m/z 950 $[Fe(L^7)_2]^{2+}$. $^{31}P\{^1H\}$ NMR (CD_3CN): $^{31}P\{^1H\}$ NMR (CD_3CN): δ 26.8 ppm (d (96 Hz), 4P), -59.25 (broad, 2P). ^1H NMR (CD_3CN): δ 14.0 ppm (4H), 8.94 (4H), 8.11 (4H), 7.86-7.12 (42H), 6.95 (4H), 6.48 (4H), 6.34 (4H).[e] Anal. Calc. $C_{98}H_{66}B_2F_8N_{16}O_{12}P_6 \cdot 2¾OC_5H_{12}$: C, 59.35; H, 4.41; N, 9.91 %. Found: C, 59.74; H, 4.33; N, 9.49 %.

[e] NMR proton coupling data unavailable for $[Fe(L^7)_2](BF_4)_2$ due to the complex being slightly paramagnetic.

B.2 Selected Bond Lengths

Table B.2.1 Selected bond lengths for $[Fe(L^1)_2](PF_6)_2 \cdot CH_3CN$

Bond	Bond length (Å)	Bond	Bond length (Å)
Fe(1) – N(1A)	1.883 (2)	Fe(1) – N(1B)	1.882 (2)
Fe(1) – N(2A)	1.992 (2)	Fe(1) – N(2B)	1.976 (2)
Fe(1) – N(3A)	1.983 (2)	Fe(1) – N(3B)	1.975 (2)
P(1A) – N(4A)	1.579 (2)	P(1B) – N(4B)	1.585 (2)
P(1A) – N(5A)	1.578 (2)	P(1B) – N(5B)	1.582 (2)
P(2A) – N(4A)	1.592 (2)	P(2B) – N(4B)	1.594 (2)
P(2A) – N(6A)	1.591 (2)	P(2B) – N(6B)	1.578 (2)
P(3A) – N(5A)	1.595 (2)	P(3B) – N(5B)	1.593 (2)
P(3A) – N(6A)	1.578 (2)	P(3B) – N(6B)	1.581 (2)

Table A3.2.2 Selected bond lengths for $[Fe(L^1)_2](ClO_4)_2 \cdot CH_3CN$

Bond	Bond length (Å)	Bond	Bond length (Å)
Fe(1) – N(1A)	1.887 (3)	Fe(1) – N(1B)	1.890 (3)
Fe(1) – N(2A)	1.954 (4)	Fe(1) – N(2B)	1.962 (4)
Fe(1) – N(3A)	1.972 (4)	Fe(1) – N(3B)	1.974 (4)
P(1A) – N(4A)	1.565 (4)	P(1B) – N(4B)	1.575 (4)
P(1A) – N(5A)	1.567 (3)	P(1B) – N(5B)	1.584 (4)
P(2A) – N(5A)	1.590 (4)	P(2B) – N(5B)	1.585 (4)
P(2A) – N(6A)	1.578 (4)	P(2B) – N(6B)	1.591 (4)
P(3A) – N(4A)	1.599 (4)	P(3B) – N(4B)	1.585 (4)
P(3A) – N(6A)	1.570 (3)	P(3B) – N(6B)	1.559 (4)

Table A3.2.3 Selected bond lengths for $[Fe(L^2)_2](PF_6)_2 \cdot CH_3CN$

Bond	Bond length (Å)	Bond	Bond length (Å)
Fe(1) – N(1A)	1.888 (3)	Fe(1) – N(1B)	1.878 (3)
Fe(1) – N(2A)	1.985 (3)	Fe(1) – N(2B)	1.976 (3)
Fe(1) – N(3A)	1.994 (3)	Fe(1) – N(3B)	1.976 (4)
P(1A) – N(4A)	1.569 (3)	P(1B) – N(4B)	1.582 (3)
P(1A) – N(6A)	1.572 (3)	P(1B) – N(6B)	1.575 (3)
P(2A) – N(4A)	1.571 (4)	P(2B) – N(4B)	1.588 (3)
P(2A) – N(5A)	1.579 (4)	P(2B) – N(5B)	1.575 (3)
P(3A) – N(5A)	1.573 (4)	P(3B) – N(5B)	1.582 (3)
P(3A) – N(6A)	1.577 (3)	P(3B) – N(6B)	1.589 (3)

Table A3.2.4 Selected bond lengths for $[Fe(L^3)_2](BF_4)_2 \cdot C_3H_5O \cdot C_5H_{12}O$

Bond	Bond length (Å)	Bond	Bond length (Å)
Fe(1) – N(1A)	1.910 (5)	Fe(1) – N(1B)	1.908 (6)
Fe(1) – N(2A)	1.987 (5)	Fe(1) – N(2B)	1.990 (5)
Fe(1) – N(3A)	1.993 (5)	Fe(1) – N(3B)	1.996 (5)
P(1A) – N(6A)	1.559 (7)	P(1B) – N(6B)	1.575 (6)
P(1A) – N(8A)	1.570 (7)	P(1B) – N(8B)	1.557 (6)
P(2A) – N(6A)	1.582 (7)	P(2B) – N(6B)	1.577 (6)
P(2A) – N(7A)	1.586 (9)	P(2B) – N(7B)	1.571 (6)
P(3A) – N(7A)	1.605 (9)	P(3B) – N(7B)	1.580 (6)
P(3A) – N(8A)	1.601 (8)	P(3B) – N(8B)	1.583 (6)

B.3 References

1. Akermark, B.; Vitagliano, A. *Organometallics* **1985**, *4*, 1275-1283.

Appendix C: Chapter 4 Supplementary

C.1 Ruthenium(II) Complex Synthesis

C.1.1 General Experimental

Analytical grades of solvents were used without further purification. Ru(Terpy)Cl_3[1] and Ru(PhTerpy)Cl_3[2] were synthesised by literature methods. $RuCl_3 \cdot 3H_2O$ and NH_4PF_6 were all sourced from Aldrich. All manipulations were carried out under an argon atmosphere, using standard Schlenk techniques. Microanalysis was performed at the Campbell Microanalytical Laboratory, University of Otago after samples were dried under vacuum at 50°C for at least 24 hours. Phosphorus nuclear magnetic resonance (NMR) spectra were recorded on a Bruker Avance A400 spectrometer, and proton NMR data was recorded on a Bruker Avance A500 spectrometer. Proton data were internally referenced to TMS, phosphorus data were referenced to an external sample of 80% ortho phosphoric acid. NMR data were assigned using 2D NMR and density function theory (DFT) simulations. Electrospray mass spectra were obtained from an acetonitrile solution on a micromass ZMD spectrometer run in the positive ion mode. Listed peaks correspond to the most abundant isotopomer. Assignments were made by comparison of observed and measured spectra. All values stated in this section were recorded at room temperature.

C.1.2 Experimental Details

C.1.2.1 $[Ru(L^1)_2](PF_6)_2$

To a stirred solution of L^1 (250 mg, 0.29 mmol) in MeOH (25 mL), $RuCl_3 \cdot 3H_2O$ (37 mg, 0.15 mmol) and 5 drops of N-methylmorpholine were added. The solution was heated to reflux for 12 hours before being cooled and filtered. NH_4PF_6 (98 mg, 0.60 mmol) was added to the filtrate immediately forming an orange precipitate. The precipitate was filtered, washed with MeOH and diethyl ether, leaving an orange powder. Crystals were grown by dissolving the solid in acetonitrile and diffusing in diethyl ether, producing orange blocks. Yield: 266 mg (88 %).

ESMS: m/z 900 $[Ru(L^1)_2]^{2+}$. $^{31}P\{^1H\}$ NMR (CD_3CN): δ 10.28 ppm (s, 6P), -143.19 (sept (710 Hz), 2P). ^1H NMR (CD_3CN): δ 8.91 ppm (s, 4H), 8.61 (d (8 Hz), 4H), 8.07 (d (8), 4H), 7.94 (t (8), 4H), 7.42 (d (6), 4H), 7.35-7.16 (m, 30H), 7.06 (d (8), 8H), 6.97 (d (8), 4H), 6.91 (d (8), 8H). Anal. Calc. for $C_{90}H_{70}F_{12}N_{12}O_{12}P_8Ru \cdot ½C_4H_{10}O$: C, 52.01; H, 3.51; N, 7.91 %. Found: C, 52.17; H, 3.42; N, 8.06 %.

C.1.2.2 $[Ru(L^1)Cl_3]$

To a stirred solution of L^1 (250 mg, 0.29 mmol) in MeOH (25 mL), $RuCl_3 \cdot 3H_2O$ (75 mg, 0.29 mmol) was added. The solution was refluxed for three hours before being cooled forming a brown precipitate. The precipitate was filtered, washed successively with diethyl ether and hexane. Yield: 242 mg (79 %).

ESMS: m/z 1021 $[Ru(L^1)Cl_2]^+$. Anal. Calc. for $C_{45}H_{35}Cl_3N_6O_6P_3Ru \cdot ¾H_2O$: C, 50.53; H, 3.44; N, 7.86 %. Found: C, 50.53; H, 3.41; N, 7.68 %.

C.1.2.3A $[Ru(L^1)(Terpy)](PF_6)_2$ Method A

The same procedure as for $[Ru(L^1)_2](PF_6)_2$ was used, except $Ru(Terpy)Cl_3$ was used in place of $RuCl_3 \cdot 3H_2O$, producing an orange powder. Yield: mg 335 (75 %).

C.1.2.3B $[Ru(L^1)(Terpy)](PF_6)_2$ Method B

To a stirred suspension of $[Ru(L^1)Cl_3]$ (250 mg, 0.23 mmol) in MeOH (25 mL), terpy (53 mg, 0.23 mmol) was added. The reaction was refluxed for 12 hours before the solution was cooled, filtered and NH_4PF_6 (145 mg, 0.92 mmol) was added forming and orange precipitate. Crystals were grown by vapour diffusion of diethyl ether into acetonitrile, producing orange blocks. Yield: mg 254 (75 %).

ESMS: m/z 592 $[Ru(L^1)(Terpy)]^{2+}$. $^{31}P\{^1H\}$ NMR (CD_3CN): δ 11.48-8.59 ppm (m, 3P), -143.19 (sept (710 Hz), 2P). ^1H NMR (CD_3CN): δ 8.71 ppm (d (8 Hz), 2H), 8.49 (s, 2H), 8.47 (d (8), 2H), 8.39 (t (8), 1H), 8.16 (d (8), 2H), 7.89 (t (8), 2H), 7.78 (t (8), 2H), 7.36 (t (8), 2H), 7.31-7.07 (m, 25H), 7.04 (t (8), 2H), 6.88 (d (8), 2H). Anal. Calc. for $C_{60}H_{46}F_{12}N_9O_6P_5Ru \cdot CH_3CN$: C, 49.18; H, 3.26; N, 9.25 %. Found: C, 49.48; H, 3.20; N, 9.15 %.

C.1.2.4A $[Ru(L^1)(PhTerpy)](PF_6)_2$ Method A

The same procedure as for $[Ru(L^1)(Terpy)](PF_6)_2$ was used, except $Ru(PhTerpy)Cl_3$ was used in place of $Ru(Terpy)Cl_3$, producing and orange powder. Yield: 320 mg (90 %).

C.1.2.4B $[Ru(L^1)(PhTerpy)](PF_6)_2$ Method B

The same procedure as for $[Ru(L^1)(Terpy)](PF_6)_2$ method B was used, except PhTerpy was used in place of terpy. Crystals were grown by vapour diffusion of diisopropyl ether into an acetonitrile solution, producing orange platelets. Yield: 302 mg (85 %).

ESMS: m/z 630 $[Ru(L^1)(PhTerpy)]^{2+}$. $^{31}P\{^1H\}$ NMR (CD_3CN): δ 10.95-9.25 ppm (m, 3P), -143.19 (sept (710 Hz), 2P). ^1H NMR (CD_3CN): δ 8.97 ppm (s, 2H), 8.61 (d (8 Hz), 2H), 8.51 (s, 2H), 8.17 (d (8), 4H), 7.91 (t (8), 2H), 7.79-7.73 (m, 4H), 7.66 (t (8), 1H), 7.38-7.34 (m, 4H), 7.30-7.11 (m, 21H), 7.07 (d (8), 2H), 7.02 (t (8), 2H), 6.86 (d (8), 4H). Anal. Calc. for $C_{66}H_{50}F_{12}N_9O_6P_5Ru$: C, 51.17; H, 3.25: N, 8.14 %. Found: C, 51.28; H, 3.19; N, 8.32 %.

C.1.2.5 $[Ru(L^1)(bbp)](PF_6)_2$

$[Ru(L^1)Cl_3]$ (284 mg, 0.27 mmol) was added to a stirred solution of bbp (84 mg, 0.27 mmol) and 1 drop of N-methylmorpholine. The solution was heated to reflux for 12 hours before being cooled and filtered. NH_4PF_6 (90 mg, 0.55 mmol) was added, the solution was cooled forming a dark red precipitate. The precipitate was filtered and washed with diethyl ether, leaving a dark red powder. Crystals were formed by vapour diffusion of diethyl ether into an acetonitrile solution, forming red blocks. Yield: 263 mg (63 %).

ESMS: m/z 631 $[Ru(L^1)(bbp)]^{2+}$. $^{31}P\{^1H\}$ NMR (CD_3CN): δ 11.96-9.13 ppm (m, 3P), -143.29 (sept (710 Hz), 2P). ^1H NMR (CD_3CN): δ 8.58 ppm (d (8 Hz), 2H), 8.56 (s, 2H), 8.46 (t (8), 1H), 7.99 (d (8), 2H), 7.63 (t (8), 2H), 7.53 (d (8), 2H), 7.37-7.20 (m, 14H), 7.12-6.97 (m, 12H), 6.87 (d (8), 2H). Anal. Calc. for $C_{64}H_{48}F_{12}N_{11}O_6P_5Ru \cdot 2½H_2O$: C, 48.16; H, 3.35; N, 9.65 %. Found: C, 48.08; H, 3.17; N, 10.05 %.

C.1.2.6 $[Ru(L^1)(bpp)](PF_6)_2$

The same procedure as for $[Ru(L^1)(bbp)](PF_6)_2$ was used, except bpp was used in place of bbp, producing and orange powder. Crystals were grown by vapour diffusion of diethyl ether into an acetonitrile solution, producing orange platelets. Yield: 219 mg (56 %).

ESMS: m/z 581 $[Ru(L^1)(bpp)]^{2+}$. $^{31}P\{^1H\}$ NMR (CD_3CN): δ 11.65-9.28 ppm (m, 3P), -143.19 (sept (710 Hz), 2P). ^1H NMR (CD_3CN): δ 8.74 ppm (d (4 Hz), 2H), 8.50 (t (8), 1H), 8.24 (s, 2H), 8.20 (d (8), 2H), 8.15 (d (8), 2H), 7.80 (t (8), 2H), 7.34 (d (8), 4H), 7.28-7.13 (m, 17H), 7.02 (d,d (8), 4H), 6.85 (d,d (8), 6H), 6.47 (t (4), 2H). Anal. Calc. for $C_{56}H_{44}F_{12}N_{11}O_6P_5Ru \cdot CH_3CN$: C, 46.69; H, 3.18; N, 11.27 %. Found: C, 46.51; H, 3.22; N, 11.32 %.

C.1.2.7 $[Ru(L^2)_2](PF_6)_2$

The same procedure as for $[Ru(L^1)_2](PF_6)_2$ was used, except L^2 was used in place of L^1.Crystals were grown by dissolving the solid in acetonitrile and diffusing in diethyl ether, producing thin needles. Yield: 278 mg (90 %).

ESMS: m/z 976 $[Ru(L^2)_2]^{2+}$. $^{31}P\{^1H\}$ NMR (CD_3CN): δ 10.29 ppm (s, 6P), -143.19 (sept (710 Hz), 2P). ^1H NMR (CD_3CN): δ 8.91 ppm (s, 4H), 8.62 (d (8 Hz), 4H), 8.08 (d (8), 4H), 7.94 (t (8), 4H), 7.42 (d (6), 4H), 7.35-7.16 (m, 38H), 7.06 (d (8), 8H), 6.98 (d (8), 4H), 6.92 (d (8), 8H). Anal. Calc. for $C_{102}H_{78}F_{12}N_{12}O_{12}P_8Ru \cdot ¾H_2O$: C, 54.35; H, 3.55; N, 7.46 %. Found: C, 54.34; H, 3.67; N, 7.33 %.

C.1.2.8 $[Ru(L^2)Cl_3]$

The same procedure as for $[Ru(L^2)Cl_3]$ was used, except L^2 was used in place of L^1, producing a brown powder. Yield: 270 mg (89 %).

ESMS: m/z 1097 $[Ru(L^2)Cl_2]^+$. Anal. Calc. for $C_{51}H_{39}Cl_3N_6O_6P_3Ru \cdot 1^1/_4H_2O$: C, 53.05; H, 3.62; N, 7.28 %. Found: C, 53.19; H, 3.66; N, 6.92 %.

C.1.2.9A $[Ru(L^2)(Terpy)](PF_6)_2$ Method A

The same procedure as for $[Ru(L^2)(Terpy)](PF_6)_2$ method A was used, except L^2 was used in place of L^1. Yield: 314 mg (73 %).

C.1.2.9B $[Ru(L^2)(Terpy)](PF_6)_2$ Method B

The same procedure as for $[Ru(L^2)(Terpy)](PF_6)_2$ method B was used, except L^2 was used in place of L^1. Non-diffractable crystals were grown by dissolving the solid in acetonitrile and diffusing in diethyl ether. Yield: 301 mg (70 %).

ESMS: m/z 630 $[Ru(L^2)(Terpy)]^{2+}$. $^{31}P\{^1H\}$ NMR (CD_3CN): δ 10.29 ppm (s, 3P), -143.19 (sept (710 Hz), 2P). ^1H NMR (CD_3CN): δ 8.89 ppm (s, 2H), 8.74 (d (8 Hz), 2H), 8.60 (d (8), 2H), 8.48 (d (8), 2H), 8.40 (t (8), 1H), 8.07 (d (8), 2H), 7.93-7.90 (m, 4H), 7.40 (d (6), 2H), 7.35-7.14 (m, 26H), 7.05 (d (8), 4H), 6.97 (d (8), 2H), 6.92 (d (8), 4H). Anal. Calc. for $C_{66}H_{50}F_{12}N_9O_6P_5Ru\cdot¾H_2O$: C, 50.73; H, 3.32; N, 8.07 %. Found: C, 50.63; H, 3.27; N, 8.26 %.

C.1.2.10A $[Ru(L^2)(PhTerpy)](PF_6)_2$ Method A

The same procedure as for $[Ru(L^2)(PhTerpy)](PF_6)_2$ method A was used, except L^2 was used in place of L^1. Yield: 391 mg (89 %).

C.1.2.10B $[Ru(L^2)(PhTerpy)](PF_6)_2$ Method B

The same procedure as for $[Ru(L^1)(PhTerpy)](PF_6)_2$ method B was used, except L^2 was used in place of L^1, producing an orange powder. Yield: 386 mg (88 %).

ESMS: m/z 668 $[Ru(L^2)(PhTerpy)]^{2+}$. $^{31}P\{^1H\}$ NMR (CD_3CN): δ 10.29 ppm (s, 3P), -143.19 (sept (710 Hz), 2P). ^1H NMR (CD_3CN): δ 9.00 ppm (s, 2H), 8.90 (s, 2H), 8.62 (d,d (8 Hz), 4H), 8.19 (d (8), 2H), 8.07 (d (8), 2H), 7.94 (t,d (8), 4H), 7.75 (t (8), 2H), 7.67 (t (8), 1H), 7.42 (t (8), 4H), 7.40-7.20 (m, 19H), 7.17 (t (8), 4H), 7.05 (d (8), 4H), 6.97 (d (8), 2H), 6.91 (d (8), 4H). Anal. Calc. for $C_{72}H_{54}F_{12}N_9O_6P_5Ru\cdot½CH_3CN$: C, 53.28; H, 3.40; N, 8.09 %. Found: C, 53.53; H, 3.40; N, 8.04 %.

C.1.2.11 $[Ru(L^2)(bbp)](PF_6)_2$

The same procedure as for $[Ru(L^2)(bbp)](PF_6)_2$ was used, except $[Ru(L^2)Cl_3]$ was used in place of $[Ru(L^1)Cl_3]$. Non-diffractable crystals were grown by vapour diffusion of diethyl ether into an acetonitrile solution. Yield: 277 mg (63 %).

ESMS: m/z 669 $[Ru(L^2)(bbp)]^{2+}$. $^{31}P\{^1H\}$ NMR (CD_3CN): δ 11.1-9.55 ppm (m, 3P), -143.19 (sept (710 Hz), 2P). ^1H NMR (CD_3CN): δ 8.98 ppm (s, 2H), 8.60 (d (8 Hz), 2H), 8.54 (d (8), 2H), 8.49 (t (8), 1H), 8.19 (d (8), 2H), 7.82 (t (8), 2H), 7.55 (d (8), 2H), 7.39-7.20 (m, 21H), 7.11 (t (8), 2H), 7.07 (d (8), 4H), 6.99 (t (8), 4H), 6.94 (d (8), 4H), 6.18 (d (8), 2H). Anal. Calc. for $C_{70}H_{52}F_{12}N_{11}O_6P_5Ru \cdot 2^1/_4H_2O$: C, 50.41; H, 3.41; N, 9.24 %. Found: C, 50.45; H, 3.54; N, 9.32 %.

C.1.2.12 $[Ru(L^2)(bpp)](PF_6)_2$

The same procedure as for $[Ru(L^1)(bpp)](PF_6)_2$ was used, except $[Ru(L^2)Cl_3]$ was used in place of $[Ru(L^1)Cl_3]$, producing an orange powder. Non-diffractable crystals were grown by dissolving the solid in acetonitrile and diffusing in diethyl ether. Yield: 239 mg (58 %).

ESMS: m/z 619 $[Ru(L^2)(bpp)]^{2+}$. $^{31}P\{^1H\}$ NMR (CD_3CN): δ 10.29 ppm (s, 3P), -143.19 (sept (710 Hz), 2P). ^1H NMR (CD_3CN): δ 8.82 ppm (s, 2H), 8.78 (d (4 Hz), 8.58 (d (8), 2H), 8.53 (t (8), 1H), 8.24 (d (8), 2H), 8.04 (d (8), 2H), 7.96 (t (8), 2H), 7.42 (d (8), 7.49-7.19 (m, 19H), 7.06 (d,d (8), 6H), 6.96 (d (8), 2H), 6.91 (d (8), 4H), 6.51 (t (3), 2H). Anal. Calc. for $C_{62}H_{48}F_{12}N_{11}O_6P_5Ru \cdot {}^1/_4H_2O$: C, 48.62; H, 3.19; N, 10.06 %. Found: C, 48.62; H, 3.20; N, 10.20 %.

C.1.2.13 $[Ru(L^3)Cl_3]$

The same procedure as for $[Ru(L^2)Cl_3]$ was used, except L^3 was used in place of L^2, producing a brown powder. Yield: 223 mg (73 %).

ESMS: m/z 1099 $[Ru(L^3)Cl_2]^+$. Anal. Calc. for $C_{49}H_{37}Cl_3N_8O_6P_3Ru \cdot C_2H_6O$: C, 51.90; H, 3.67; N, 9.49 %. Found: C, 51.52; H, 3.48; N, 9.19 %.

C.1.2.14 $[Ru(L^3)(Terpy)](PF_6)_2$

The same procedure as for $[Ru(L^2)(Terpy)](PF_6)_2$ method A was used, except L^3 was used in place of L^2 and 5 drops of N-ethylmorpholine was used in place of 1. Crystals were grown by dissolving the solid in acetonitrile and diffusing in diethyl ether, producing red blocks. Yield: 259 mg (62 %).

ESMS: m/z 631$[Ru(L^3)(Terpy)]^{2+}$. $^{31}P\{^1H\}$ NMR (CD_3CN): δ 10.91-8.59 ppm (m, 3P), -143.19 (sept (710 Hz), 2P). ^1H NMR (CD_3CN): δ 8.71 ppm (d (8 Hz), 2H), 8.49 (s, 2H), 8.46 (d (8), 2H), 8.38 (t (8), 1H), 8.15 (d (8), 2H), 7.88 (t (8), 2H), 7.76 (t (8), 2H), 7.34 (d (8), 2H), 7.29-7.01 (m, 29H), 6.86 (d (8), 4H). Anal. Calc. for $C_{64}H_{48}F_{12}N_{11}O_6P_5Ru\cdot 1^1/_4CH_3CN$: C, 49.85; H, 3.26; N, 10.71 %. Found: C, 49.72; H, 3.27; N, 10.76 %.

C.1.2.15 $[Ru(L^3)(PhTerpy)](PF_6)_2$

The same procedure as for $[Ru(L^2)(PhTerpy)](PF_6)_2$ was used, except L^3 was used in place of L^2. Crystals were grown by vapour diffusion of diethyl ether into an acetonitrile solution, producing red blocks. Yield: 306 mg (69 %).

ESMS: m/z 669 $[Ru(L^3)(PhTerpy)]^{2+}$. $^{31}P\{^1H\}$ NMR (CD_3CN): δ 10.55-10.09 ppm (m, 3P), -143.19 (sept (710 Hz), 2P). ^1H NMR (CD_3CN): δ 13.11 ppm (s, 2H), 9.10 (s, 2H), 8.57 (d (8 Hz), 2H), 8.42 (s, 2H), 8.34 (d (8), 2H), 7.98 (t (8), 1H), 7.17-7.65 (m, 4H), 7.70 (t (8), 2H), 7.57 (d (8), 2H), 7.41-7.08 (m, 25H), 7.01 (t (8), 2H), 6.89 (d (8), 4H), 6.15 (d(8), 2H). Anal. Calc. for $C_{70}H_{52}F_{12}N_{11}O_6P_5Ru\cdot ½H_2O$: C, 51.39; H, 3.26; N, 9.42 %. Found: C, 51.42; H, 3.30; N, 9.39 %.

C.1.2.16 $[Ru(L^4)Cl_3]$

The same procedure as for $[Ru(L^2)Cl_3]$ was used, except L^3 was used in place of L^2, and precipitation from a CH_2Cl_2 solution using hexane to produce a brown powder. Yield: 156 mg (51 %).

ESMS: m/z 1075 $[Ru(L^4)Cl_2]^+$. Anal. Calc. for $C_{47}H_{37}Cl_3N_8O_6P_3Ru\cdot 1¾CH_2Cl_2$: C, 46.51; H, 3.24; N, 8.90 %. Found: C, 46.40; H, 3.19; N, 8.50 %.

C.1.2.17 $[Ru(L^4)(Terpy)](PF_6)_2$

The same procedure as for $[Ru(L^2)(Terpy)](PF_6)_2$ method A was used, except L^4 was used in place of L^2, producing a red powder. Yield: 237 mg (56 %).

ESMS: m/z 619 $[Ru(L^4)(Terpy)]^{2+}$. $^{31}P\{^1H\}$ NMR (CD_3CN): δ 10.33-10.03 ppm (m, 3P), -143.19 (sept (710 Hz), 2P). ^1H NMR (CD_3CN): δ 9.06 ppm (d (4 Hz), 2H), 8.83 (d (4), 2H), 8.51 (d (8), 2H), 8.41 (d (8), 2H), 8.10 (t (8), 2H), 8.06 (s, 2H), 7.92 (t (4), 2H), 7.76 (d (8), 2H), 7.71 (t (8), 1H), 7.55 (d (8), 2H), 7.38 (t (8), 2H), 7.28-7.19 (m, 14H), 7.12 (t, 2H), 7.03 (d (8), 2H), 6.94-6.89 (m, 9H). Anal. Calc. for $C_{62}H_{48}F_{12}N_{11}O_6P_5Ru \cdot C_4H_{10}O$: C, 49.51; H, 3.65: N, 9.62 %. Found: C, 49.51; H, 3.47; N, 9.52 %.

C.1.2.18 $[Ru(L^4)(PhTerpy)](PF_6)_2$

The same procedure as for $[Ru(L^2)(PhTerpy)](PF_6)_2$ method A was used, except L^4 was used in place of L^2 and the complex was precipitated from a dichloromethane solution using hexane, producing a red powder. Yield: 262 mg (49 %).

ESMS: m/z 657 $[Ru(L^4)(PhTerpy)]^{2+}$. $^{31}P\{^1H\}$ NMR (CD_3CN): δ 10.19 ppm (s, 3P), -143.19 (sept (710 Hz), 2P). ^1H NMR (CD_3CN): δ 9.11 ppm (d (4 Hz), 2H), 8.92 (d(4), 2H), 8.74 (s, 2H), 8.67 (t(8), 2H), 8.56 (d (8), 2H), 8.52 (s, 2H), 8.13 (d(8), 2H), 7.98 (d (8), 2H), 7.92 (d (8), 2H), 7.80 (t (8), 1H), 7.70 (t (4), 2H), 7.64 (d (8), 2H), 7.37-7.21 (m, 14H), 7.13 (d (8), 2H), 7.05 (d (8), 2H), 6.94-6.89 (m, 9H). Anal. Calc. for $C_{68}H_{52}F_{12}N_{11}O_6P_5Ru \cdot 2¾CH_2Cl_2$: C,46.27; H, 3.16; N, 8.39 %. Found: C, 46.33; H, 2.95; N, 7.99 %.

C.2 Selected bond lengths

Table C.2.1 Selected Bond Lengths (Å) for $[Ru(L^1)_2](PF_6)_2$ and $[Ru(L^2)_2](PF_6)_2 \cdot CH_3CN$

$[Ru(L^1)_2](PF_6)_2 \cdot CH_3CN$		**$[Ru(L^2)_2](PF_6)_2$**	
Ru(1) – N(1A)	1.980 (3)	Ru(1) – N(1A)	1.975 (4)
Ru(1) – N(2A)	2.060 (3)	Ru(1) – N(2A)	2.066 (4)
Ru(1) – N(3A)	2.074 (3)	Ru(1) – N(3A)	2.068 (5)
Ru(1) – N(1B)	1.978 (3)	Ru(1) – N(1B)	1.974 (4)
Ru(1) – N(2B)	2.071 (3)	Ru(1) – N(2B)	2.072 (4)
Ru(1) – N(3B)	2.053 (3)	Ru(1) – N(3B)	2.083 (4)
P(1A) – N(4A)	1.578 (4)	P(1A) – N(4A)	1.578 (5)
P(1A) – N(6A)	1.573 (3)	P(1A) – N(6A)	1.578 (4)
P(2A) – N(4A)	1.592 (4)	P(2A) – N(4A)	1.593 (4)
P(2A) – N(5A)	1.579 (3)	P(2A) – N(5A)	1.585 (4)
P(3A) – N(5A)	1.585 (4)	P(3A) – N(5A)	1.579 (4)
P(3A) – N(6A)	1.591 (4)	P(3A) – N(6A)	1.587 (4)
P(1B) – N(4B)	1.574 (4)	P(1B) – N(4B)	1.573 (5)
P(1B) – N(6B)	1.583 (3)	P(1B) – N(6B)	1.590 (5)
P(2B) – N(4B)	1.582 (3)	P(2B) – N(4B)	1.571 (5)
P(2B) – N(5B)	1.578 (4)	P(2B) – N(5B)	1.579 (5)
P(3B) – N(5B)	1.565 (4)	P(3B) – N(5B)	1.585 (6)
P(3B) – N(6B)	1.579 (3)	P(3B) – N(6B)	1.579 (5)

Table C.2.2 Selected Bond Lengths (Å) for $[Ru(L^1)(Terpy)](PF_6)_2 \cdot CH_3CN$ and $[Ru(L^1)(PhTerpy)](PF_6)_2$

$[Ru(L^1)(Terpy)](PF_6)_2 \cdot CH_3CN$		**$[Ru(L^1)(PhTerpy)](PF_6)_2$**	
Ru(1) – N(1)	1.982 (3)	Ru(1) – N(1)	1.980 (4)
Ru(1) – N(2)	2.079 (3)	Ru(1) – N(2)	2.091 (6)
Ru(1) – N(3)	2.072 (3)	Ru(1) – N(3)	2.055 (6)
Ru(1) – N(4)	1.980 (3)	Ru(1) – N(4)	1.965 (4)
Ru(1) – N(5)	2.080 (3)	Ru(1) – N(5)	2.072 (5)
Ru(1) – N(6)	2.095 (3)	Ru(1) – N(6)	2.066 (5)
P(1) – N(7)	1.575 (2)	P(1) – N(7)	1.574 (6)
P(1) – N(9)	1.584 (3)	P(1) – N(9)	1.565 (5)
P(2) – N(7)	1.579 (3)	P(2) – N(7)	1.593 (6)
P(2) – N(8)	1.577 (3)	P(2) – N(8)	1.558 (6)
P(3) – N(8)	1.585 (3)	P(3) – N(8)	1.583 (6)
P(3) – N(9)	1.588 (2)	P(3) – N(9)	1.585 (5)

Table C.2.3 Selected Bond Lengths (Å) for $[Ru(L^1)(bpp)](PF_6)_2 \cdot CH_3CN$ and $[Ru(L^1)(bbp)](PF_6)_2 \cdot C_3H_5O$

$[Ru(L^1)(bpp)](PF_6)_2 \cdot CH_3CN$		**$[Ru(L^1)(bbp)](PF_6)_2 \cdot C_3H_5O$**	
Ru(1) – N(1)	1.971 (3)	Ru(1) – N(1)	1.968 (4)
Ru(1) – N(2)	2.071 (3)	Ru(1) – N(2)	2.062 (4)
Ru(1) – N(3)	2.069 (3)	Ru(1) – N(3)	2.074 (4)
Ru(1) – N(4)	1.997 (3)	Ru(1) – N(4)	2.006 (4)
Ru(1) – N(6)	2.060 (3)	Ru(1) – N(5)	2.069 (4)
Ru(1) – N(7)	2.071 (3)	Ru(1) – N(7)	2.066 (4)
P(1) – N(9)	1.583 (3)	P(1) – N(9)	1.578 (5)
P(1) – N(11)	1.580 (3)	P(1) – N(11)	1.571 (5)
P(2) – N(9)	1.579 (3)	P(2) – N(9)	1.577 (5)
P(2) – N(10)	1.567 (3)	P(2) – N(10)	1.575 (6)
P(3) – N(10)	1.577 (4)	P(3) – N(10)	1.586 (5)
P(3) – N(11)	1.582 (3)	P(3) – N(11)	1.583 (5)

Table C.2.4 Selected Bond Lengths (Å) for $[Ru(L^3)(Terpy)](PF_6)_2 \cdot CH_3CN$ and $[Ru(L^3)(PhTerpy)](PF_6)_2 \cdot CH_3CN$

$[Ru(L^3)(Terpy)](PF_6)_2 \cdot CH_3CN$		**$[Ru(L^3)(PhTerpy)](PF_6)_2 \cdot CH_3CN$**	
Ru(1) – N(1)	2.000 (5)	Ru(1) – N(1)	1.985 (6)
Ru(1) – N(2)	2.062 (4)	Ru(1) – N(2)	2.059 (5)
Ru(1) – N(4)	2.072 (4)	Ru(1) – N(4)	2.067 (5)
Ru(1) – N(6)	1.979 (5)	Ru(1) – N(6)	1.939 (5)
Ru(1) – N(7)	2.071 (4)	Ru(1) – N(7)	2.064 (5)
Ru(1) – N(8)	2.063 (4)	Ru(1) – N(8)	2.075 (5)
P(1) – N(9)	1.590 (4)	P(1) – N(9)	1.574 (6)
P(1) – N(11)	1.575 (5)	P(1) – N(11)	1.582 (7)
P(2) – N(10)	1.584 (5)	P(2) – N(10)	1.567 (6)
P(2) – N(11)	1.591 (5)	P(2) – N(11)	1.607 (6)
P(3) – N(9)	1.588 (5)	P(3) – N(9)	1.577 (6)
P(3) – N(10)	1.577 (5)	P(3) – N(10)	1.577 (6)

C.3 References

1. Sullivan, B. P.; Calvert, J. M.; Meyer, T. J. *Inorganic Chemistry* **1980**, *19*, 1404-1407.

2. Murphy, F. A.; Suarez, S.; Figgemeier, E.; Schofield, E. R.; Draper, S. M. *Chemistry-a European Journal* **2009**, *15*, 5740-5748.

Appendix D: Chapter 5 Supplementary

D.1 Metal-free polyphosphazene synthesis

D.1.1 General Experimental

All manipulations were carried out under argon using standard Schlenk techniques. Tetrahydrofuran (THF) and toluene were dried on alumina columns under argon. Other analytical grade solvents were purchased from standard chemical suppliers without further purification. The chloropolyphosphazene was synthesised according to Allcocks ROP method.[1] 4-tert-butylphenol ($HOPh^{tBu}$), K_2CO_3, NaH (60% dispersed in mineral oil) and tetrabutyl-ammonium bromide (TBAB) were purchased from Sigma-Aldrich. Substituents 2,6-Bis(2-pyridyl)-4(1*H*)-pyridone (HOTerpy)[2], 4-(2,6-di{pyridin-2-yl}-pyridine-4-yl)phenol (HOPhTerpy)[3], 2,6-di(1*H*-benzimidazol-2-yl)pyridine-4(1*H*)-one (HObbp)[4], 4-phenol-2,6-bis(1-pyrazolyl)pyridine (HOPhbpp)[5] were synthesised via known literature methods.

Microanalyses were performed by Campbell Microanalytical Laboratory, University of Otago. ^{31}P NMR spectra were recorded on a Bruker Avance 400 MHz spectrometer using an external reference of ortho-phosphoric acid, ^{1}H NMR spectra were recorded on a Bruker Avance 500 MHz spectrometer using an internal reference of tetramethylsilane.

DSC measurements were performed by Mark Hindenlang on a Perkin-Elmer DSC-7 unit controlled by a PE7500 computer at the research group of Prof. H. R. Allcock at the Pennsylvania State University, USA. Each sample was annealed twice, 22°C to 80°C and -100°C to 100°C, then -100°C to 150°C.

Molecular weights were performed by Mark Hindenlang. Samples were recorded in THF(+0.1% tetrabutyl-ammonium nitrate salt) at 1mL/minute on a Hewlett-Packard HP 1090 GPC with an HP-1047A refractive index detector with AM gel 10 μm and AM gel 10^4 Å column at the research group of Prof. H. R. Allcock at the Pennsylvania State University, USA.

D.1.2 Experimental Details

D.1.2.1 $[\{NP(OPh^{tBu})(OTerpy)\}_{0.20}\{NP(OPh^{tBu})_2\}_{0.60}\{NP(OPh^{tBu})Cl\}_{0.20}]_n$ (L^{1P})

$[NPCl_2]_n$ (1 g, 8.77 mmol) was dissolved in THF (50 mL), to this a solution containing $HOPh^{tBu}$ (526 mg, 3.51 mmol), HOTerpy (436 mg, 1.76 mmol), and NaH (158 mg, 3.95 mmol) in THF (30 mL) was added. The solution was refluxed for two hours before an additional solution of $HOPh^{tBu}$ (526 mg, 3.51 mmol), NaH (140 mg, 3.51 mmol) and TBAB (10 mol%) in THF (30 mL) were added. This solution was refluxed overnight before an additional solution of $HOPh^{tBu}$ (2.63 g, 17.54 mmol) in THF (30 mL) and toluene (30 mL) was added. This solution was refluxed for an additional two days. The solvent was removed on a rotary evaporator. The solid was redissolved in a minimal amount of THF; this viscous oil was slowly poured into slightly acid water forming thin white strings. The white strings of polymer were collected and dissolved in CH_2Cl_2, then reduced in volume to form the viscous oil again; this was slowly poured into methanol forming white strings of polymer. This process was repeated one more time before being dried under a high vacuum. Yield: 1.20 g (40 %).

$^{31}P\{^1H\}$ NMR ($CDCl_3$): δ -15.38 ppm (1P), -18.43 (4P). ^1H NMR ($CDCl_3$): δ 8.52 ppm (4H), 7.76 (2H), 6.99 (66H), 1.16 (72H). Anal. Calc. for $C_{95}H_{114}N_8O_9P_5Cl\cdot 1^1/_3NaCl$: C, 64.10; H, 6.45; N, 6.29; Cl, 4.65 %. Found: C, 64.24; H, 6.57; N, 6.40; Cl, 4.63 %.

D.1.2.2 $[\{NP(OPh^{tBu})(OPhTerpy)\}_{0.20}\{NP(OPh^{tBu})_2\}_{0.74}\{NP(OPh^{tBu})Cl\}_{0.06}]_n$ (L^{2P})

$[NPCl_2]_n$ (1 g, 8.77 mmol) was dissolved in THF (50 mL), to this a solution containing $HOPh^{tBu}$ (526 mg, 3.51 mmol), HOPhTerpy (572 mg, 1.76 mmol), and NaH (158 mg, 3.95 mmol) in THF (30 mL) was added. The solution was refluxed for two hours before an additional solution of $HOPh^{tBu}$ (526 mg, 3.51 mmol), NaH (140 mg, 3.51 mmol) and TBAB (10 mol%) in THF (30 mL) were added. This solution was refluxed overnight before an additional solution of $HOPh^{tBu}$ (2.63 g, 17.54 mmol) in THF (30 mL) and toluene (30 mL) was added. This solution was refluxed for an additional two days. The solvent was removed on a rotary evaporator. The solid was redissolved in a minimal amount of THF; this viscous oil was slowly poured into slightly acid water forming thin white strings. The white strings of polymer were collected and dissolved in CH_2Cl_2, then reduced in volume to form the viscous oil again; this was slowly poured into

methanol forming white strings of polymer. This process was repeated one more time before being dried under a high vacuum. Yield: 1.60g (50 %)

$^{31}P\{^{1}H\}$ NMR ($CDCl_3$): δ -15.38 ppm (0.3P), -18.58 (4.7P). ^{1}H NMR ($CDCl_3$): δ 8.67 ppm (4H), 7.87 (2H), 7.33 (2H), 6.98 (40.8H), 1.12 (78.3H). Anal. Calc. for: $C_{108}H_{127.1}N_8O_{9.7}P_5Cl_{0.3}\cdot 1^1/_3NaCl$: C, 67.00; H, 6.62; N, 5.79; Cl, 2.99 %. Found: C, 63.44; H, 7.06; N, 4.89; Cl, 3.06 %.

D.1.2.3 $[\{NP(OPh^{tBu})(Obbp)\}_{0.05}\{NP(OPh^{tBu})_2\}_{0.70}\{NP(OPh^{tBu})Cl\}_{0.25}]_n$ (L^{3P})

$[NPCl_2]_n$ (1 g, 8.77 mmol) was dissolved in THF (50 mL), to this a solution containing $HOPh^{tBu}$ (526 mg, 3.51 mmol) and NaH (158 mg, 3.95 mmol) in THF (30 mL) was added. The solution was refluxed for two hours before a solution of HObbp (143 mg, 0.44 mmol), K_2CO_3 (60 mg, 0.44 mmol) and TBAB (10 mol%) in acetone (30 mL) was added to the reaction, the solution was refluxed for a further two hours before a solution containing $HOPh^{tBu}$ (526 mg, 3.51 mmol) and NaH (158 mg, 3.95 mmol) in THF (30 mL) was added. The reaction was refluxed for an additional 3 days before an additional solution of $HOPh^{tBu}$ (2.63 g, 17.54 mmol) in THF (30 mL) and toluene (30 mL). This solution was refluxed for an additional two days. The solvent was removed on a rotary evaporator. The solid was redissolved in a minimal amount of THF; this viscous oil was slowly poured into slightly acid water forming thin white strings. The white strings of polymer were collected and dissolved in CH_2Cl_2, then reduced in volume to form the viscous oil again; this was slowly poured into methanol forming white strings of polymer. This process was repeated one more time before being dried under a high vacuum. Yield: 1.78 g (62 %).

$^{31}P\{^{1}H\}$ NMR ($CDCl_3$): δ -15.37 ppm (5P), -18.45 (15P). ^{1}H NMR ($CDCl_3$): δ 6.98 ppm (148H) 1.29 (306H). Anal. Calc. for: $C_{359}H_{454}N_{25}O_{35}Cl_5P_{20}\cdot 2^1/_3NaCl$: C, 65.21; H, 6.92; N, 5.30; Cl, 3.93%. Found: C, 62.76; H, 6.78; N, 5.39; Cl, 3.92%.

D.1.2.4 $[\{NP(OPh^{tBu})(OPhbpp)\}_{0.20}\{NP(OPh^{tBu})_2\}_{0.55}\{NP(OPh^{tBu})Cl\}_{0.25}]_n$ (L^{4P})

The same procedure was used as for L^{2P}, except HOPhbpp was used in place of HOPhTerpy. Yield: 1.80 g (59 %).

$^{31}P\{^{1}H\}$ NMR ($CDCl_3$): δ -15.33 ppm (1.25P), -18.37 (3.75P). ^{1}H NMR ($CDCl_3$): δ 8.61 ppm (2H), 7.75 (2H), 7.50 (2H), 6.98 (37H), 1.29 (69.75). Anal. Calc. for

$C_{94.50}H_{112.75}N_{10}O_{8.75}P_5Cl_{1.25}\cdot$½NaCl: C, 64.60; H, 6.47; N, 7.97; Cl, 3.53 %. Found: C, 63.78; H, 7.28; N, 9.55; Cl, 3.79 %.

D.2 Synthesis of iron(II) polyphosphazene complexes

D.2.1 General Experimental

All manipulations were carried out under argon using standard Schlenk techniques. All solvents were analytical grade purchased from standard chemical suppliers without further purification. The $Fe(ClO_4)_2.6H_2O$ was purchased from Aldrich.

Microanalyses were performed by Campbell Microanalytical Laboratory, University of Otago. ^{31}P NMR were recorded on a Bruker Avance 400 MHz spectrometer using an external reference of ortho-phosphoric acid.

DSC measurements were performed by Mark Hindenlang on a Perkin-Elmer DSC-7 unit controlled by a PE7500 computer at the research group of Prof. H. R. Allcock at the Pennsylvania State University, USA. Each sample was annealed twice, 22°C to 80°C and -100°C to 100°C, then -100°C to 150°C.

Caution! Perchlorate salts with organic ligands are potentially explosive and should be handled with the necessary precautions

D.2.2 Experimental Details

D.2.2.1 $[Fe(L^{1P})_2](ClO_4)_2$

L^{1P} (300 mg, 0.17 mmol) was dissolved in $CHCl_3$ (50 mL), once dissolved CH_3CN (0.5 mL) was added. $Fe(ClO_4)_2.6H_2O$ (32 mg, 0.088 mmol) was added to the solution, forming a purple solution over an hour. All characterisations in the solution phase were recorded using this solution. The volume of solvent was reduced to 25 mL under vacuum; methanol was gradually added until a precipitate formed. The supernatant liquid was decanted, before additional methanol was added, then the solid was sonicated, before the supernatant liquid was decanted again. The remaining solid was dried under vacuum, producing a purple solid. Yield: 138 mg (42 %).

^{31}P $\{^1H\}$ NMR: δ -14.95 ppm (2P), -18.20 (8P). Anal. Calc. for $C_{190}H_{228}Cl_4FeN_{16}O_{26}P_{10}\cdot$½$CHCl_3$: C, 61.52; H, 6.19; N, 6.03; Cl, 5.24 %. Found: C, 57.63; H, 6.44; N, 6.13; Cl, 5.28 %.

D.2.2.2 $[Fe(L^{2P})_2](ClO_4)_2$

The same method was used for $[Fe(L^{1P})_2](ClO_4)_2$ except L^{2P} was used in place of L^{1P}, forming a purple solid. Yield: 172 mg (54 %).

^{31}P $\{^1H\}$ NMR: δ -14.95 ppm (0.6P), -18.20 (9.4P). Anal. Calc. for $C_{216}H_{252.9}Cl_{2.6}FeN_{16}O_{27.4}P_{10}\cdot$2¾$CHCl_3$: C, 61.13; H, 6.00; N, 5.21; Cl, 8.95 %. Found: C, 58.07; H, 6.26; N, 5.74; Cl, 9.22 %.

D.2.2.3 $[Fe(L^{3P})_2](ClO_4)_2$

The same method was used for $[Fe(L^{1P})_2](ClO_4)_2$ except L^{3P} was used in place of L^{1P}, forming a purple solid.Yield: 177 mg (58%).

^{31}P $\{^1H\}$ NMR: δ -15.01 ppm (10P), -18.07 (30P). Anal. Calc. for: $C_{718}H_{908}Cl_{12}FeN_{50}O_{78}P_{40}\cdot 1^1/_4CHCl_3$: C, 64.68; H, 6.86; N, 5.24; Cl, 4.18 %. Found: C, 60.24; H, 6.93; N, 5.94; Cl, 4.20 %.

D.2.2.4 $[Fe(L^{4P})_2](ClO_4)_2$

The same method was used for $[Fe(L^{1P})_2](ClO_4)_2$ except L^{4P} was used in place of L^{1P}, forming a yellow solid. Yield: 164 mg (51 %).

^{31}P {^{1}H} NMR: δ -12.61 ppm (2.5P), -15.68 (7.5P). Anal. Calc. for $C_{189}H_{225.5}Cl_{4.5}FeN_{20}O_{25.5}P_{10}\cdot{}^{1}/_{4}CHCl_3$: C, 60.77; H, 6.08; N, 7.49; Cl, 4.98 %. Found: C, 62.83; H, 7.32; N, 6.56; Cl, 4.75 %.

D.3 Synthesis of ruthenium(II) polyphosphazene complexes

D.3.1 General Experimental

All manipulations were carried out under argon using standard Schlenk techniques. All solvents were analytical grade purchased from standard chemical suppliers without further purification. The $RuCl_3\cdot 3H_2O$ was purchased from Aldrich. Ru(Terpy)Cl_3[6] and Ru(PhTerpy)Cl_3[7] were synthesised according to literature methods.

Microanalyses were performed by Campbell Microanalytical Laboratory, University of Otago. ^{31}P NMR spectra were recorded on a Bruker Avance 400 MHz spectrometer using an external reference of ortho-phosphoric acid, ^{1}H NMR spectra were recorded on a Bruker Avance 500 MHz spectrometer using an internal reference of tetramethylsilane.

DSC measurements were performed by Mark Hindenlang on a Perkin-Elmer DSC-7 unit controlled by a PE7500 computer at the research group of Prof. H. R. Allcock at the Pennsylvania State University, USA. Each sample was annealed twice, 22°C to 80°C and -100°C to 100°C, then -100°C to 150°C.

D.3.2 Experimental Details

D.3.2.1a [Ru(L^{1P})(Terpy)]Cl_2

L^{1P} (300 mg, 0.17 mmol) was dissolved in THF (20 mL), the solution was heated to 70°C before methanol (15 mL) was slowly added. Once the methanol was fully dispersed Ru(Terpy)Cl_3 (78 mg, 0.17 mmol) and 5 drops of ethylmorpholine was added. The solution was refluxed for 12 hours before being cooled and filtered. The filtrate was reduced in volume to 10 mL before methanol was slowly added until the polymer precipitated. The supernatant liquid was decanted; additional methanol was added and decanted again. The remaining solid was redissolved in dichloromethane; methanol was added to precipitate the polymer again.Yield: 203 mg (55 %).

^{31}P {^{1}H} NMR: δ -15.37 ppm (1P), -18.58 (4P). ^{1}H NMR: δ 6.96 ppm (53 H), 1.13 (72H). Anal. Calc. for $C_{110}H_{125}Cl_3N_{11}O_9P_5Ru\cdot{}^{1}/_{4}CHCl_3$: C, 61.95; H, 5.91; N, 7.21; Cl, 6.22 %. Found: C, 58.16; H, 6.12; N, 7.76; Cl, 3.12 %.

D.3.2.1b [Ru(L^{1P})(PhTerpy)]Cl_2

The same method was used for [Ru(L^{1P})(Terpy)]Cl_2 except Ru(PhTerpy)Cl_3 was used in place of Ru(Terpy)Cl_3. Yield: 191 mg (50 %).

^{31}P {^{1}H} NMR: δ -15.40 ppm (1P), -18.47 (4P). ^{1}H NMR: δ 6.96 ppm (70H), 1.13 (72H). Anal. Calc. for $C_{116}H_{142}Cl_3N_{11}O_9P_5Ru\cdot 2{}^{1}/_{3}CH_4O$: C, 62.57; H, 6.71; N, 6.78; Cl, 4.68 %. Found: C, 63.15; H, 7.40; N, 5.59; Cl, 3.18 %.

D.3.2.2a [Ru(L^{2P})(Terpy)]Cl_2

The same method was used for [Ru(L^{1P})(Terpy)]Cl_2 except L^{2P} was used in place of L^{1P}. Yield: 383 mg (63 %).

^{31}P {^{1}H} NMR: δ -15.67 ppm (0.3 P), -18.47 (4.7 P). ^{1}H NMR: δ 6.96 ppm (59.8 H), 1.13 (78.3 H). Anal. Calc. for $C_{123}H_{138.1}N_{11}O_{9.7}P_5Cl_{2.3}Ru\cdot$½$CHCl_3$: C, 63.86; H, 6.01; N, 6.63; Cl, 5.80 %. Found: C, 59.44; H, 5.88; N, 7.48; Cl, 3.58 %.

D.3.2.2b [Ru(L^{2P})(PhTerpy)]Cl_2

The same method was used for [Ru(L^{2P})(Terpy)]Cl_2 except Ru(PhTerpy)Cl_3 was used in place of Ru(Terpy)Cl_3. Yield: 365 mg (58 %).

^{31}P {^1H} NMR: δ -15.67 ppm (0.3 P), -19.20 (4.7 P). ^1H NMR: δ 6.96 ppm (63.8 H), 1.13 (78.3 H). Anal. Calc. for $C_{129}H_{142.1}N_{11}O_{9.7}P_5Cl_{2.3}Ru$: C, 66.23; H, 6.12; N, 6.59; Cl, 3.49 %. Found: C, 71.21; H, 10.15; N, 3.21; Cl, 4.02 %.

D.3.2.3a [Ru(L^{3P})(Terpy)]Cl_2

The same method was used for [Ru(L^{1P})(Terpy)]Cl_2 except L^{3P} was used in place of L^{1P}. Yield: 263 mg (83 %).

^{31}P {^1H} NMR: δ -15.42 ppm (5 P), -18.62 (15 P). ^1H NMR: δ 6.96 ppm (159 H), 1.13 (306 H). Anal. Calc. for $C_{374}H_{465}N_{28}O_{35}Cl_7P_{20}Ru \cdot ½CH_2Cl_2$: C, 64.96; H, 6.78; N, 5.66; Cl, 4.10 %. Found: C, 59.60; H, 6.76; N, 4.86; Cl, 3.99 %.

D.3.2.3b [Ru(L^{3P})(PhTerpy)]Cl_2

The same method was used for [Ru(L^{3P})(Terpy)]Cl_2 except Ru(PhTerpy)Cl_3 was used in place of Ru(Terpy)Cl_3. Yield: 261 mg (81 %).

^{31}P {^1H} NMR: δ -15.42 ppm (5 P), -18.61 (15 P). ^1H NMR: δ 6.96 ppm (163 H), 1.13 (306 H). Anal. Calc. for $C_{380}H_{469}N_{28}O_{35}Cl_7P_{20}Ru \cdot ½CH_2Cl_2$: C, 65.29; H, 6,77; N, 5.60; Cl, 4.05 %. Found: C, 63.18; H, 7.08; N 5.24; Cl, 4.12%.

D.3.2.4a [Ru(L^{4P})(Terpy)]Cl_2

The same method was used for [Ru(L^{1P})(Terpy)]Cl_2 except L^{4P} was used in place of L^{1P}. Yield: 226 mg (61 %).

^{31}P {^1H} NMR: δ -15.67 ppm (1.25 P), -18.60 (3.75 P). ^1H NMR: δ 6.96 ppm (54 H), 1.13 (69.75 H). Anal. Calc. for $C_{109.5}H_{123.75}N_{13}O_{8.75}P_5Cl_{3.25}Ru \cdot 4CH_4O$: C, 60.28; H, 6.23; N, 8.05; Cl, 5.10 %. Found: C, 60.88; H, 6.63; N, 6.45; Cl, 4.68 %.

D.3.2.4b [Ru(L^{4P})(PhTerpy)]Cl_2

The same method was used for [Ru(L^{4P})(Terpy)]Cl_2 except Ru(PhTerpy)Cl_3 was used in place of Ru(Terpy)Cl_3. Yield: 210 mg (55 %).

^{31}P {^{1}H} NMR: δ -15.63 ppm (1.25 P), -18.60 (3.75 P). ^{1}H NMR: δ 6.96 ppm (58 H), 1.13 (69.75 H). Anal. Calc. for: $C_{115.6}H_{127.75}N_{13}O_{8.75}P_5Cl_{3.25}Ru \cdot 4^2/_3CH_4O$: C, 61.19; H, 6.26; N, 7.72; Cl, 4.89 %. Found: C, 61.72; H, 6.92; N 6.24; Cl, 4.92 %.

D.4 References

1. Allcock, H. R.; Kugel, R. L. *Journal of the American Chemical Society* **1965**, *87*, 4216-4217.

2. Constable, E. C.; Ward, M. D. *Journal of the Chemical Society-Dalton Transactions* **1990**, 1405-1409.

3. Spahni, W.; Calzaferri, G. *Helvetica Chimica Acta* **1984**, *67*, 450-454.

4. Drew, M. G. B.; Hill, C.; Hudson, M. J.; Iveson, P. B.; Madic, C.; Vaillant, L.; Youngs, T. G. A. *New Journal of Chemistry* **2004**, *28*, 462-470.

5. Madhu, N. T.; Salitros, I.; Schramm, F.; Klyatskaya, S.; Fuhr, O.; Ruben, M. *Comptes Rendus Chimie* **2008**, *11*, 1166-1174.

6. Sullivan, B. P.; Calvert, J. M.; Meyer, T. J. *Inorganic Chemistry* **1980**, *19*, 1404-1407.

7. Murphy, F. A.; Suarez, S.; Figgemeier, E.; Schofield, E. R.; Draper, S. M. *Chemistry-a European Journal* **2009**, *15*, 5740-5748.